A Unified Approach to Unbiased Frictional Contact Modelling from First-order to Higher-order Finite Elements



Indrajeet Sahu

St Cross College

University of Oxford

A thesis submitted for the degree of

Doctor of Philosophy

Trinity 2024

To my family, for their unwavering love and support

Acknowledgements

This doctoral journey has been an enriching experience marked by challenges and moments of joy. I am deeply grateful to all who have supported me along the way.

Firstly, I sincerely thank my supervisor, Prof. Nik Petrinic, for providing me with this research opportunity and sharing valuable insights. I also extend my gratitude to Prof. Daniel Eakins, Dr. Simone Falco, Dr. Mattia Montanari, and Dr. Huifang Liu for their suggestions and expertise. Additionally, I would like to thank Prof. Edmund Tarleton and Prof. Maria Charalambides for their encouraging feedback.

I gratefully acknowledge the financial support by the Engineering and Physical Sciences Research Council (EPSRC) and Rolls-Royce through the Strategic Partnership in Computational Science for Advanced Simulation and Modelling of Engineering Systems - ASiMoV (EPSRC Reference EP/S005072/1).

Thanks to my friends, lab mates, the college, OUWC, and OUCKC for making this journey memorable. Lastly, my heartfelt thanks to my family for their constant support in making this possible.

Abstract

Contact modelling is a critical part of simulations used in the design and development of complex engineering systems, as contact is the principal method of force transmission between solids. It helps analyse surface interactions to predict stress distribution, motion, and deformation of systems. However, the currently available methods to model contact with explicit finite element method do not offer high levels of accuracy. These methods are also biased due to the master-slave labelling of surfaces and incur additional computational costs in their dual-pass approaches for offsetting the effect of biasing. Such biasing is also seen in the available frictional contact formulations which are based on the sliding of slave nodes over master surface. The complexity of the aforementioned challenging issues increases in the contact interaction of higher-order elements due to their nonlinear mathematical behaviour. Higher-order elements are a lucrative choice for sophisticated designs owing to the enhanced capability of their nonlinear shape functions to better represent surface curvature.

This thesis presents highly accurate single-pass unbiased frictional contact algorithms using the penalty method. The proposed methodology penalises the true interpenetration for compressive loads and evaluates the frictional states of stick and slip on the patches of contact interface formed by overlapping segment-to-segment (STS) pairs. For each STS pair, a local midplane is defined for unbiased constraint enforcement such that the equality of tractions evaluated on opposite segments is inherently maintained. The relative sliding between pairs is penalised through the elastoplastic analogy of friction in the predictor-corrector approach, accounting for changes in convective coordinates of both facets, thus ensuring no biasing. For higher-order elements, local midplanes are defined per subfacet pair obtained by subdivision of interacting element facets, which can also be corrected to account for local surface curvature. All contact algorithms have been rigorously tested for various surface interactions, including flat and curved surfaces under compressive load and frictional conditions. The algorithms successfully passed multiple tests - contact patch test, Hertzian contact with and without friction for different materials, two beam test, indentation with rigid punch, frictional self-contact, high-rate impact of two bars with elastic and inelastic materials, frictional sliding for stick-slip effect, twisting indentation problem, frictional rolling, elastic collisions, etc. Here, the

complex challenge of self-contact problems is conveniently handled by the proposed unbiased methodology in solving compressive and frictional traction with auto-detection. Surfaces on the same body do not run in the master-slave labelling issues, and the constraint enforcement also does not face the issues of self-redundancy on shared edges in self-contact. Fundamentally, the overarching capability of the proposed algorithms unifies contact interactions across all orders of finite elements.

The series of developments presented in this thesis, going from first-order to higher-order elements, will offer finite element analysts a range of discretisation choices for practical problems. The proposed robust and versatile methodology will immensely help in diverse applications where high-accuracy frictional contact algorithms will accelerate the robust design and development of complex systems by enabling high confidence in numerical solutions.

Publications

Manuscripts

- Sahu, Indrajeet, and Nik Petrinic. 2024. "Midplane Based 3D Single Pass Unbiased Segment-to-Segment Contact Interaction Using Penalty Method." *under submission*.
- Sahu, Indrajeet, and Nik Petrinic. 2024. "Patch Based Unbiased 3D Frictional Contact Formulation for Finite Element Algorithms." *accepted in Computer Methods in Applied Mechanics and Engineering*.
- Sahu, Indrajeet, and Nik Petrinic. 2024. "Unbiased Higher-order Frictional Contact Using Midplane Based Segment-to-Segment Penalty Method." *Draft Completed*.

Conferences

- Sahu, Indrajeet, and Nik Petrinic. "A Novel 3D Surface-to-Surface Unbiased Contact Algorithm for Penalty Method Solution of Frictional Contact Problems." U.S. National Congress on Computational Mechanics, 23-27 July 2023, Albuquerque, New Mexico - USA.
- Sahu, Indrajeet, and Nik Petrinic. "An Unbiased Surface-to-Surface Frictional Contact Algorithm for Higher Order Finite Elements." International Conference on Computational Plasticity, Fundamentals and Applications (COMPLAS), 5-7 Sep 2023, Barcelona - Spain.
- Sahu, Indrajeet, and Nik Petrinic. "Unbiased Segment-to-Segment Frictional Contact Algorithms for Surfaces with Various Discretisation Topologies." International Conference on the Dynamic Behaviour of Composites (DyCOMP), 3-5 Sep 2024, Enna, Sicily - Italy.

Contents

List of Notation x

1 Introduction 1
- 1.1 Motivation . . . 1
- 1.2 Research objectives . . . 4
- 1.3 Contributions and achievements . . . 5
- 1.4 Outline of this thesis . . . 8

2 Background 11
- 2.1 Introduction . . . 11
- 2.2 Continuum solid mechanics . . . 12
  - 2.2.1 Kinematics . . . 12
  - 2.2.2 Stress measures . . . 15
  - 2.2.3 Balance equations . . . 16
  - 2.2.4 Governing equations in strong form . . . 17
  - 2.2.5 Material modelling . . . 18
- 2.3 Continuum contact mechanics . . . 19
  - 2.3.1 Contact kinematics . . . 20
  - 2.3.2 Contact constraints . . . 22
- 2.4 Finite element methods . . . 23
  - 2.4.1 Spatio-temporal discretisation and numerical integration . . . 25
  - 2.4.2 First and higher-order finite elements . . . 30
- 2.5 Computational contact mechanics . . . 32
  - 2.5.1 Contact discretisation strategies . . . 32
  - 2.5.2 Contact constraint enforcement techniques . . . 33
  - 2.5.3 Solution procedure . . . 34

3 First-order elements in frictionless contact 37
- 3.1 Introduction . . . 39
- 3.2 Problem description . . . 42
  - 3.2.1 Strong formulation of the continuum problem of contact . . . 43
  - 3.2.2 Variational form of the solution . . . 44

3.2.3 Contact constraints 46
3.3 Midplane based segment-to-segment contact discretisation 46
3.3.1 Continuum based description 47
3.3.2 Description in 3D discretised domains 48
3.3.3 Contact integral 56
3.4 Solution procedure 60
3.5 Some numerical experiments 62
3.5.1 *Contact patch test* 63
3.5.2 *Two beam bending test* 67
3.5.3 *Hertzian contact* 67
3.5.4 *Indentation test with a rigid flat punch* 76
3.5.5 *Self-contact tests* 78
3.5.6 *Impact between two bars* 82
3.5.7 *Inclined impact of a ball on a rigid plane* 85
3.6 Conclusion 87
References 88
3.7 Supplementary discussion 92

4 Unbiased frictional contact **96**
4.1 Introduction 98
4.2 Unbiased frictional contact 101
4.2.1 Description in continuum 101
4.2.2 Description in discretised domain 103
4.3 Finite element solution 111
4.4 Numerical experiments 114
4.4.1 *Block pushed against a slab* 115
4.4.2 *Hertzian frictional contact - Cattaneo and Mindlin's problem* 120
4.4.3 *Twisting Indentation Problem* 123
4.4.4 *Self-contact test* 125
4.4.5 *Impact of a ring at an angle* 127
4.4.6 *Rolling of a cylinder* 130
4.5 Conclusion 130
References 131
4.6 Supplementary discussion 133

5 Higher-order elements in frictional contact **136**
5.1 Introduction . . . 137
5.2 Problem description . . . 141
5.2.1 Variational formulation . . . 142
5.3 Contact problem with higher-order elements . . . 143
5.3.1 Midplane-based contact for higher-order elements . . . 143
5.3.2 An additional midplane correction . . . 148
5.3.3 Unbiased frictional contact . . . 150
5.3.4 Error of interpolation . . . 151
5.4 Solution algorithm . . . 153
5.5 Case of serendipity elements . . . 155
5.6 Numerical experiments . . . 157
5.6.1 *Contact patch test* . . . 158
5.6.2 *Hertzian contact* . . . 158
5.6.3 *Elastic collision of spheres* . . . 164
5.6.4 *Frictional sliding: Block sliding against a slab* . . . 166
5.6.5 *Frictional self-contact* . . . 169
5.6.6 *Inelastic collision of two bars* . . . 169
5.7 Conclusion . . . 171
References . . . 172
5.8 Supplementary discussion . . . 175

6 Conclusion and outlook **176**
6.1 Summary and achievements . . . 176
6.2 Limitations and remedies . . . 180
6.3 Future perspectives . . . 182

References **185**

List of Notation

Representation style for scalars, tensors and matrices

f, F . . . . . Scalar

$\boldsymbol{f}$ . . . . . Continuous Vector (first-order tensor)

$\boldsymbol{F}$ . . . . . Second-order tensor

$\mathbf{f}$ . . . . . Discrete vector

$\mathbf{F}$ . . . . . Discrete matrix

Operators and Symbols

$\dot{(\cdot)}$ . . . . . First time derivative

$\ddot{(\cdot)}$ . . . . . Second time derivative

$\tilde{(\cdot)}$ . . . . . A quantity on boundary

$\bar{(\cdot)}$ . . . . . Prescribed quantity

$\|(\cdot)\|$ . . . . . Euclidean vector norm

$\mathbf{Proj}_{\gamma}(\cdot)$ . . . . Projection of $(\cdot)$ on plane γ

$\otimes$ . . . . . Dyadic product

$\delta(\cdot)$ . . . . . Variation of $(\cdot)$

$\Delta(\cdot)$ . . . . . Increment in $(\cdot)$ in one time step

$\boldsymbol{I}$ . . . . . Identity tensor

$\mathbb{R}$ . . . . . Set of real numbers

Domains and boundaries

Ω . . . . . Reference configuration of domain

Ω_t . . . . . Current configuration of domain

$\gamma, \partial\Omega$ . . . . . Domain boundary in the current configuration

γ_h . . . . . Discretised boundary in the current configuration

γ_u . . . . . Dirichlet boundary

γ_σ . . . . . Neumann boundary

(ξ_1, ξ_2, ξ_3) . . . . Element parametric coordinates

(ξ_1, ξ_2) . . . . . Surface convective coordinates

Kinematics

$\mathbf{e}_i$ . . . . . Basis vector along the ith direction

$\boldsymbol{X}$ . . . . . A reference configuration point

$\boldsymbol{x}$ . . . . . A current configuration point

$\boldsymbol{u}$ . . . . . Displacement

$\dot{\boldsymbol{u}}, \dot{\boldsymbol{x}}$ . . . . . Velocity

$\ddot{\boldsymbol{u}}, \ddot{\boldsymbol{x}}$ . . . . . Acceleration

Contact .

$\boldsymbol{n}_{\mathbf{mp}}$ . . . . . Midplane normal

$\boldsymbol{n}_{\mathbf{rp}}$ . . . . . Representative plane normal

$\boldsymbol{x}_m$ . . . . . A point on midplane

$\boldsymbol{g}_N$ . . . . . Normal gap vector between surfaces

$\boldsymbol{g}_N^i$ . . . . . Normal gap vector of facet i at any midplane point

$\boldsymbol{g}_T$ . . . . . Tangential sliding

$\boldsymbol{t}$ . . . . . Traction

$(\cdot)_N, (\cdot)^N$ . . . . Normal component

$(\cdot)_T, (\cdot)^T$ . . . . Tangential component

Φ . . . . . Slip function

ϵ_N . . . . . Normal penalty

f_s . . . . . Normal penalty scaling factor

ϵ_T . . . . . Tangential penalty

μ . . . . . Coefficient of friction

Functions

$H(\cdot)$ . . . . . Heaviside function

δ_{ij} . . . . . Kronecker delta function

Finite Elements

ψ_i . . . . . Shape function associated with i^{th} node

Ψ . . . . . Shape function matrix

$\mathbf{R}$ . . . . . Nodal force matrix

Abbreviations

NTN . . . . . Node-to-node

NTS . . . . . Node-to-segment

NTS-AR . . . Node-to-segment area regularisation

STS . . . . . Segment-to-segment

FEM . . . . . Finite element method

FEA . . . . . Finite element analysis

PDE . . . . . Partial differential equation

2D . . . . . Two-dimensional

3D . . . . . Three-dimensional

1 Introduction

1.1 Motivation

Contact is ubiquitous in all systems around us - whether natural or human-made. Simple or complex, these systems consist of different parts that interact through contact, and this interaction is critical in a wide range of applications, including automotive, aerospace, defence, manufacturing, railways, robotics, biomedical and biomechanical engineering, consumer products, sports equipment, space systems etc., see Fig. 1.1. The phenomenon of contact interaction encompasses different length scales ranging from nanoscale to macroscopic level and time scales from slow quasi-static contact to fast high-velocity impact. Contacting surfaces can be studied for a multitude of physical aspects at different length scales in tribology - mechanical, thermal, electromagnetic, metallurgy, quantum, etc. [1]. This thesis, in particular, focuses on the mechanical aspect of contact modelling at a macroscopic level, which is sufficient for most systems of engineering interest.

Developing an understanding of contact is very crucial in solid mechanics, as contact is the principal method by which loads are applied on solids. The only other general loads are due to pressure exerted on a body by fluids or body forces like gravitational and electromagnetic forces. However, in nearly all



Figure 1.1: Contact challenges are prevalent in all physical systems.[1]

practical applications, the bodies are invariably held in equilibrium or motion by contact forces.

For a mathematical representation, all physical problems are, in general, described by mathematical models of partial differential equations (PDEs) with initial and boundary conditions, thereby implying a continuum. Contact is a common interface between two close bodies with separate continuous surfaces. So mathematically, contact is a problem of complex boundary conditions that can evolve with time depending on system changes. General systems can have nonlinearities due to material (having nonlinear constitutive behaviour), geometry (e.g. large deformation), and contact introduces an additional nonlinearity. Numerous studies

[1]Some images are reproduced with permission from Springer Nature [2][3][4][5].

in contact mechanics have provided analytical solutions to some general problems, with the earliest well-known study being the work on contact pressure distribution for elastic bodies by Hertz in 1882 [6]. The frictional effect is a crucial aspect of interface mechanics, with the initial understanding of the subject being developed by Amonton and Coulomb. Some well-regarded theoretical foundations of contact mechanics can be referred to in the textbooks by Johnson [7] and Barber [8].

In practical settings, general systems have complex domain descriptions and boundary conditions, so the governing mathematical models do not have closed-form analytical solutions. This challenge led to the development of finite element methods (FEM) in the past century (refer [9] for a brief history), which seek to find solutions in an approximate sense, with the accuracy being dependent upon element type, accuracy of input data, numerical methodology, computational power, etc. In the last half-century, FEM has established itself as a default research and development tool in engineering applications. Along with advances in computational science, a diverse set of solution strategies have been devised with continuous research developments for boosting the solution accuracy of finite element analysis. Yet, one critical and often bottleneck challenge for practical problems of multibody physical systems is estimating the contact forces between solids that might interact at any point in time.

Accurate modelling of contact is critical in finite element analysis as the boundary effects determine the prediction of system evolution. Given the omnipresence of contact, there is an ever-growing demand for high-accuracy simulations of interface mechanics in broad applications of both scientific and industrial interests. In scientific fields, such high-accuracy simulations can aid in unravelling some fundamental mysteries in physical and biological systems. On the other hand, in industrial environments, the ability to accurately simulate virtual designs with precise contact modelling is quintessential for rapid and innovative product development with minimal resource consumption in building prototypes. Accurate modelling is also central to monitoring the performance and structural integrity of digital twins that are gaining high popularity recently [10][11].

With this motivation, this thesis focuses on developing accurate frictional contact algorithms for complex surface descriptions while rigorously testing them under various contact conditions to establish their robustness and versatility.

1.2 Research objectives

Contact modelling in the explicit finite element framework remains an active research challenge for seeking high-accuracy techniques in nonlinear solid mechanics of multibody contact. Converting an original mathematical problem into a corresponding numerical model and its subsequent algorithmic implementation requires specific strategies to handle contact interactions while closely adhering to the underlying physics. Although multiple methods have been proposed in the past, the demand for methods providing greater accuracy is ever-increasing with the continuous development of complex systems. Advancements in techniques for high-accuracy modelling of contact problems that also include frictional effects are the core theme of this work. In FEM, first-order elements are typically used for discretisation in general analysis. However, they differ significantly from any original surfaces having smooth curvature. On the other hand, higher-order elements can better capture the curvature and present an opportunity for more accurate contact modelling. Numerous questions on extending capabilities to model frictional contact are answered in this thesis; these are aimed towards

I. High-accuracy frictionless contact model for first-order elements

II. High-accuracy frictional contact model

III. High-accuracy frictional contact model for higher-order elements to handle complex surface description

These three fundamental questions guide the developments presented in this thesis while referencing an exposition of multiple past pursuits in the literature.

1.3 Contributions and achievements

This thesis is a compilation of work on multiple fronts of research objectives and the arc of its presentation follows a sequential development of contact formulations ranging from frictionless and frictional first-order elements to higher-order elements. Prediction of changes in system configuration in multibody systems is reliant upon the boundary conditions enforced by contact. While there have been advancements in high accuracy modelling of contact in implicit finite element method [12][13], there is a lack of an equivalent development in explicit FEM, which potentially restricts the choice of time integration scheme for analysis. A methodology to handle contact with high accuracy will expand the choices of schemes for finite element analysts. This work seeks to expand the scope of applicability to provide (1) high accuracy of solutions using explicit methods and (2) prospects of competitive advantage in selecting explicit schemes over implicit ones for contact problems that involve geometric or material nonlinearities. Although contact formulations in this work are presented in an environment of explicit FEM, the concepts presented herein would also be of immense help in developing similar methodologies in implicit FEM.

The questions presented in the research objective are answered through an in-depth conceptual description of the proposed novel formulations with major contributions being

- **Unbiased segment-to-segment contact:** In discretised domains used in FEM, contact constraints are applied over pairs of discrete entities on interacting surfaces. While NTS has been the most widely used scheme, it is highly prone to erroneous results. STS methods [12] provide better accuracy owing to the constraint enforcement over interacting regions of both surfaces. However, both NTS and STS methods presented in the literature are biased in how they treat interacting surfaces by assigning master and slave labelling over them. To account for this biasing, a midplane-based 3D STS method is proposed, which enforces contact constraints using the penalty method in an unbiased manner over the entire contact region without master-slave labelling.

- **Single-pass technique:** In typical master-slave approaches, biasing issues are addressed by carrying out a second pass contact traction evaluation in each solution step, referred to as the dual pass approach [14]. However, all the contact formulations presented in this work inherently preserve the unbiased nature by only carrying out a single pass. These formulations ensure the equality of tractions and avoid the expensive computational cost of a second pass.

- **Unbiased friction formulation:** All surfaces in the real world have roughness that offers a response to external loads on a system attempting to induce relative motion at the interface. While there are some frictional formulations available in the literature [15][16][17][18], they consider the biased traditional approach of contact interactions of discrete points of slave surface moving over the master surface. To address this issue of biasing, a patch-based STS 3D frictional contact formulation is presented in this work, which uses a predictor-corrector approach for directly enforcing constraints of stick and slip states of friction over the overlapping regions (patches) of interacting segments, thereby maintaining an unbiased approach.

- **Self-contact:** In some cases, the deformation of bodies might lead to contact between their surfaces, referred to as self-contact problems. Biased formulations in a self-contact problem pose an anomaly in labelling the two parts of the same surface as slave and master. Moreover, under compression, there is also an issue of redundancy of constraints on a shared edge in self-contact being a part of contacting segments on opposite sides, e.g. near cracks, as shown recently in [14]. However, the inherent unbiased nature of the presented formulation does not have any anomaly of contacting segments as the self-contact problems are treated akin to contact between different bodies. The proposed formulations for normal and frictional contact also do not encounter the self-redundancy issue as they enforce constraints on the

common interface, which may result in equivalent nodal forces on shared nodes, thereby maintaining the mathematical consistency of element technology.

- **Higher-order elements in contact:** Unlike first-order ones, higher-order finite elements have nonlinear basis functions that allow them to better capture the curvature of boundaries. Discretised boundaries that better capture the complexity of surface description offer a promising choice in contact problems, as contact is a surface-dependent phenomenon. Contact algorithms presented in the first-order and frictional formulations are further extended to higher-order elements and, in particular, are presented through contact between second-order Lagrangian elements.

- **Robustness in handling flat and curved surfaces:** All the algorithms can accurately model interfaces formed by combinations of flat and curved surfaces in both frictionless and frictional cases. For frictional cases, different possibilities of friction states like fully stick, fully slip, and partial slip are all shown through various examples.

- **Non-conformal meshes in contact:** General contact problems would involve interactions between surfaces that have different discretisations. Although this becomes challenging in biased approaches, the proposed approach robustly handles contact between meshes with non-matching nodes on the interface. For contact between flat surfaces, the accuracy of solutions even matches the accuracy of underlying finite elements.

- **Versatility to handle both static and dynamic contact:** Contact cases can range from slow static to dynamic problems depending upon the initial and boundary conditions. In this work, a range of examples are presented that cover both static and dynamic problems.

- **Elastic, Inelastic, and dissimilar materials in contact:** Examples involving contact between both elastic and inelastic materials are presented in this work. For contact between flat and curved surfaces, combinations of

materials with a range of differences in stiffness are presented to show the versatility of the proposed methodology.

- **Large deformation:** Both compressive and frictional formulations across finite elements work remarkably well not only in small strain problems but have also been demonstrated to work in the large deformation problems involving contact in diverse settings.

- **Studying the effect of interpenetration:** While a strong description of contact problems imposes a strict impenetrability requirement, the use of the penalty method in this work allows for interpenetration between surfaces. The effect of this interpenetration in stress distribution in the contacting bodies studied in this work shows the requirement of allowing controlled interpenetration between curved surfaces for the smoothness of contact pressure. This is particularly essential for first-order elements as they have high sudden jumps in surface normals around the nodes and edges. In comparison, the higher-order elements are still able to provide good smoothness.

- **Techniques that aid in large scale modelling:** Contact constraint enforcement in normal and tangential directions is studied using the penalty method. This helps avoid the large system size typically seen when using Lagrange multipliers. Although the penalty method leads to interpenetration, a study on the oscillations in Hertzian contact highlights the importance of allowing interpenetration in a controlled manner.

1.4 Outline of this thesis

This is an integrated thesis that includes a compilation of three manuscripts in Chapters 3,4,5. The overall content is ordered to present all contributions with increasing complexity and intricacies of conceptual descriptions. All the core chapters follow the same arc of presenting a brief of historical developments, followed by

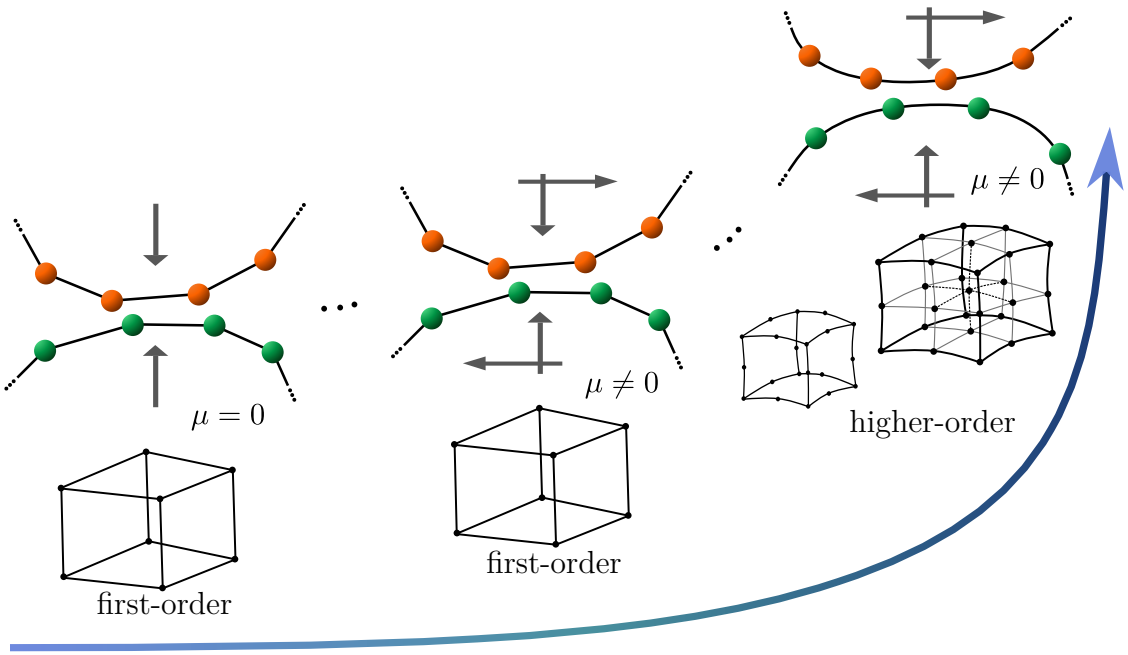

Figure 1.2: Thesis outline: arc of development going from first-order frictionless to higher-order frictional contact formulations.

novel formulations and their conceptual descriptions, procedure of computational implementation, and rigorous testing through a diverse set of numerical experiments. The increasing level of complexity of development is depicted in Fig. 1.2. All symbols in the thesis have usual meanings, as shown in notation, but contextual symbols have been used in some places with local explanations. The remainder of this thesis is organised as follows -

Chapter 2 presents a brief background on fundamentals of continuum solid mechanics together with its extension to contact mechanics, finite element analysis as a numerical tool to solve real-world problems, and finally, it gives an overview of computational procedures employed for handling contact problems.

Chapter 3 presents the unbiased contact formulation for frictionless contact using first-order elements. It introduces the concept of midplane for STS contact that is consistently utilised in all further chapters for enforcing contact constraints in normal as well as tangential directions. It describes the procedure of constructing representative facet planes and the midplane where the contact region is defined for each contact pair. A computational procedure of finding contact pairs and

interpenetration between them is described which subsequently progresses towards contact traction and equivalent nodal force calculations. This paper is an extended version of the submitted paper, including a convergence study using curved-on-flat surface contact interaction.

Chapter 4 continues the theme of an unbiased approach for developing a single pass frictional contact formulation. It starts with a continuum description of the interface that is decomposed into patches that correspond to the overlapping region of STS pairs in discrete settings. Using the elastoplastic analogy, a novel frictional contact formulation is proposed that accounts for the tangential motion between the STS pairs to enforce the notion of stick-slip.

Chapter 5 extends the development of frictionless and frictional contact formulation to higher-order elements by focusing on second-order Lagrangian elements. It describes how facets of higher-order elements can be subdivided into subfacets, and contact constraints in normal and tangential directions can be applied over pairs of subfacets from opposite surfaces.

Finally, Chapter 6 summarises key achievements in this thesis and highlights some of the most important results. It continues the discussion on some limitations along with their remedies and envisions future directions for the possibilities that lie ahead.

2 Background

2.1 Introduction

The numerical solutions to general structural problems are rooted in transforming continuum assumption into discretised space and time. Mathematical models representing the physics of continuum are PDEs. These are converted into a corresponding variational form for developing finite element methods to obtain a computationally possible solution. This chapter provides a brief background of continuum mechanics and finite element methods for understanding computational frameworks used in contact problems. Section 2.2 introduces the continuum assumption used to solve structural problems along with major equations that govern the deformation of solids. Within this continuum framework, Section 2.3 provides a description of contact problems and the equations therein. The continuum description of solids is subsequently utilised to develop the finite element method presented in Section 2.4. Finally, the computational methodologies employed in the solution of contact problems, which is also the core theme of this thesis, are presented in Section 2.5.

2.2 Continuum solid mechanics

All materials are composed of discrete entities - atoms or molecules. However, to study engineering systems designed at the macroscopic scale, the continuum hypothesis is applied to materials with the assumption of continuity in their spatial description. Under this assumption, all quantities in the material domain, like material points, displacements, densities, etc., are describable at all spatial points, allowing us to deploy the full force of calculus machinery, i.e. derivatives at any point and integrals over spatial regions, for formulating governing equations and devising their solutions.

This section provides an outline of quantities and relations that govern the deformation of continuum solids, e.g. kinematic relations, equations of balance, governing equations, constitutive equations, etc. A holistic account of continuum mechanics can be referred to in [19][20][21][22][23].

2.2.1 Kinematics

Kinematics refers to those results of continuum mechanics that do not depend on their dynamical nature and solely depend upon the geometrical description. In this section, a description of geometric quantities in a body undergoing motion and deformation is presented through kinematic measures.

Consider a body described in a reference configuration as Ω_0 in $\mathbb{R}^3$ at time $t = 0$ and its current configuration as $\Omega_t (\subset \mathbb{R}^3)$ as shown in Fig. 2.1. Any material point $\boldsymbol{X}$ in the reference configuration is related to its corresponding position $\boldsymbol{x}$ in the current configuration through an orientation preserving one-to-one mapping (except a possibility of self-contact), i.e. $\boldsymbol{x}(\boldsymbol{X}, t) = \phi(\boldsymbol{X}, t)$. One-to-one mapping excludes the physical impossibility of self-intersection; however, in the case of self-contact, two distinct material points on the boundary in the original configuration might occupy the same point in the contact region. The one-to-one mapping also allows us to invert the mapping ϕ, i.e., $\boldsymbol{X} = \phi^{-1}(\boldsymbol{x}, t)$. The point $\boldsymbol{x}$ is also related to its

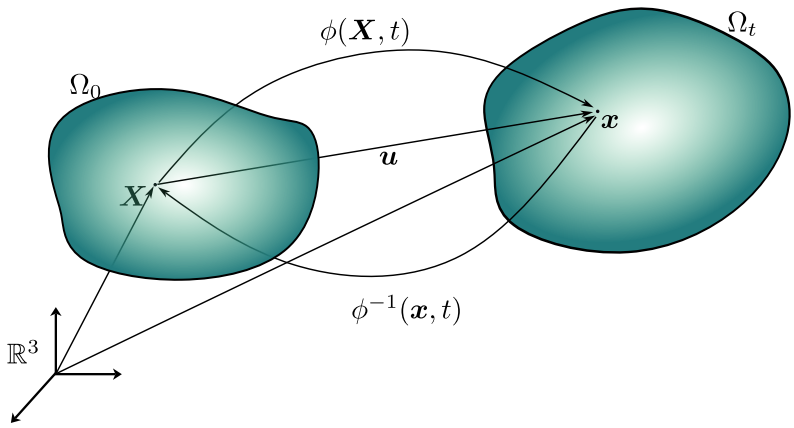

Figure 2.1: Reference (Ω_0) and current (Ω_t) configurations of a body undergoing motion and deformation with time

displacement from the original position in the reference configuration as

$$\boldsymbol{x} = \boldsymbol{X} + \boldsymbol{u}(\boldsymbol{X}, t) \tag{2.1}$$

In order to describe the deformation at any spatial point $\boldsymbol{X}$, any infinitesimally small material fibre $d\boldsymbol{X}$ considered about this point deforming to be $d\boldsymbol{x}$ in the current configuration can be given by

$$d\boldsymbol{x} = \boldsymbol{F} d\boldsymbol{X} \tag{2.2}$$

where $\boldsymbol{F}$ is the deformation gradient, which is a fundamental measure for deformation and strain in solid mechanics and is defined as

$$\boldsymbol{F} = \frac{\partial \boldsymbol{x}}{\partial \boldsymbol{X}} = \boldsymbol{I} + \frac{\partial \boldsymbol{u}}{\partial \boldsymbol{X}} \tag{2.3}$$

$$\text{or, } F_{ij} = \frac{\partial x_i}{\partial X_j} = \delta_{ij} + \frac{\partial u_i}{\partial X_j} \tag{2.4}$$

where $\boldsymbol{I}$ is second-order identity tensor. Physically possible deformations that exclude self-penetration and collapsing of material fibre ensure positivity of the Jacobian, i.e. $J = \det\boldsymbol{F}$. The Jacobian represents the change in infinitesimal volume around $\boldsymbol{X}$ on mapping to $\boldsymbol{x}$, i.e.

$$dV = J dV_0 \tag{2.5}$$

Further, the deformation gradient also aids in mapping of an infinitesimal area $d\boldsymbol{A}_0$ about $\boldsymbol{X}$ oriented in some direction $\boldsymbol{N}$ (i.e., $d\boldsymbol{A}_0 = dA_0\boldsymbol{N}$), deformed to the current configuration $d\boldsymbol{A}$ $(= dA\boldsymbol{n})$ as

$$d\boldsymbol{A} = J\boldsymbol{F}^{-T}d\boldsymbol{A}_0 \tag{2.6}$$

which is commonly known as the Nanson's formula.

Using the polar decomposition theorem, the deformation about any point can be characterised by the *twin action* of a volume-preserving rigid body rotation $\boldsymbol{R}$ and a volume changing right symmetric stretching $\boldsymbol{U}$ (material tensor) or left symmetric stretching $\boldsymbol{V}$ (spatial tensor) as

$$\boldsymbol{F} = \boldsymbol{R}\cdot\boldsymbol{U} = \boldsymbol{V}\cdot\boldsymbol{R} \tag{2.7}$$

where $\boldsymbol{R}$ is an orthogonal rotation tensor (i.e. $\boldsymbol{R}\boldsymbol{R}^T = \boldsymbol{I}$). Here, the term $\boldsymbol{R}\boldsymbol{U}$ as deformation gradient implies that, mathematically, first, the stretching is applied on the body, and then its rigid body rotation is taken to obtain the current configuration.

Other deformation measures, the right and left Cauchy-Green strain tensors, $\boldsymbol{C}$ and $\boldsymbol{B}$, respectively, are defined as

$$\boldsymbol{C} = \boldsymbol{F}^T\boldsymbol{F} = \boldsymbol{U}^T\boldsymbol{U} \tag{2.8}$$

$$\boldsymbol{B} = \boldsymbol{F}\boldsymbol{F}^T = \boldsymbol{V}\boldsymbol{V}^T \tag{2.9}$$

The Green-Lagrange strain tensor, which ensures a consistent definition of zero strain in the undeformed reference configuration, is defined as

$$\boldsymbol{E} = \frac{1}{2}\left(\boldsymbol{F}^T\boldsymbol{F} - \boldsymbol{I}\right) = \frac{1}{2}\left(\boldsymbol{C} - \boldsymbol{I}\right) \tag{2.10}$$

It is based on the right Cauchy-Green strain tensor $\boldsymbol{C}$ as it is an objective measure implying that any rigid body rotation $\boldsymbol{R}$ can be imposed on the actual deformation obtained by $\boldsymbol{U}$ without changing $\boldsymbol{C}$ (which solely depends on $\boldsymbol{U}$). In the undeformed configuration, $\boldsymbol{C}$ is not-zero ($\boldsymbol{F} = \boldsymbol{I} \implies \boldsymbol{C} = \boldsymbol{I}$), whereas, $\boldsymbol{E} = \boldsymbol{0}$. The Green-Lagrange strain tensor is the most important strain measure in nonlinear solid mechanics with the Lagrangian approach. Some other well-known

strain measures are the Euler-Almansi strain tensor, which is the spatial counterpart of the Green-Lagrange strain tensor, and the logarithmic strain tensor, which is a preferred choice in large strain inelasticity.

2.2.2 Stress measures

Changes in the configurations of the bodies induce internal forces, which are characterised by defining some pointwise tensors referred to as stress. There are various stress measures, some of which are highlighted below.

In the current configuration, the traction at any arbitrary point $\boldsymbol{x}$ around a direction $\boldsymbol{n}$ can be defined as a limit over any arbitrarily small area around it on the plane passing through this point and oriented along unit normal $\boldsymbol{n}$, i.e.

$$\boldsymbol{t} = \lim_{\Delta A \to 0} \frac{\boldsymbol{f}}{\Delta A} \tag{2.11}$$

Using the well-known derivation of employing an infinitesimally small tetrahedral in the Cauchy theorem, the traction can be related to the Cauchy (or *true*) stress tensor $\boldsymbol{\sigma}$ as

$$\boldsymbol{t} = \boldsymbol{\sigma}\boldsymbol{n} \tag{2.12}$$

The Cauchy stress tensor is a symmetric stress tensor (i.e., $\boldsymbol{\sigma} = \boldsymbol{\sigma}^T$), as can be derived by the balance of angular momentum along the three basis directions at its spatial point.

The Kirchhoff stress tensor, which depends upon the Cauchy stress tensor and the Jacobian described previously, is written as

$$\boldsymbol{\tau} = J\boldsymbol{\sigma} \tag{2.13}$$

and, it is in effect a weighted Cauchy stress tensor.

Other crucial measures, the first and second Piola-Kirchhoff stress tensors, $\boldsymbol{P}$ and $\boldsymbol{S}$, respectively, are defined as

$$\boldsymbol{P} = J\boldsymbol{\sigma}\boldsymbol{F}^{-T} \tag{2.14}$$

$$\boldsymbol{S} = J\boldsymbol{F}^{-1}\boldsymbol{\sigma}\boldsymbol{F}^{-T} \tag{2.15}$$

While the Cauchy stress tensor is defined in the current configuration, the first Piola-Kirchhoff stress $\boldsymbol{P}$ relates the area vector in the reference configuration to the forces acting on it in the current configuration. Unlike Cauchy stress, which is generally symmetric, $\boldsymbol{P}$ is not symmetric in general; however, the tensor $\boldsymbol{S}$ is symmetric.

Although many measures for stresses and strain are defined in the literature, they can not be combined arbitrarily. Rather, only energy (or work) conjugate pairs of stresses and strains are used in practice [20].

2.2.3 Balance equations

All mechanical systems follow fundamental physics described by conservation laws of mass, linear momentum, angular momentum and energy. These laws are written in the form of balance equations, which can be described at both local material points in differential form or over the whole body in integral form.

Conservation of mass

General systems do not have material growth or loss, implying the mass of the material matter is constant throughout motion and deformation. By considering the reference and current configuration density ρ_0 and ρ, respectively, the conservation of mass can be described in the integral form as

$$\frac{dm}{dt} = \frac{d}{dt}\int_{\Omega_0} \rho_0 dV_0 = \frac{d}{dt}\int_{\Omega_t} \rho dV = 0 \tag{2.16}$$

Using the Reynold's transport theorem, the conservation of mass can be defined at a point as

$$\frac{\partial \rho}{\partial t} + \nabla \cdot (\rho \dot{\boldsymbol{u}}) = 0 \tag{2.17}$$

$$\dot{\rho} + \rho \ \mathrm{div} \dot{\boldsymbol{u}} = 0 \tag{2.18}$$

$$\dot{\rho}_0 = 0 \tag{2.19}$$

Conservation of linear momentum

The time derivative of the momentum of a body is given by the net external force acting over it, including both the traction $\boldsymbol{t}$ over its boundary and the body forces $\boldsymbol{b}$ (e.g. gravity). The net force $\hat{\boldsymbol{F}}$ acting on the body is

$$\hat{\boldsymbol{F}} = \int_{\partial\Omega} \boldsymbol{t} da + \int_{\Omega} \rho \boldsymbol{b} dV \tag{2.20}$$

Using the relation between the traction and the Cauchy stress ($\boldsymbol{t} = \boldsymbol{\sigma n}$) together with the Gauss divergence theorem, the following equation is obtained in the spatial description

$$\frac{d}{dt}\int_{\Omega_t} \rho \dot{\boldsymbol{u}} dV = \int_{\Omega_t} \rho \ddot{\boldsymbol{u}} dV = \int_{\Omega_t} \left(\mathrm{div}\boldsymbol{\sigma} + \boldsymbol{b}\right) dV \tag{2.21}$$

In the local form of this spatial description, it can be written as

$$\rho \ddot{\boldsymbol{u}} = \mathrm{div}\boldsymbol{\sigma} + \boldsymbol{b} \tag{2.22}$$

which is also referred to as Cauchy's first equation of motion and is the strong equilibrium equation.

2.2.4 Governing equations in strong form

Using the balance equations described in the previous section together with the boundary conditions on the single body, a set of coupled partial differential equations poses the boundary value problem governing the evolution of the state of the system. The boundary $\partial\Omega_t$ can be decomposed into two complementary sets: γ_u and γ_σ, representing the Dirichlet and Neumann boundaries. The Neumann boundary also includes free surfaces with zero traction applied over them. Both Dirichlet and Neumann boundaries are also disjoint sets, so we can write

$$\gamma_u \cup \gamma_\sigma = \partial\Omega_t, \gamma_u \cap \gamma_\sigma = \emptyset \tag{2.23}$$

Now, the boundary value problem in spatial description can be written as

$$\begin{aligned} \nabla \cdot \boldsymbol{\sigma} + \boldsymbol{b} &= \rho \partial_t^2 \boldsymbol{x} \qquad && \forall\ \boldsymbol{x} \in \Omega \times (0,T) \\ \boldsymbol{u}(\boldsymbol{x}) &= \overline{\boldsymbol{u}} && \forall\ \boldsymbol{x} \in \gamma_u \times (0,T) \\ \boldsymbol{\sigma n} &= \bar{\boldsymbol{t}}_\sigma && \forall\ \boldsymbol{x} \in \gamma_\sigma \times (0,T) \end{aligned} \tag{2.24}$$

These governing equations are also referred to as *strong* formulation of nonlinear solid mechanics, which, being in differential form, are imposed at each point in the domain Ω_t. While these strong equations describe physics in its original strong sense, the analytical solutions to general problems are mathematically challenging. So, a *weak* formulation is derived from these strong equations. These weak formulations are the foundation of numerical procedures like finite element methods.

2.2.5 Material modelling

While the continuum description of material presumes a continuity of matter, the forces resisting the deformation of the material are exerted between discrete entities in the bulk of the material. Although the physical behaviour of these discrete entities and the forces acting between them is a complex phenomenon, the continuum description allows capturing this behaviour through a pointwise measure of loading and deformation in the continuum, precisely, the stress and the strain. Different materials have different responses under the same loading or deformation, and this is described by the constitutive law of the respective material that describes the relation between the kinematics of deformation and the material response. Materials can exhibit both elastic behaviour, being able to recover deformation, and plastic behaviour, which is irrecoverable deformation. Material laws for different materials differ in their expression. In rate-dependent materials, the stress states depend upon the deformation rate. The neo-Hookean model is typically expressed in energy density form, and the stress tensor is derived from the strain energy function. Some aspects of material modelling can be referenced in [24][25][26][22][27][28][29][30][28].

While multiple constitutive laws exist, this thesis focuses on resolving contact-based boundary conditions rather than the constitutive modelling of the material. So, the emphasis will be concentrated on the computational modelling of contact.

2.3 Continuum contact mechanics

The description of nonlinear solid mechanics in the previous section solely focused on the deformation of a single body under the pre-known Dirichlet and Neumann boundary conditions. In the physical presence of multiple bodies, contact-based interaction between solids will lead to an additional boundary condition for the interacting solids. This additional boundary condition due to contact is not only unknown a priori but can also change with time, depending upon the motion and deformation of bodies with the evolution of the system configuration. While both the kinematics of finite deformation and constitutive behaviour of materials might bring non-linearity in the system, the tractions acting on the bodies due to the contact interface and their distributions also introduce a non-linearity in the boundary condition [7][16][15].

Contact and impact problems are generally classified based on problem configuration, such as the number of interacting bodies or their physical behaviour related to contact. Contact between two deformable bodies is called unilateral contact. However, the frictionless contact between a linear elastic body and a rigid foundation is called Signorini contact. While all bodies are generally deformable, contact in certain scenarios like impact and metal forming can be considered as Signorini contact, which offers simplicity in solution in implicit procedures. However, the work presented in this thesis is for general contact between deformable bodies, which has broad applicability. Analytical solutions to special cases of contact, like the interaction of ellipsoidal surfaces with elastic material for small deformation, have been provided in Hertzian theory of contact [6], and some other classical problems can be referred to in [7][8].

Contact problems, in general, may have a geometric and material discontinuity at the interface due to abrupt changes in the shape and different materials coming into contact, respectively. This is in stark contrast to the continuum assumption in classical solid mechanics. This leads to high nonlinearity and non-smoothness in contact problems, posing a challenge in contact detection and accurate numerical solutions for contact tractions.

This section presents a brief account of the conceptual framework and quantities employed to model contact between continuous surfaces with a special focus on contact kinematics and contact constraints for compressive load and frictional traction. An extension of the general continuum contact with variational formulations is presented in Chapter 3.

2.3.1 Contact kinematics

The unilateral contact problem is the most general case and is used for fundamental mathematical derivation and subsequent computational implementation. Problems of a single body having contact between its own surfaces (self-contact) and contact among multiple bodies present special cases of contact; however, the mathematical description of contact kinematics and constraints derived using unilateral contact is a general formulation of contact and can be applied to these special cases.

A full derivation of the mathematical description of the *general contact problem* between two deformable bodies is presented later in Chapter 3, Section 3.2 and is omitted here to avoid the repetition.

The kinematics of contacting bodies is generally initiated based on a gap function. In the traditional master-slave definition of contacting bodies, for each point $\tilde{\boldsymbol{x}}_s$ on the slave surface a corresponding point $\tilde{\boldsymbol{x}}_m$ on the master surface γ_m is evaluated by orthogonal projection as shown in Fig. 2.2. Mathematically, this can be written as a distant minimisation problem to find the closest point of projection (CPP) and written as

$$\tilde{\boldsymbol{x}}_m = \arg \min_{\tilde{\boldsymbol{x}}_m \in \gamma_m} \|\tilde{\boldsymbol{x}}_m - \tilde{\boldsymbol{x}}_s\| \tag{2.25}$$

A gap function describing the distance between this slave point and its projection as

$$g_N = (\tilde{\boldsymbol{x}}_s - \tilde{\boldsymbol{x}}_m) \cdot \boldsymbol{n} \tag{2.26}$$

where $\boldsymbol{n}$ is the normal to the master surface. This gap function is a signed distance function. If it is positive, the bodies are not in contact; if it is zero, they are in contact; and if it is negative, they are interpenetrating. Note that, however, this

gap function definition using master-slave labelling of surfaces may suffer issues arising from the geometry of the two bodies near the contact region as depicted in Fig. 2.3. This, in effect, affects the geometrical description of contacting surfaces and their points in contact constraint enforcement.

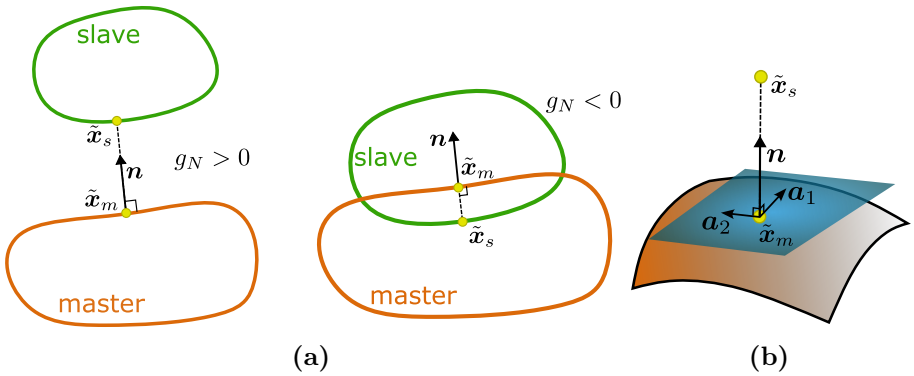

Figure 2.2: Geometrical position of a point on slave surface and its orthogonal projection on the master surface: (a) normal gap for two contacting 2D bodies, and (b) normal gap in 3D with the tangent plane at $\tilde{\boldsymbol{x}}_m$.

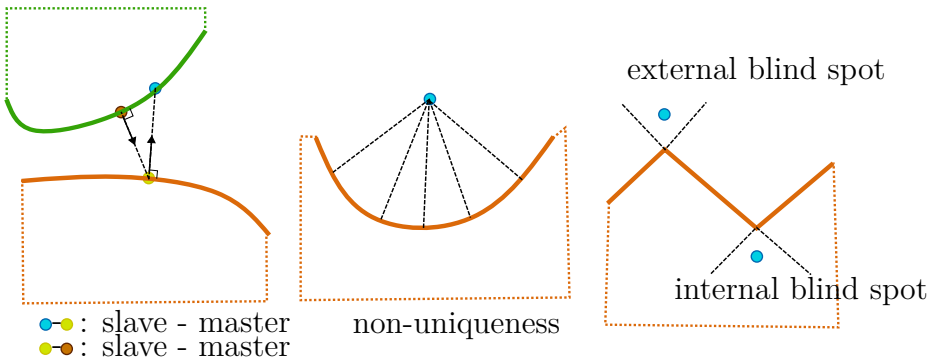

Figure 2.3: Possible issues with slave-master approach in finding CPP: (a) asymmetry of CPP from both sides, (b) multiple orthogonal projections, and (c) no orthogonal projection with slave nodes *hiding* in blind spots resulting in no contact detection.

Similar to the normal gap definition, the classical description of the frictional effect is based on the tangential sliding of each slave point (striker) onto the master surface (target) [31][32]. This tangential sliding, denoted as $\boldsymbol{g}_T$, is used to demarcate the stick-slip status of the slave point sliding over the master surface. A detailed description of this tangential sliding and the associated concepts can be referred in [33][17][16][15].

2.3.2 Contact constraints

In the continuum description of contact between bodies, the contacting surfaces are constrained at their interacting regions using the normal and tangential gap. These constraints appear in the form of tractions being applied on the two surfaces in both normal and tangential directions and are coupled at each point on the two surfaces. The constitutive law for normal and frictional traction is described below.

Unilateral Contact Law

The unilateral contact law, requiring the physical impenetrability between the two bodies at each contact point, is expressed using the Karush-Kuhn-Tucker condition (also known as Hertz-Signorini-Moreau condition) and is written as

$$g_N \geq 0,\ t_N \leq 0,\ t_N g_N = 0 \tag{2.27}$$

It is a strong condition that prohibits the kinematic inadmissibility of interpenetration ($g_N \leq 0$) between the two surfaces. The normal contact traction, considered here, is only compressive in nature ($t_N \leq 0$) and only acts over the zone where the two surfaces are pressed against each other ($g_N = 0$). Its graphical depiction can be seen in Fig. 2.4a.

Frictional Contact

Friction, a ubiquitous phenomenon, is observed in its effect on opposing the relative tangential motion between contacting bodies. Practically, the stick-slip status of friction is of primary interest in our numerical studies of physical problems and is limited to the macroscopic observation of dry friction utilised in Coulomb's law. In the stick condition, there is no relative tangential motion, i.e. $\dot{\boldsymbol{g}}_T = \mathbf{0} \leftrightarrow \boldsymbol{g}_T = \mathbf{0}$ in the current configuration at the contact point. The Coulomb's friction during the sliding phase is written as

$$\boldsymbol{t}_T = -\mu \|\boldsymbol{t}_N\| \frac{\dot{\boldsymbol{g}}_T}{\|\dot{\boldsymbol{g}}_T\|} \tag{2.28}$$

where μ is the coefficient of friction, which depends upon the materials of two solids, surface roughness, relative velocity, normal pressure, temperature, etc. The graphical depiction of this stick-slip phase can be seen in Fig. 2.5b.

The net traction at the contact point of the two surfaces can be written as

$$\boldsymbol{t}_c = \boldsymbol{t}_N + \boldsymbol{t}_T \tag{2.29}$$

$$\boldsymbol{t}_N = (\boldsymbol{t}_c \cdot \boldsymbol{n})\boldsymbol{n} \tag{2.30}$$

$$\boldsymbol{t}_T = (\boldsymbol{I} - \boldsymbol{n} \otimes \boldsymbol{n})\boldsymbol{t}_c \tag{2.31}$$

where the normal component of traction $t_N = \boldsymbol{t}_c \cdot \boldsymbol{n}$ is always negative as we do not consider adhesive forces in this work. The contact $\boldsymbol{t}_c$ acts equal and opposite on the two surfaces, i.e. $\boldsymbol{t}_c^1 = -\boldsymbol{t}_c^2$.

In the numerical solution, the contact constraints can be enforced using the optimisation methods, with the Lagrangian and penalty methods being the most widely used. To avoid the increase in the system size due to a higher number of degrees of freedom, *penalty method* has been employed in the current work. The use of the penalty method leads to a regularisation of the normal and tangential traction condition using respective penalty parameters, ϵ_N and ϵ_T as shown in Fig. 2.5. While it violates the physical impenetrability condition, the system size does not increase as with Lagrange multipliers, and the interpenetration can be minimized using a suitably high penalty parameter. For the tangential traction, the stick status allows for a small tangential sliding before the transition to the slip phase of friction. This is analogous to the elastoplastic behaviour of materials, which has been widely studied in theoretical and numerical studies [32][31][16][15][17][25]. It should be noted that the frictional response is a path-dependent process as is evident in its dependency on the relative tangential velocity.

2.4 Finite element methods

Generally, the original boundary value problem of continuum mechanics does not have an analytical solution to complex nonlinear solid mechanics problems in practical scenarios and requires numerical solution strategies. Using the variational approach by employing virtual displacement, a weak formulation is developed with the aim of progressing towards a numerical solution. Both the physical space of bodies and time are discretised to construct a numerically feasible solution.

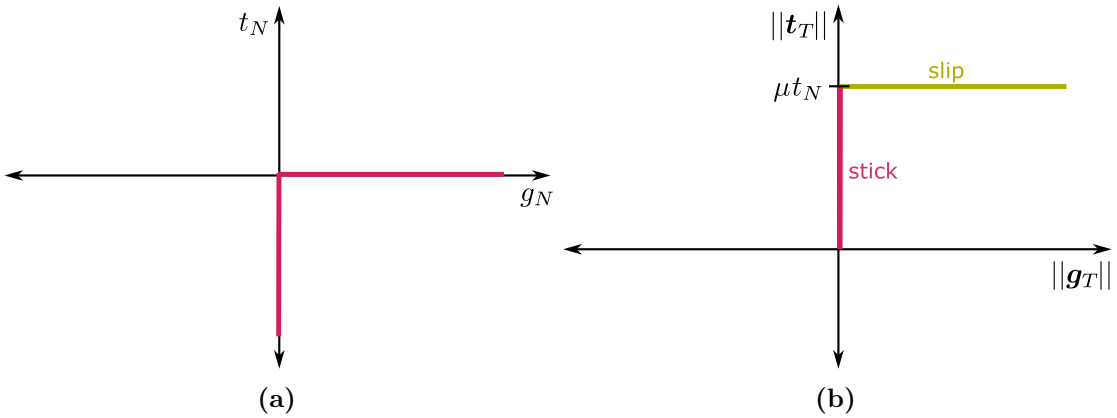

Figure 2.4: Graphical representation of (a) unilateral contact law relating the normal gap of interpenetration and the normal traction, and (b) Coulomb's frictional law relating the tangential sliding with the tangential traction, where both laws are based on the Karush-Kuhn-Tucker condition.

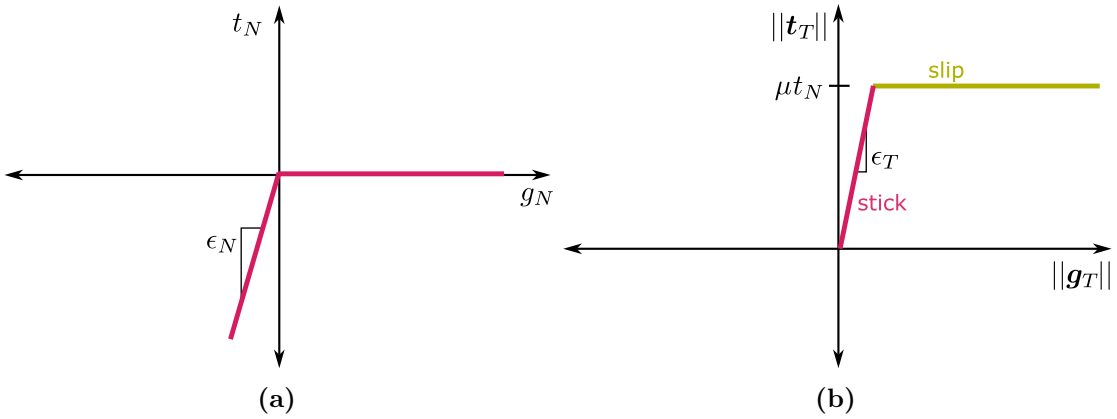

Figure 2.5: Penalty method for enforcing contact constraint: (a) penalty regularised unilateral contact law, and (b) penalty regularised Coulomb's friction law.

The discrete spatial entities approximating the original domain are called finite elements. In this section, the finite element formulation is presented for only a single body without considering the contact problem for the sake of simplicity. Problems involving contact lead to an additional constraint over the surfaces of the bodies, which is presented for frictionless contact for first-order elements in Chapter 3, frictional contact in Chapter 4 and frictional contact with second-order elements in Chapter 5. The development of weak formulation using the virtual work principle is presented in Chapter 3 Section 3.2. A detailed discussion on all aspects of FEM is beyond the scope of this thesis and can be referred to in [34][35][36][37][38][39][40][41][42][20][43].

2.4.1 Spatio-temporal discretisation and numerical integration

The numerical solution of the weak formulation using computational algorithms seeks to find the solution to the continuum problem at a finite number of points in space at a finite number of *instants* in time. Numerous strategies can be applied to this spatio-temporal discretisation to achieve the desired accuracy and speed of the computational solution. The discretisation of both spatial domain and time is discussed below.

Spatial discretisation of domains

In the finite element discretisation, the original domain in the reference configuration is discretised into a finite number of points called *nodes*. The weak form in eq. 3.6 is solved for obtaining the configuration of dynamic equilibrium at these finite number of points to find the solution. These nodes are parts of finite elements Ω_h^e with special topological connectivity, and the entire domain Ω_0 is represented by the set of these finite elements, i.e.,

$$\Omega_0 \approx \Omega_h = \bigcup_{e=1}^{e=n_e} \Omega_h^e \tag{2.32}$$

where the subscript h indicates spatial discretisation and n_e is the total number of elements. Note that, in general, Ω_h might partially occupy spatial points outside Ω_0 or might not have part of the spatial domain Ω_0 near its boundary depending upon the discretisation strategy and the given domain.

The configuration of the domain at any instant is defined by the spatial positions of the nodes. Any point $\boldsymbol{x}$ within the physical space of element Ω_h^e can be written as a linear combination of the spatial coordinates of its vertices $\mathbf{x}_i$ weighted by the interpolation functions (or shape functions/basis functions) ψ_i $(i \in \{1, 2, ..., \text{nnod}\})$and written as

$$\boldsymbol{x} = \sum_{i=1}^{\text{nnod}} \psi_i \mathbf{x}_i, \quad \forall \boldsymbol{x} \in \Omega_h^e \tag{2.33}$$

The displacement of nodes is used to define the displacement at any non-nodal point in the domain Ω_h using finite elements and their interpolation functions. The displacement $\boldsymbol{u}^e$ of any point $\boldsymbol{X}$ inside an element e is written as

$$\boldsymbol{u}_h^e(\boldsymbol{X},t) = \sum_{n=1}^{\text{nnod}} \psi_i(\boldsymbol{X})\,\mathbf{u}_i(t) \tag{2.34}$$

where $\mathbf{u}_i$ is the displacement of the ith node in the element e. The shape functions can be linear (first-order) or nonlinear (higher-order) depending upon the particular choice of element formulation. While different elements have different mathematical behaviour, they all ensure the partition of unity for shape functions. These shape functions also meet the differentiability requirement for the weak form. In this work, isoparametric elements are used, and they represent both the geometry and the field variables using the same shape functions. Similar to the displacement field, any physical quantity $(\cdot)_h$ in an element can be described using its nodal values $(\cdot)_i$ and the shape functions as

$$(\cdot)_h(\boldsymbol{\xi},t) = \sum_{i=1}^{i=\text{nnod}} \psi_i(\boldsymbol{\xi})\,(\cdot)_i \tag{2.35}$$

where $\boldsymbol{\xi} = (\xi_1, \xi_2, \xi_3)$ is the set of parametric coordinates in the reference (or master/parent) element that maps to the physical element. All quantities in the weak form $(\boldsymbol{u}, \partial_t^2\boldsymbol{u}, \delta\boldsymbol{u})$ are interpolated using the shape functions, which leads to the building of the finite element equations. This convention is widely referred to as the Bubnov-Galerkin approach as opposed to the Petrov-Galerkin approach that utilises independent shape functions for the interpolation of weighting function $\delta\boldsymbol{u}$.

As can be seen in the eq. 2.34, the solution of finite element method differs from the solution space $\mathscr{U}$ and the weighting space $\mathscr{V}$ in the weak form to $\mathscr{U}_h\,(\approx \mathscr{U})$ and $\mathscr{V}_h\,(\approx \mathscr{V})$. The weak form is converted to a discrete form, which is different from the strong and weak forms. So, the finite element solution using discrete form is only an approximation of the analytical solution.

To evaluate the quantities at nodes using the discretised weak form, quantities are integrated at all elements using a chosen numerical quadrature scheme and are

assembled using an assembly operator to construct the global vector that decides the arrangement of local vector quantities in the global matrix, i.e.

$$\int_{\Omega_0} (\cdot)\, dV \approx \overset{\text{nelem}}{\underset{e=1}{\mathsf{A}}} \int_{\Omega^e_{0,h}} (\cdot)\, dV \tag{2.36}$$

Using the shape functions, the virtual work equation applied over constituting finite elements subdomains that represent the original geometry of the solids can be written as -

$$\delta \boldsymbol{u}^T \left(\sum_{e=1}^{\text{nelem}} \left(\int_{\Omega^e_h} \rho \mathbf{N}^T \mathbf{N} \ddot{\mathbf{u}} dV + \int_{\Omega^e_h} \mathbf{B}^T \sigma dV - \int_{\Omega^e_h} \mathbf{N}^T \boldsymbol{b} dV - \int_{\gamma^e_h} \mathbf{N}^T \boldsymbol{t} d\gamma \right) \right) = 0 \tag{2.37}$$

where $\mathbf{B}^T$ is strain-displacement matrix, $\mathbf{N}$ is shape function matrix, $\ddot{\mathbf{u}}$ is the acceleration vector, and $\boldsymbol{t}$ is the traction vector. Here, the summation over all elements implies the net contribution is taken from the local element to the global domain. So, for the global discretised domain, it is expressed as

$$\delta \mathbf{u}^T \left(\mathbf{M}\ddot{\mathbf{u}} + \mathbf{f}_{\text{int}} - \mathbf{f}_{\text{ext}} \right) = 0 \tag{2.38}$$

where $\mathbf{M}$ is the (global) consistent mass matrix (called consistent due to the use of same shape functions in evaluation of stiffness matrix and load vectors), $\mathbf{f}_{\text{int}}$ and $\mathbf{f}_{\text{ext}}$ are the global internal and external nodal force vectors, respectively, and $\mathbf{u}$ is the global nodal displacement vector. The vector $\mathbf{f}_{\text{ext}}$ includes the effect of Dirichlet boundary conditions that specify the displacements as well as Neumann boundary conditions that specify the surface tractions and contact-induced surface tractions. At dynamic equilibrium, the above equation holds true for any virtual displacement $\delta\mathbf{u}$, so it becomes

$$\mathbf{M}\ddot{\mathbf{u}} + \mathbf{f}_{\text{int}} - \mathbf{f}_{\text{ext}} = 0 \tag{2.39}$$

which is a system of ndof ($= \mathsf{ndim} \times \mathsf{nnod}$) ordinary differential equation (ODE), also called a semi-discrete system of equations of motion. It is called semi-discrete as it is discrete in space but continuous in time. For numerical modelling, an

additional term of viscous dissipation is added to the above system of equations. So, using the Rayleigh damping, the above eqn becomes

$$\mathbf{M}\ddot{\mathbf{u}} + \mathbf{C}\dot{\mathbf{u}} + \mathbf{f}_{\text{int}} - \mathbf{f}_{\text{ext}} = 0 \tag{2.40}$$

where $\dot{\mathbf{u}}$ is the global nodal velocity vector, and $\mathbf{C}$ is the global damping matrix that is phenomenologically represented as a combination of mass matrix and initial tangent stiffness matrix, i.e.,

$$\mathbf{C} = \alpha\mathbf{M} + \beta\mathbf{K} \tag{2.41}$$

Time discretisation

For the numerical solution of the above presented semi-discrete eq. 2.40, finite instants of time are considered. The time-based derivatives of nodal displacements are approximated using the finite discrete steps in time. The time steps are finite, so any duration Δt in the simulation time $t \in [0, T]$ is considered in intervals as $[t_n, t_{n+1}]$ where $n \in \mathbb{N}_0$. Thus enabling the numerical solution of the system of differential equations representing the equations of motion of the discretised domain Ω_h; so, the discrete displacements of nodes along with the discrete steps in time can be numerically solved.

Time integration can be performed in two ways - implicit and explicit schemes. In the implicit scheme, the configuration of the system at a current timestep is dependent upon the subsequent timestep, whereas, in the explicit scheme, the configuration of the system at any timestep depends upon the previous timestep. The implicit schemes are generally used in the solution of systems with low frequency, whereas explicit schemes are preferred for problems with rapidly changing configurations of the system or those having high nonlinearity to better capture the information. Only the explicit scheme has been considered for the work presented in this thesis. While the Newmark beta method is typically employed in the implicit schemes, the central difference scheme is used in the explicit schemes for time integration, which also comes out as a special case of the Newmark beta method by setting $\beta = 0, \gamma = 0.5$, see [35]. Note that this factor β is different than the one mentioned above in eq. 2.41.

Explicit time integration scheme

The state of the system through the discrete linear momentum equation can be written as

$$\mathbf{M}\,\ddot{\mathbf{u}}\,(t_{n+1}) + \mathbf{C}\dot{\mathbf{u}}\,(t_{n+1}) + \mathbf{f}_{\text{int}}\,(t_{n+1}) = \mathbf{f}_{\text{ext}}\,(t_{n+1}) \tag{2.42}$$

In the explicit time integration scheme, the state of the system at any timestep is dependent upon the kinematic quantities of previous timesteps. Using the central difference time integration, the time-based evolution of the displacement and its derivatives are written as

$$\mathbf{u}_{n+1} = \mathbf{u}_n + \Delta t\dot{\mathbf{u}}_{n+\frac{1}{2}},\ \dot{\mathbf{u}}_{n+\frac{1}{2}} = \dot{\mathbf{u}}_{n-\frac{1}{2}} + \ddot{\mathbf{u}}_n\Delta t,\ \ddot{\mathbf{u}}_n = \frac{\mathbf{u}_{n+1} - 2\mathbf{u}_n + \mathbf{u}_{n-1}}{(\Delta t)^2} \tag{2.43}$$

The system of equations in 2.42 are coupled, so they are interdependent due to the masses of interaction between nodes. However, for practical computational efforts, the system of equations can be decoupled by replacing the full mass matrix with a diagonal matrix, which is referred to as mass lumping. The mass lumping can be achieved by row-summation technique or by appropriate scaling of the diagonal entries in HRZ (Hinton-Rock-Zienkiewicz) lumping of masses[37][38][44][45]. In this work, HRZ lumping of masses has been considered. The decoupled system of equations allows a computationally faster and more efficient solution of the otherwise coupled system of equations, with relatively unaffected results. However, they are dependent upon the elements being used.

In eq. 2.42, the external force vector $\mathbf{f}_{\text{ext}}$ contains the forces due to the Neumann boundary conditions specifying the surface tractions applied on the boundary, as well as the effect of Dirichlet boundary conditions prescribing the kinematic quantities. Also, the presence of any active contact constraint results in the addition of some entries in $\mathbf{f}_{\text{ext}}$. The sole aim of this work is to detect those nodes getting constrained in physical contact and calculate the resulting forces acting on them.

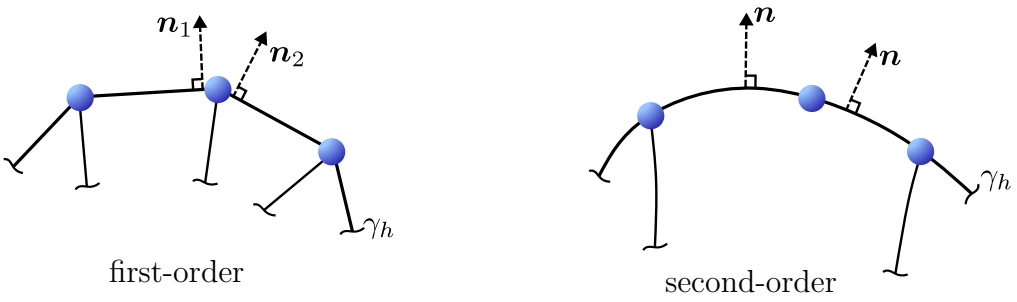

Figure 2.6: Variation of boundary normal on edges of two first-order elements v/s the edge of one second-order element.

2.4.2 First and higher-order finite elements

In this work, hexahedral elements (or brick elements) are studied for contact. An extension to tetrahedral elements will be a straightforward procedure using the proposed methodology. Two types of hex elements are studied in particular – 8-noded first-order hex and 27-noded Lagrangian second-order hex. Both types of elements are represented by piecewise polynomial functions. The first-order elements have linear shape functions, so the edges connecting the nodes are straight-line segments. However, the second-order elements have quadratic shape functions, so the edges connecting the nodes are curved segments, which can provide a better approximation of any originally curved geometry. While the first-order elements have the same normal direction on moving along their edge, the edges of second-order elements can have curvature, thus allowing for a smooth change in the normal, see Fig. 2.6. If the two elements are used to represent a curved geometry, edges of first-order elements will see a jump in the normal direction at element corners. Note that the edges of both elements have piecewise polynomial interpolation, so second-order elements, depending upon the discretised geometry and nodal positions, may also have jumps in the normal direction at edge corners. However, even so, the jump will be very small compared to the first-order elements if the original surface does not have a sharp change.

All finite elements have different behaviours due to different mathematical constructs. Second-order elements, due to their nonlinear nature of mathematical description, have a non-intuitive distribution of forces compared to the first-order

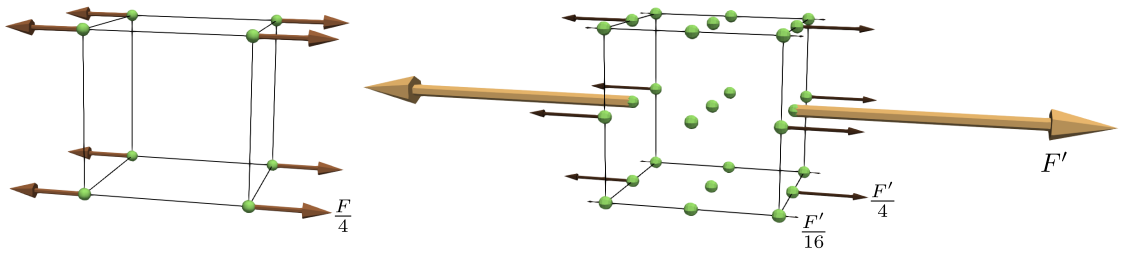

Figure 2.7: Comparison of nodal force distribution on 8-noded first-order v/s 27-noded second-order elements for opposite facets being pulled apart by equal displacement.

elements. If the same displacement is applied on opposite facets of a first-order and a second-order element representing the same cubic geometry, the nodal forces acting on opposite facets have different distributions. While the first-order element has a uniform distribution of forces, the second-order element has a non-uniform distribution, as shown in Fig. 2.7. This is an outcome of the intrinsic mathematical nature of the two elements. So, the nodal forces acting on the element facets are not a good representative of the traction on the facets for analysing contact pressure in higher-order elements. Rather, the stress states evaluated at the quadrature points inside the elements are a better choice.

The two types of elements used in this work are fully integrated, i.e. first-order and second-order Lagrangian elements are used with 2^3 and 3^3 quadrature points, respectively, with the only difference of using under-integrated first-order elements in the case of Hertzian contact.

The accuracy of the solution obtained by Finite Element methods is often improved by using h-refinement and p-refinement. The h-refinement involves increasing the discretisation of domains, which leads to reduced sizes of the discrete entities and an increased number of degrees of freedom. On the other hand, p-refinement refers to using higher-order basis functions in the interpolation of discrete entities, thereby enabling better capturing of the smoothness of the solution. These two approaches have been employed in the development of the work presented in the subsequent chapters.

2.5 Computational contact mechanics

The solution of a single discretised body for given initial and boundary conditions is a direct problem within the context of nonlinear finite element methods with known boundary conditions. When a system of multiple bodies is considered for numerical solution, an additional challenge arises in the form of unknown boundary conditions resulting from a possibility of contact with the motion and deformation. Such contacts can occur between different bodies as well as on the same body itself (self-contact/auto-contact). A numerical solution to such a multi-body problem of solids coming into contact requires consideration of multiple aspects involved in the problem definition. These different aspects are briefly discussed in this section, and the details can be referred to in [15][16][33][46][47][48][49][50], and some more practical details in [51][33][52].

2.5.1 Contact discretisation strategies

Contact between two opposite discretised surfaces is geometrically described by forming pairs of discrete entities where the contact constraints are enforced. These discrete entities are nodes and the segments connecting those nodes. These segments are edges of the finite elements in 2D problems and facets in 3D problems. Only 3D problems have been studied in this work and are the primary focus; equivalent translation to 2D problems will be fairly straightforward. There are multiple ways of describing contact discretisation, which are discussed below.

The most primitive approach to contact discretisation is forming pairs of nodes on opposite surfaces having matching (or conformal) discretisation, referred to as Node-to-Node (NTN). The contact pairs of nodes are utilised to enforce the contact constraints. This approach, although very simplistic, is restricted to matching meshes and does not allow for relative sliding between them as the contact pairs will break.

The Node-to-Segment (NTS) approach, which is also the most widely used in commercial solvers, forms pairs between the nodes on one surface (slave) and the segments on the other (master). For each node on the slave side, its projection

is found on the master surface segments, and the contact constraint is enforced on each NTS pair. This method, however, is also not very accurate and fails to pass the contact patch test for a single-pass approach. It might also suffer from issues of the slave-master approach in finding CPP, as shown in Fig. 2.3. NTS is still widely used in industries, especially in nonlinear analysis where the computational costs are higher.

The Segment-to-segment (STS) approach enforces constraints on contact between the pairs of segments on the opposite surfaces. This approach provides a solution with high accuracy compared to NTS. However, the traditional methods using STS pairs are also biased, like NTS, as they label surfaces as slave and master. To remove biasing, a very traditional route is to apply a second pass in the same solution step by reversing the master-slave labelling of segments. The net effect in the dual pass approach is a weighted average of the effect of two passes. This dual pass approach, however, incurs an additional computational cost. In this work, a single-pass unbiased STS approach is presented without master-slave labelling, thereby ensuring a fair treatment of contacting surfaces.

2.5.2 Contact constraint enforcement techniques

Interacting discrete entities on opposite surfaces are restricted against intersection by imposing constraints over them that result in the application of contact traction on the two surfaces, effectively resulting in the action of nodal forces. Constraints are most commonly applied by using either the penalty method, Lagrange multiplier, or augmented Lagrange multiplier. In the Lagrange multiplier approach, each node on the opposite discrete entities is assigned a Lagrange multiplier λ_i, which is utilised in enforcing a strict impenetrability condition. Although, it is able to maintain the strict kinematic inadmissibility of interpenetration, the use of Lagrange multipliers adds to the total number of degrees of freedom to the system, increasing the overall computational cost.

The penalty method restricts interpenetration by applying contact pressure, which is proportional to the interpenetration gap. This is based on the micromechanical approach of physical description of surfaces [53]. In the case of linear penalty, which is used throughout this work, the contact pressure is

$$p_N = \epsilon_N g_N \tag{2.44}$$

where, ϵ_N is the penalty factor and g_N is the normal gap. The constitutive law of contact can also consider a nonlinear penalty, e.g., the nonlinear penalty law of Kragelsky [53]

$$p_N = c_N (g_N)^n \tag{2.45}$$

where c_N and n are constitutive parameters that are determined experimentally.

The penalty method has been chosen as a preferred method of enforcing contact constraint in this work owing to its effectiveness in large systems where additional degrees of freedom will otherwise add to the computational cost.

2.5.3 Solution procedure

The numerical solution to contact problems addresses both sources of contact nonlinearity - the determination of contact region and the contact traction distribution. In a multibody dynamic system, the motion and deformation of bodies might result in contact between different bodies or even the self-contact of a body with itself. The general computational procedure followed in solving contact problems in a dynamically evolving system is a two-step procedure: contact search and contact constraint enforcement.

The contact search determines the regions of contact in the system. It is typically performed in two stages: spatial search to find the potential contact pairs and contact detection to confirm the geometrical regions on element boundaries that are actually in physical contact. Subsequently, contact constraints are applied in the second step, resulting in contact traction in the contact region, leading to an additional boundary condition on the interacting solids. These steps are briefly described below, and more details can be referred to in [53][15][16].

Contact search

Spatial Search:

In the time-based changes of positions of bodies in the system, the first stage is to run a superficial contact search that aims to establish a list of pairs of surface segments that are close to each other but without actually testing them for contact. This reduces the high computational overhead associated with the test of actual contact between all segments in the given problem and yields a list of potential contact pairs, which can then be tested for interpenetration.

This work uses the classical bounding box algorithm for spatial search to establish this list of potential contact pairs. Here, each facet (segment) on all the boundaries is enclosed within a box that extends from the lower to upper limits of the coordinate values in each dimension. In an n-dimensional space $\mathbb{R}^n$, these bounding boxes for each facet Γ_k^h can be written using the extreme coordinates of the facet as

$$(\cdot)_{\Gamma_k^h} = \{(x_1, ..., x_n) \in \mathbb{R}^n : x_{i_{\min}} - \delta_{\text{bzt}} < x_i < x_{i_{\max}} + \delta_{\text{bzt}}, \quad \forall i \in \{1, ..., n\}\} \tag{2.46}$$

where δ_{bzt} is the buffer zone thickness for expanding the bounding boxes to aid in contact search. These bounding boxes are constructed for each facet over the entire discretized boundary for all surfaces, thereby becoming a respective territory of each facet for contact search.

After this construction of bounding boxes, alternating digital tree algorithm [54] is used for establishing a list of intersecting bounding boxes which represent the potential contact pairs. As all the bounding boxes would be tested for intersection, the case of self-contact is self-contained within this search.

Contact detection:

Following the generation of the list of potential contact pairs through spatial search, these pairs are checked for actual contact. The NTS approach involves finding the CPP and checking the relative position of the node to confirm the geometrical intersection. On the other hand, the STS approach involves finding the geometrical intersection between the segments. Generally, it involves finding the interpenetration

of nodal vertices against the facets of opposite surfaces. This is followed by an evaluation of the intersection between the projections of the opposite facets over a plane, which is generally an approximation of the master segment as a plane in traditional methods and midplane in this thesis research. This intersection is performed using a polygon clipping algorithm [55]. Details of how contact detection is performed in this work are presented in Chapter 3 Section 3.4.

Once the list of potential contact pairs is generated through the spatial search, the facet pairs are further tested to confirm contact between them.

Constraint enforcement

Following the determination of the contact region between intersecting segments on opposite boundaries, contact constraints are applied over the segments. For explicit FEM, this requires an evaluation of contact traction and its subsequent application as nodal forces on the contacting segments. While normal traction results from the imposition of impenetrability conditions, tangential traction due to the frictional effect results from the opposition of relative tangential motion. This tangential traction is, however, also dependent upon the normal traction. Subsequent chapters discuss this enforcement of constraints using penalty methods.

The foundational concepts briefly discussed in this chapter form the bedrock of conceptual development in the subsequent chapters, where the novel propositions in this thesis are sequentially presented, building up the complexity from first-order to high-order elements for frictional contact.

3

First-order elements in frictionless contact

Most common method of discretisation of solids uses first-order elements. Solving contact between such solids for compressive loads on interacting surfaces with high-accuracy has been a complex challenge. This chapter focuses on developing unbiased contact formulation for interacting segment pairs by introducing midplane for constraint enforcement. The robust and versatile single-pass approach is not only highly accurate but can also handle self-contact problems with ease.

Some highlights of this chapter are

- A midplane-based unbiased contact methodology is proposed for fair treatment of surfaces without labelling them as master and slave
- The proposed methodology evaluates contact traction unbiasedly in a single pass instead of the dual approach used to eliminate biasing in the master-slave treatment of surfaces
- The work also explains the different possible geometrical configurations that contacting segments can have for the evaluation of contact forces using the penalty method for nonconformal meshes
- The unbiased nature of the proposed methodology is also of direct benefit to the problems involving self-contact and large deformation

Midplane based 3D single pass unbiased segment-to-segment contact interaction using penalty method

Indrajeet Sahu, Nik Petrinic

Abstract

This work introduces a contact interaction methodology for an unbiased treatment of contacting surfaces without labelling surfaces as master and slave. The contact tractions between interacting discrete segments are evaluated with respect to a midplane in a single pass, inherently maintaining the equilibrium of tractions. These tractions are based on the penalisation of true interpenetration between opposite surfaces, and the procedure of integrating them for discrete contacting segments is described in this paper. A meticulous examination of the different possible geometric configurations of interacting 3D segments is presented to develop visual understanding and better traction evaluation accuracy. The accuracy and robustness of the proposed method are validated against the analytical solutions of the contact patch test, two-beam bending, Hertzian contact, and flat punch test, thus proving the capability to reproduce contact between flat surfaces, curved surfaces, and sharp corners in contact, respectively. The method passes the contact patch test with the uniform transmission of contact pressure. It converges towards the analytical solution with mesh refinement and a suitably high penalty factor. The effectiveness of the proposed algorithm also extends to self-contact problems and has been tested for self-contact between flat and curved surfaces with inelastic materials. Dynamic problems of elastic and inelastic collisions between bars and oblique collision of a sphere are also presented. The ability of the algorithm to resolve contacts between flat and curved surfaces for nonconformal meshes with high accuracy demonstrates its versatility in general contact problems. The formulation has been implemented in an explicit time integration framework, which will not only improve the solution for traditional problems solved using explicit methods

but also enable it to have prospects of a competitive choice over implicit schemes for achieving solutions with highly accurate contact traction.

3.1 Introduction

The design and development of complex systems in engineering applications, like manufacturing, automotive, and aerospace industries, have accelerated in the last few decades due to the increasing capability to simulate physical problems at larger scales with higher accuracy. While in any system, there will be an effect of non-contact forces, e.g. gravity and electromagnetic forces, all components in assemblies are generally either supported in equilibrium or maintained in a desired motion by contact forces. The analysis of contact problems poses a critical challenge due to the nonlinearities arising from the lack of prior knowledge of contact area and the contact traction distribution [7][56]. The finite element method (FEM) has been a widely accepted methodology for numerical solutions to structural problems [9]. Computational solutions using finite elements can generally proceed through a route of either implicit or explicit time integration, with the explicit method being generally preferred for problems with high dynamic nature or nonlinearities [34][16]. The nonlinearities in the system can be induced by both material and geometric behaviour, with contact conditions often playing a critical role. Having a highly accurate contact interaction methodology in explicit methods will provide an improved solution to traditional problems where explicit methods are preferred and introduce a viable alternative in scenarios where implicit methods are typically used for accurate contact solutions. Such an accurate contact method would allow explicit methods to offer a competitive advantage in a broader range of applications, and is a core theme of this work.

In continuously evolving systems, the changing positions and configurations of all bodies imply that certain surfaces might have physical interactions. Numerical solutions for such physical interactions between discretised domains involve two aspects: contact discretisation and contact constraint enforcement. Contact discretisation describes the procedure of forming contact pairs between discrete

entities on opposite surfaces. The motion of these contacting discrete entities is resisted against interpenetration using contact constraint enforcement techniques such as the widely used Lagrange multiplier and penalty methods. While the Lagrange multiplier method seeks an exact enforcement of constraints, the increased degrees of freedom add to the computational cost. On the other hand, the penalty method penalises interpenetration between contacting surfaces by using a penalty factor without increasing degrees of freedom in the system [15]. It is not only relatively easier to implement the penalty method in any solver, but it also becomes particularly advantageous to use in large-scale problems where the computational cost of a large number of degrees of freedom may be a concern.

For finite element solutions, multiple contact discretisation schemes have been used - node-to-node(NTN), node-to-segment (NTS), and segment-to-segment (STS). The NTN method, a very primitive approach, forms contact pairs between nodes on conforming meshes with matching nodes [57], and it also passes the contact patch test for transferring uniform pressure along the contact interface. However, it is restricted to infinitesimally small sliding, as any large deformation or finite sliding leads to nonconformity between the meshes, requiring the contacting entities to be remeshed to form node-to-node pairs. Recent works in [25][58][59] present 2-dimensional (2D) and 3-dimensional (3D) NTN schemes by employing variable node elements, where hexahedral elements are replaced by polyhedral elements, and it passes the contact patch test while also working with large deformations. Polyhedral elements for the NTN scheme based on the scaled boundary finite element method have also been used to convert nonconformal meshes (non-matching nodes) into conformal ones and pass the contact patch test [60][61].

The NTS scheme forms contact pairs between nodes of one surface labelled as slave and the segments on the other surface labelled as master [40, 57][62]. It opposes the penetration of slave nodes into the master surface, thereby resulting in contact traction between the two surfaces. Unlike NTN, it is not limited to conformal meshes but can also be applied to nonconformal meshes experiencing sliding with large deformations [63]. It is well suited for linear solid elements with

a single integration point [64]. The NTS scheme with a single pass suffers from bias due to the master/slave approach, allowing the master nodes to penetrate the slave surface without generating a contact force. Regardless of using the Lagrange multiplier or penalty method, it fails the contact patch test, with the mesh refinement not alleviating this issue [65]. The one-pass approach can be improved by adding a virtual slave node with the penalty method to satisfy the contact patch test [66][67], by smoothed FEM [68], by area regularisation techniques [69], or by a dual-pass strategy with Lagrange multipliers [14][2]. In the explicit framework, a double pass-based approach using the penalty method can be referred to in [70]. The NTS scheme, however, suffers issues in the detection phase with non-smooth C^0 continuous surfaces for unique projection of slave nodes [46], leading to jumps in nodal forces at the contact interface. Additionally, it also suffers from locking and over-constraining problems [67].

In the STS approach initially proposed in 2D [71], contact constraints are enforced between pairs of segments on opposite surfaces. With the work of [72], the STS method transitioned from pointwise imposition of contact constraints to continuous imposition over contacting segments. Initial approaches also involved the imposition of constraints over the integration points of contacting segments [73]. Generally, in STS methods, one surface is projected over another, and contact constraints are applied on a common intersection area [12]. While the NTS method suffers from a sudden jump in nodal force for the sliding of nodes from one segment to another, the STS method exhibits a gradual change in the volume of interpenetration, which predicts a physically smooth variation of the generated contact forces. This is particularly advantageous with large deformations, finite sliding, and curved surfaces, leading to improved accuracy in solutions. Consequently, even with a lower number of elements, the results on the contact interface are qualitatively well represented [74]. Mortar methods, initially developed for domain decomposition problems [75], have also been extensively studied with STS approach [76][12][77][78] for different integration strategies [79], and with dual pass approach for self-contact [14]. The dual pass approach is generally used to eliminate the biasing of the master-slave labelling

in NTS and STS methods by having an additional contact contribution coming from swapping of slave and master surfaces in each iteration or step of the solution [80]; however, this comes at the cost of additional computation due to the second pass. The enforcement of contact constraints has also been studied with intermediate surfaces in 2D for unbiased contact traction evaluation in mortar methods [71][81].

This paper proposes an unbiased approach for contact traction evaluation in a single pass. By defining a midplane, true interpenetration between the contacting segments is penalised through nodal forces obtained by integrating traction over the midplane, which is in contrast to the interpolation of nodal constraints [12][82]. As the methodology is inherently unbiased, it can also maintain consistency in contact constraint enforcement in the case of self-contact. The presented contact formulation is implemented with an explicit finite element scheme using first-order elements based on central difference time integration and HRZ lumping of nodal masses [37][70].

The work in this paper is organized as follows - section 2 describes the analytical problem and development of its weak form for finite element solution. Section 3 presents the midplane-based contact methodology applied with the penalty method for contact traction. The solution procedure with the algorithm for the proposed method is described in section 4. Finally, numerous benchmark tests in section 5 demonstrate the robustness of the proposed algorithm.

3.2 Problem description

The problem of solids in motion in continuum mechanics often involves physical contact between them, resulting in the transfer of loads and subsequent deformation of the solids. These contacts impose external constraints on the solids, influencing the evolution of state changes in the system. This section provides a mathematical description of the laws governing the motion and constraint-induced deformation of solids. Initially, the problem is described in its strong form, outlining the fundamental equations that govern the system's behaviour. Subsequently, a

variational principle-based weak solution is introduced to formulate its finite element-based solution. This mathematical description forms the basis for the proposed solution methodology, which is presented in the subsequent sections.

3.2.1 Strong formulation of the continuum problem of contact

Consider a general case of a system of two deformable solids Ω^i $(i = 1, 2)$ in $\mathbb{R}^{n_{sd}}$ (where, $n_{sd} = 3$ for a 3D problem) undergoing motion and deformation leading to a mutual imposition of contact constraint as shown in Fig. 3.1. The position of any point $\boldsymbol{x}^i$ in either of the two bodies Ω^i at any time t is related to its undeformed position $\boldsymbol{X}_i$ by displacement $\boldsymbol{u}$ as $\boldsymbol{x} = \boldsymbol{X} + \boldsymbol{u}(\boldsymbol{X}, t)$. In the 3D Euclidean space, the boundary value problem at any point $\boldsymbol{x}^i$ for each solid Ω^i will be represented through the following equations:

$$\begin{aligned} \nabla \cdot \boldsymbol{\sigma}^i + \boldsymbol{b}^i = \rho^i \partial_t^2 \boldsymbol{x} \qquad & \forall\ \boldsymbol{x}^i \in \Omega^i \times (0, T) \\ \boldsymbol{u}^i(\boldsymbol{x}^i) = \overline{\boldsymbol{u}}^i \qquad & \forall\ \boldsymbol{x}^i \in \gamma_u^i \times (0, T) \\ \boldsymbol{\sigma}^i \boldsymbol{n}^i = \overline{\boldsymbol{t}}_\sigma^i \qquad & \forall\ \boldsymbol{x}^i \in \gamma_\sigma^i \times (0, T) \end{aligned} \tag{3.1}$$

The first equation follows from the conservation of momentum, with the symbols $\boldsymbol{\sigma}^i$ and $\boldsymbol{b}^i$ representing Cauchy stress and body force per unit volume. The second and third equations represent the imposed Dirichlet and Neumann boundary conditions on γ_u^i and γ_σ^i, respectively, where the overbars in the notation $\overline{(\cdot)}$ are used to denote prescribed boundary conditions of imposed displacements and surface tractions over the two domains ($\gamma^i = \partial\Omega^i$). Here, $\gamma_\sigma^i \cap \gamma_u^i = \gamma_\sigma^i \cap \gamma_c^i = \gamma_u^i \cap \gamma_c^i = \emptyset$. The above set of equations governs the change of positions of the points in both domains. In the event the two bodies come into contact, the traction $\boldsymbol{t}_c^i$ generated at any point in their contact interface γ_c $(= \gamma_1 \cap \gamma_2)$ can be decomposed into a normal component $\boldsymbol{t}_N^i$ and a tangential component $\boldsymbol{t}_T^i$. The normal contact traction can be written as

$$\boldsymbol{t}_N^i = (\boldsymbol{t}_c^i \cdot \boldsymbol{n}^i)\boldsymbol{n}^i \tag{3.2}$$

where, $\boldsymbol{n}^i$ denotes the outward normal at the contact point on Ω^i. By projection on the tangential plane, the frictional traction vector, if the problem also involves

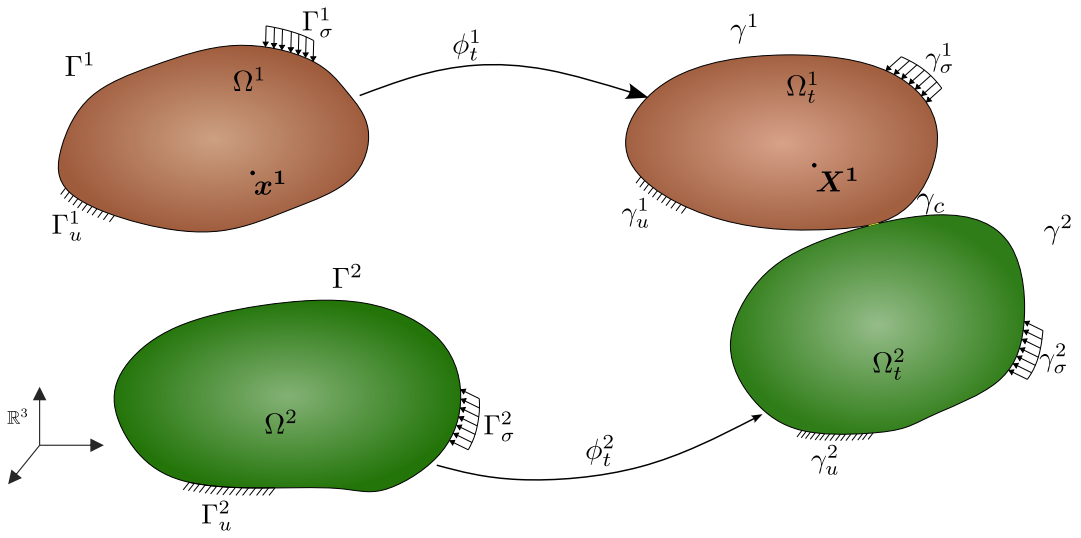

Figure 3.1: A general finite deformation frictional contact problem

frictional effect, can be written as

$$\boldsymbol{t}^i_T = (\boldsymbol{I} - \boldsymbol{n}^i \otimes \boldsymbol{n}^i)\boldsymbol{t}^i_c \tag{3.3}$$

The action-reaction principle implies that the tractions acting on the two bodies at any infinitesimally small area $d\gamma_c$ is equal in magnitude and opposite in direction, i.e., $\boldsymbol{t}^1_c = -\boldsymbol{t}^2_c$. The forthcoming proposition of the contact formulation satisfies this fundamental requirement in a single-pass approach. In this work, only frictionless surfaces in contact are considered, so determining $\boldsymbol{t}_N$ will be the sole focus of the work presented in this paper.

3.2.2 Variational form of the solution

By applying the variational principle to the strong formulation of the problem, a finite element solution to the nonlinear boundary value problem is developed that maintains the dynamic equilibrium at any instant for the given boundary conditions on the bodies. To develop the variational form, consider the space $\mathscr{U}^i$ containing all kinematically admissible deformations in the solid Ω^i to define the solution space

$$\mathscr{U}^i = \{\boldsymbol{u}^i : \Omega^i \to \mathbb{R}^3 | \boldsymbol{u}^i \in [H^1(\Omega^i)]^{n_{sd}}, \boldsymbol{u}^i = \overline{\boldsymbol{u}}^i \ \ \forall \boldsymbol{x} \in \gamma^i_u\} \tag{3.4}$$

and the space of kinematically admissible variations to define the weighting space as

$$\mathscr{V}^i = \{\delta\boldsymbol{u}^i : \Omega^i \to \mathbb{R}^3 | \delta\boldsymbol{u}^i \in [H^1(\Omega^i)]^{n_{sd}}, \delta\boldsymbol{u}^i = \boldsymbol{0} \ \ \forall \boldsymbol{x} \in \gamma^i_u\} \tag{3.5}$$

where $H^1(\Omega^i)$ denotes the Sobolev space of functions which are square integrable functions over its values and their first-derivatives. The weak form representing the virtual work for dynamic equilibrium at any instant to determine the deformation $\boldsymbol{u}^i$ can be written as

$$\int_{\Omega^i} \rho^i \partial_t^2 \boldsymbol{u}^i \cdot \delta \boldsymbol{u}^i dV + \int_{\Omega^i} \boldsymbol{\sigma}^i(\boldsymbol{u}^i) : \nabla(\delta \boldsymbol{u})^i dV = \int_{\Omega^i} \rho^i \boldsymbol{b}^i \cdot \delta \boldsymbol{u}^i dV + \int_{\gamma_\sigma^i} \boldsymbol{t}_\sigma^i \cdot \delta \boldsymbol{u}^i d\gamma^i + \int_{\gamma_c^i} \boldsymbol{t}_c^i \cdot \delta \boldsymbol{u}^i d\gamma^i \ , \quad \forall \delta \boldsymbol{u}^i \in \mathscr{V}^i \quad (3.6)$$

Here, the terms on the left side represent the internal virtual work ($\delta\Pi_{int}$) due to the inertia and the strain energy of the body, respectively. The terms on the right side denote the external virtual work ($\delta\Pi_{ext}$) due to the body forces($\boldsymbol{b}$), external surface tractions($\boldsymbol{t_\sigma}$), and the contact traction ($\boldsymbol{t}_c$) on this body Ω^i, respectively. The Cauchy stress tensor $\boldsymbol{\sigma}^i$ in Ω^i is a function of deformation $\boldsymbol{u}^i$ through the constitutive model for the material of the body. The contact traction $\boldsymbol{t}_c^i$ is generated with the changing domain states that bring the two solids into contact and constrain their motion due to the so-established contact interface. In the traditional description, the potential contact surface γ_c^i is decomposed into so-called active contact surface γ_A^i and inactive contact surface $\gamma_I^i = \gamma_C^i \setminus \gamma_A^i$ that are possibly changing continuously with time. Determining γ_A^i and γ_I^i, along with $\boldsymbol{t}_c^i$ is the objective of the contact problem. Notice that displacement and its first derivatives both appear in the weak form and are contained in the Sobolev spaces defined above, which put a condition of square integrability.

Summing up the virtual work due to contact constraint over the contact interface $\gamma_c(= \gamma_c^1 = \gamma_c^2)$ we get

$$\delta\Pi_c(\boldsymbol{u}, \delta\boldsymbol{u}) = \int_{\gamma_c^1} \boldsymbol{t}_c^1 \cdot \delta \boldsymbol{u}^1 d\gamma + \int_{\gamma_c^2} \boldsymbol{t}_c^2 \cdot \delta \boldsymbol{u}^2 d\gamma \quad (3.7)$$

$$= \int_{\gamma_c} \boldsymbol{t}_c^1 \cdot (\delta \boldsymbol{u}^1 - \delta \boldsymbol{u}^2) d\gamma = \int_{\gamma_c} (||\boldsymbol{t}_N|| \delta g_N + \boldsymbol{t}_T \cdot \delta \boldsymbol{g}_T) d\gamma \quad (3.8)$$

where δg_N and δg_T represent variation in normal and tangential gaps, respectively. The quantity $\delta\Pi_C$ represents the virtual work due to contact traction acting between the two surfaces and presents a challenge for its calculation in the finite element framework.

3.2.3 Contact constraints

The boundaries γ^1, γ^2 of the two interacting bodies $\Omega_i, (i = 1, 2)$ will have a normal gap between them, which is mathematically expressed in the traditional master-slave form as

$$g_N = (\tilde{\boldsymbol{x}}_2 - \tilde{\boldsymbol{x}}_1) \cdot \boldsymbol{n}_1 \tag{3.9}$$

Here, $\tilde{\boldsymbol{x}}_1$, $\tilde{\boldsymbol{x}}_2$ are points on the opposite surfaces having the smallest gap along the normal $\boldsymbol{n_1}$ at $\tilde{\boldsymbol{x}}_1$. For any physical contact between two solid bodies, the kinematical constraint on their boundaries will not allow for any interpenetration ($g_N < 0$) between the two surfaces, as compressive traction ($t_N = \boldsymbol{t}_N \cdot \boldsymbol{n}$) acting between the two bodies restricts them with $g_N = 0$. This condition, known as the Karush-Kuhn-Tucker (KKT) condition, is written as

$$g_N \geq 0,\ t_N \leq 0,\ t_N g_N = 0 \tag{3.10}$$

The contact law is non-smooth and multivalued for $g_N = 0$ as there are infinite possible values of t_N, which can be understood through the fact that the contact pressure is a reaction force generated to maintain the equilibrium between the two solids. So, techniques from optimization theory like the Lagrange multiplier and the penalty method can be utilised to solve this problem involving inequality constraints. It should be noted that while the condition of impenetrability is, theoretically, exactly enforced by Lagrangian methods, it is inherently violated in the penalty methods, and the numerical solutions depend upon the choice of the penalty.

3.3 Midplane based segment-to-segment contact discretisation

In this section, we propose the methodology for imposing contact constraints unbiasedly using the penalty method. Initially, the approach is presented in the continuum framework, followed by its description in the discretised setting. Here, the focus is on defining the contact interface between the two surfaces,

where the contact traction and its integral are evaluated, as presented in the last subsection. The entire conceptual development follows the key idea of ensuring unbiased treatment of both surfaces.

3.3.1 Continuum based description

For the two bodies Ω^1 and Ω^2 coming into contact over their boundaries γ^1 and γ^2, respectively, there will be a shared part of the two boundaries defining the contact interface $\gamma_c (= \gamma_c^1 = \gamma_c^2 = \gamma^1 \bigcap \gamma^2)$. With the ongoing motion and deformation of the two bodies, the sub-regions of the two boundaries coming into contact (γ_c^1 and γ_c^2) forming the contact interface (γ_c) will change continuously. To enforce the contact constraint between the interacting surfaces, this work employs penalty method-based restrictions to oppose interpenetration of the contacting surfaces. The interpenetration is penalised by opposing traction that acts to restrict or limit this overlap between the two domains. Physically, the penalty method can be seen as analogous to a bed of springs between the surfaces resembling the asperities [83], and the material stiffness of these asperities opposes their compression, Fig. 3.2, [66].

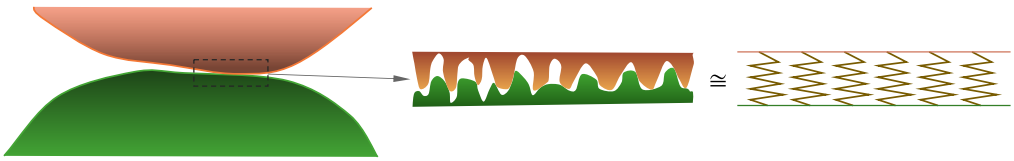

Figure 3.2: Physical analogy of penalty method with a bed of springs

To evaluate contact tractions in an unbiased manner, the geometrical intersection of the two bodies can be interpreted to be occurring with respect to a common interface, referred to as midsurface, which follows the geometry of both surfaces γ_c^1 and γ_c^2, Fig. 3.3. Here, the definition of the normal gap g_N is slightly altered from the traditional form stated in eq.3.9 that utilises the closest point of projection, which often poses a challenge of its own. The normal gap g_N considering the two end points of the analogous spring on both surfaces $\tilde{\boldsymbol{x}}_1$ and $\tilde{\boldsymbol{x}}_2$ is

$$g_N = (\tilde{\boldsymbol{x}}_2 - \tilde{\boldsymbol{x}}_1) \cdot \boldsymbol{n}_{\text{ms}} \tag{3.11}$$

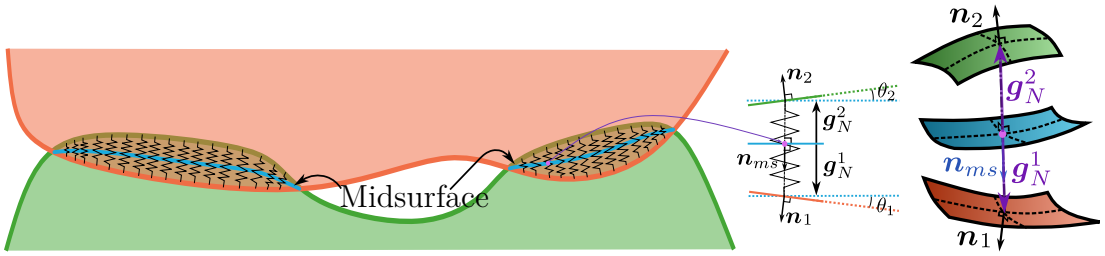

Figure 3.3: 2D analogue of exaggerated geometrical interpenetration of two solids during contact and the gap between surfaces and corresponding 3D elements

where $\boldsymbol{n}_{\text{ms}}$ is the normal to the midsurface and the gap g_N is negative only in the case of interpenetration.

Using the penalty method, the gap of interpenetration is utilised to evaluate the normal traction t_N. This normal traction or contact pressure is proportional to both the normal gap g_N and the stiffness of the analogous springs, which is contained in the penalty factor ϵ_N and written as -

$$||\boldsymbol{t}_N|| = -\epsilon_N g_N H(-g_N) \tag{3.12}$$

where $H(\cdot)$ is the Heaviside function. The analogous springs, generated following the interpenetration, are normal to this midsurface which allows splitting the normal gap vector $\boldsymbol{g}_N$ in two parts $\boldsymbol{g_N}^1$ and $\boldsymbol{g_N}^2$ with each representing the interpenetration with respect to the midsurface point $\boldsymbol{x}_m$ as

$$\boldsymbol{g}_N = \boldsymbol{g}_N^2 - \boldsymbol{g}_N^1 = (\tilde{\boldsymbol{x}}_2 - \boldsymbol{x}_m) - (\tilde{\boldsymbol{x}}_1 - \boldsymbol{x}_m) = \tilde{\boldsymbol{x}}_2 - \tilde{\boldsymbol{x}}_1 \tag{3.13}$$

Using this description of the normal traction, the net normal force acting between the two bodies at contact interface γ_c can be evaluated using

$$\boldsymbol{F}_N = \int_{\gamma_c} \boldsymbol{t}_N d\gamma = \int_{\gamma_c} -\epsilon_N \boldsymbol{g}_N H(-g_N) d\gamma \tag{3.14}$$

3.3.2 Description in 3D discretised domains

Proceeding towards the discretised setting of the contact problem, consider the domains Ω_h^1 ($\simeq \Omega^1$)and Ω_h^2 ($\simeq \Omega^2$) with their discrete surfaces γ_h^i described using parameterisation of the form

$$\tilde{\boldsymbol{x}}^i = \sum_{j=1}^{m^i} \psi_j^i(\xi_1, \xi_2)\tilde{\mathbf{x}}_j^i \quad \text{where,} \quad \tilde{\boldsymbol{x}}^i, \tilde{\mathbf{x}}_j^i \in \gamma_h^i \tag{3.15}$$

where ψ_j^i represents the shape function associated with the jth node (having position $\tilde{\mathbf{x}}_j^i$) in the ith discretised boundary with the parameterisation of (ξ_1, ξ_2). The symbol $(\tilde{\cdot})$ has been used to denote that these points are over the boundaries of the respective domains. Any physical interpenetration between Ω_h^1 and Ω_h^2 results in the geometrical overlap between surfaces $\tilde{\boldsymbol{x}}^1$ and $\tilde{\boldsymbol{x}}^2$. This geometrical overlap for contact interaction is considered in a piecewise-pairwise manner by taking discrete facets (or segments) of finite elements on opposite boundaries. So, only the support of the basis functions over the facets is considered here for their pairwise interaction.

For each potentially contacting facet pair, a local midplane is defined in this discretised setting for the system in its current solution step, and the interpenetration of both facets with respect to this midplane is utilised in evaluating the contact traction. The construction of the midplane and the application of this contact traction is described in the following sections.

Construction of midplane per facet pair

Consider two interpenetrating facets A and B on the opposite boundaries with the region $\gamma_{h_A}^1$ and $\gamma_{h_B}^2$, respectively, the contact interface in a current solution step is chosen as a region over the midplane between the two facets and is written as $\gamma_{h_{c_{A,B}}}$. With this, the overall contact interface for boundaries γ_h^1 and γ_h^2 becomes $\bigcup_{A,B} \gamma_{h_{c_{A,B}}}$.

For the sake of initial explanation, a simplified illustration of this midplane concept is shown in Fig. 3.4 for two orthogonal hexahedral elements having interpenetration between their facets labelled as A and B. The midplane equi-inclined to both facets is constructed to define the contact interface and evaluate the contact traction for this pair of facets. The contact interface is defined by taking the intersection of the polygons of projections of both facets over the midplane. However, as shown in Fig. 3.4b, only a sub-region of the intersection corresponds to the interpenetration. This sub-region is the intersection of the projections of penetrating portions of both facets.

However, facet nodes are not necessarily co-planar in the general finite element representation of facets based on interpolation, so representative facet planes are

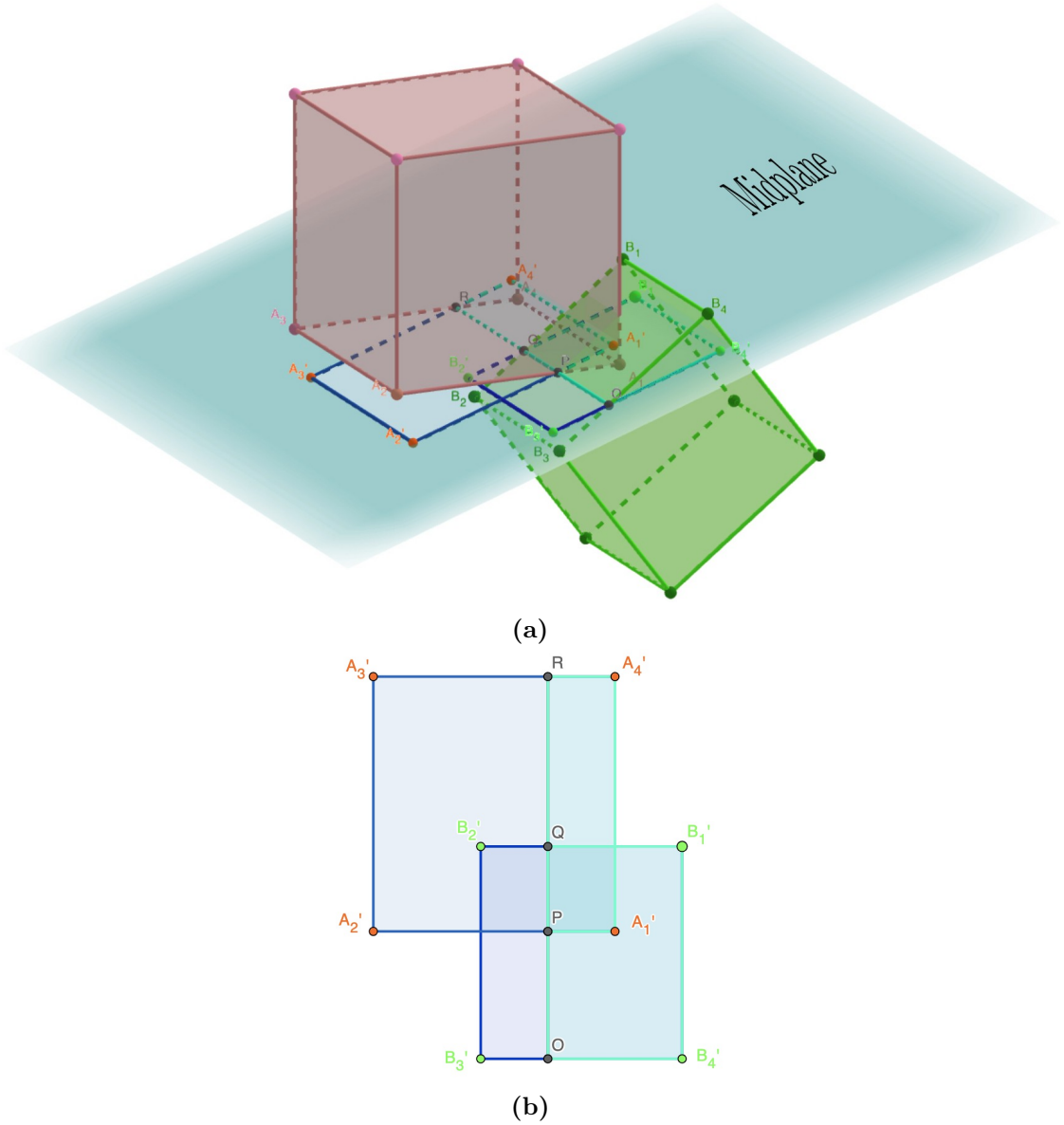

(a)

(b)

Figure 3.4: Simplified illustration of interpenetration between contacting elements shown for a pair of facets (a), and the overlap of the projections (b). Notice that only a sub-region of the intersection polygon corresponds to interpenetration between facets.

constructed for two contacting facets to define their midplane. The orientation of the representative plane for each facet is calculated by averaging the cross-products of edge vectors at all corners of the facet. So, the unit normal perpendicular to this plane can be written as

$$\boldsymbol{n}_{\mathrm{rp}} = \frac{\frac{1}{4}\sum_{i=1}^{4}\mathbf{n}_i}{\left\|\left(\frac{1}{4}\sum_{i=1}^{4}\mathbf{n}_i\right)\right\|} \text{where } \mathbf{n}_i = \mathbf{l}_i \times \mathbf{l}_{i-1} \tag{3.16}$$

with $\mathbf{l}_i$ and $\mathbf{l}_{i-1}$ denoting the edge vectors at the corner i, both being directed away from the corner node. Both $\mathbf{l}_i$ and $\mathbf{l}_{i-1}$ are ordered in a such way that each $\mathbf{n}_i$ gets directed outside the element. Each representative facet plane is considered to be passing through the mean position of the nodes (x_0), so its equation takes the form

$$\boldsymbol{n}_{\mathrm{rp}} \cdot \boldsymbol{x} - d = 0, \quad \text{where } d = \boldsymbol{n}_{\mathrm{rp}} \cdot x_0 \tag{3.17}$$

In this definition of the representative plane, the distances of all four nodes with the representative plane are equal. This definition also turns out to be the same as the concept of using normal to the plane formed by parametric lines joining the mid-points on the opposite edges [84]. An example of the two interpenetrating physical facets with their respective representative planes is shown in Fig. 3.5.

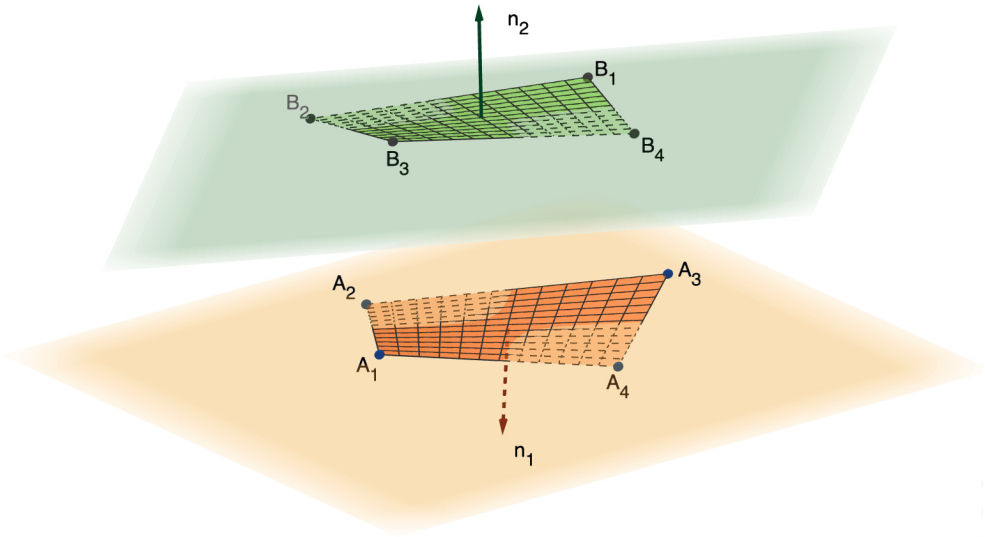

Figure 3.5: Two contacting physical facets with their representative planes. Also shown are the outward normal directions for both planes.

The midplane for the facet pair is defined to be equi-inclined to the two representative planes, so the unit normal to the midplane $\boldsymbol{n}_{\text{mp}}$ is written as

$$\boldsymbol{n}_{\text{mp}} = \frac{(\boldsymbol{n}_1 - \boldsymbol{n}_2)}{\|(\boldsymbol{n}_1 - \boldsymbol{n}_2)\|} \tag{3.18}$$

where $\boldsymbol{n_1}, \boldsymbol{n_2}$ are unit normals perpendicular to the representative facet planes for the first and second facet, respectively, as described in eq.3.16. The midplane is taken to be passing through the intersection of the two facet planes if they are non-parallel or through a point equidistant to both representative planes in case they are parallel. However, as will be shown later only the direction of the midplane affects the solution and not its position. It is evident that for well-formed surface facets undergoing interpenetration during solution, their continuously changing spatial configurations will result in smooth changes in the midplane direction.

Interpenetration zone between facets

The interpenetration between the per-facet pairs is evaluated using the midplane defined in the previous section and its orientation. This interpenetration is studied through two choices, and only the second one is selected as it yields true interpenetration.

In the first possibility, if only the penetration through the midplane is considered for defining the interpenetration between facets, then facets of hexahedral elements having bilinear interpolation can have five different possible configurations of penetration through the midplane as shown in Fig. 3.6. The approximated projections of the penetrating portion for defining the contact region are also shown. The construction of these projection polygons progresses as follows: first, the relative positions of all nodes of the facets are evaluated with respect to the midplane. Any node penetrating the midplane will be normally projected onto it. Next, if the nodes at both ends of any edge are on opposite sides of the midplane, then the intersection of this edge with the midplane is evaluated. Finally, a convex hull constructed over all these points defines the approximated projection polygon.

Now, to define the region on the midplane over which contact tractions will be evaluated, two possible regions of interest exist. One option is to consider the

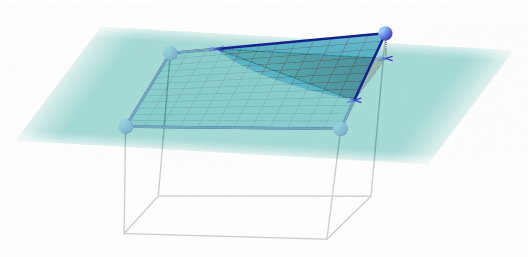

(a) One node penetrating the midplane

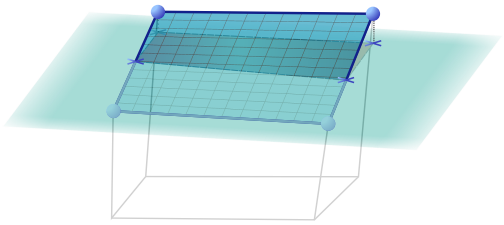

(b) Two adjacent nodes penetrating the midplane

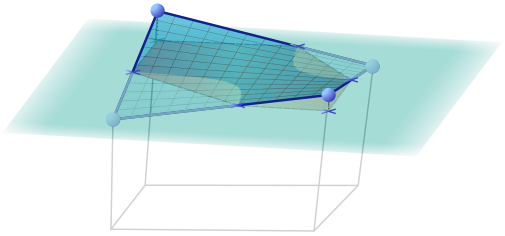

(c) Opposite nodes penetrating the midplane

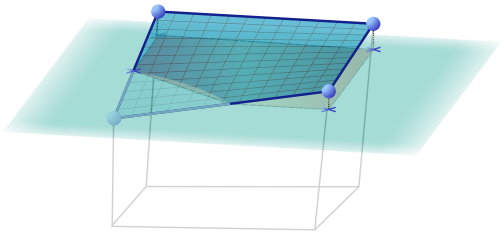

(d) Three nodes penetrating the midplane

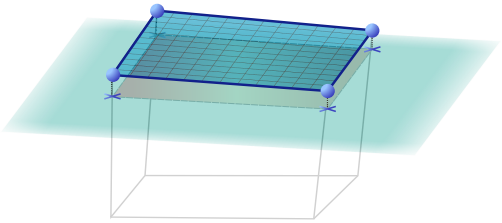

(e) All four nodes penetrating the midplane

Figure 3.6: Different possible configurations of a facet penetrating the midplane. Also shown are the projection polygons of penetrating portions

intersection between the projection polygons of midplane penetrating portions of both facets, as described in Fig. 3.6. The alternative is to consider the intersection between the quad polygons, formed by full projections of both facets over the midplane.

While projections of penetrating portions will capture the interpenetration between facets for many cases, there is a possibility that the curvature of the opposite facets results in some interpenetration outside the midplane. One such differentiating scenario between the two choices is shown through a cross-sectional view of the interpenetration between 3-dimensional facets in Fig. 3.7. If two different projections are considered - full projection of the facets and projection of only the penetrating portion of the facets, then both will lead to different contact interface

definitions. While the full projection will capture the entire interpenetration between the two facets (P+Q+R+S), the projection of only the portions penetrating the midplane will only capture the region Q+R. Although the interpenetration in regions P and S does not involve the midplane, the full projection of both facets has been chosen in this work for the evaluation of contact tractions. This will also allow us to capture the overlapping region outside the midplane, thereby corresponding to the *true* interpenetration. The projection of the interpenetrating volume over the midplane defines the contact region $\gamma_{h_{c_{A,B}}}$ for this facet pair. Note that irrespective of the choice of projections of full facets or only their midplane penetrating portions, the overall contact interface $\bigcup_{A,B} \gamma_{h_{c_{A,B}}}$ between full surfaces γ_h^1 and γ_h^2 will not be necessarily continuous.

So, to establish local contact interface for the facets $\gamma_{h_A}^1$ and $\gamma_{h_B}^2$ having a midplane $\gamma_{\text{mp}}^{A,B}$, the projections of both facets over the midplane can be written as

$$\gamma_{h_A}^{1,\text{mp}} = \text{Proj}_{\gamma_{\text{mp}}}\left(\gamma_{h_A}^1\right) \ , \quad \text{where } \gamma_{h_A}^1 = \sum_{j=1}^{w^A} \psi_j^A \mathbf{x}_j^A \tag{3.19}$$

$$\gamma_{h_A}^{2,\text{mp}} = \text{Proj}_{\gamma_{\text{mp}}}\left(\gamma_{h_A}^2\right) \ , \quad \text{where } \gamma_{h_A}^2 = \sum_{j=1}^{w^B} \psi_j^B \mathbf{x}_j^B \tag{3.20}$$

where w^A and w^B are the number of nodes on both facets. These projections can be directly evaluated by projecting facet nodes over the midplane and using the same bilinear interpolation functions. Thus, the contact interface, local to this pair of facets A and B, can be written as

$$\gamma_{h_{c_{A,B}}} = \gamma_{h_A}^{1,\text{mp}} \bigcap \gamma_{h_B}^{1,\text{mp}} \tag{3.21}$$

and the area corresponding to the true interpenetration will be its subset (i.e. $\subseteq \gamma_{h_{c_{A,B}}}$).

Contact traction

The interpenetration-based traction evaluation per facet pair in the discretised setting, following the original definition presented in eq.3.12, utilises the gap between facets measured normal to any point on the midplane. The split gap vector of either facet i ($i \in \{1, 2\}$) with respect to any point $\boldsymbol{x}_m$ on the midplane γ_{mp} are written as

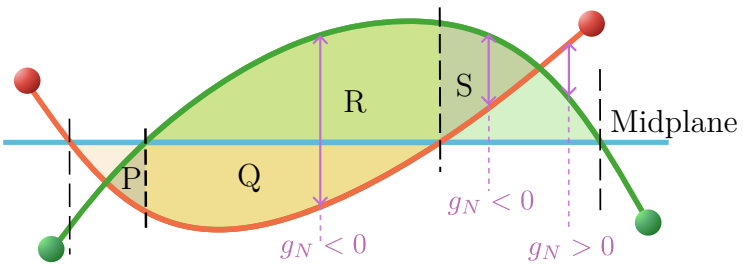

Figure 3.7: Cross-sectional view of a possible interpenetration between curved facets. Here, P+Q+R+S corresponds to actual interpenetration between facets, whereas only Q+R is accounted for if the projections of only the midplane penetrating portions of both facets are considered.

$$\boldsymbol{g_N}^i(\boldsymbol{x}_m) = \sum_{j=1}^{w^i} \psi_j^i \Big|_{(\xi_1^i,\xi_2^i)} \boldsymbol{x}_j^i - \boldsymbol{x}_m$$
$$\text{where } \left(\xi_1^i, \xi_2^i\right) : \text{Proj}_{\gamma_{\text{mp}}} \left(\sum_{j=1}^{w^i} \psi_j^i \Big|_{(\xi_1^i,\xi_2^i)} \boldsymbol{x}_j^i \right) = \boldsymbol{x}_m, \quad \boldsymbol{x}_m \in \gamma_{\text{mp}} \tag{3.22}$$

where w^i is the number of nodes. Here, the parametric coordinates (ξ_1^i, ξ_2^i) on the ith physical surface correspond to the physical point lying on the normal to the midplane. With this knowledge, the gap vector between facets with respect to $\boldsymbol{x}_m$ becomes

$$\boldsymbol{g}_N = \boldsymbol{g}_N^2 - \boldsymbol{g}_N^1 = \sum_{j=1}^{w^2} \psi_j^2(\xi_1^2, \xi_2^2)\boldsymbol{x}_j^2 - \sum_{j=1}^{w^1} \psi_j^1(\xi_1^1, \xi_2^1)\boldsymbol{x}_j^1 \tag{3.23}$$

The gap vector decides whether the facets are interpenetrating at this point (i.e. $g_N = \boldsymbol{g}_N \cdot \boldsymbol{n}_{\text{mp}} < 0$). Also, note that it satisfies $\boldsymbol{g}_N^i \times \boldsymbol{n}_{\text{mp}} = 0, \forall\, i \in \{1, 2\}$. Only the normal direction of the midplane is relevant in calculating the gap and all parallel planes will yield the same gap. This definition of normal gap captures the true continuous interpenetration between the surfaces, unlike the definition based on interpolation of the discrete normal gaps at nodes [82].

With this definition of the gap vector, the virtual work of contact defined in eq.3.7, knowing that the variation in surface displacements and positions are the

same (i.e., $\delta\boldsymbol{u} = \delta\boldsymbol{x}$), can be now written as

$$\delta\Pi_c \approxeq \delta\Pi_{c_h} = \sum_{\gamma_h} \int_{\gamma_{h_c}} \boldsymbol{t}_c^1 \cdot (\delta\boldsymbol{u}^1 - \delta\boldsymbol{u}^2) d\gamma = \sum_{\gamma_h} \int_{\gamma_{h_c}} \boldsymbol{t}_N^1 \cdot (\delta\boldsymbol{x}^1 - \delta\boldsymbol{x}^2) d\gamma \tag{3.24}$$

$$= \sum_{\gamma_h} \int_{\gamma_{h_c}} \boldsymbol{t}_N^1 \cdot \left(\sum_{j=1}^{w^1} \psi_j^1 \delta\boldsymbol{x}_j^1 - \sum_{j=1}^{w^2} \psi_j^2 \delta\boldsymbol{x}_j^2 \right) d\gamma = \sum_{\gamma_h} \int_{\gamma_{h_c}} \boldsymbol{t}_N^1 \cdot \delta\boldsymbol{g}_N d\gamma \tag{3.25}$$

So, the normal normal traction at any point on the midplane γ_{mp} can be written as

$$\boldsymbol{t}_N = -\epsilon_N \boldsymbol{g}_N H(-(\boldsymbol{g}_N \cdot \boldsymbol{n}_{\text{mp}})) d\gamma \tag{3.26}$$

and it is non-zero only at the points corresponding to true interpenetration between surfaces, i.e. at $\gamma_{h_{c_{A,B}}}$. This traction is applied equal and opposite on the two interacting facets along the direction of the midplane normal, thereby being compressive in nature, i.e.,

$$\boldsymbol{t}_N^1 = -\boldsymbol{t}_N, \quad \boldsymbol{t}_N^2 = \boldsymbol{t}_N \tag{3.27}$$

3.3.3 Contact integral

Contact tractions, evaluated using per facet pair interpenetration described in the previous section, provide the necessary contact constraint on the entire surfaces γ_h^1 and γ_h^2. These tractions are, however, defined pairwise between facets and act normal to their midplanes. For the finite element approach, these tractions are converted into effective nodal forces and the net nodal forces due to contributions by all pairs constraints the contact between bodies Ω_h^1 and Ω_h^2.

Mathematically, the distribution of nodal forces due to any traction $\boldsymbol{t}$ on a facet γ_{h_e} is given by

$$\mathbf{R} = \int_{\gamma_{h_e}} \boldsymbol{\Psi} \boldsymbol{t} d\gamma \tag{3.28}$$

where $\boldsymbol{\Psi}$ contains the shape functions corresponding to all nodes on the facet γ_{h_e}, and $\mathbf{R}$ contains forces that will act upon these nodes [34]. Individually, the ith nodal force ($i \in \{1, 2, .., w^e\}, w^e =$ total number of facet nodes) on facet A can be written using its associated shape function ψ_{i_A} as

$$\mathbf{R}_{i_A} = \int_{\gamma_{h_e}} \psi_{i_A} \boldsymbol{t} d\gamma \tag{3.29}$$

Using the above eq.3.29, the contribution of this interaction's normal traction $\boldsymbol{t}_N$ $(= \epsilon_N g_N H(-g_N)\boldsymbol{n}_{\text{mp}})$ towards the nodal forces on facet γ_{h_A} is given by

$$\mathbf{R}^N_{i_A} = \int_{\gamma_{h_A}} \psi_{i_A} \boldsymbol{t}_N d\gamma = \int_{\gamma_{h_{\text{mp}}}} \psi_{i_A} \epsilon_N g_N H(-g_N) \boldsymbol{n}_{\text{mp}} d\gamma \tag{3.30}$$

where g_N is the interpenetration gap between the facets and $\gamma_{h_{c_{A,B}}}$ is the polygon of the intersection of projections of both facets over the midplane. Similarly, nodal forces $\mathbf{R}^N_{i_B}$ on the opposite facet γ_{h_B} can be written using its shape functions ψ_{i_B} and will act in the opposite direction, so $\mathbf{R}^N_{i_A}$ and $\mathbf{R}^N_{i_B}$ will be together compressive in nature for the contact interface. In this work, the minimum of the bulk moduli of the two contacting surfaces is chosen as the penalty factor, which is further amplified by a scaling factor f_s.

The intersection of the polygons of full facet projections over the midplane $\gamma^I_{h_{\text{mp}}}$ $\left(\in \gamma_{h_{\text{mp}}}\right)$ represents the common span of both facets (with possible interpenetration) where contact traction is evaluated. The contact traction is zero elsewhere on the midplane as this region is outside the possible interpenetration volume between the bounded surfaces of facets. To evaluate the integrals numerically, the intersection polygon is subdivided into triangles $(\gamma^I_{h_{\text{mp}}} = \Delta_1 + \Delta_2 + ... + \Delta_k)$ formed by its edges and centroid, as shown in Fig. 3.8, allowing to write the nodal forces as

$$\mathbf{R}^N_{i_A} = f_s \epsilon_N \boldsymbol{n}_{\text{mp}} \left[\int_{\Delta_1} \psi_i g_N H(-g_N) d\gamma + \int_{\Delta_2} \psi_i g_N H(-g_N) d\gamma + \right. \tag{3.31}$$

$$\left. ... + \int_{\Delta_k} \psi_i g_N H(-g_N) d\gamma \right] \tag{3.32}$$

The intersection polygon is decomposed into triangles using the centre-based triangulation over the Delaunay triangulation as the Delaunay triangulation is not a unique procedure, so it can potentially contribute to error in the solution due inconsistency [79]. With this subdivision, the integrals are evaluated using the quadrature points over each triangle using the numerical integration technique described in [85],[86]. One of the possible integration schemes from different numbers of quadrature points over triangles can be chosen depending on the desired level of accuracy.

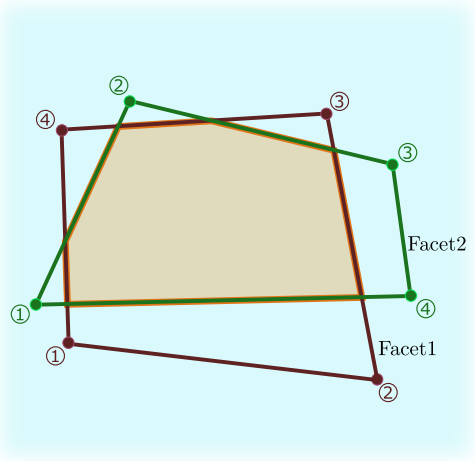

(a) Projections of the two quad facets onto the midplane

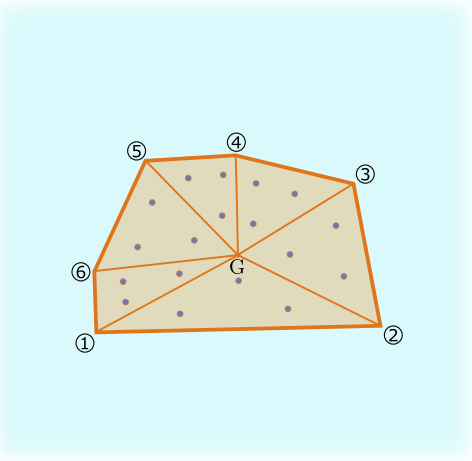

(b) Triangulation of the overlapping region and the quadrature points inside it

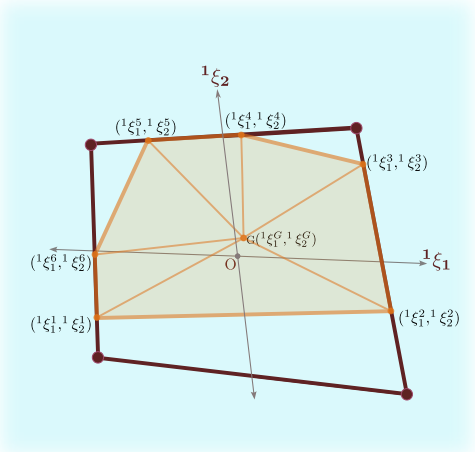

(c) Parametric coordinates of points in the overlapping region with respect to facet1

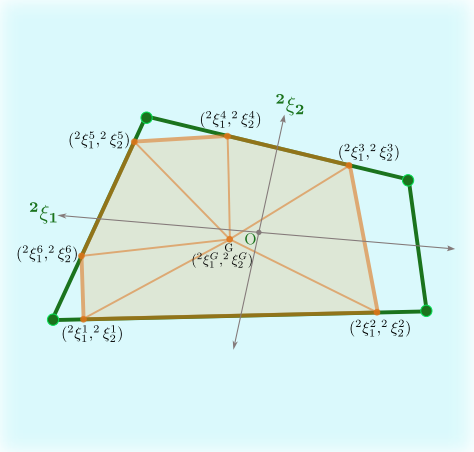

(d) Parametric coordinates of points in the overlapping region with respect to facet2

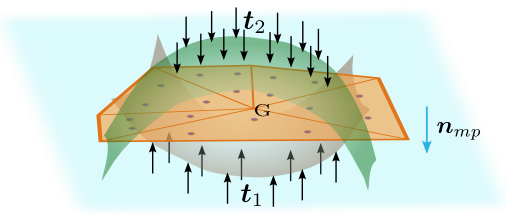

(e) Tilted view of the intersection polygon on the midplane in 3D with the interpenetration of opposite surfaces

Figure 3.8: Illustration of projections of both facets on the midplane, triangulation of the overlapping region, and inverse bilinear mapping in both projected quadrilaterals for parametric coordinates of quadrature points.

The interpenetration gap g_N at any quadrature point on the midplane is determined by employing both split gap vectors $\boldsymbol{g}_N^1$ and $\boldsymbol{g}_N^2$ as described in the eq.3.22. This requires finding the pair of parametric coordinates for each facet where a line normal to the quadrature point intersects the facet. For a first-order interpolation, the parametric coordinates of any point on the physical facet with respect to the physical facet and the parametric coordinates of this point's projection on the midplane with respect to the projected facet are the same. So, while the positions of the quadrature points on each triangle are evaluated using the physical coordinates of the vertices of the intersection polygon, their relative locations with respect to each projected quadrilateral are written using the parametric coordinates of bilinear mapping over the respective projected quadrilateral. These parametric coordinates (ξ_1, ξ_2) for each quadrature point are calculated using the inverse mapping of the bilinear interpolation as described in [87]. After determining (ξ_1, ξ_2), physical points on both facets are determined using shape functions.

At each quadrature point q, the interpenetration gap g_N is evaluated using both split gap vectors $\boldsymbol{g}_N^1\,({}^1\xi_1, {}^1\,\xi_2)$ and $\boldsymbol{g}_N^2\,({}^2\xi_1, {}^2\,\xi_2)$. It is only negative in the case of interpenetration, as explained previously and illustrated in Fig. 3.7.

Using m quadrature points per triangle, these integrals inside $[\cdot]$ in the eq.3.31 can be written as

$$\sum_{j=1}^{k} \int_{\Delta_j} \psi_i g_N H(-g_N) d\gamma = \sum_{j=1}^{k} A_{\Delta_j} \left[\Sigma_{q=1}^{m} \psi_{i_q} w_q g_{N_q} H(-g_{N_q}) \right] = \left[\Psi_q V_{encl} \right]_i \tag{3.33}$$

with the w_q's denoting the weights of the associated quadrature points, ψ_{i_q}, the value of the shape function corresponding to the ith node at this quadrature point, and g_{N_q}, the interpenetration gap between the facets at the qth quadrature point. The expression $[\Psi_q V_{encl}]_i$ is being used as a shorthand notation for the quantity on the left, which will correspond to the normal force on the ith node of the selected facet.

The presented formulation inherently maintains the force-moment equivalency in the forces applied on the nodes with the acting contact traction. It can also be observed that the nodal forces calculated using this midplane-based method depend upon the interpenetration between facets, so changes in nodal forces due to

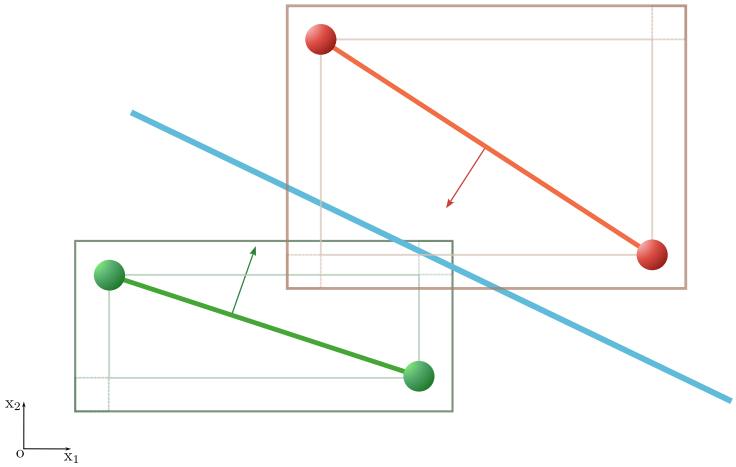

Figure 3.9: A 2D analogue of geometrical intersection check for a facet pair along with its midlpane

the time-based configurational changes in the system follow the smoothly changing interpenetration volume between facets. Thus, the penalization of interpenetration provides a smooth variation of nodal forces during deformation and avoids the jumping of contact forces, as is typical in NTS schemes.

3.4 Solution procedure

Computational solution of contact problems for given discretised geometries undergoing motion and deformation is a two-stage methodology. In the first stage, a contact search is performed to establish contact pairs of facets having interpenetration, whereas, in the second stage, contact constraint enforcement is carried out for physically interacting boundaries.

Contact search involves finding out which part of the surfaces of solids are in contact. It involves two phases: first, spatial search to establish potential contact pairs and second, detection to confirm the contact pairs with a geometrical intersection. This work uses the bounding box algorithm for spatial search to form a list of facet pairs [54] whose Axis Aligned Bounding Boxes (AABB) have an intersection. These bounding boxes are expanded by a pre-decided width in each dimension to avoid possible degeneracy before being tested for their intersection to form the list of potential contact pairs. This list of potential contact pairs

of facets also considers facets on the same body, thus accounting for self-contact problems. Once this list is generated, a geometrical intersection algorithm is used to confirm the facet pairs having interpenetration.

The geometrical intersection algorithm primarily involves three sequential contact checks to confirm the potential contact facet pairs with interpenetration. In the first check, facets with their representative planes having angles greater than a pre-decided value (e.g., 80° in this work) will be discarded. For facet pairs passing the first check, the positions of nodes on each facet will be checked with respect to the midplane. If all nodes of both facets lie on the opposite sides of the midplane (i.e., no interpenetration), then this second contact check will discard such facet pairs. One such facet pair with the bounding boxes of both facets having their nodes on the opposite sides of the midplane are shown for a 2D analogue in Fig. 3.9. Lastly, the remaining facet pairs will be tested for the intersection of the polygons of projections of both facets over the midplane using a clipping algorithm [55]. Only the facet pairs with non-zero areas of intersection of projection polygons are considered for the contact traction evaluation.

Contact traction evaluation for any interpenetrating facet pair is carried out over the intersection polygon on the midplane, and it will act normal to the midplane. The intersection polygon is triangulated, and quantities of interest are calculated at quadrature points of each triangle for numerical integration. This algorithm for evaluating contact forces acting on nodes of both facets is described in Algorithm1. One important property of bilinear interpolation of quadrilaterals that has been realised in the presented methodology is that when a bilinear quadrilateral surface in 3D is projected over a plane to form a 2D quadrilateral, the bilinear parametric lines of quadrilateral surface in 3D also get projected on to the bilinear parametric lines of the 2D quadrilateral formed by projection. Thus, using parametric coordinates of quadrature points with respect to both 2D quadrilaterals to find the shape functions of both facets is a valid approach.

The contact forces, calculated for each node of the interacting facets, are added on to the column matrix containing the external nodal forces acting on the system,

Algorithm 1 Multipoint integration of contact traction for interpenetrating facet pairs

get the polygon of the intersection of full projections of opposite facets
triangulate the intersection polygon using edges and its centroid
find the area of all triangles
Set $[\Psi_q V_{encl}]_i = 0$
for each triangle **do**
    for each quadrature point **do**
        locate this quadrature point on this triangle using the physical coordinates of vertices
        find the parametric coordinates $({}^i\xi_1, {}^i\xi_2)$ for this quadrature point w.r.t both projected quadrilaterals.
        find the physical points on both facets at this quadrature point using the parametric coordinates
        find the split gap vectors $\boldsymbol{g}_N^1$ and $\boldsymbol{g}_N^2$ at this quadrature point on the midplane
        find the interpenetration gap $g_N (= \boldsymbol{g_N} \cdot n_{\text{mp}})$
        if $g_N < 0$ **then**
            continue to the next quadrature point as there is no interpenetration
        else
            update the quantity $[\Psi V_{encl}]_i$ for both facets by taking contribution from this quadrature point.
        end if
    end for
end for
Calculate the normal forces $f_s \epsilon_N [\Psi_q V_{encl}]_i$ on each node of both facets in this pair, with the direction being decided by the midplane.

following the consideration of the contact constraint as boundary conditions on the interacting bodies. These contact forces are calculated in each solution step, and assembled prior to calculation of new kinematic quantities in the current step. The addition of contact forces in the external column matrix causes a contact constraint effect on the system configuration changes in the current step. This procedure is continued in each solution step afresh by solely focusing on the interpenetrating STS pairs in the current step and penalising their true interpenetration.

3.5 Some numerical experiments

The above-conceptualised segment-to-segment contact constraint enforcement strategy is analysed for its accuracy and validity through multiple benchmarks for

contacts between solids composed of first-order elements by implementation in the in-house solver DEST [88]. The presented tests consider contact between both flat and curved surfaces, and 13 quadrature points are used per triangle for integration in all cases. Different sets of strong discretisation schemes and material properties have been employed to demonstrate the versatility and robustness of the proposed scheme. To achieve the quasi-static nature of deformation in some tests, the dynamic relaxation technique is used, which helps in attaining the static solution by considering the steady state part of the transient response [36]. All the plots showing contact pressure variation are based on directly extracting stress states from the subsurface quadrature points inside finite elements of the contacting surface.

3.5.1 *Contact patch test*

This test, originally proposed in [65], [73] checks for the transmission of uniform pressure between two flat surfaces in contact. In this work, a version of the contact patch test used in [2] is employed for verifying the transmission of uniform pressure. Here, two blocks, with identical geometries and materials, are compressed against each other with frictionless conditions by placing one block on top of the other, see Fig. 3.10a. The bottom surface of the lower block is restricted against downward motion, while the lateral faces of both upper and lower blocks are constrained against motion in directions normal to those faces. The top surface of the upper block is uniformly pressed downwards and, theoretically, a uniform stress state is generated in both blocks.

For the discretised problem, both blocks have size $20 \times 20 \times 10$ mm^3 and elastic material with the Young's modulus of elasticity, $E_1 = E_2 = 207$ GPa, and Poisson's ratio, $\nu = 0$. The top surface of the upper block is pressed downwards by 0.01mm. Here, four different discretisation schemes are studied for uniformity of stress states - conformal meshes (matching nodes) with regular discretisation (Fig. 3.10b), non-conformal meshes (non-matching nodes) with regular discretisation (Fig. 3.10c), and non-conformal meshes with two types of irregular discretisations (Fig. 3.11b and Fig. 3.12). The proposed scheme passed the contact patch test in all cases,

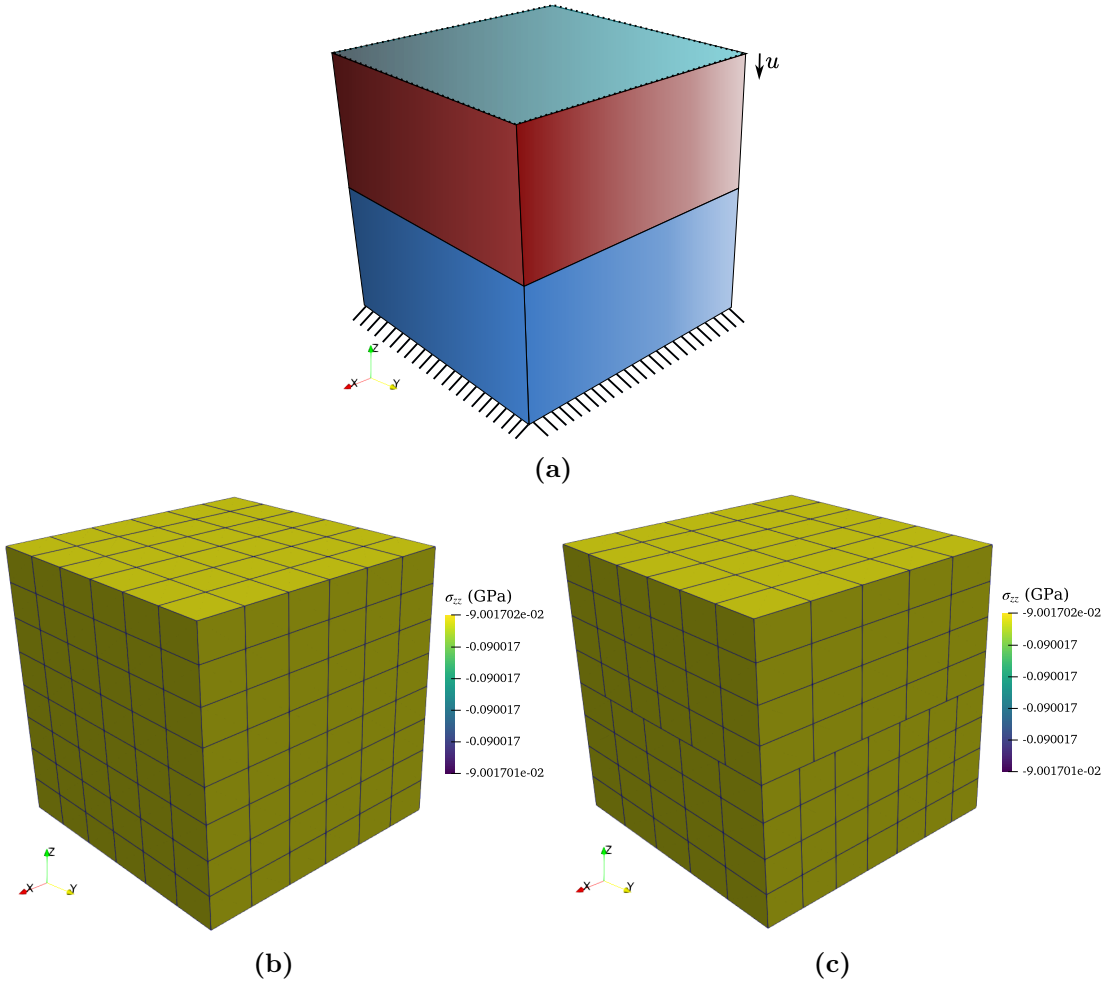

Figure 3.10: Contact patch test: (a) Original problem geometry, (b) stress distribution in both blocks for conformal meshes, and (c) non-conformal meshes, with both cases having regular discretisation.

with uniform stress states generated in both blocks. For regular meshes, stress values at all quadrature points are the same up to 15 digits after the decimal places. In the case of irregular meshes, this dropped to 10 digits in Fig. 3.11b and 9 digits in case of Fig. 3.12 which are nearly the same as the solution accuracy in element patch test with an irregular mesh. While Abaqus passes the contact patch test for conformal meshes, it does not pass this test in the case of non-conformal meshes [58][59]. A comparison of the performance of the proposed methodology with Abaqus for irregular non-conformal mesh demonstrates the robustness of the proposed scheme in general scenarios.

Additionally, the same problem is also studied against a range of material

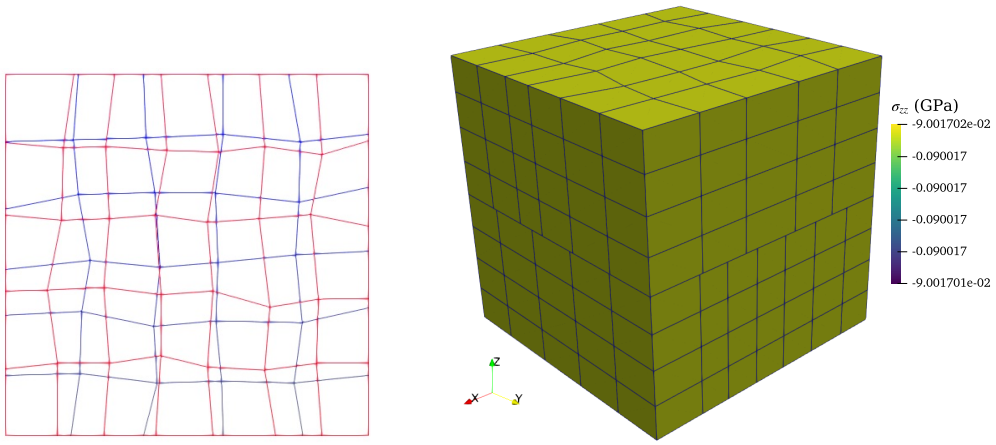

(a) **(b)**

Figure 3.11: Contact patch test: (a) Irregular discretisation of non-conformal meshes along contact interface, and (b) stress distribution in both blocks.

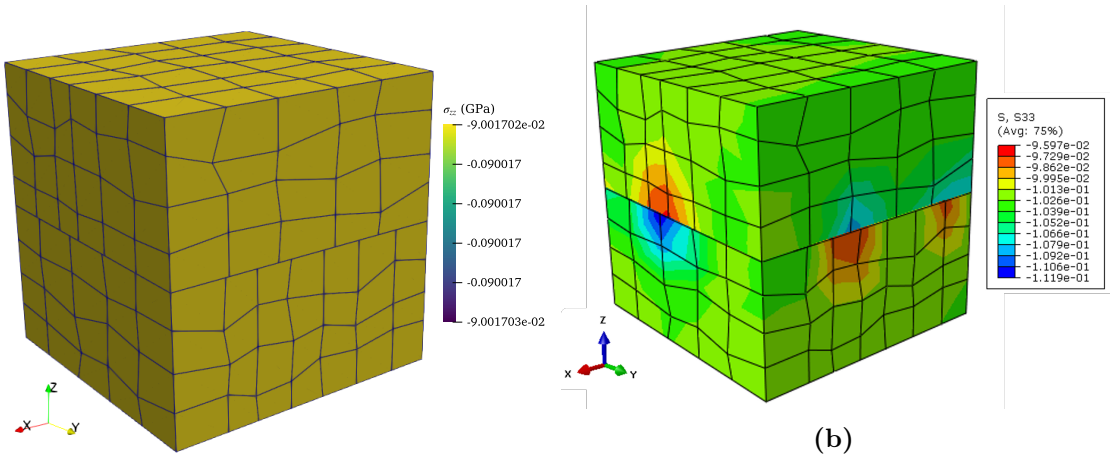

(a) **(b)**

Figure 3.12: Contact patch test for non-conformal meshes of both blocks having irregular discretisation along all directions : (a) Stress distribution in the proposed method, and (b) Abaqus.

properties and contact penalty for meshes with irregular discretisation. Two blocks are assigned elastic materials with the Young's modulus of elasticity, $E_1 = 10$ GPa, $E_2 \in \{10, 100, 1000\}$ GPa, and Poisson's ratio, $\nu_1 = 0.3$, $\nu_2 = 0.35$. The combinations of materials with a range of stiffness ratios and penalty scaling factors provide a diverse variety in testing the unbiased nature of the contact algorithm. The top surface of the upper block is pressed downwards by 0.01 mm, with the penalty scaling factor in contact being $f_s \in \{1, 10, 100\}$. Here, both blocks are discretised with non-regular meshes having a strong contrast in discretisation at

the interface, as shown in Fig. 3.13a. In all cases, the proposed scheme passed the contact patch test, with uniform stress states generated in both blocks. The stress values in all cases were the same up to 10 or 11 digits after the decimal point, which matches the accuracy of the element patch test that has the same 11 digits, implying that the contact algorithm is as accurate as the element patch test. To compare the performance, a dual pass version of the Node-to-Segment Area Regularisation (NTS-AR) [89] with equal weighting of both passes was also implemented. The results of the proposed test against the NTS-AR scheme using material stiffness ratio $E_2 : E_1 = 100$ and $f_s = 100$ are shown in Figs. 3.13b,3.13c. While the proposed scheme successfully passes the contact patch test, the equally weighted dual pass NTS-AR scheme suffers from undesirable variation in the contact pressure. Thus, the presented formulation will be of significant importance in modelling contact that is critically affected by the accuracy of contact pressure distribution, e.g. wear studies.

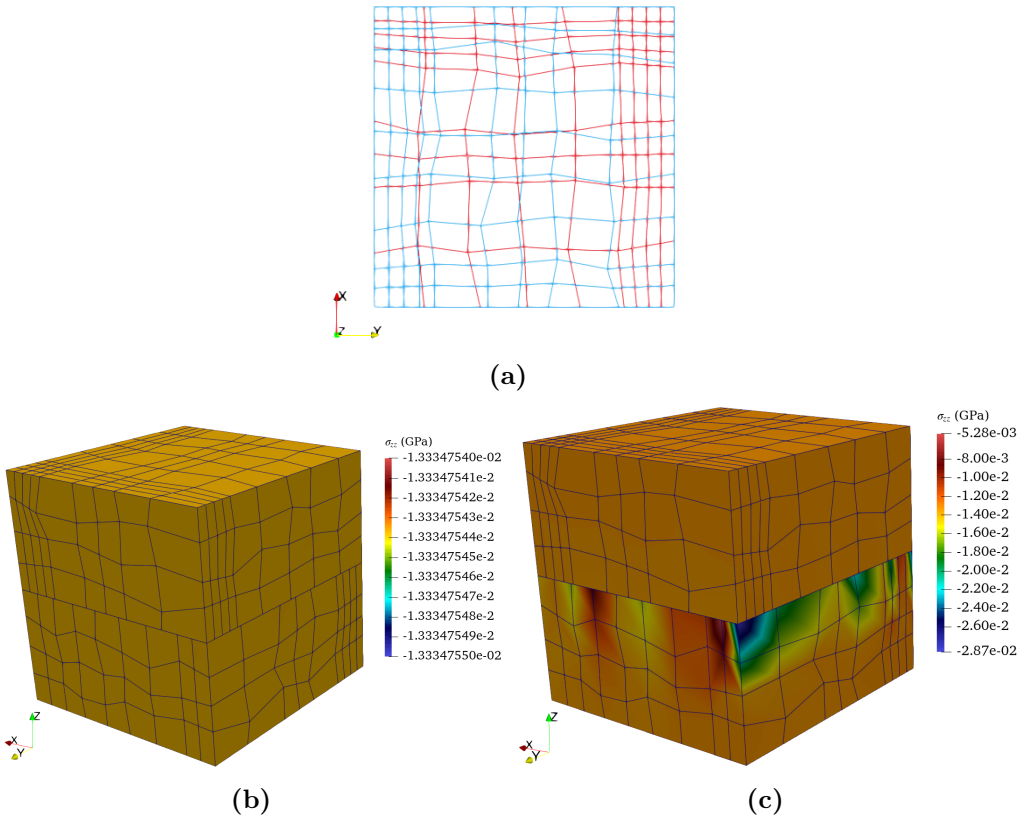

Figure 3.13: Contact Patch test: (a) wireframe of interface facets coming in contact, (b) result from the proposed methodology, (c) result from the equi-weighted double pass NTS-AR scheme.

3.5.2 *Two beam bending test*

In this test, the bending of two-beams is carried out to check the locking tendency of the algorithm [12]. For variation in contact conditions, two types of interfaces are considered between the non-matching meshes of beams - flat and curved as shown in Figs. 3.14a,3.14b. The outer dimensions of the two-beam system in both cases are $100 \times 10 \times 20$ mm^3, with the two beams in the first case having identical sizes. The same linear elastic material is used for all beams having a modulus of elasticity, E= 100 GPa and zero Poisson's ratio. The left ends of the two beams in both cases are fixed and loading is applied to the top surface of the upper beam. A uniform pressure $p = 0.1$ GPa is applied on the top surface, followed by a vertical line loading of $q = 0.1$ kN/mm, with both acting through the vertical nodal forces applied on the nodes of the top surface and calculated in the undeformed configuration. As can be seen in Figs. 3.15a,3.15b,3.15c,3.15d, both beams undergo continuous bending for both types of interfaces, thereby demonstrating a locking-free behaviour. The penalty method allows interpenetration between the beams in both cases, enabling a continuous deformation along the interface through constraints on contact surfaces.

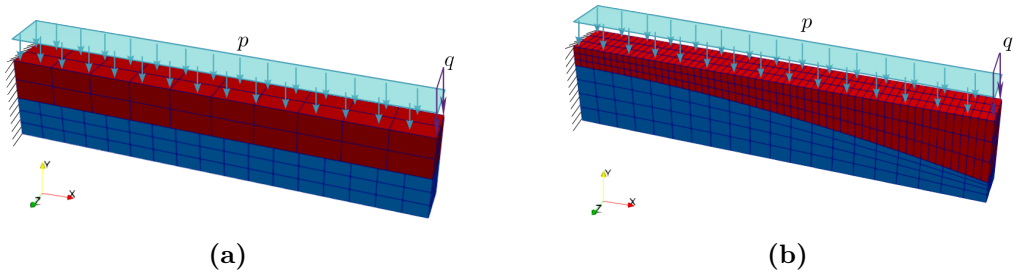

(a) (b)

Figure 3.14: Two-beam bending test to validate the locking-free behaviour: (a),(b) show undeformed meshes with flat and curved contact interface.

3.5.3 *Hertzian contact*

Developed by Heinrich Hertz in 1882 [6], the Hertzian contact theory has served as a gold standard in computational contact mechanics as it provides the analytical solution for non-conformal smooth surfaces in contact [90]. The non-conformal surfaces have a point or line as the initial contact, that turns into a finite area

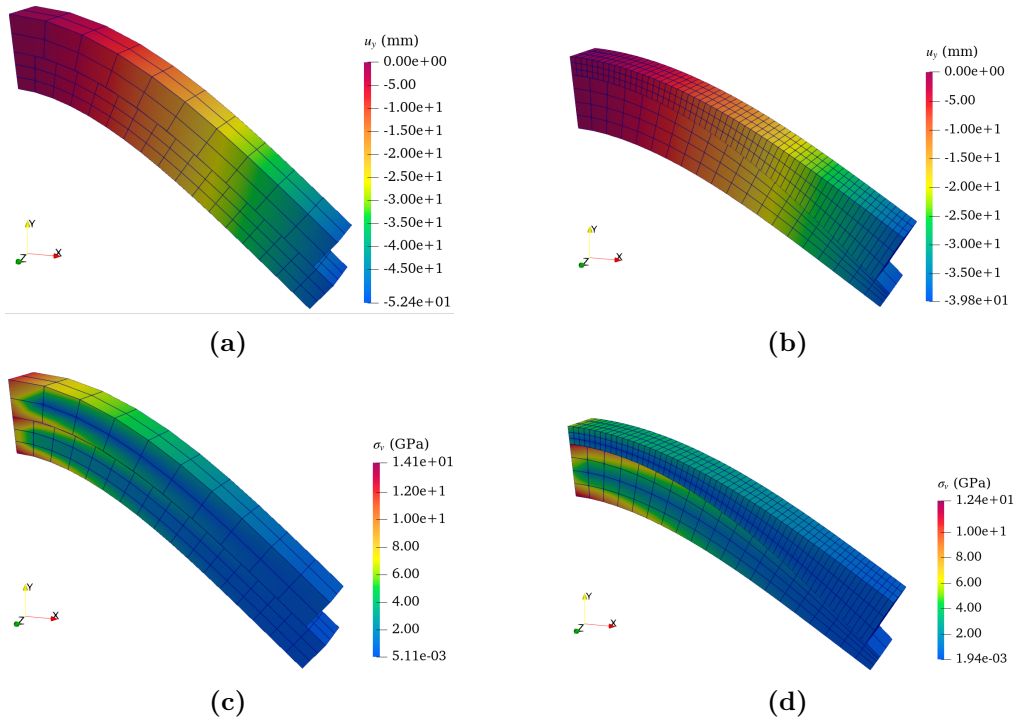

Figure 3.15: Two-beam bending test: (a),(b) show net displacements, and (c),(d) show von Mises stress for beams with flat and curved contact interface, respectively.

under deformation. This theory is based on the assumption of small deformation for elastic solids with homogeneous and isotropic material.

Two sets of problems are studied in this work. First set of problems tests contact between cylindrical and flat surface, whereas the second set tests the contact between two cylindrical surfaces.

A cylindrical and a flat surface in contact

In order to analyse the performance of the proposed algorithm, a canonical problem is considered wherein a cylindrical body with a radius, $R = 200$mm, is loaded against a flat surface for comparison against Hertz's analytical solution. As shown in Fig. 3.16a, the symmetry of the problem is leveraged and only a quarter of the slice of the cylindrical body (Fig. 3.16b) is used for the analysis. While the original problem has a line loading atop the cylindrical surface, a uniform loading is considered on top of the quarter symmetrical cylinder [74][78]. Both bodies have the Young's modulus of elasticity, $E_1 = E_2 = 210$ GPa, and the Poisson's ratio,

$\nu = 0.3$. The uniform pressure applied on the top of the quarter cylindrical body corresponds to the line loading of $P = 45\text{kN/mm}$ on top of the whole cylindrical body. For constraining the quarter geometry of this problem with the plane strain assumption, the lateral surfaces of both block and quarter cylinder, with normal along the axis of the cylinder, are restricted against any motion along the z-axis. Similarly, the use of symmetrical geometry implies that faces of both bodies with their planes passing through the initial contact point (having their normals along x-axis) are restricted to in-plane motion only. Lastly, the bottom of the block is also restricted to in-plane motion.

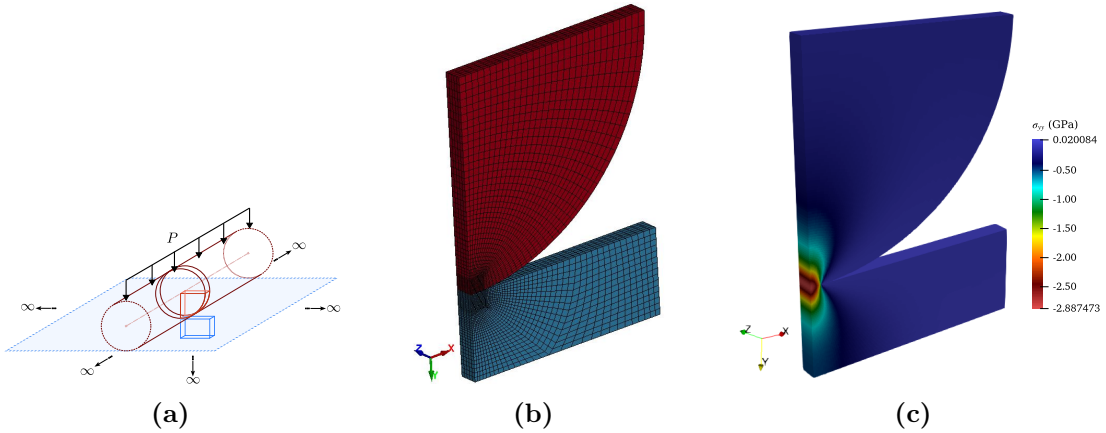

Figure 3.16: (a) Schematic of Hertzian contact problem for a cylindrical surface over an infinite plane, including the symmetric subpart used for the numerical study in this work. (b) Discretisation used for the conformal meshes. (c) Distribution of σ_{yy} in the refined conformal meshes.

This investigation encompasses three distinct discretisations: conformal coarse meshes (Fig. 3.17a), conformal refined meshes (Fig. 3.18a), and non-conformal meshes (Fig. 3.19a). Within each discretisation scheme, the influence of the increasing penalty scaling factors (f_s) on the contact pressure is studied.

For the case of conformal coarse meshes, the variation of the contact pressure is shown in Fig. 3.17. As can be inferred from the plot, a lower penalty implies analogous springs with lower stiffness, which leads to a higher interpenetration to counterbalance the applied loading. The contact pressure near the initial point of contact is under-predicted, while it is over-predicted near the end of the contact region to maintain the equilibrium with the applied total load. Effectively, the

contact region is overpredicted. On the other hand, higher penalty scaling factors of 10 and 40 lead to contact pressure variation more closely following the analytical solution. In this case of conformal mesh, the solution provided by Abaqus also closely follows the analytical solution. When this conformal mesh is refined by subdividing the elements ($h/2$), see Fig. 3.18, the numerical solution converges towards the analytical solution. The stress distribution for this refined mesh is shown in Fig. 3.16c.

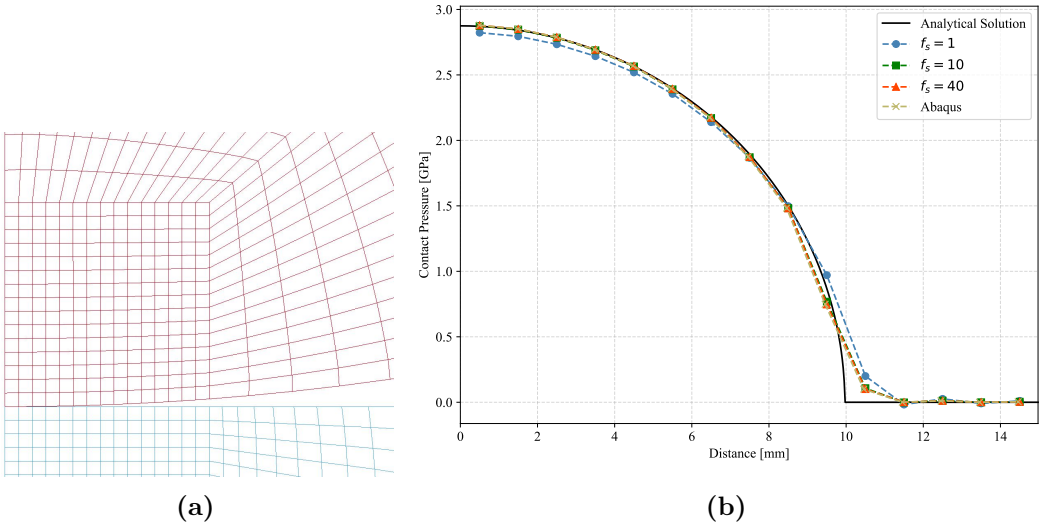

(a) **(b)**

Figure 3.17: Hertz contact for conformal coarse mesh with their interface shown in (a), and plot in (b).

When non-conformal meshes are tested for this Hertzian contact, the numerical solution of the proposed methodology was relatively unaffected, whereas the solution from Abaqus showed a divergence from the analytical solution as nodes became non-matching Fig. 3.19. The errors corresponding to the use of different penalty scaling factors for coarse conformal and nonconformal meshes are shown in Fig. 3.20. It shows that while the error decreases with a bigger penalty, the use of an increasingly very high penalty does not necessarily lead to a direct improvement in the solution accuracy, as the choice of a very high penalty scaling factor leads to an increasingly high force being applied with continuous interpenetration during incremental finite time steps, which in turn causes inaccuracies in the solution. So, the choice of an appropriate penalty scaling factor is crucial for the numerical solution.

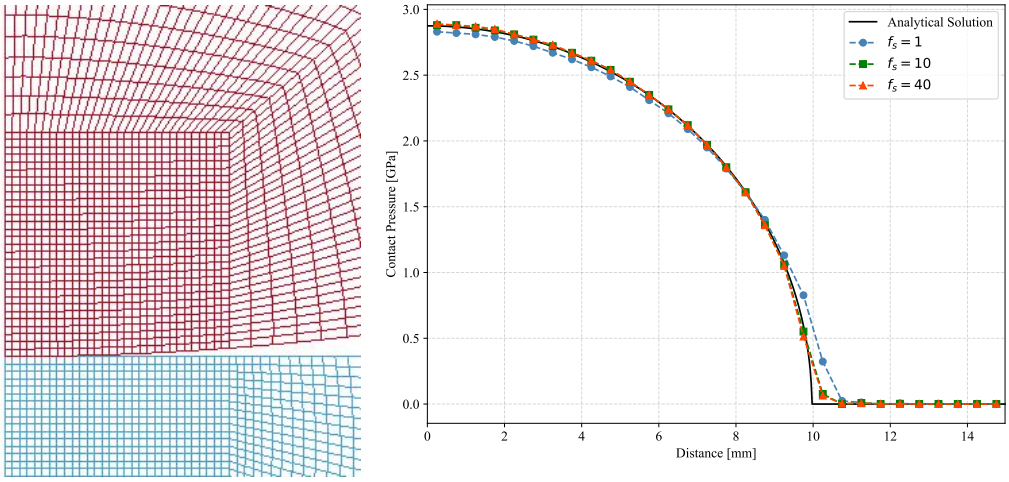

(a) **(b)**

Figure 3.18: Hertz contact for refined conformal mesh with their interface shown in (a), and plot in (b).

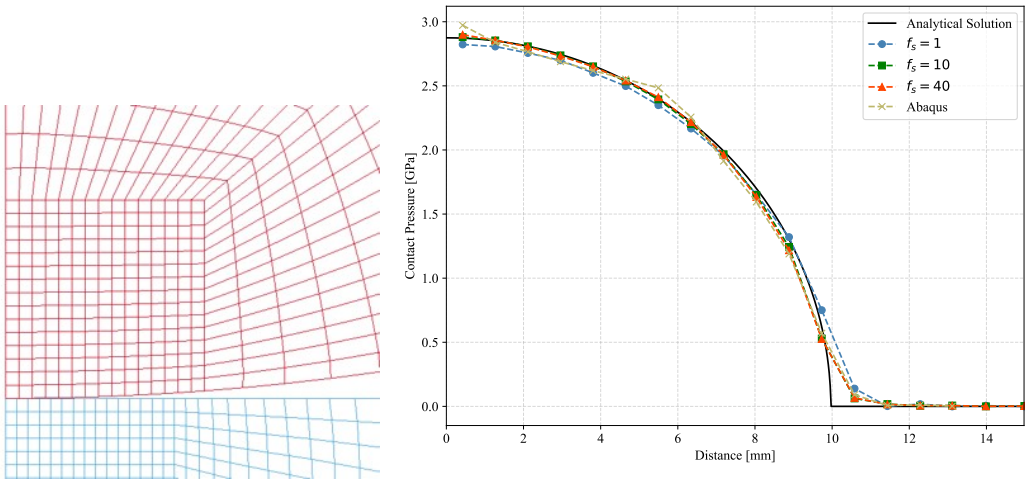

(a) **(b)**

Figure 3.19: Hertz contact for nonconformal mesh with the interface shown in (a), and plot in (b).

In all cases, the contact pressure variation of numerical solutions around the periphery of the contacting region suffers from inaccuracy emanating from the piecewise linear discretisation of the originally circular geometry. The disparity in the geometries of the original problem and the discretised versions alters the variation of the gap between the contacting surfaces, leading to an increased area of contact region. However, with increasing refinement of the mesh, the disparity with the original geometry decreases, and the curvature of the original geometry

is better captured, as proven by the convergence towards the analytical solution with increasing mesh refinement.

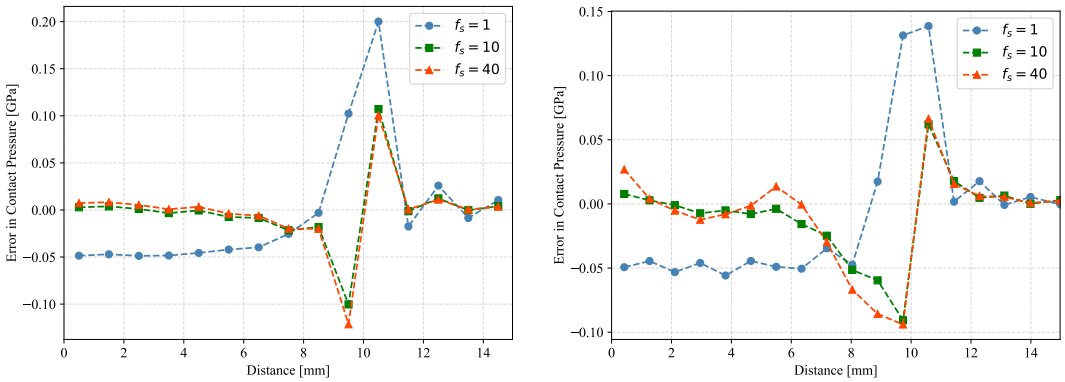

Figure 3.20: Hertz contact: Error in numerical solutions for (a) coarse conformal mesh, and (b) nonconformal mesh compared to the analytical solution.

Two cylindrical surfaces in contact

To analyse the performance of the proposed algorithm, a canonical problem is considered wherein two cylindrical bodies having radii, $R_1 = 200$ mm and $R_2 = 250$ mm, are loaded against each other for comparison against Hertz's analytical solution. The symmetry of the problem is leveraged, and only a quarter of the slices of the two cylindrical bodies are used in the analysis, see Fig. 3.21a. While the original problem has a line loading atop the cylindrical surface, a uniform pressure is applied on top of the upper cylindrical body [74][78], the three lateral surfaces of upper and lower cylinders, and the bottom surface of the lower cylinder are all constrained against motion in direction normal to their surface, thus, maintaining the plane strain condition in the original problem.

Two different non-matching meshes and three different combinations of materials are studied to thoroughly examine the contact algorithm. The two meshes are discretised with different number of elements in the same geometrical region to have a ratio 15:19 and 10:27 of elements at the interface, see Figs. 3.21b,3.21c. For the upper and lower cylinders, Young's modulus of Elasticity is $E_1 = 10$ GPa,

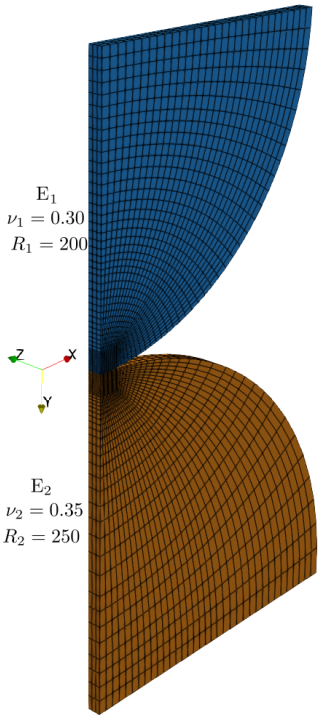

(a) Undeformed Mesh 15:19

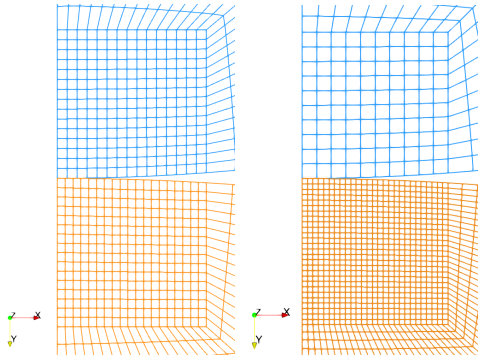

(b) Mesh ratio 15:19 (c) Mesh ratio 10:27

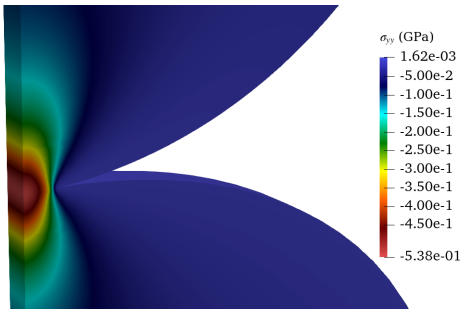

(d) Stress distribution σ_{yy} for mesh 15:19, E_2:E_1 = 100, $f_s = 10$

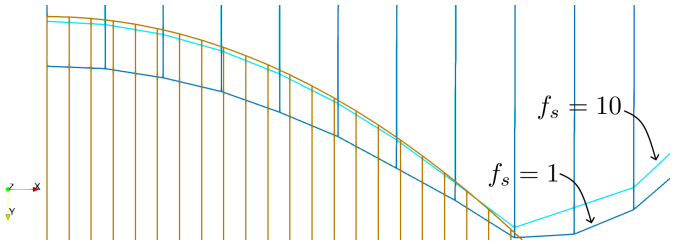

(e) Two deformed meshes (ratio 10:27) for E_2:E_1 = 100 corresponding to two scaling factors ($f_s = 1, 10$). The two lower meshes are nearly overlapping as they behave relatively rigidly. All meshes are vertically scaled up to observe the interpenetration.

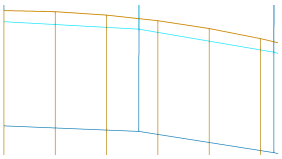

(f) Zoomed in view near the first point of contact

Figure 3.21: Hertz contact: (a) geometry of two cylinder problem, (b) and (c) two types of meshes used, (d) stress distribution near contact region, and (e) comparison of interpenetration for different penalties.

$E_2 \in \{10, 100, 1000\}$ GPa, and Poisson's ratio is $\nu_1 = 0.30$, $\nu_2 = 0.35$, respectively, and the contact definition in most cases uses a penalty scaling factor of $f_s = 10$.

The variation of the contact pressure for both upper and lower cylinders for two types of meshes discretised with under-integrated first-order elements with three different material combinations are shown in Figs. 3.22,3.23 and stress state in the two cylinders are depicted for one case in Fig. 3.21d. It can be observed that

for the same material stiffness (E_2:E_1 = 1), albeit different Poisson's ratio, the variation of contact pressure in both upper and lower cylinders is relatively smooth, Figs. 3.22a,3.22b. Both types of meshes show edge effect near the periphery of the contact zone which is not only an outcome of the discrete nature of contacting segments but also depends on their sizes. When the lower cylinder is composed of material with increasingly higher stiffness (E_2:E_1 = 10, 100), the discrepancy in the contact pressure in the case of two types of meshes becomes evident and is more pronounced with higher stiffness ratio, see Figs3.22c, 3.22d, 3.23a, 3.23b.

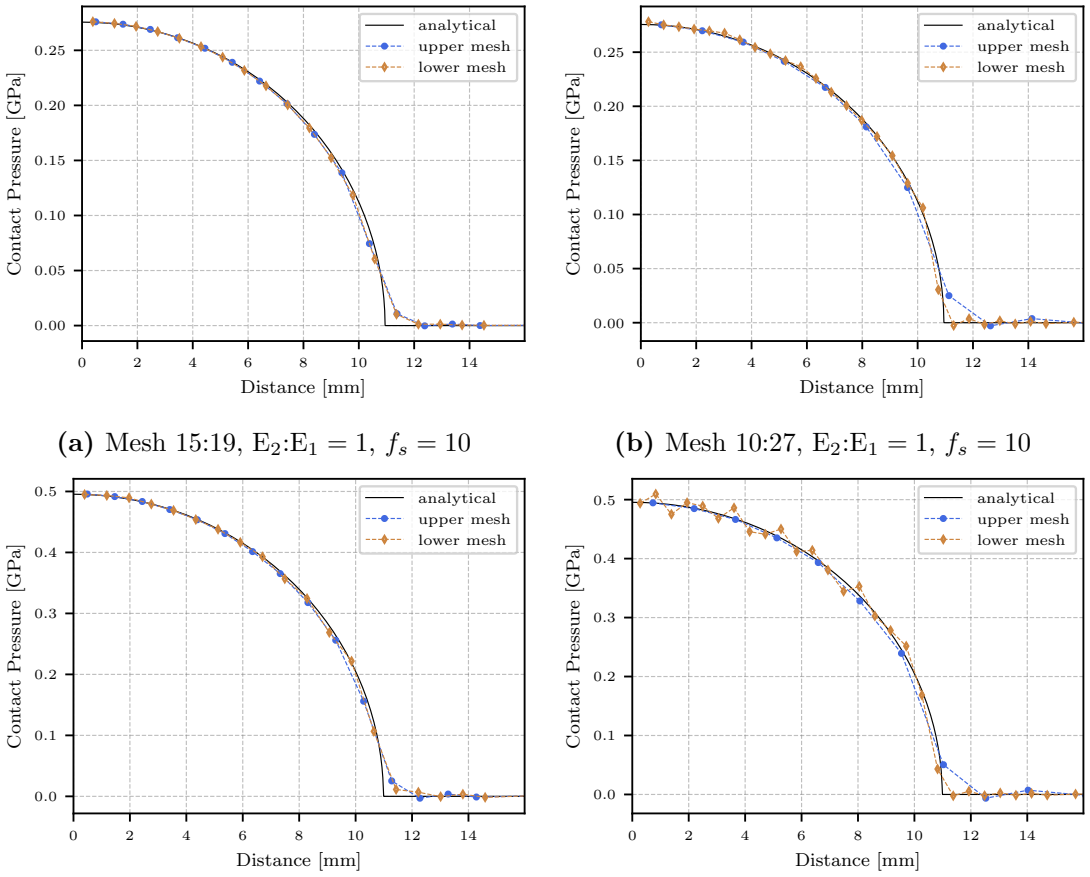

(a) Mesh 15:19, E_2:E_1 = 1, $f_s = 10$

(b) Mesh 10:27, E_2:E_1 = 1, $f_s = 10$

(c) Mesh 15:19, E_2:E_1 = 10, $f_s = 10$

(d) Mesh 10:27, E_2:E_1 = 10, $f_s = 10$

Figure 3.22: Hertz contact: contact pressure variation on both cylinders for mesh 15:19 (a,c), and mesh 10:27 (b,d), all with the same penalty scaling factor $f_s = 10$.

It can be observed that the oscillations only occur in lower cylinders (having fine mesh) and result from discrete finite elements lacking the ability to have continuity in their deformations. These oscillations increase with an increase in either mesh

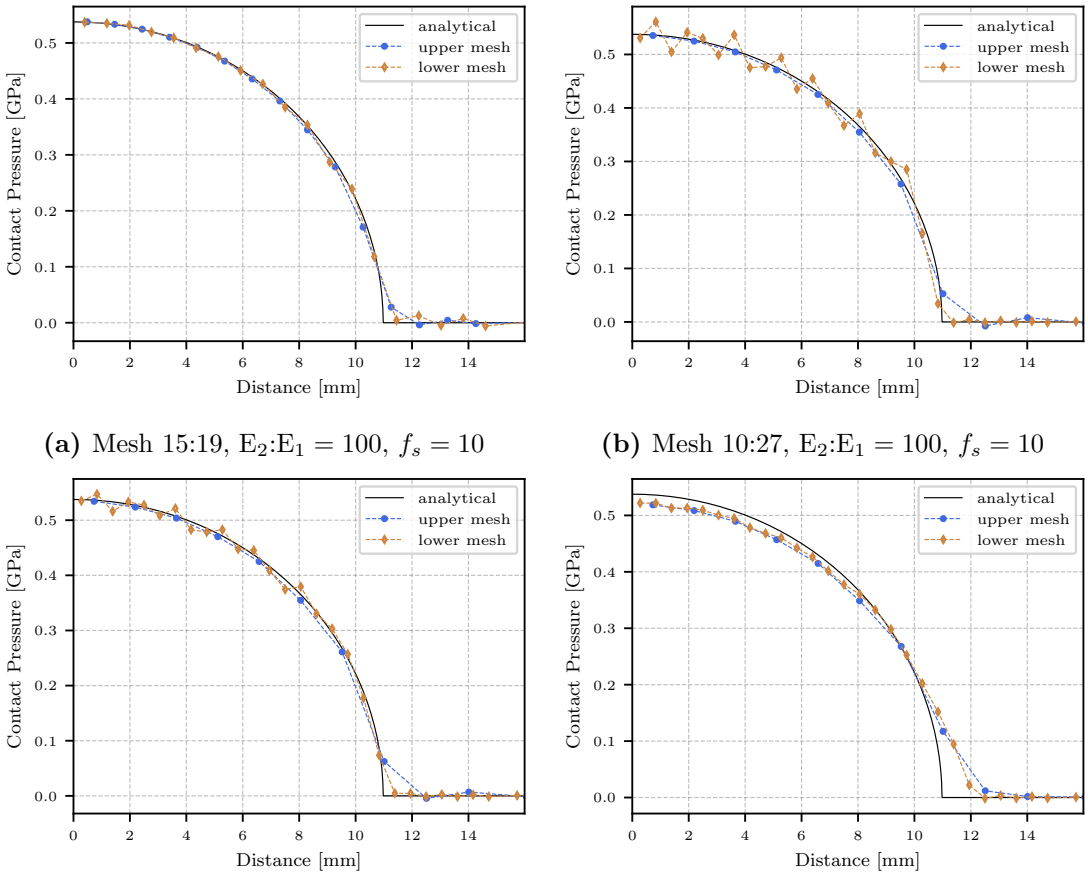

(a) Mesh 15:19, E_2:$E_1 = 100$, $f_s = 10$

(b) Mesh 10:27, E_2:$E_1 = 100$, $f_s = 10$

(c) Mesh 10:27, E_2:$E_1 = 100$, $f_s = 5$

(d) Mesh 10:27, E_2:$E_1 = 100$, $f_s = 1$

Figure 3.23: Hertz contact: contact pressure variation on both cylinders for mesh 15:19 (a), and mesh 10:27 (b,c,d) with different penalty scaling factor

ratio or stiffness ratio. The higher oscillations with differences in the sizes of contact segments are due to the pronounced effect of the deformation of finite segments not exhibiting the same smoothness as the deformation of the original circular geometry. For the mesh ratio 10:27, more segments on the lower mesh are in contact per upper cylinder segment, compared to the mesh ratio 15:10. So, the already present discrepancy with the original geometry gets worsened with the application of the contact constraints on the finite segments, causing higher oscillations in the fine mesh. When the lower cylinder has higher stiffness, it behaves more rigidly and requires the upper cylinder to have a higher surface curvature on deformation to adapt to the lower cylinder. The inability of the coarse finite segments to provide smoothness on deformation becomes more pronounced here,

causing a rise in oscillations in the fine mesh.

The upper mesh (coarse) can receive better curvature from the lower mesh (fine) deformation, so it does not have oscillations. Nevertheless, it cannot provide the required smooth curvature of deformation to the fine mesh, which leads to oscillations in the fine mesh. These oscillations get attenuated with the use of softer penalty scaling factors, see Figs. 3.23c,3.23d. Softer penalties allow higher interpenetration until the required counter balancing contact forces are generated. However, the unit penalty, $f_s = 1$, which can provide a better smoothness in the contact pressure, comes at the cost of an over-prediction of the contact zone and an under-prediction of the maximum contact pressure. Comparison of the interpenetration gap for two penalties ($f_s = 1, 10$) for the mesh 10:27 with stiffness ratio E_2:E_1 = 100 is shown in Figs. 3.21e,3.21f. While a high interpenetration implies a higher violation of the impenetrability constraint of contact, the variation in the interpenetration gap between segments along the entire contact interface is relatively smoother for $f_s = 1$ in comparison to $f_s = 10$, leading to a more smooth variation in the contact traction.

In all cases, the numerical solutions follow the analytical solutions, and disparities result from the piecewise finite element discretisation. So, the solution accuracy improves if the two contacting curved meshes have similar element sizes and/or stiffness. The proposed methodology reveals the importance of allowing and controlling the interpenetration between meshes for a desirable smoothness in the solution.

3.5.4 *Indentation test with a rigid flat punch*

Indentation of an elastic half-space by a flat rigid punch is a standard problem in contact mechanics that also has an analytical solution[7][91]. The analytical solution assumes that the elastic half-space has homogenous and isotropic material, and the deformation is small, so the small strain theory is applicable. In 2D, this problem exhibits a line loading over the half-space with plane strain assumption. The contact pressure increases radially along the contact region and approaches a theoretically infinite value at the edges of the punch, where a stress singularity is seen.

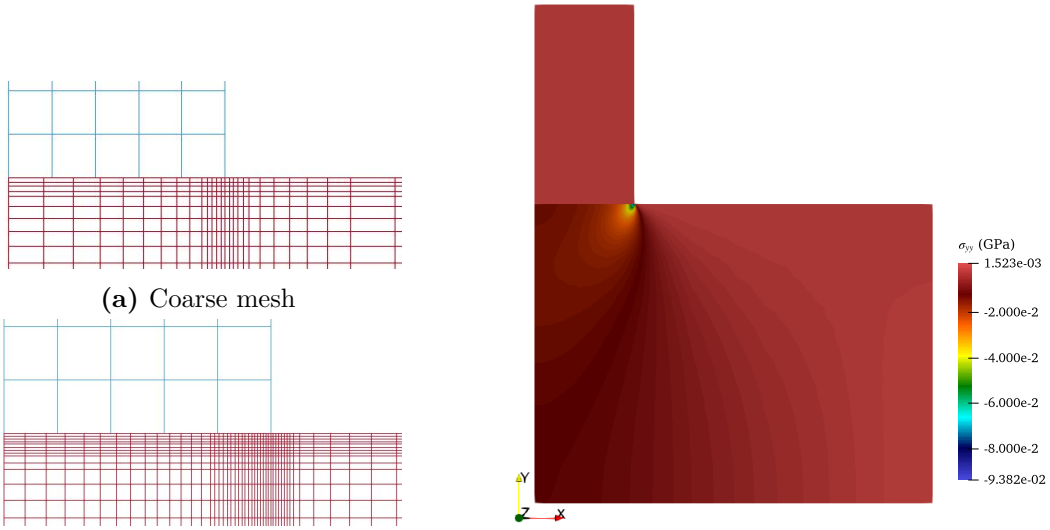

(a) Coarse mesh

(b) Refined mesh

(c) Distribution of stress σ_{yy}

Figure 3.24: (a) and (b) show the meshes used for the punch test, and (c) shows the stress distribution in the block for the refined mesh with $f_s = 40$.

For setting up the numerical problem in 3D, the half symmetry of the original problem is used. With this, only halves of the punch and the block underneath, representing the elastic half-space, are employed for the numerical test. Young's modulus of the block and Poisson's ratio are 210 GPa and zero, respectively. Similar to the Hertzian contact problem in the previous section, the non-free surfaces of both the punch and the block are restricted to in-plane motion only. To adhere to the rigid punch assumption in the analytical solution, all the nodes in the punch are prescribed a uniform downward displacement of 0.001mm. The half-width of the punch is $a = 5$mm, and the vertical load P is recovered from the contact forces applied on the interacting surfaces.

Two nonconformal discretisation schemes are studied here - (a) coarse mesh shown in Fig. 3.24a, and (b) refined mesh shown in Fig. 3.24b. Only the elements in the block have been subdivided for the case of the refined mesh, as the punch behaves in a rigid manner with prescribed displacement applied on all of its nodes. Similar to Hertzian contact, the same three penalty scaling factors are used here, i.e. $f_s = 1, 10$ and $, 40$.

To compare the numerical solution in both discretisation schemes, the contact pressure is normalized with respect to the analytical contact pressure under the

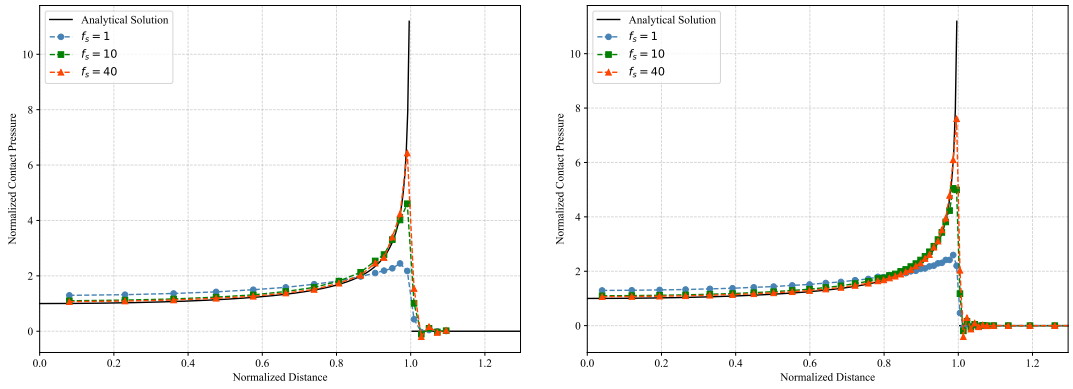

(a) **(b)**

Figure 3.25: Plots for the coarse mesh (a) and the refined mesh (b), showing the variation of the normalized contact pressure with the normalized distance.

punch's axis in each case. The radial distance along the contact region is normalized with respect to the half-width of the punch. Fig. 3.24 shows the stress distribution in the case of the refined mesh for the block. The plots for both the coarse and refined mesh are shown in Fig. 3.25. In contrast to the Hertzian contact, using a lower penalty scaling factor in this test results in over-prediction of the contact pressure near the vertical axis of symmetry and under-prediction along the edges of the contact region. With the increase in the penalty scaling factor, the numerical solution converges towards the analytical solution and the numerical contact pressure near the edge becomes higher. When the refined mesh is used for this test, the increased number of elements results in better capturing of the contact pressure variation, and the normalized plots show an improvement over the coarse mesh for each penalty scaling factor. Thus, the proposed algorithm can be concluded to pass the indentation test.

3.5.5 *Self-contact tests*

In some practical scenarios, the deformation of solid parts may result in contact between surfaces of the same original part, a phenomenon referred to as self-contact or auto-contact. This subsection investigates the developed methodology's capability to address such self-contact problems by assessing its performance through three self-contact problems for auto-detection and constraint application. The first problem

entails self-contact in a boxed structure with cavities and cracks that deform under loading and also experience sliding. The other two problems are carefully defined to verify the contact performance through flat and curved interfaces in contact.

For the first test, the discretised geometry of the box having size $200 \times 200 \times 50$ mm^3 is shown in Fig. 3.26a. It is composed of isotropic elasto-plastic material with linear hardening having Young's modulus, E= 10 GPa, zero Poisson's ratio, initial yield stress $\sigma_{y_0} = 1.0$ GPa, and hardening modulus of H = 0.1 GPa. The top surface of the box is uniformly pressed downwards by 40 mm while the bottom surface is held fixed. With deformation, cavities and cracks undergo interaction between their surfaces with auto-detection of contact, transferring load that results in deformation of the complete structure, Fig. 3.26b. Some domain regions also deform by sliding over the cracks due to the combined effect of material deformation and contact traction generated over contacting surfaces. Even for self-contact problems, contact search provides potential contact pairs based on the intersection of bounding boxes around all facets of the body, and contact detection finds oppositely facing facets with geometrical interpenetration. It should be noted that there is no redundancy problem at any contact edge [14] in the proposed method, as it applies contact constraints based on the continuous interpenetration between segments. The net distribution of nodal forces on the two opposite segments, sharing any edge, due to the contact traction might lead to net nodal forces acting on the edge nodes, which is an artefact of the mathematical nature of the elements and is inherently preserved in the proposed formulation to ensure the mathematical consistency.

For the second test, a discretised geometry of a single part as shown in Fig. 3.27(a) was selected with Young's modulus of elasticity, $E = 210$ GPa, and the Poisson's ratio, $\nu = 0$. Its geometry comprises three identical cubical blocks with sides of 20 mm each and four cylindrical subcomponents with inner and outer radii of 7mm and 8mm, respectively, at 5mm distance from the nearest edges of the blocks. The upper surface of the top block is pressed downward uniformly by 1.01mm, while the lower surface of the bottom block is held in place. Both pairs of blocks have an initial gap of 0.5mm between flat surfaces, which decreases with

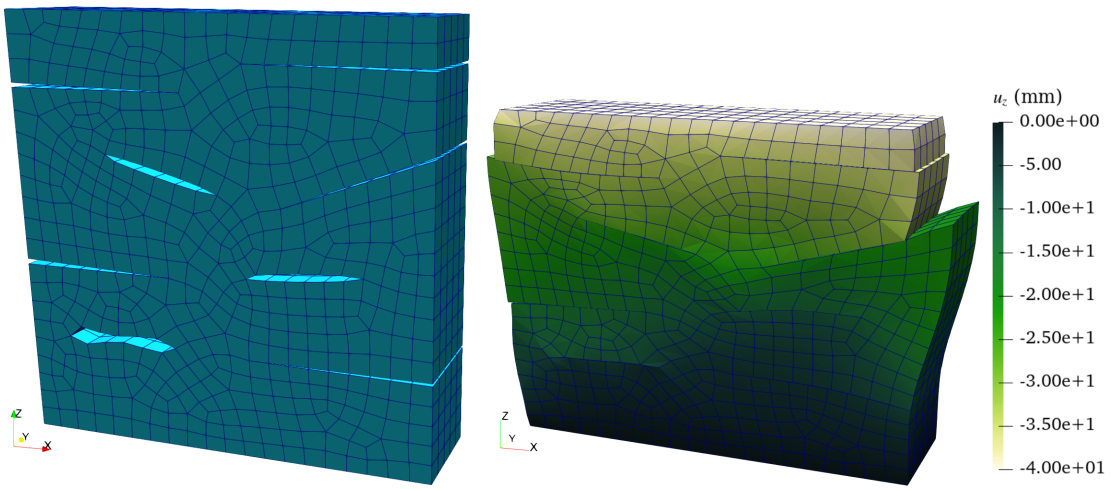

(a) **(b)**

Figure 3.26: Self-contact in a block with presence of cracks: (a) undeformed geometry, (b) deformed geometry under downward displacement of the top surface.

the top block's downward motion. As soon as the gap between the top and middle block closes, both start moving together until the gap between the middle and the bottom block closes. Continual pressing of the top surface results in a further compression of all three blocks. While this test attempts to combine self-contact with a contact patch test, the presence of *'ears'* (cylindrical subpart) in the geometry brings deviation from uniform compression. The stress components σ_{yy} in all three blocks are identical to the third decimal place.

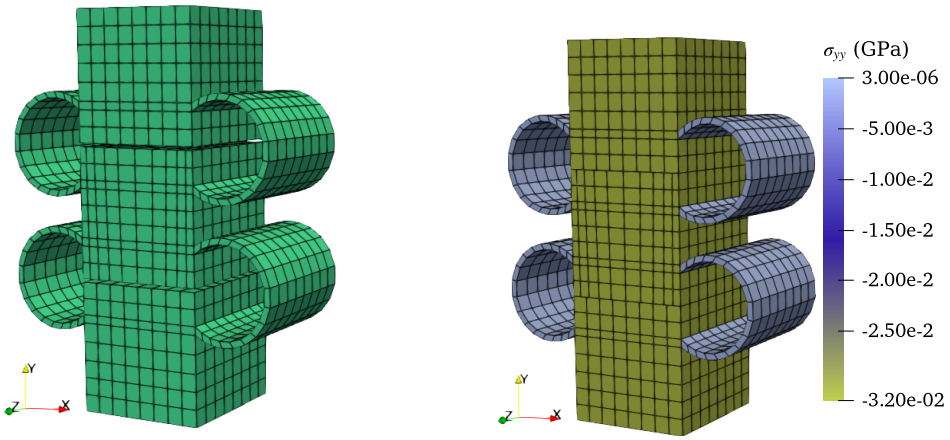

(a) **(b)**

Figure 3.27: Self-contact between flat surfaces of a single part : (a) mesh. and (b) stress distribution σ_{yy} in the entire domain upon compression.

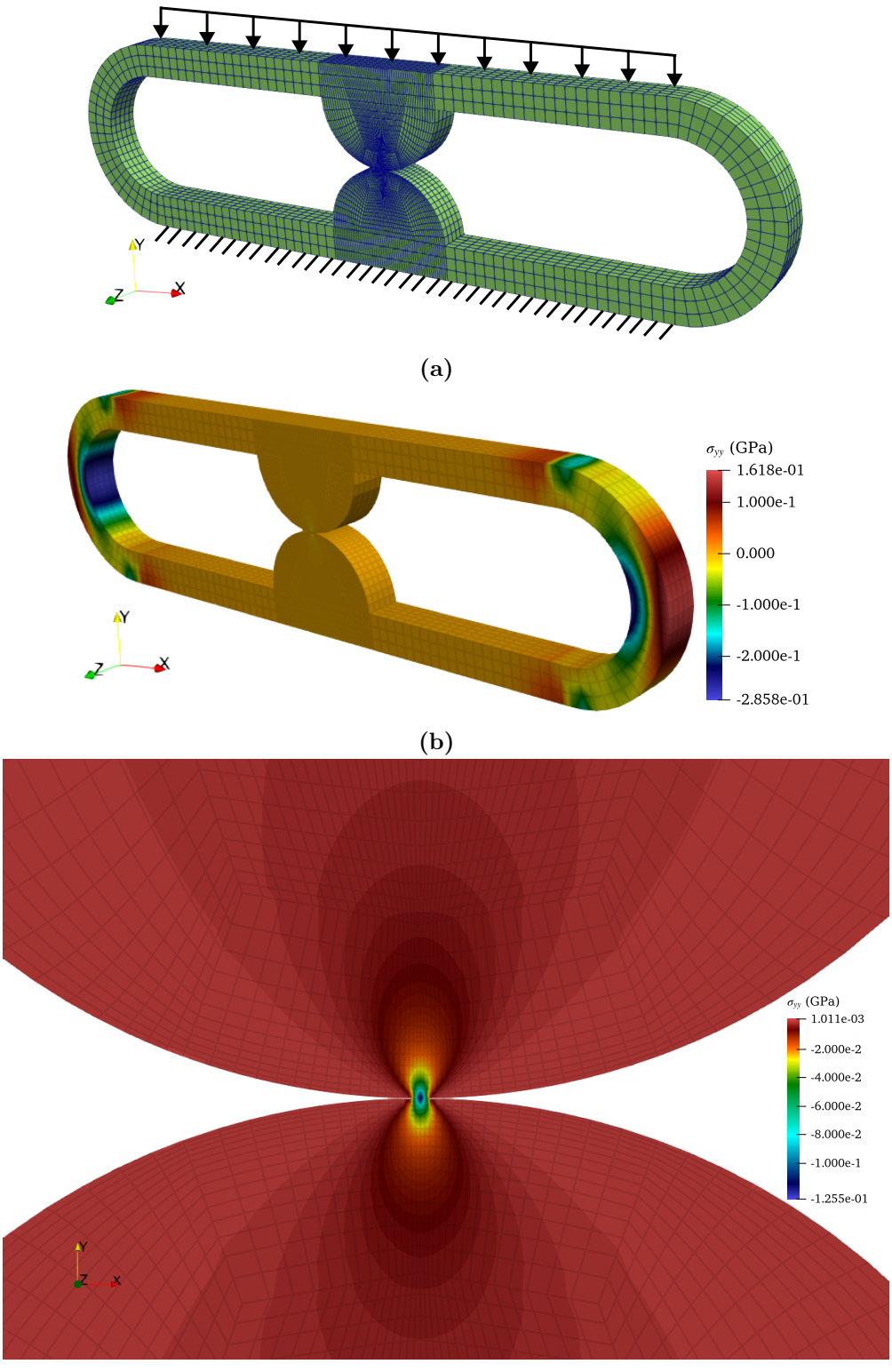

Figure 3.28: Self-contact between curved surfaces of a single part : (a) mesh and boundary conditions, (b) stress distribution in the entire part upon loading, and (c) stress distribution σ_{yy} near the contact region.

For the third test, the discretised geometry tested for self-contact between curved boundaries is shown in Fig. 3.28. It consists of a single part with two cylindrical surfaces in close proximity that come into contact with non-matching meshes when the top and bottom surfaces are compressed. The radii of curvature of both cylindrical surfaces are 10mm, with an initial gap of 0.1 mm that closes upon compression of the part. The bottom surface is fixed while the top surface is pressed downward by 0.1056 mm, as depicted in Fig. 3.28a. The consequent deformation leads to contact between the curved surfaces in this test, which combines self-contact with Hertzian contact. The resulting stress distribution near the contact region is depicted in Fig. 3.28c. As can be observed, it follows the Hertzian contact solution between curved surfaces, as shown previously in Fig. 3.21d.

All self-contact tests presented above demonstrate the inherent fair treatment of surfaces while symmetrically evaluating contact tractions in just a single pass in each solution step. Also, the solution procedure here is similar to the contact between facets of different parts, with just the difference of contact search yielding potential contact facet pairs from the same parts.

3.5.6 *Impact between two bars*

For evaluating the algorithm's performance in dynamic environments, two cases of symmetric collision between bars are considered - elastic bars with a flat interface and elasto-plastic bars with a curved interface.

Elastic symmetric collision

Two bars with equal and opposite velocities along the same direction are considered for collision [92][89]. The dimensions of both bars are $1 \times 1 \times 10\text{mm}^3$, and both are discretised to have non-matching meshes at the contact interface during the collision, as shown in Fig. 3.29a. Initially, both bars have a gap of 0.01 mm between them and an equal speed of 1.0 mm/ms along their axis. The elastic material in both bars has Young's modulus of 210 GPa, Poisson's ratio $\nu = 0$, and density $7.85 \times 10^{-6}\text{kg/mm}^3$. For contact interaction, three different penalty scaling factors

are considered. Artificial bulk viscosity is used to smooth out oscillations due to high-velocity gradients caused by high f_s, with linear and quadratic factors being 0.6 and 15, respectively. Plots for the variation of contact force, average velocity and average displacement for nodes on the contacting face of the left bar are shown in Fig. 3.29. While the contact force attains a constant analytical value for the duration of contact, the numerical solution has a gradual change in the contact force due to the penalisation of gradual interpenetration in the two bars. Similarly, a gradual change is observed in the average velocity of the contacting face of the left bar during contact, and some oscillations persist even after the collision. The overshoot in the average displacement of the contacting face of the left bar above the analytical solution during contact indicates penetration between the two bars, resulting in a lag in displacement in the further numerical solution. In all results, using a higher penalty scaling factor brings the numerical solution closer to the analytical solution, but it suffers from increased oscillations, as has also been reported in [93]. Higher penalties also decrease the size of stable time step increments. The overall deviation of the numerical solution compared to the analytical solution is an artefact of the penalty method, as can also be seen in [92]. However, the use of non-matching meshes in the presented solution proves the validity of the proposed method in general contact problems.

Inelastic collision between two bars with curved interface

This test, inspired by the symmetric Taylor impact test, considers the high-speed symmetric collision between two elasto-plastic bars (linear-hardening) having a curved interface, see Fig. 3.30a. Both bars have Young's modulus E = 69 GPa, Poisson's ratio $\nu = 0.33$, density $\rho = 2.71 \times 10^{-6}$ kg/mm^3, initial yield stress $\sigma_{y_0} = 0.276$ GPa, hardening modulus H = 0.2 GPa, and are moving co-axially towards each other with a speed of $v = 330$ m/s. The maximum dimensions of the two bars are the same, $1 \times 1 \times 10.5$ mm^3, with the circular geometry having a diameter of 1 mm. Two cases are considered here: (a) dissimilar discretisation, Fig. 3.30b, and (b) same discretisation of meshes, Fig. 3.30c. In both cases, the two bars

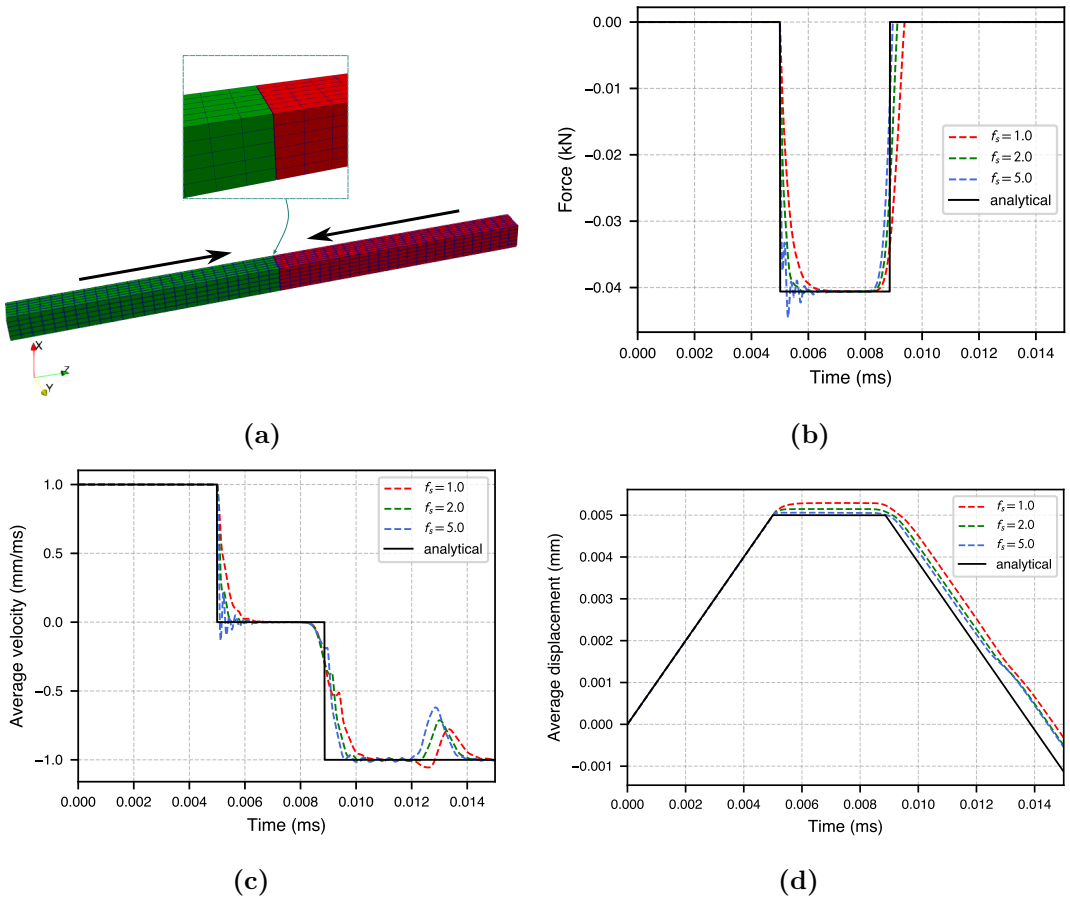

Figure 3.29: Impact between two bars : (a) discretisation in both bars, (b) variation of force on contacting face of the left bar, (c) variation of the average velocity of contacting face of the left bar, and (d) variation of average displacement of contacting face of the left bar.

undergo plastic deformation upon collision, with both rods bulging laterally, and the contact interface gradually deforms, going from the initial edge contact to a full surface-to-surface contact. Continual deformations in the bars during the collision about $t = 0.0139$ ms are shown in Figs. 3.31a,3.31b. While the second case has a symmetric distribution of nodal velocities owing to full symmetry in the two bars, the first case has an unequal distribution, emphasising the effect of slight change in discretisation causing mismatch in masses of the two bars. The two deformed meshes near the contact region upon rebound are dissimilar or same depending upon whether the two bars have dissimilar discretisation or same discretisation, respectively, Figs. 3.31c3.31d. In the case of dissimilar discretisation, the net non-axial mass in the fine mesh is larger than that of the coarse mesh due to the nodes

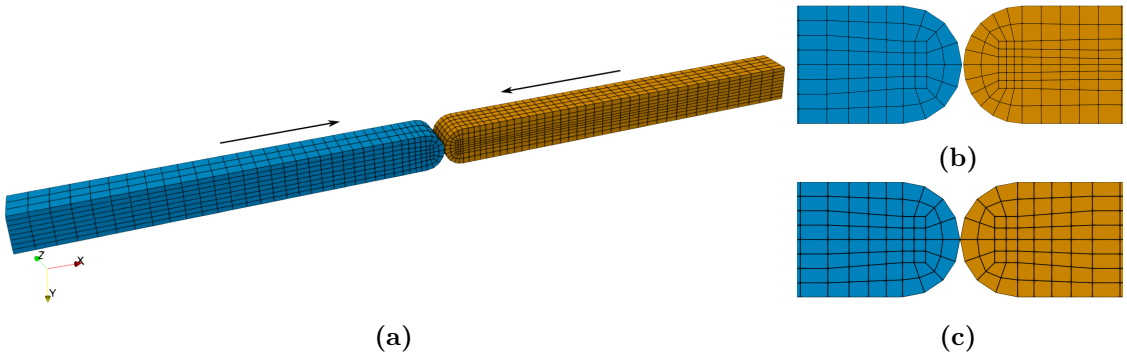

Figure 3.30: Inelastic collision: (a) geometry of the two bars moving towards each other, (b) dissimilar discretisation and (c) same discretisation of curved surfaces.

in the coarse mesh having larger nodal masses. This asymmetry in the non-axial masses in the two rods leads to the formation of a concave-convex interface due to the higher inertia of non-axial nodal mass. Also, the fine mesh in dissimilar discretisation captures circular geometry better with its smaller segments, so it has a slightly higher mass compared to the opposite bar.

3.5.7 *Inclined impact of a ball on a rigid plane*

The impact of a ball on a rigid plane is studied to determine the effect of the contact algorithm on the resulting motion in dynamic conditions. For this, a spherical ball of diameter 20 mm having linear elastic material with the modulus of 210 GPa, no Poisson's ratio, and density of 7.83e-6 kg/mm^3, is impacted on a rigid plane at 45° angle as shown in Fig. 3.32a. Three plots are shown for the effect of the contact dynamics. The plot in Fig. 3.32b shows the variation of the contact forces on the ball with time. The discretised geometry, following the original spherical geometry, observes an increase in the interpenetration with the initial pressing of the ball against the plane, resulting in an increased contact force. As the ball's motion reverses in the vertical direction, the contact force decreases with the decreasing interpenetration. Plots in Fig. 3.32c show the variation of the momentum components in all three directions. While the ball's impact is at 45°, it is reflected at an angle of 45.07° with the plane.

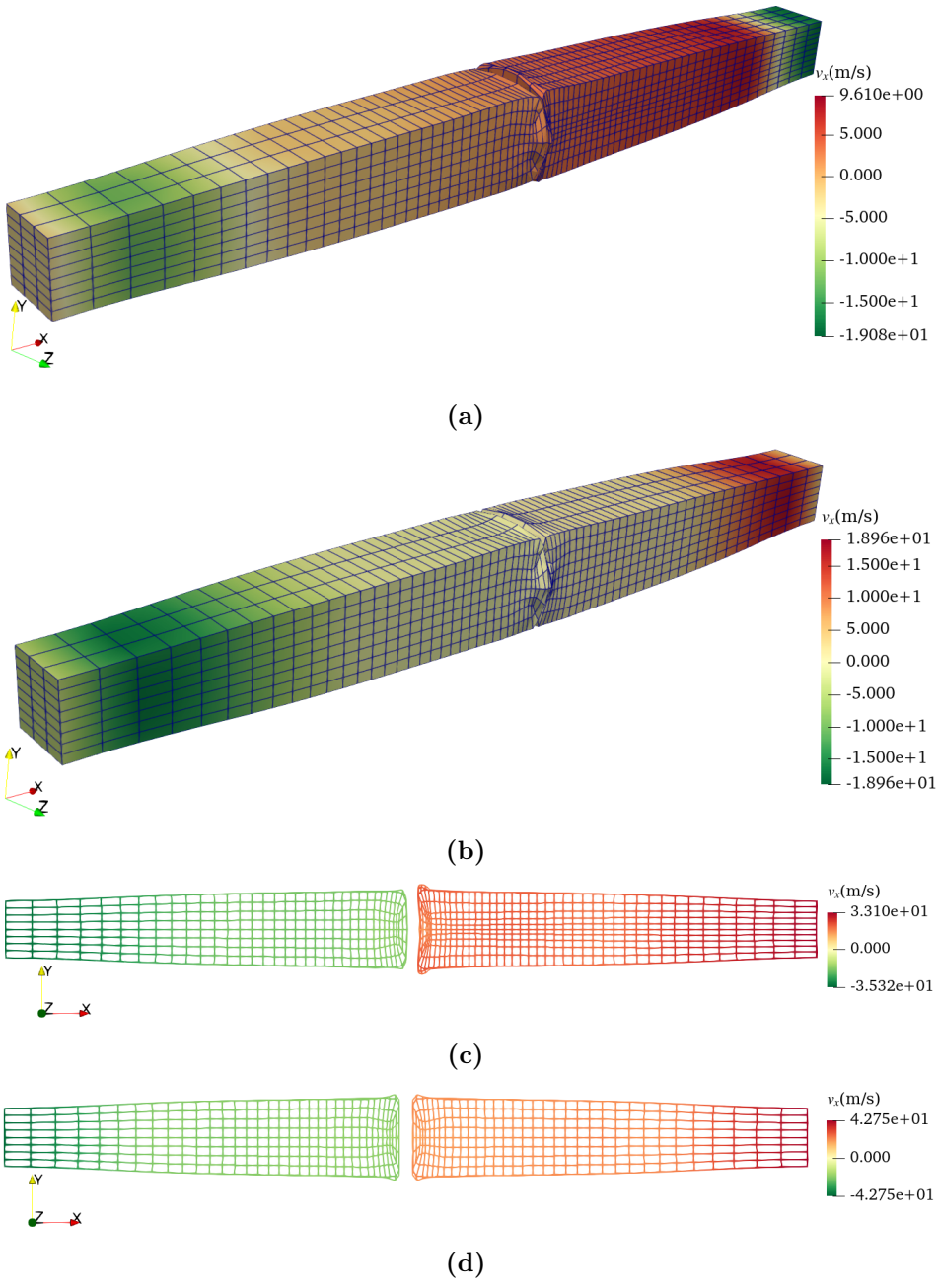

Figure 3.31: Inelastic collision: bars with (a) dissimilar and (b) same discretisation undergoing deformation at around t=0.0139 ms. Same bars upon rebound are shown for (c) dissimilar (d) same discretisation.

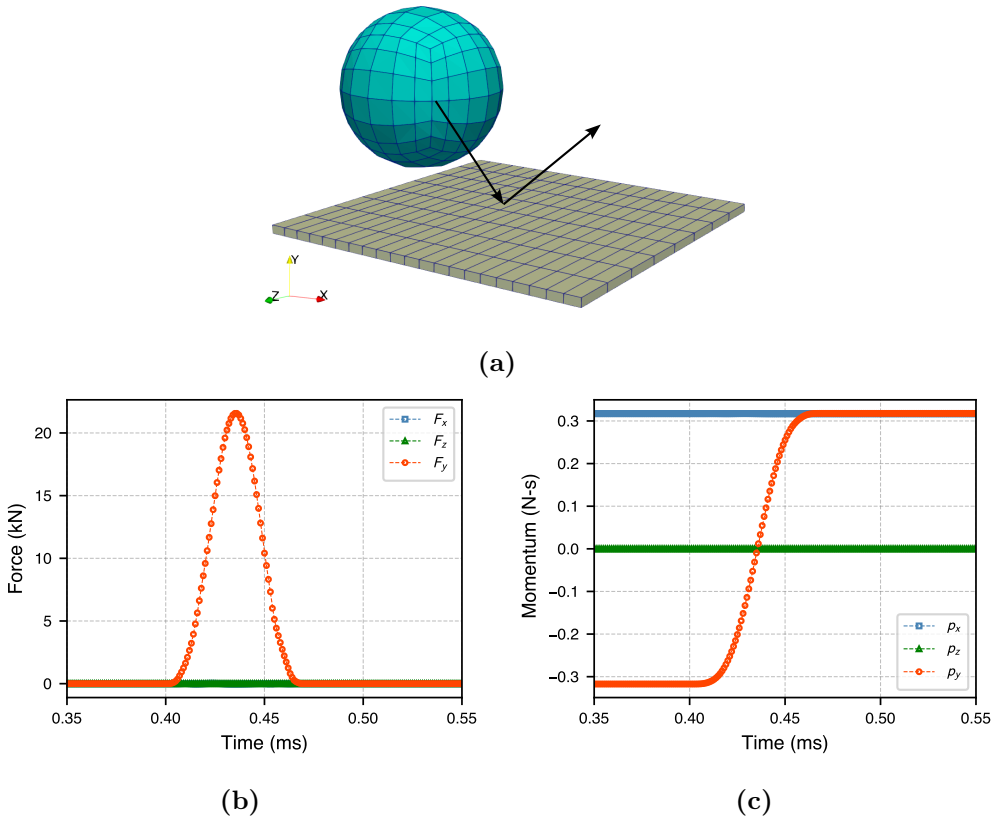

Figure 3.32: Impact of a ball on a rigid plane: (a) mesh, (b) variation of contact force, and (c) variation of momentum

3.6 Conclusion

This work presents a robust contact processing methodology for evaluating contact tractions using a midplane-based approach for segment-to-segment contact pairs, enforcing contact constraints symmetrically using the penalty method, thus ensuring an unbiased treatment of the surfaces coming into contact. Consequently, it obviates the need for a second pass, generally applied to deal with the issue of biasing while maintaining the force-moment equilibrium. The development of a mathematical framework describing this approach in both continuum and discrete settings of the contact problems has been presented in this work, with a special focus on the algorithmic implementation of the methodology. An extensive exposition of the geometrical configurations of the facets coming into contact has been showcased, which allows for the continuous enforcement of contact constraints with high accuracy. The formulation has been rigorously tested through multiple standard

benchmark tests for contact, including flat surfaces, curved surfaces, and sharp corners in contact for non-matching meshes. It successfully passed the contact patch test with an accuracy level matching the finite element accuracy. The two-beam test demonstrated its locking-free behaviour. The extensive study of Hertzian contact with different materials and nonconformal meshes highlighted the method's capability to represent contact between curved surfaces. Also, it emphasised the importance of allowing and controlling interpenetration for smoothness in contact traction between discretised curved surfaces. The method showed convergence towards analytical solutions in Hertzian contact and indentation problems with increasing penalty factor. The proposed method's versatility also extends to problems of self-contact, where its inherent unbiased nature helps to provide accurate solutions while working in a single pass. Lastly, dynamic problems of co-axial collision between two elastic and inelastic rods with different meshes and oblique collision of two cylinders demonstrated its performance in dynamic contact problems. Numerical solutions to contact problems obtained through this method can be improved by choosing a suitably high penalty scaling factor and mesh refinement in the contact region.

For future work, this contact interaction methodology is being studied with frictional effects to formulate a tangential traction evaluation that preserves the unbiased nature of the contact. Additionally, the methodology is being extended to contact between discretised domains composed of elements with higher-order interpolation, which can better describe complex surfaces.

References

[2] D. M. Neto, M. C. Oliveira, and L. F. Menezes. "Surface Smoothing Procedures in Computational Contact Mechanics". en. In: *Archives of Computational Methods in Engineering* 24.1 (2017), pp. 37–87.

[6] Heinrich Hertz. "Ueber die Berührung fester elastischer Körper." en. In: *crll* 1882.92 (1882), pp. 156–171.

[7] K. L. Johnson. *Contact mechanics*. en. Cambridge University Press, 1985.

[9] Wing Kam Liu, Shaofan Li, and Harold S. Park. "Eighty Years of the Finite Element Method: Birth, Evolution, and Future". en. In: *Archives of Computational Methods in Engineering* (2022).

[12] Michael A. Puso and Tod A. Laursen. "A mortar segment-to-segment contact method for large deformation solid mechanics". en. In: *Computer Methods in Applied Mechanics and Engineering* 193.6 (2004), pp. 601–629.

[14] M.A. Puso and J.M. Solberg. "A dual pass mortar approach for unbiased constraints and self-contact". en. In: *Computer Methods in Applied Mechanics and Engineering* 367 (2020), p. 113092.

[15] Peter Wriggers. *Computational contact mechanics*. en. Hoboken, NJ: J. Wiley & Sons, 2002.

[16] Tod A. Laursen. *Computational Contact and Impact Mechanics*. en. Berlin, Heidelberg: Springer Berlin Heidelberg, 2003.

[25] Nam-Ho Kim. *Introduction to Nonlinear Finite Element Analysis*. en. New York, NY: Springer US, 2015.

[34] Klaus-Jürgen Bathe. *KJ Bathe – Finite element procedures*. en. 2nd ed. Englewood Cliffs, N.J: Prentice-Hall, 2014.

[36] Ted Belytschko, Thomas JR Hughes, and P Burgers. "Computational methods for transient analysis". In: (1985).

[37] O. C. Zienkiewicz, Robert L. Taylor, and J. Z. Zhu. *The finite element method: its basis and fundamentals*. Seventh edition. Amsterdam: Elsevier, Butterworth-Heinemann, 2013.

[40] Thomas JR Hughes, Robert L Taylor, and Worsak Kanoknukulchai. "A finite element method for large displacement contact and impact problems". In: *Formulations and computational algorithms in FE analysis* (1977), pp. 468–495.

[46] Vladislav A. Yastrebov. *Numerical methods in contact mechanics*. en. Numerical methods in engineering series. London : Hoboken, NJ: ISTE ; Wiley, 2013.

[54] Javier Bonet and Jaime Peraire. "An alternating digital tree (ADT) algorithm for 3D geometric searching and intersection problems". en. In: *International Journal for Numerical Methods in Engineering* 31.1 (1991), pp. 1–17.

[55] Ivan E. Sutherland and Gary W. Hodgman. "Reentrant polygon clipping". In: *Communications of the ACM* 17.1 (1974), pp. 32–42.

[56] A. Munjiza, D.R.J. Owen, and N. Bicanic. "A combined finite-discrete element method in transient dynamics of fracturing solids". en. In: *Engineering Computations* 12.2 (1995), pp. 145–174.

[57] Thomas J. R. Hughes et al. "A finite element method for a class of contact-impact problems". en. In: *Computer Methods in Applied Mechanics and Engineering* 8.3 (1976), pp. 249–276.

[58] Seungmin Jin et al. "A node-to-node scheme with the aid of variable-node elements for elasto-plastic contact analysis". en. In: *International Journal for Numerical Methods in Engineering* 102.12 (2015), pp. 1761–1783.

[59] Seungmin Jin, Dongwoo Sohn, and Seyoung Im. "Node-to-node scheme for three-dimensional contact mechanics using polyhedral type variable-node elements". en. In: *Computer Methods in Applied Mechanics and Engineering* 304 (2016), pp. 217–242.

[60] Weiwei Xing, Chongmin Song, and Francis Tin-Loi. "A scaled boundary finite element based node-to-node scheme for 2D frictional contact problems". In: *Computer Methods in Applied Mechanics and Engineering* 333 (2018), pp. 114–146.

[61] Weiwei Xing et al. "A node-to-node scheme for three-dimensional contact problems using the scaled boundary finite element method". en. In: *Computer Methods in Applied Mechanics and Engineering* 347 (2019), pp. 928–956.

[62] J. O. Hallquist. *NIKE2D: An implicit, finite-deformation, finite-element code for analyzing the static and dynamic response of two-dimensional solids*. Tech. rep. California Univ., Livermore (USA). Lawrence Livermore Lab., 1979.

[63] J. O. Hallquist, G. L. Goudreau, and D. J. Benson. "Sliding interfaces with contact-impact in large-scale Lagrangian computations". In: *Computer Methods in Applied Mechanics and Engineering* 51.1 (1985), pp. 107–137.

[64] D. P. Flanagan and T. Belytschko. "A uniform strain hexahedron and quadrilateral with orthogonal hourglass control". en. In: *International Journal for Numerical Methods in Engineering* 17.5 (1981), pp. 679–706.

[65] R. L. Taylor and Panayiotis Papadopoulos. "On a patch test for contact problems in two dimensions". In: *Computational methods in nonlinear mechanics* 690 (1991), p. 702.

[66] Giorgio Zavarise and Laura De Lorenzis. "A modified node-to-segment algorithm passing the contact patch test". en. In: *International Journal for Numerical Methods in Engineering* 79.4 (2009), pp. 379–416.

[67] Giorgio Zavarise and Laura De Lorenzis. "The node-to-segment algorithm for 2D frictionless contact: Classical formulation and special cases". en. In: *Computer Methods in Applied Mechanics and Engineering* 198.41 (2009), pp. 3428–3451.

[68] Chao Sun et al. "A novel node-to-segment algorithm in smoothed finite element method for contact problems". en. In: *Computational Mechanics* (2023).

[69] Seung-Hoon Kang, Seok-Min Lee, and SangJoon Shin. "Improved area regularization technique for penalty-method-based node-to-segment contact analysis". en. In: *Computational Mechanics* 71.4 (2023), pp. 801–825.

[70] Kent T. Danielson. "Curved node-to-face contact schemes for higher-order finite elements in lumped-mass explicit methods". en. In: *Computer Methods in Applied Mechanics and Engineering* 395 (2022), p. 115056.

[71] Juan C. Simo, Peter Wriggers, and Robert L. Taylor. "A perturbed Lagrangian formulation for the finite element solution of contact problems". In: *Computer Methods in Applied Mechanics and Engineering* 50.2 (1985), pp. 163–180.

[72] G. Zavarise and P. Wriggers. "A segment-to-segment contact strategy". en. In: *Mathematical and Computer Modelling* 28.4-8 (1998), pp. 497–515.

[73] Nagi El-Abbasi and Klaus-Jürgen Bathe. "Stability and patch test performance of contact discretizations and a new solution algorithm". en. In: *Computers & Structures* 79.16 (2001), pp. 1473–1486.

[74] Laura De Lorenzis, Peter Wriggers, and Thomas J. R. Hughes. "Isogeometric contact: a review". en. In: *GAMM-Mitteilungen* 37.1 (2014), pp. 85–123.

[75] Christine Bernardi, Naïma Debit, and Yvon Maday. "Coupling finite element and spectral methods: first results". en. In: *Mathematics of Computation* 54.189 (1990), pp. 21–39.

[76] Michael A. Puso. "A 3D mortar method for solid mechanics". en. In: *International Journal for Numerical Methods in Engineering* 59.3 (2004), pp. 315–336.

[77] Alexander Popp et al. "A dual mortar approach for 3D finite deformation contact with consistent linearization". en. In: *International Journal for Numerical Methods in Engineering* 83.11 (2010), pp. 1428–1465.

[78] R. Pinto Carvalho et al. "An efficient algorithm for rigid/deformable contact interaction based on the dual mortar method". en. In: *Computational Mechanics* (2022).

[79] Philipp Farah, Alexander Popp, and Wolfgang A. Wall. "Segment-based vs. element-based integration for mortar methods in computational contact mechanics". en. In: *Computational Mechanics* 55.1 (2015), pp. 209–228.

[80] T. A. Laursen and J. C. Simo. "A continuum-based finite element formulation for the implicit solution of multibody, large deformation-frictional contact problems". en. In: *International Journal for Numerical Methods in Engineering* 36.20 (1993), pp. 3451–3485.

[81] T. W. McDevitt and T. A. Laursen. "A mortar-finite element formulation for frictional contact problems". en. In: *International Journal for Numerical Methods in Engineering* 48.10 (2000), pp. 1525–1547.

[82] Michael A. Puso, T. A. Laursen, and Jerome Solberg. "A segment-to-segment mortar contact method for quadratic elements and large deformations". en. In: *Computer Methods in Applied Mechanics and Engineering* 197.6 (2008), pp. 555–566.

[83] G. Zavarise et al. "Real contact mechanisms and finite element formulation—a coupled thermomechanical approach". en. In: *International Journal for Numerical Methods in Engineering* 35.4 (1992), pp. 767–785.

[84] P. Papadopoulos and R.L. Taylor. "A simple algorithm for three-dimensional finite element analysis of contact problems". en. In: *Computers & Structures* 46.6 (1993), pp. 1107–1118.

[85] G. R. Cowper. "Gaussian quadrature formulas for triangles". en. In: *International Journal for Numerical Methods in Engineering* 7.3 (1973), pp. 405–408.

[86] D. A. Dunavant. "High degree efficient symmetrical Gaussian quadrature rules for the triangle". en. In: *International Journal for Numerical Methods in Engineering* 21.6 (1985), pp. 1129–1148.

[87] Indrajeet Sahu. *Bilinear-Inverse-Mapper: Analytical Solution and Algorithm for Inverse Mapping of Bilinear Interpolation of Quadrilaterals*. en. SSRN Scholarly Paper. Rochester, NY, 2024.

[88] Kevin Bronik et al. *DEST documentation*. University of Oxford, 2022.

[89] Seung Lee Kwon et al. "A fully nonlinear three-dimensional dynamic frictional contact analysis method under large deformation with the area regularization". en. In: *Engineering with Computers* (2023).

[90] K L Johnson. "One Hundred Years of Hertz Contact". en. In: *Proceedings of the Institution of Mechanical Engineers* 196.1 (1982), pp. 363–378.

[91] Valentin L. Popov, Markus Heß, and Emanuel Willert. *Handbook of Contact Mechanics: Exact Solutions of Axisymmetric Contact Problems*. en. Berlin, Heidelberg: Springer Berlin Heidelberg, 2019.

[92] Nicholas J. Carpenter, Robert L. Taylor, and Michael G. Katona. "Lagrange constraints for transient finite element surface contact". en. In: *International Journal for Numerical Methods in Engineering* 32.1 (1991), pp. 103–128.

[93] Mengyan Zang, Wei Gao, and Zhou Lei. "A contact algorithm for 3D discrete and finite element contact problems based on penalty function method". en. In: *Computational Mechanics* 48.5 (2011), pp. 541–550.

3.7 Supplementary discussion

This final section provides further clarification on several key points not elaborated in the paper, which will help provide a more comprehensive understanding of the work.

In the contact force integral over any segment, the shape function matrix corresponds to the shape functions associated with the nodes on the segment. These shape functions are the same as the shape functions of a 2D quadrilateral. So, the shape function matrix used in evaluating the matrix of nodal forces $\mathbf{R}$ can be written as

$$\mathbf{\Psi} = \begin{bmatrix} \psi_1 \\ \psi_2 \\ \psi_3 \\ \psi_4 \end{bmatrix} = \begin{bmatrix} \frac{1}{4}(1-\xi_1)(1-\xi_2) \\ \frac{1}{4}(1-\xi_1)(1+\xi_2) \\ \frac{1}{4}(1+\xi_1)(1+\xi_2) \\ \frac{1}{4}(1+\xi_1)(1-\xi_2) \end{bmatrix} \tag{3.34}$$

With this, the nodal force matrix can be written as

$$\mathbf{R} = \begin{bmatrix} \mathbf{R}_1 \\ \mathbf{R}_2 \\ \mathbf{R}_3 \\ \mathbf{R}_4 \end{bmatrix} = \begin{bmatrix} R_{1_x} & R_{1_y} & R_{1_z} \\ R_{2_x} & R_{2_y} & R_{2_z} \\ R_{3_x} & R_{3_y} & R_{3_z} \\ R_{4_x} & R_{4_y} & R_{4_z} \end{bmatrix} = \int_{\gamma_{h_s}} \begin{bmatrix} \psi_1 \\ \psi_2 \\ \psi_3 \\ \psi_4 \end{bmatrix} \begin{bmatrix} t_x & t_y & t_z \end{bmatrix} d\gamma \tag{3.35}$$

where $\mathbf{R}_i$ is force on the ith node ($i \in 1, ..., \text{nnod}$) and γ_{h_s} is surface of the contacting segment.

Some key points connecting to different aspects of the work are presented below -

- For each segment-to-segment pair, nodal forces coming from contact integral are continuously added to the global external force matrix $\mathbf{f_{ext}}$ acting on the

system using an assembly operator as

$$\mathbf{f}_{\text{ext}} \mathrel{+}= \mathop{\mathbf{A}}_{s=1}^{s=\text{nseg}} \mathbf{f}_{\text{ext}}^{i,s} \tag{3.36}$$

where $\mathbf{f}_{\text{ext}}^{i,s}$ contains contact forces acting on the ith node of the segment s.

- Adaptive time-step sizes are used in this work to account for timely detection and contact-induced rapid boundary changes. If there is no influence of contact, minimum stable timestep size [35] is

$$\Delta t_{\text{crit}} = \frac{l_0}{c_0} \tag{3.37}$$

where l_0 and c_0 are the minimum characteristic length and wave speed in the entire system. However, during the contact detection phase in this work, timestep size can be further reduced during approach or retraction of any node from interpenetration depending upon its location between outside or inside the representative plane of the opposite facet. For an outside node, this limiting timestep size is decided by its relative approach velocity normal to the opposite representative facet plane, v_{rel}^n, as

$$\Delta t_{\text{out}} = \frac{d_{\text{out}}}{v_{\text{rel}}^n} = \frac{d_{\text{rfp}} + d_{\text{czt}} \cdot f_{\text{red}}}{v_{\text{rel}}^n} \tag{3.38}$$

where d_{out} includes the distance of the node from the opposite facet plane, d_{rfp}, a user-decided virtual contact zone envelope thickness d_{czt}, and a reduction factor f_{red}. It allows for a smoother detection of interpenetration, restricting the nodes to a maximum penetration of $f_{\text{red}} d_{\text{czt}}$. For nodes that have penetrated the opposite facet plane, the limiting timestep size is

$$\Delta t_{\text{in}} = \frac{d_{\text{czt}} \cdot f_{\text{red}}}{v_{\text{rel}}^n} \tag{3.39}$$

So, the final timestep size is decided as $\Delta t = \min\left(\Delta t_{\text{crit}}, \Delta t_{\text{out}}, \Delta t_{\text{in}}\right)$. In high-speed contacts where inertial effects are dominating, contact forces may not be sufficient to avoid large overlap between objects, so while an alternative of nonlinearly smaller timesteps can be used, associated costs can be prohibitive.

Here, a possible idea could be to control the uniformly imposed penalty and timestep sizes based on the contact region stress, and this remains to be explored.

- For very high penalties, contact pressure, and thus, the effective nodal forces are also very high. This leads to a lowering of stable time-step size due to high nodal velocities. Practically, it can lead to increased oscillations in the contacting nodes. So, a suitable choice of penalty is a critical requirement.

- Only the normal direction of the midplane is required in the normal traction calculations. However, choosing a midplane that passes through the intersection of the two representative facet planes aids in the geometrical intersection check in the contact detection phase.

- The selection of scaling factor f_s depends upon contact being static or dynamic in nature. Based on the numerical experiments, f_s can be recommended to be in the range of $f_s \in (1, 10)$ for static tests and $f_s \in (1, 5)$ for dynamic tests with appropriate damping, e.g. using artificial bulk viscosity. However, for highly dynamic impacts where inertia has a considerably dominating effect over material stiffness, larger values of f_s will be required to provide the necessary contact constraints.

- The distribution of stress states in contact patch tests was uniform for all penalties, implying the success of the contact patch test, but the absolute values of the stress were slightly different. However, as the penalties are high enough, the difference is minor, thus showing a converging behaviour. Yet, extremely high penalties are not recommended to avoid instability.

- A general description of contact involves unilateral inequalities of having only compressive loads and no interpenetration between materials [8]. Although this condition is violated by the use of the penalty method, allowing controlled interpenetration is also critical to smooth out oscillations in contact between curved surfaces, as has been shown in the Hertzian contact.

- A key computational advantage of the proposed single-pass formulation is that with the increase in contact pairs n, the associated computational cost of processing contact constraint enforcement scales as $O(n)$ compared to a dual-pass approach where the computational cost is higher and increases by $O(2n)$.

All formulations presented here and in subsequent chapters in this thesis are implemented in the in-house solver DEST [88]. And the open-source visualisation software Paraview [94][95] is used for all numerical experiments.

This work on presenting a novel midplane-based unbiased contact methodology has provided a detailed, in-depth discussion of its distinctive features in contrast to the existing methods, along with its achievements highlighted through numerous exhaustive sets of experiments. This work on explicit finite element methods will be especially beneficial to highly nonlinear slow dynamic problems where the use of NTS-based methods presented in literature does not have matching levels of accuracy.

4

Unbiased frictional contact

Continuing on the midplane concept presented in the previous chapter, this chapter develops unbiased frictional contact formulation by studying the relative movement between the shared patches on the interacting segments on the two surfaces.

The resistive force of friction opposes relative motion between surfaces under compressive loads and this phenomenon can be studied across multiple scales, from atomic-level interactions to forces between asperities. At a microscopic scale, all real surfaces are rough, and this roughness forms the basis of many models representing the phenomenon of friction and wear [96][97][98].

Classical description of friction, based on Mohr-Coulomb friction model, is widely used in numerical modelling together with the penalty method based elastoplastic analogy of friction. Coulomb friction is a history dependent phenomenon. A well-known example of history loading dependence of the Coulomb frictions is the Hertzian contact problem for similar materials in contact with a monotonic increase in the tangential loading given by Cattaneo (1938). Cattaneo showed that a slip occurs in the elliptical annulus in the contact region oriented along contact area where the net tangential traction is a difference between the distribution of limiting traction with an opposite self-similar distribution in the inner elliptical region, see [97][7], e.g. Fig. 4.14b. With increasing tangential loading, the annular region of slip increases in size inwards and the inner elliptical region of stick zone decreases

in size, causing a fully slip region upon crossing the limiting friction. This work utilises such a description of friction for unbiased modelling.

Some highlights of the work presented in this chapter are

- A midplane-based unbiased frictional contact formulation is proposed for segment-to-segment interaction that does not have a biased master-slave approach
- The presented formulation evaluates frictional traction in a single pass over midplane as opposed to the dual pass approach generally used to deal with biasing in the master-slave approach
- Self-contact problems can also be dealt with using the unbiased nature of the presented formulation
- States of stick and slip are enforced over the patches formed by overlaps of the pairs of segments in contact instead of enforcing over nodes sliding against segments

Patch based unbiased 3D frictional contact formulation for finite element algorithms

Indrajeet Sahu, Nik Petrinic

Abstract

A new unbiased frictional contact formulation which purely uses the segment-to-segment(STS) interaction in a single pass for the predictor-corrector algorithm is presented in this work. The relative motion between the contacting segments is evaluated through the changes in the convective coordinates of the representative contact point in the overlap of two contacting opposite segments, thereby ensuring the unbiased nature of the formulation without labelling surfaces as slave and master. The traction equality on opposite surfaces is inherently maintained in all contact pairs, and the frictional states of stick or slip are enforced over each interacting STS pair instead of node on segment pair. This work details the development of penalty method-based STS frictional contact for contact between discrete surfaces with an equivalent description in the continuum space. Simultaneous changes in the material points coming into contact on both surfaces are utilised in the development of the unbiased tangential traction evaluation with the return mapping algorithm. Several numerical experiments have been presented that demonstrate the robustness and performance of the proposed algorithm in stick and slip conditions for flat and curved surfaces in contact.

4.1 Introduction

The frictional phenomenon is ubiquitous in all engineering systems, where multiple parts stay in a particular configuration and undergo specific changes depending upon the resistance to the relative tangential motion in static or dynamic processes(e.g., automotive, metal forming, tyres, railroads, drilling pile, aerospace, etc.). Despite its ubiquity, the numerical modelling of the frictional phenomenon remains a significant challenge due to the complexities involved in accurately capturing the physical

behaviour of surfaces resisting tangential motion due to interactions of asperities coming into contact [15]. Current numerical methods, such as those employing master-slave labelling of surfaces, have an inherent biasing in their formulations. Although widely used, these biased techniques may not capture the symmetric nature of frictional interactions, leading to a potential inconsistency.

The two characteristic friction states, stick and slip, result from the interaction between the asperities in contact with variation in the loading conditions [97]. Classically, the frictional formulations have been developed with analogy to the elastoplastic behaviour of materials at a phenomenological level, where the contact between the surfaces resists tangentially motion elastically before transitioning into the plastic behaviour [32][31]. The plasticity concepts of associated and non-associated flow rule with plastic slip criteria have been widely used in numerical modelling techniques [15][99][16][17]. Moreover, the frictional slip is an incremental process and so it is dependent upon the loading history [97].

Generally, two-stage algorithms are used to model friction where normal and frictional tractions are evaluated in succession, as the frictional traction formulations depend upon the normal tractions. Numerical modelling considers the frictional traction evaluation as an optimisation problem, with the Lagrange multiplier and the penalty method being the widely used techniques.

The use of Lagrange multiplier terms provides a sharp distinction between stick and slip zone by introducing additional degrees of freedom [100] together with the predictor-corrector approach of determining frictional tractions. These have also been used for elastic contact and non-linear friction law using a regularisation parameter for the concept of contact element [101], and in 2D segment-to-segment for large deformations using the mortar method [102]. Frictional formulations have also been developed with the penalty regularisation based on the predictor-corrector approach (return mapping algorithm[103]) [104][16][15][13], e.g., [105] used the mortar method concept for employing penalty formulation in 2-dimensional problems along with the moving friction cone algorithm, which uses a single gap vector for both normal and tangential contact [106]. Apart from the simplicity in formulations,

one additional benefit of using penalty regularisation is that it does not increase the total number of degrees of freedom, which offers a computational advantage.

The most commonly used frictional theory considers the trajectory of a set of material points of one surface (striker) over the other surface (target) [31]. In discretised setting, striker and target surfaces correspond to slave and master surfaces, respectively. Here, the frictional constraints are applied pointwise by considering the tangential sliding of the projection of the nodes of the slave surface over the master surface. The stick and slip points are assigned over the convective coordinates of the master surface, with the traversal of the slave node over the master surface [107]. To overcome this biasing of slave and master surfaces, [17] applied a two-half-pass approach by utilising the projections of quadrature points on the opposite surfaces; however, the two-half-pass approach might not necessarily maintain the equality of opposite tractions.

While the notion of friction can be enforced as a geometrical constraint disallowing any tangential motion in the stick case, the alternative of using the constitutive equation for tangential traction [107] dependent upon the relative tangential motion is utilised in this work. In this approach, the sliding of a material point in contact is split into a reversible elastic part (corresponding to a stick) and an irreversible plastic part (corresponding to a slip). In the physical interpretation, these elastic and plastic parts can be related to the elastic and plastic behaviour of asperities in contact. A description of the transition from stick to slip and different states of sliding can be referred to in [33].

This work presents an elastoplastic analogy-based segment-to-segment tangential traction formulation that considers the relative motion between facets over their midplane [108] without master-slave consideration, thereby maintaining a completely unbiased nature. It is based on Coulomb's non-associated friction law with analogy of the elastoplastic behaviour of materials [32][31], which is applied in a single pass over the common interface to ensure true unbiased approach. With consideration of the contact between segments on opposite surfaces, the states of stick or slip are dependent upon the relative tangential displacement between segments and

are assigned to their overlapping regions in physical contact. So, the net effect of stick or slip for any node will depend upon the traction contribution from all STS pairs containing the node. The sliding between a pair of segments is penalised for predicting the tangential traction, following which a correction is applied to maintain the traction within the limiting value. In this work, only the contact between first-order elements is considered. All the numerical experiments presented in this work are based upon the explicit finite element scheme with central time difference using HRZ mass lumping.

This paper is organised as follows - Section 2 describes the proposed approach in the continuum and discretised domain, Section 3 describes its implementation in finite element solution, Section 4 offers numerous numerical experiments to test the performance of the proposed approach, and Section 5 provides the concluding remarks.

4.2 Unbiased frictional contact

This section presents a novel approach to resolving tangential tractions for segment-to-segment interacting pairs in a completely unbiased manner. The proposed formulation is first briefly described in the continuum domain for physical justification before continuing the development of the formulation in the discrete domain. The unbiased nature of the proposed formulation relies upon the definition and relative tangential motion of a representative contact point for contacting segments. The equality of tractions is inherently maintained in the prescribed distribution of the contact forces.

4.2.1 Description in continuum

Consider two surfaces γ^1 and γ^2 on the solid bodies Ω^1 and Ω^2 loaded against each other and coming into contact to form a contact zone γ_c as shown in Fig. 4.1. This contact zone γ_c can be decomposed into a large number of small

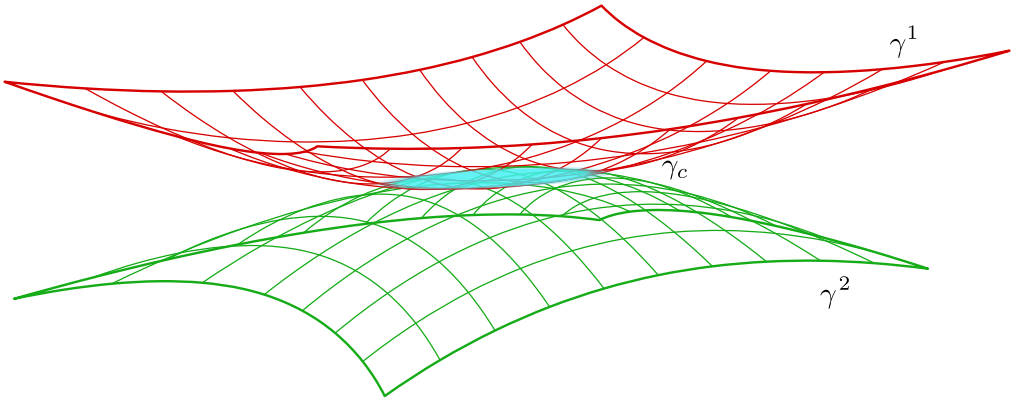

Figure 4.1: Surfaces $\gamma^{(1)}$ and $\gamma^{(2)}$ sharing surfaces at contact zone γ_c

patches ($\delta\gamma_c$), and each of these patches shares the same physical space on the two contacting surfaces, i.e.,

$$(\delta\gamma)_c = (\delta\gamma)^1 = (\delta\gamma)^2, \tag{4.1}$$

$$\gamma_c = \bigcup_k (\delta\gamma)^1_k = \bigcup_k (\delta\gamma)^2_k \tag{4.2}$$

For any loading on the two normally pressed bodies that attempts to induce a relative tangential motion, these pairs of shared patches on both surfaces have a gradual relative tangential displacement. The initial relative tangential motion resists the elastic deformation between patches with tangential stiffness ϵ_T in *stick* mode of friction, beyond which an irreversible plastic deformation sets in corresponding to the *slip* mode. The net tangential motion between the two patches $(\delta\gamma)^1$ and $(\delta\gamma)^2$ comprises both a reversible elastic part and an irreversible inelastic part. For a sufficiently high stiffness ϵ_T, the size of the reversible elastic deformation will be very small compared to the size of the patches on both surfaces. With continual tangential motion, the pairs of patches in contact break away and new pairs of patches come into contact, where the stick and slip modes are observed in succession.

For the theoretical case of a perfect stick, there is no relative tangential motion between these pairs of patches, and any relative motion implies a transition from the stick to the slip mode. As the finite number of patches on both surfaces implies non-uniqueness, the presented formulation is essentially a pseudo-continuum approach with the sole purpose of describing frictional behaviour in the STS contact of discrete

entities. More so, in the limit, $\epsilon_T \to \infty$ [103], the elastic displacement in the stick mode tends to zero, thus allowing for the infinitesimally small size of the patches on both surfaces, which will represent a true continuum description of the approach.

As the frictional slip is an incremental process, thereby being dependent upon the loading history [97], the relative displacement between any pair of patches over the contact interface is gradually added up from the first instance of contact for the continual sliding between the two surfaces. The cumulative sum of this incremental displacement with infinitesimally small time increments contains both elastic and inelastic parts depending upon the loading history.

The updating tangential traction formulation presented in the subsequent Section 4.2.2 for discretised space with incremental finite-sized time-steps will also apply to the continuous variation of time with time-step size $\Delta t \to 0$.

4.2.2 Description in discretised domain

For the STS contact discretisation scheme with the frictional effect, segments (or facets) on interacting surfaces experience resistance against tangential relative motion while the bodies are pressed against each other. In this work, which utilises the penalty method-based STS contact discretisation [108], discretised surfaces experience interpenetration and the midplane between each pair of interacting segments on opposite surfaces is taken as the local contact interface. The polygons of the intersections of projections of pairs of segments over their respective midplanes correspond to patches in the contact interface in the continuum methodology. However, an artefact of interpenetration observed in the penalty method based contact is that the overall contact interface formed by the union of all intersection polygons between STS pairs does not necessarily form a continuous surface in general. The frictional interaction between the interpenetrating segments is characterised by the relative tangential motion between the projections of the two physical segments over the midplane. The changes in the system effectuating any relative tangential motion between the projections on the contact interface will be resisted

by frictional tangential traction acting over this intersection polygon and directed along the midplane.

The linear transformation of opposite facets by projection over the midplane enables us to quantify the relative tangential motion between the physical facets through their 2D projections on the midplane, see Fig. 4.3. In this dimension reduction approach, the relative motion between the projections is a proxy for the relative motion between the actual physical facets where the frictional forces will be applied. The relative motion between the changing states of projections is quantified through the displacement of the centroid of the overlap, which is taken as the representative point of contact[1] for an STS pair at any given instant. With incrementation in the solution steps, the physical nodes might get displaced in a way that alters the positions of the projected nodes over the midplane, effectively leading to changes in the position of the centroid. This work explains how the convective coordinates of both facet projections at the centroid of the intersection polygon can be utilised to penalise relative tangential motion for each STS pair with the elastoplastic analogy of friction.

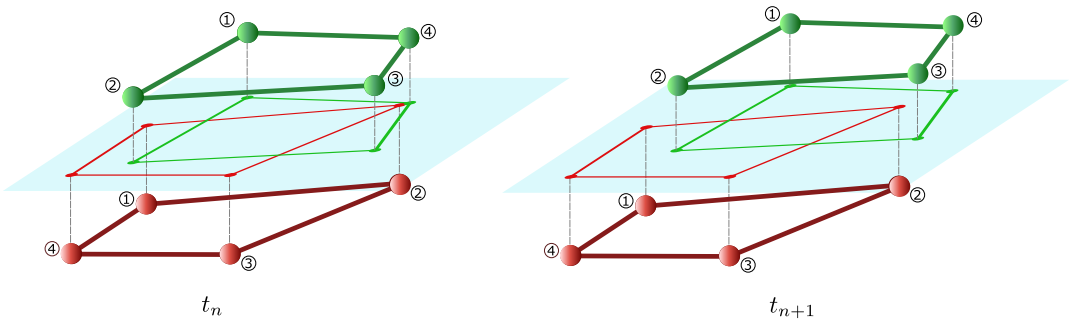

Figure 4.2

Figure 4.3: Contact interaction showing the relative movement between the projections of 3D physical facets over the midplane and the shared patch formed by the overlapping region.

[1]There could be an alternative choice of representative point of contact by taking an average of quadrature points weighted by their normal tractions (proportional to interpenetration gaps). However, this choice can potentially lead to cases where changes in the interpenetration between contacting facets, without relative tangential motion with respect to the midplane, get accounted for. So, this choice is discarded from further consideration.

The projections of parametric lines of the bilinear interpolation of physical facets directly overlay the parametric lines of the projected quadrilateral. Using the bilinear mapping over the projected quad facets, the pair of convective coordinates $({}^{i}\xi^{1}, {}^{i}\xi^{2})$ for both facets (i.e. $i \in \{1, 2\}$) at the centroid are utilised for the relative tangential displacement calculation at an aggregate level accounting for the relative displacement between all material points on the two facets in this intersection polygon. Convective coordinates of both facet projections at the centroid of overlap correspond to the material points in contact. Only the spatial changes in the nodes of surfaces causing changes in the convective coordinates at the centroid get accounted for in the tangential traction calculation. While this choice might neglect the effect of rotation between facets about the centroid or the effect of any nodal position changes that do not cause a change in convective coordinates of the centroid, the concurrent changes in the adjacent facet pairs will account for the relative motion between the contacting surfaces. More so, using meshes with sufficiently high refinement will only improve the solution.

With the first instance of detection of interaction between the facets, the intersection polygon between the projections of physical facets is evaluated using clipping algorithm [55]. From here on, the convective coordinates $({}^{i}\xi_{1}, {}^{i}\xi_{2})$ are calculated for both projections at the representative point of contact in each solution step. In the subsequent step, these coordinates might change, and this change is utilised for relative tangential displacement calculations, Fig. 4.4. To store the history of the tangential traction in the predictor-corrector approach of the trial traction formulation utilised in this work, an edge of the first facet is chosen to define the basis $(\mathbf{e}_1, \mathbf{e}_2)$. The direction of this edge defines the basis vector $\mathbf{e}_1$, and the direction orthogonal to it defines the other basis vector $\mathbf{e}_2$, i.e., for the normal direction to the midplane for the facet pair $\mathbf{n}_{\text{mp}}$, the basis vector $\mathbf{e}_2$ is evaluated as

$$\mathbf{e}_2 = \mathbf{n}_{\text{mp}} \times \mathbf{e}_1 \tag{4.3}$$

This basis is attached to the projection of a node of the first facet but aligned along the projection of the edge of the physical facet, thereby being effectively

connected to a material fibre direction. While this arbitrary choice of node and edge direction might appear to induce a bias in the formulation, this material direction is only utilised for storing the tangential traction, and this tangential traction calculation is solely based upon the relative changes in the convective coordinates of the two facet projections.

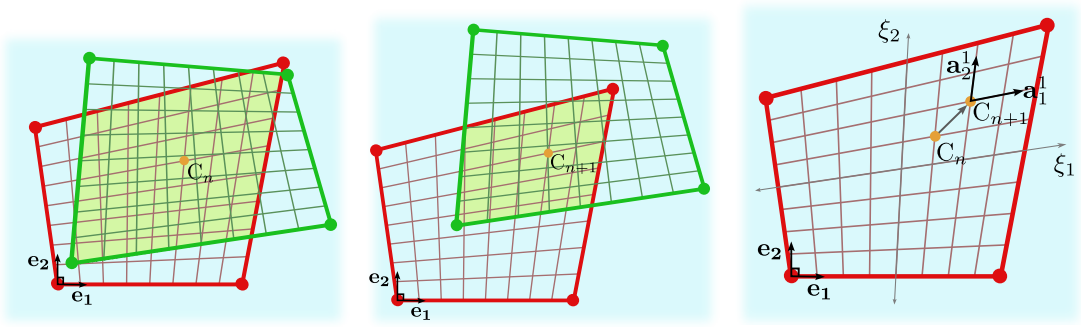

(a) **(b)** **(c)**

Figure 4.4: (a) and (b): Changes in the representative contact point from one solution step to the next. (c) Convective coordinates along with the covariant vectors at this representative contact point for facet1.

The parameterisation of each physical surface γ_h^i, $(i = \{1, 2\})$ enables us to write any point on this surface as

$$\tilde{\boldsymbol{x}}^i_{\gamma_h} = \tilde{\boldsymbol{x}}^i_{\gamma_h}(\boldsymbol{\Xi}), \qquad \boldsymbol{\Xi} \in \mathcal{P}, \tilde{\boldsymbol{x}}^i_{\gamma_h} \in \mathbb{R}^3 \tag{4.4}$$

where $\boldsymbol{\Xi} = [\xi^1, \xi^2]^T$ denotes the convective coordinates in the parametric space $\mathcal{P}$ mapping to the point $\tilde{\boldsymbol{x}}^i_{\gamma_h}$ on the surface γ_h^i, with $\tilde{(\cdot)}$ denoting quantity on boundary. Both surfaces γ_h^i mapped from the 2D parametric space to the 3D physical space can be characterised by the co-variant vectors $\tilde{\boldsymbol{a}}^i_j$ defined as

$$\tilde{\boldsymbol{a}}^i_{j_{\gamma_h}} = \frac{\partial \boldsymbol{x}^i_{\gamma_h}}{\partial \xi^j} \tag{4.5}$$

where $i \in \{1, 2\}$, $j \in \{1, 2\}$ for each surface i along each of its convective coordinate j. Using projections of both physical facets over the midplane and utilising the basis $(\mathbf{e}_1, \mathbf{e}_2)$, any point inside the projected facet can be written using the convective coordinates $\boldsymbol{\Xi}$ as

$$\boldsymbol{x}^i = \boldsymbol{x}^i(\boldsymbol{\Xi}), \qquad \boldsymbol{\Xi} \in \mathcal{P}, \boldsymbol{x}^i \in \mathbb{R}^2 \tag{4.6}$$

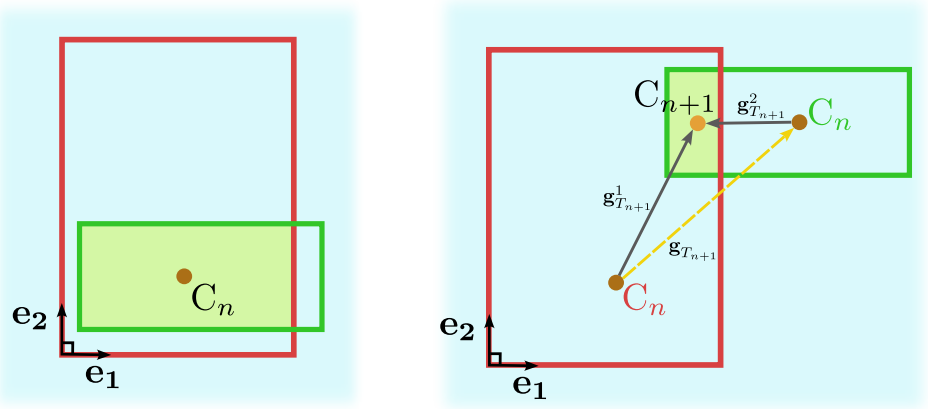

Figure 4.5: Simplified representation for tangential sliding of contact point using two rectangular facets between steps n and $n+1$.

for each facet i such that $\boldsymbol{x}^i$ has only two components for the basis $(\mathbf{e}_1, \mathbf{e}_2)$. Note that the convective coordinates of any point on the physical surface are the same as that of the convective coordinates of this point's projection with respect to the projected facet [87]. The co-variant vectors $\mathbf{a}^i_j$ for any point on the midplane also follow a similar definition as its counterpart in the physical surface. The co-variant vectors $\mathbf{a}^i_j$ at the representative contact point of both facets, Fig. 4.4c, are used in calculating the incrementing relative sliding. These can be expressed as

$$\mathbf{a}^i_j = (\boldsymbol{I} - \boldsymbol{n}_{\text{mp}} \otimes \boldsymbol{n}_{\text{mp}})\, \tilde{\boldsymbol{a}}^i_j \tag{4.7}$$

where both co-variant vectors in the physical facet and projected facet have the same set of convective coordinates. Here, two transformations are used: first, both facets are projected over the midplane, where the tangential tractions are calculated with respect to the basis $(\mathbf{e}_1, \mathbf{e}_2)$ that is attached to the projection of a material line on one facet. Second, these calculated tangential tractions are mapped to the 3D space for application over the physical facets.

With changes in the system from step n to $n+1$, any possible relative sliding $\boldsymbol{g}$ between any two points, along the normal to the midplane, on the two physical surfaces will have relative tangential displacement with respect to the midplane as

$$\boldsymbol{g}_{T_{n+1}} = (\boldsymbol{I} - \boldsymbol{n}_{mp_{n+1}} \otimes \boldsymbol{n}_{mp_{n+1}})\boldsymbol{g} \tag{4.8}$$

Note that for a very small step, the changes in the spatial positions of both facet nodes will be very small, so the midplane normal $\mathbf{n}_{\text{mp}}$ will be nearly unchanged. The representative contact point changes in the next step, implying a change in the material point of both facets corresponding to this contact point, thus effectively leading to a relative tangential displacement between the two facets written as

$$\mathbf{g}_{T_{n+1}} = (\mathbf{g}^1_{T_{n+1}} - \mathbf{g}^2_{T_{n+1}}) \tag{4.9}$$

A simplified representation of this relative tangential displacement is shown in the Fig. 4.5. This displacement $\mathbf{g}_T$ can be decomposed into an elastic part $\mathbf{g}_{T_e}$ accounting for stick and an inelastic part $\mathbf{g}_{T_s}$ accounting for slip, each with some contribution from both facets due to the change of material points corresponding to the representative contact point, i.e.

$$\mathbf{g}_T = \mathbf{g}_{T_e} + \mathbf{g}_{T_s} \tag{4.10}$$

$$= \left(\mathbf{g}^1_{T_e} + \mathbf{g}^2_{T_e}\right) + \left(\mathbf{g}^1_{T_s} + \mathbf{g}^2_{T_s}\right) \tag{4.11}$$

In each solution step, this tangential displacement updates, and its increment is used to update the tangential traction. The sliding $\mathbf{g}_{T_{n+1}}$ from step n to $(n+1)$ is linearly penalised using the tangential penalty parameter ϵ_T to update the trial (or predicted) tangential traction written as

$$\mathbf{t}^{\text{trial}}_{T_{n+1}} = \mathbf{t}^{\text{up}}_{T_n} + \epsilon_T[\mathbf{g}_{T_{n+1}}] \tag{4.12}$$

where $\mathbf{t}^{\text{up}}_{T_n}$ is the updated (or corrected) tangential traction from the previous step and is chosen as zero for the first instance of contact detection. By using the co-variant vectors $\mathbf{a}^i_j$ and changes in the convective coordinates of the centroid with respect to both facets, the trial tangential traction equation stated below is the key proposition of the presented work

$$\mathbf{t}^{\text{trial}}_{T_{n+1}} = \mathbf{t}^{\text{up}}_{T_n} + \epsilon_T[({}^1\xi^\alpha_{C_{n+1}} - {}^1\xi^\alpha_{C_n})\mathbf{a}^1_{\alpha_{n+1}} - ({}^2\xi^\alpha_{C_{n+1}} - {}^2\xi^\alpha_{C_n})\mathbf{a}^2_{\alpha_{n+1}}] \tag{4.13}$$

This equation accounts for the relative changes in the convective coordinates of the representative contact points (corresponding to the centroid of the overlap

polygon) on both facets simultaneously, thus providing a penalisation of relative tangential displacement along the contact interface.

Alternatively, using the interpolated velocities of both facets at the representative contact point, the above equation can be written as

$$\mathbf{t}^{\text{trial}}_{T_{n+1}} = \mathbf{t}^{\text{up}}_{T_n} + \epsilon_T[(\boldsymbol{I} - \boldsymbol{n}_{\text{mp}} \otimes \boldsymbol{n}_{\text{mp}})(\dot{\mathbf{x}}^1 - \dot{\mathbf{x}}^2)\Delta t_{n+1}], \quad \dot{\mathbf{x}} \in \mathbb{R}^3 \tag{4.14}$$

where $\dot{\mathbf{x}}^i$ is the velocity of the physical facet i at the representative contact point, and Δt_{n+1} is the time-step size, which, when tends to zero, both equations above will tend to give the same result.

The trial tangential traction is a predicted traction that is subsequently corrected using the radial return mapping algorithm [24]. Analogous to plasticity, a slip function Φ [99] can be defined together with the Coulomb's law of friction as -

$$\Phi = ||\mathbf{t}_T|| - \mu\|\mathbf{t}_N\| \leq 0 \tag{4.15}$$

where μ is the coefficient of friction and $\mathbf{t}_N$ is the normal traction. Using the principle of maximum dissipation classically used in theory of plasticity [15][109], the constitutive equation for plastic slip is

$$\dot{\mathbf{g}}_{T_s} = \dot{\gamma}\frac{\partial\Phi\left(\mathbf{t}_T\right)}{\partial\mathbf{t}_T} = \dot{\gamma}\mathbf{n}_T, \quad \text{where } \mathbf{n}_T = \frac{\mathbf{t}_T}{\|\mathbf{t}_T\|} \tag{4.16}$$

The above relation corresponds to the normality rule for fixed t_N. $\dot{\mathbf{g}_{T_s}}$ is the relative tangential velocity of the slip component representing rate of inelastic slipping. In the Kuhn-Tucker condition format, the loading-unloading condition can be written as

$$\dot{\gamma} \geq 0, \quad \Phi\left(\mathbf{t}_T\right) \leq 0, \quad \dot{\gamma}\Phi\left(\mathbf{t}_T\right) = 0 \tag{4.17}$$

During the slip phase, the tangential displacement of slip increment $\Delta\mathbf{g}_s$ is

$$\Delta\mathbf{g}^{n+1}_{T_s} = \frac{\Phi^{\text{trial}}}{\epsilon_T}\frac{\mathbf{t}^{\text{trial}}_{T_{n+1}}}{\|\mathbf{t}^{\text{trial}}_{T_{n+1}}\|} = \Delta\gamma\mathbf{n}_{T_{n+1}} \tag{4.18}$$

This slip increment, however, unlike the sliding of a slave point over a master surface, is a measure of overall slip between the facets in contact. Although sub-regions on these facets might undergo expansion or contraction, the slip calculated

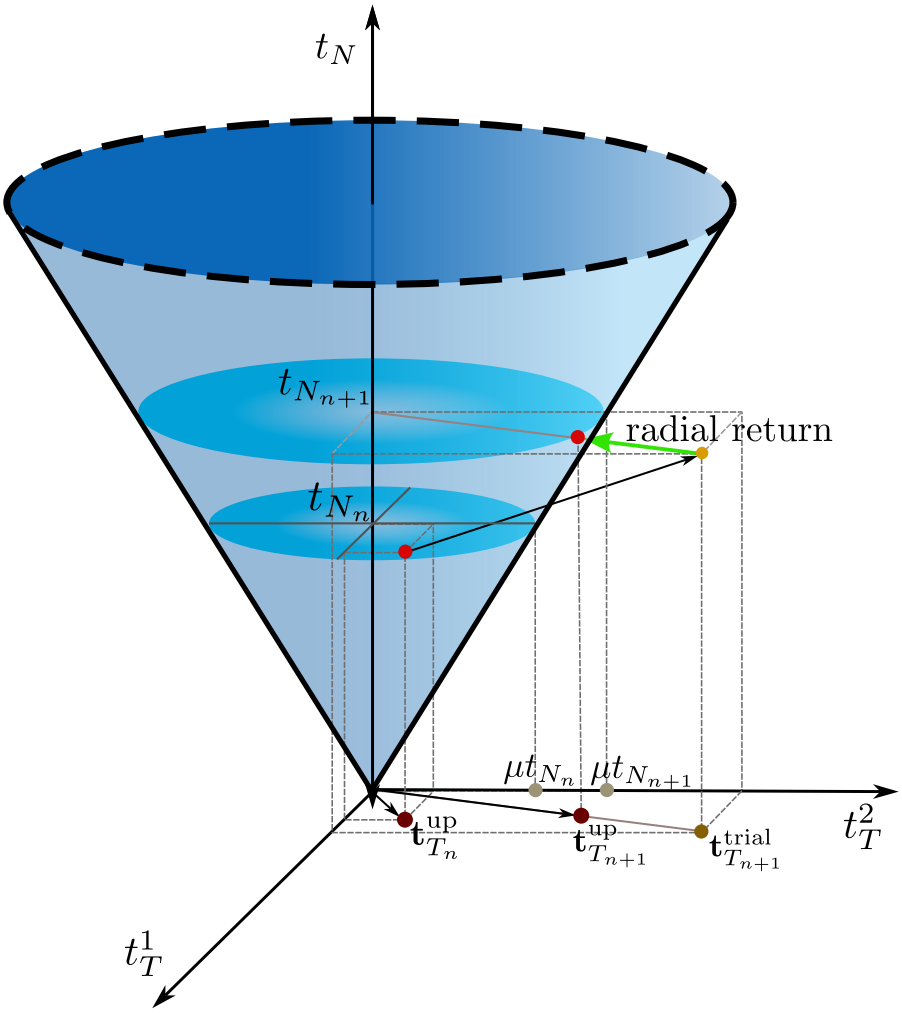

Figure 4.6: Schematic of the return mapping algorithm with the friction cone in the traction space for change in the traction state from step n to $n+1$.

above is an aggregated measure for the overlapping region of facet pair and applied at their representative contact point. When the trial tangential traction is within the limiting value of friction, its state is inside the friction cone, i.e., $\Phi \leq 0$ (stick mode). However, if its magnitude exceeds the limiting value of friction, implying that it is in a slipping state, its predicted state will be outside the friction cone's surface (yield surface), see Fig. 4.6. The tangential traction is corrected using the radial return mapping to render $\Phi = 0$, and its updated form is written as

$$\mathbf{t}_{T_{n+1}}^{\text{up}} = \mathbf{t}_{T_{n+1}}^{\text{trial}} - \epsilon_T \Delta \mathbf{g}_{T_s}^{n+1} \tag{4.19}$$

which can be simplified as

$$\mathbf{t}^{\text{up}}_{T_{n+1}} = \begin{cases} \mathbf{t}^{\text{trial}}_{T_{n+1}} & \text{if } ||\mathbf{t}^{\text{trial}}_{T_{n+1}}|| \leq \mu||\mathbf{t}_{N_{n+1}}|| \\ \mu||\mathbf{t}_{N_{n+1}}||\frac{\mathbf{t}^{\text{trial}}_{T_{n+1}}}{||\mathbf{t}^{\text{trial}}_{T_{n+1}}||} & \text{if } ||\mathbf{t}^{\text{trial}}_{T_{n+1}}|| > \mu||\mathbf{t}_{N_{n+1}}|| \end{cases} \tag{4.20}$$

Returning of the predicted tangential traction to the yield surface occurs radially, i.e., it is along the same direction as the predicted traction, implying that the corrected (or updated) tangential traction retains the same direction as the trial traction. In the case of elastic recovery, the traction components will be attracted to the zero tangential traction state.

The updated tangential traction calculated over the midplane is mapped to the physical space for application over the two interacting physical facets in an equal and opposite direction, i.e.,

$$\mathbf{t}^1_T = -\mathbf{t}^2_T = \mathbf{t}^{\text{up}}_T \tag{4.21}$$

4.3 Finite element solution

In the present work, normal traction and the resulting nodal forces are calculated using the unbiased single pass STS penalty method [108], which finds normal traction between two opposite facets due to the interpenetration over the midplane. The normal traction is integrated over the midplane using quadrature rule [85, 86] to evaluate the resulting nodal normal forces (see Fig. 4.7) as,

$${}^i\mathbf{R}^N_k = \int \Psi_{i_k} \boldsymbol{t}^i_N d\gamma \tag{4.22}$$

where, Ψ_{i_k} is the shape function associated with the kth node, ${}^i\mathbf{R}^N_k$ is the normal nodal force at the kth node on the ith facet due to the normal traction $\boldsymbol{t}^i_N$ acting over the facet. However, the normal traction used in the predictor-corrector approach is an average value calculated by dividing the net normal force between the two facets by the area of the intersection polygon (A), i.e.

$$\mathbf{t}^i_{N_{avg}} = \frac{\Sigma_k \ {}^i\mathbf{R}^N_k}{A} \tag{4.23}$$

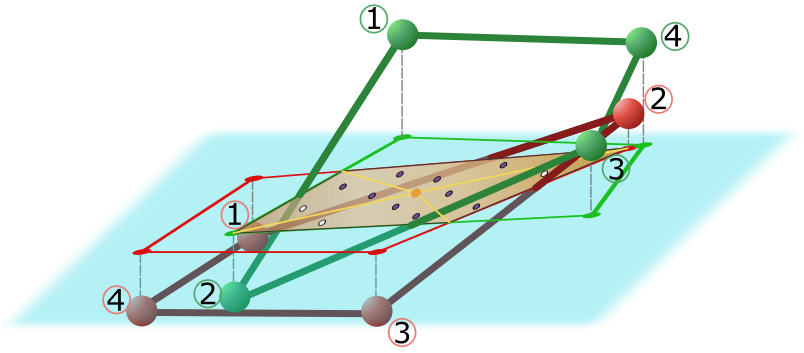

Figure 4.7: Illustration of normal traction evaluation over intersection polygon using the integration of normal traction taken as penalisation of the interpenetration with respect to quadrature points in the triangulation of the overlapping polygon. Here, dark colours of quadrature points observe interpenetration between the physical facets, whereas light colours indicate no interpenetration.

Tangential traction evaluated in the presented formulation, based on the relative motion of the representative contact point, is also an average value, which, when considered with area of the overlap, is applied as the frictional force on the nodes of the interacting physical facets. So, the slip function per segment-to-segment pair can be now written as

$$\Phi = ||\mathbf{t}_T^{\text{trial}}|| - \mu \|\mathbf{t}_{N_{avg}}\| \tag{4.24}$$

and the tangential traction is updated accordingly.

There could be multiple choices for applying the frictional traction over the two facets by considering the finite element technology of each facet. The tangential traction can be considered as uniformly distributed over the polygon of overlap, or the net frictional force ($\mathbf{t}_T A$) can be applied as a point force (by using Dirac-delta function inside the integral of eq. 4.22) at the representative contact point. However, to maintain the consistent influence of relative motion in a facet pair over all its nodes' stick/slip states, the frictional nodal forces in this work rely upon their respective normal nodal forces. The frictional nodal forces are directly proportional to the normal forces and depend upon the coefficient of friction and the pair's friction state calculated by the parameter β defined below. The frictional nodal

force ${}^{i}\mathbf{R}_k^T$ at the node k on the ith facet is

$$ {}^{i}\mathbf{R}_k^T = \beta\mu||{}^{i}\mathbf{R}_k^N||\frac{\mathbf{t}_T^i}{||\mathbf{t}_T^i||} \quad , \qquad 0 \leq \beta \leq 1 \tag{4.25} $$

$$ \beta = \frac{||\mathbf{t}_T^{\text{up}}||}{\mu\|\mathbf{t}_{N_{avg}}\|} \tag{4.26} $$

where $0 \leq \beta < 1$ when the shared patch of facet pair is in stick state and $\beta = 1$ in the slipping state. However, it should be noted that the overall frictional forces on all nodes of each surface γ_h^i will have the contribution from all facet pairs (i.e., their shared patch) formed by its neighbouring facets. So, the net effect of stick or slip will depend on the frictional states of all neighbouring facet pairs.

As the same frictional force is applied on both facets, the proposed formulation maintains an exact equilibrium of tangential traction on both facets compared to the formulations considering sliding of points on one surface over another [17]. The algorithm for the proposed predictor-corrector approach in the finite elements implementation is shown in Algorithm 2.

Algorithm 2 Predictor-corrector algorithm for each contact pair at step $n+1$ for finite elements

1: find the centroid of the intersection polygon of projections of facets on the midplane
2: find the convective coordinates $({}^{i}\xi^1, {}^{i}\xi^2)$ of the centroid w.r.t each facet i
3: find the co-variant vectors $\mathbf{a}_j^i$ $(i \in \{1,2\},\ j \in \{1,2\})$ at the representative contact point
4: *Prediction*
5: calculate $\mathbf{t}_{T_{n+1}}^{\text{trial}}$ using the eq. 4.13 by employing $({}^{i}\xi^1, {}^{i}\xi^2)$ from previous step n
6: find the average normal traction $\mathbf{t}_{N_{avg}}^i$ using eq. 4.23
7: *Correction*
8: check the slip criterion using $\Phi = ||\mathbf{t}_T^{\text{trial}}|| - \mu\|\mathbf{t}_{N_{avg}}\| \leq 0$ ($\Phi \leq 0$: stick phase, $\Phi > 0$: slip phase)
9: find $\Delta\mathbf{g}_{T_s}^{n+1}$ using the eq. 4.18
10: apply the correction $\mathbf{t}_{T_{n+1}}^{\text{up}} = \mathbf{t}_{T_{n+1}}^{\text{trial}} - \epsilon_T\Delta\mathbf{g}_{T_s}^{n+1}$
11: find β and the frictional nodal forces for both segments using the eq. 4.26 and eq. 4.25, respectively

In the proposed formulation, the updating of tangential traction is based on the relative sliding, and it does not account for the relative angular motion. However, this limitation on the rotational effect can be compensated by the contact pairs of

neighbouring facets where the traversal of the contact point is penalised, and the tangential traction opposes this relative motion. The error due to the overlapping zone of any facet pair being treated as frictionless because of rotation about the centroid can be reduced with the refinement of the surface discretisation. Mesh refinement will also help in a case of large deformation, where the rotation of the basis due to edge rotation might rotate the tangential traction.

It should be noted that this approach of penalisation of relative tangential movement limits the minimum facet size for a given penalty and normal load. With the relative motion between discretised surfaces, the list of contact pairs gets updated - some new pairs are formed and some old ones deleted. The minimum relative tangential movement for transition from stick to slip state for any facet pair requires a sufficient overlap between the two contacting facets. The sliding in the stick zone is directly proportional to the normal traction and inversely proportional to the tangential penalty. However, the same issue will also affect the slave-master approach, where the history of traversal of any node over all previously contacting segments on the opposite surface will be required to be included in the formulation. More so, in practical scenarios, the tangential penalty stiffness is very large, allowing for the transition from the stick to the slip zone within a pair of facets. With this, the sliding length corresponding to the stick zone is very small compared to the facet sizes.

4.4 Numerical experiments

Various numerical experiments are conducted to assess the accuracy and robustness of the proposed frictional contact formulation. For quasi-static tests, the technique of dynamic relaxation is used to alleviate the dynamic effect of inertia. The two states of frictional contact, stick and slip, are studied for flat and curved surfaces for complete stick, microslip, and transition between stick and slip mode. Some other tested conditions include - changes in the tangential penalty factor, performance in dynamic frictional contact, and the rolling effect of friction. A particular highlight

is the self-contact test, where the unbiased nature of the formulation offers a high fidelity in the solution.

4.4.1 *Block pushed against a slab*

In this setup, a block, pressed against a rigid slab, is pushed tangentially to induce the frictional effect in the contact region. Initially, only the stick state of the frictional algorithm is tested by applying a tangential load within the limiting value of friction. In the subsequent test, a motion is prescribed to the block such that the frictional contact transitions between stick and slip mode while dragging the block to and fro, thus allowing us to observe the hysteresis effect inherent to the elastoplastic formulation. In both experiments, a linear elastic material is chosen for the block (having size $5 \times 5 \times 10$ mm^3) with Young's modulus of elasticity $E = 210$ GPa, density 7.83×10^{-2} kg/mm^3, and Poisson's ratio $\nu = 0$. The coefficient of friction for contact between the block and the slab is taken as $\mu = 0.3$, the normal penalty scaling factor ($f_s = 1$), 13 gauss points per triangle for normal traction integration, and the dynamic relaxation coefficient for both problems is taken as 90%.

Block pushed against a slab: *stick only case*

In this experiment, the effect of three different tangential penalty values ($\epsilon_T = 10, 100, 1000$ GPa/mm) is studied on the stick zone size and the zero state recovery in the elastic zone under the removal of the external loading that induces tangential motion. An elastic block over a rigid slab with the geometry shown in Fig. 4.8a is studied for the stick mode of friction in the contact region.

For the boundary condition, the top surface of the block is initially subjected to uniform downward motion with velocity v while keeping the surface horizontal, which results in a net load P, causing the contact interface between the block and the slab to develop normal traction. Further, this top surface is subjected to ramped-up tangentially applied uniform pressure q, reaching a maximum value of $q = 0.5\mu p_{avg}$, i.e. half the limiting friction value. The loading q is initially

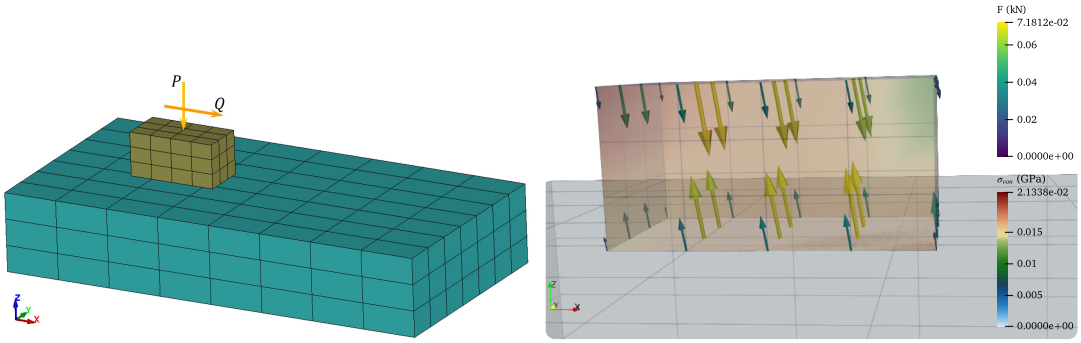

(a) (b)

Figure 4.8: (a) Mesh (mesh1) used for the sticking case of the block on rigid slab, and (b) the nodal forces on the block at $t = 40ms$.

subjected in the forward direction before it is zeroed and then applied in the reversed direction as shown in Fig. 4.9a.

The effect of applied loading on the contact region is studied through the net forces acting vertically and tangentially over the contacting surface of the block. The distribution of nodal forces corresponding to the applied load and the contact forces during the slip phase in forward motion is shown in Fig. 4.8b. Plots of the variation of the normal and frictional forces and average displacement of the bottom surface of the block are shown in Figs. 4.9,4.10. The vertical load of reaction on the block's contacting surface gradually increases under the downward motion of the top surface of the block and attains a relatively constant value in all cases. While the variation of normal and frictional forces is virtually indistinguishable over the entire operation for different tangential penalties, differences in the frictional forces become evident at small time intervals. For lower tangential penalties, the net frictional force increment is relatively delayed (see Fig. 4.9d,4.9e). The decrease in tangential traction is asymptotic in nature on the removal of q, see Fig. 4.9f, because it depends upon the elastic displacement ($\mathbf{g}_{T_e}$), which simultaneously decreases in the elastic recovery. The frictional force reduction is more prominent in the case of lower penalties due to lower stiffness, which has a weaker strength in pulling back. Using a higher tangential penalty leads to smaller sliding in the stick zone, and the size of the stick zone is reduced by the same order as the increment of tangential penalty, as can be seen in the average displacement of the contacting surface of the block in

Fig. 4.10a,4.10b,4.10c. However, if an extremely large tangential penalty were used it would lead to instability in the frictional forces as even a very tiny tangential displacement in any arbitrary direction will lead to slipping state causing sudden application of high frictional forces in the contact zone that will rapidly reorient.

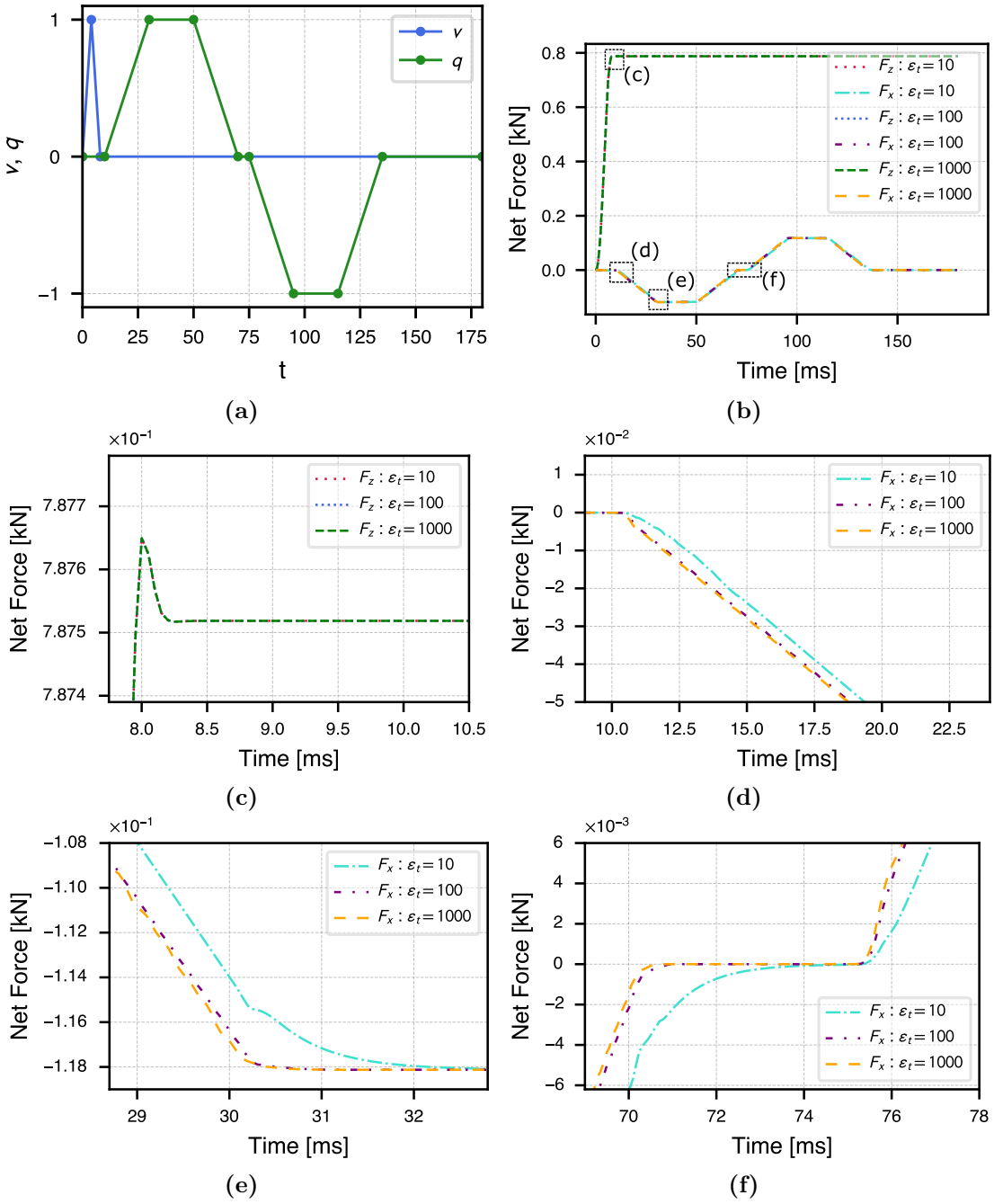

Figure 4.9: Block on slab in stick mode only for mesh1 to study the effect of ϵ_T : (a) changes in the prescribed velocity and tangential uniform pressure on the top surface of the block, and (b)...(f) show plots of vertical and horizontal forces on the block's contact surface. Inset outlines in (a) are not to scale.

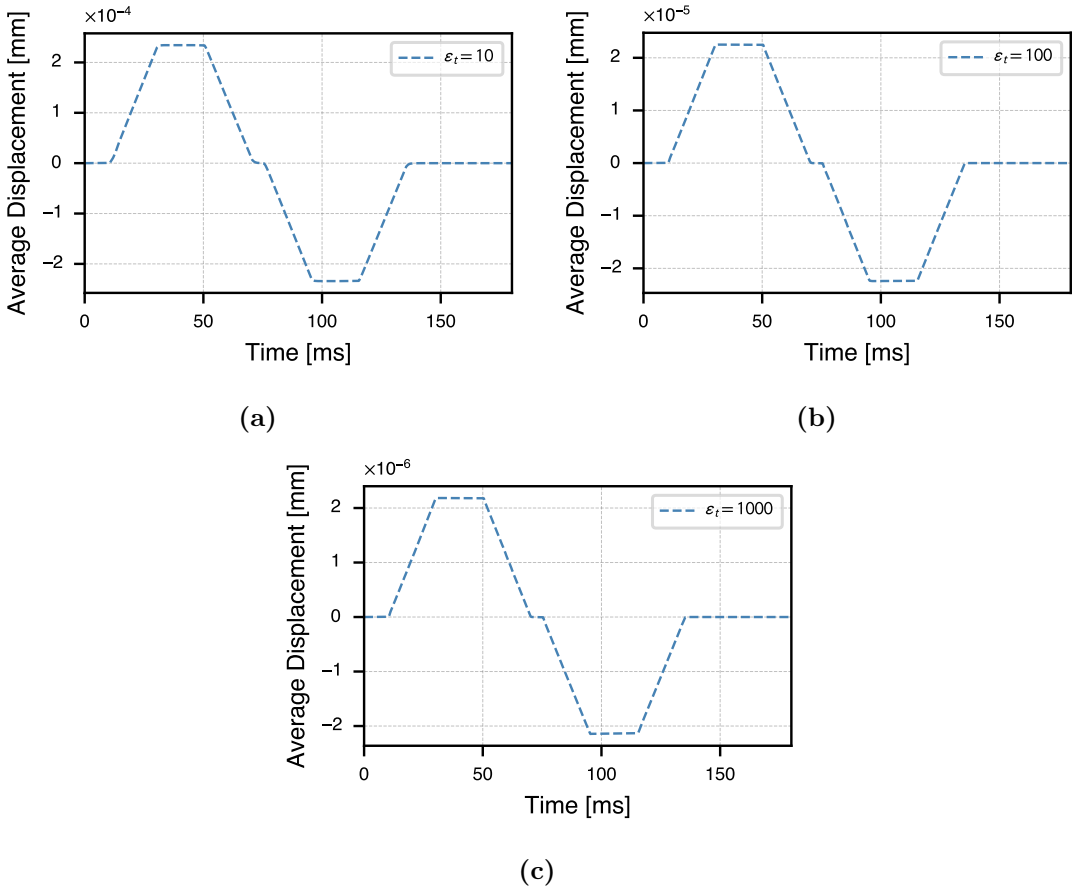

Figure 4.10: Block on slab in stick mode only: average displacement of the block's contact surface for different penalties.

Block pushed against a slab: *with transition between stick and slip states*

For testing the contact formulation in stick-to-slip transition, the top surface of the block is subjected to a prescribed motion that gradually drags the block forward before returning it to its original position. Four different discretisation schemes are used in this experiment - mesh1 (h) shown in Fig. 4.8a, mesh2 ($h/2$), mesh3 ($h/4$), and mesh4 (with irregular discretisation, shown in Fig. 4.11). The tangential penalty is $\epsilon_T = 100$ for contact definition in all four meshes.

The variation of the net vertical (F_z) and horizontal (F_x) forces representing normal and frictional forces on the block's contact surface is shown in Fig. **??**, although it should be noted that due to the curvature of the block under deformation, the contact interface (midplane) will not be completely horizontal. The normal

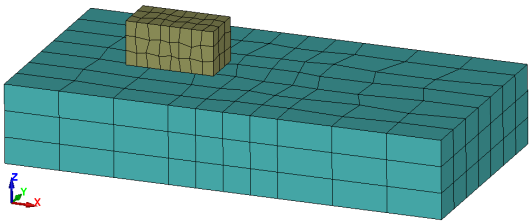

Figure 4.11: Mesh4 with irregular discretisation used for stick-slip transition study

force increases gradually under the downward motion of the block's top surface, and it settles for a near-constant value for all meshes after observing a dip with the application of the tangential load that deforms the block tangentially and decreases the net vertical force, as shown in Fig. 4.12b with oscillations shown in Fig. 4.12c. The variation of frictional forces shows that with the onset of sliding, there is a divergence in frictional forces for different meshes, Fig. 4.12d. The coarse mesh1 observes more oscillations in the gradually increasing frictional force in the stick regime, whereas it is relatively smooth for the refined mesh2 and mesh3. However, once the frictional forces reach the limiting value Fig. 4.12e, they remain constant for all discretisations. There is a dependency on the mesh in all phases, which is evident in the lag between curves in the plots.

To observe the hysteresis effect of the elastoplastic behaviour of frictional forces in the forward and backward displacement, the plot of frictional force vs average displacement of the block's contact surface is shown in Fig. 4.13a. The frictional forces initially increase in the backward direction to oppose the forward motion of the block and remain constant on reaching the limiting friction, and its direction gradually reverses with the reversal of the applied load, following a similar pattern in backtracking. When the block's top surface is returned to its original position and maintained there, the frictional forces retain the limiting value due to the hysteresis effect. While the plots for all meshes appear to overlap with the same frictional forces for the average displacement of the block's contact surface over the entire range, there is a slight deviation in the frictional forces at the small ranges of displacement as depicted in Fig. 4.13b,4.13c,4.13d. With the onset of sliding, the initial displacement corresponds to the elastic regime, i.e. it is in the stick mode,

leading to a gradual increase in the frictional traction (and, forces) with the slope corresponding to the tangential penalty or elastic stiffness. The block's contacting surface, unlike the top surface, which is prescribed uniform displacement, is displaced non-uniformly, leading to slipping in the central part of the block earlier than the region near the leading and the trailing edges, e.g. displacement at time 115 ms in Fig. 4.13e. The discrepancy in the frictional forces for different meshes in Fig. 4.13d is a direct effect of the same discrepancy observed in the normal forces in Fig. 4.12c.

In all cases, it can be observed that the mesh refinement shifts the plots of normal and frictional forces variation, but they show a converging behaviour. The use of regular meshes and mesh refinement both show an improvement in the smoothness of the obtained solution.

4.4.2 *Hertzian frictional contact - Cattaneo and Mindlin's problem*

In this example, Hertzian contact of curved profile experiencing tangential loading less than the limiting friction analysed to study the frictional effect with partial slip, also known as Cattaneo and Mindlin's problem. A half-cylindrical part with a radius of 200 mm is loaded against a block representing the elastic half-space chosen for this problem, as shown in Fig. 4.14a. Both bodies have linear elastic material with Young's modulus E = 210 GPa, Poisson's ratio, $\nu = 0.3$ and coefficient of friction of $\mu = 0.3$ in their contact interface. The normal penalty scaling factor for contact definition is $f_s = 40$, the tangential penalty is $\epsilon_T = 400$, and the entire system is subjected to dynamic relaxation of 90% for obtaining the equilibrium stage solution. The top surface of the half-cylinder is pressed downwards to induce a normal reaction with the block and is subsequently pushed tangentially, leading to frictional forces acting in the contact interface. The lower surface of the block is fixed, and the lateral surfaces of both the half-cylinder and the block are restricted against motion in the direction normal to these surfaces.

The top surface is pushed uniformly downwards by 0.9 mm, and the net vertical force P is recovered by summing up the downward forces acting on all nodes on

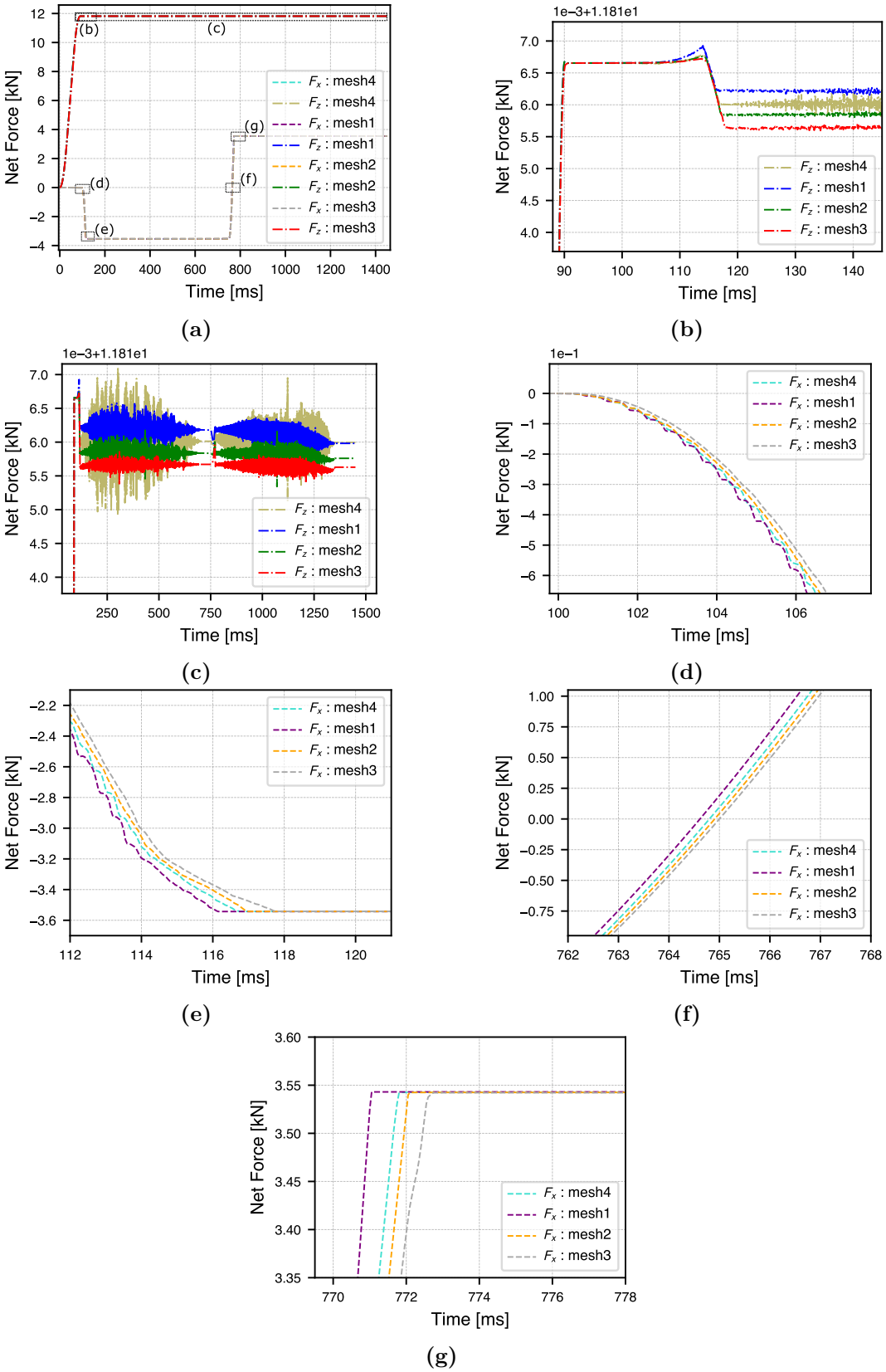

Figure 4.12: Block on slab transitioning from stick to slip mode to study effect of different meshes: plots of force v/s time (a,b,c,d,e,f,g). Inset outlines in (a) are not to scale.

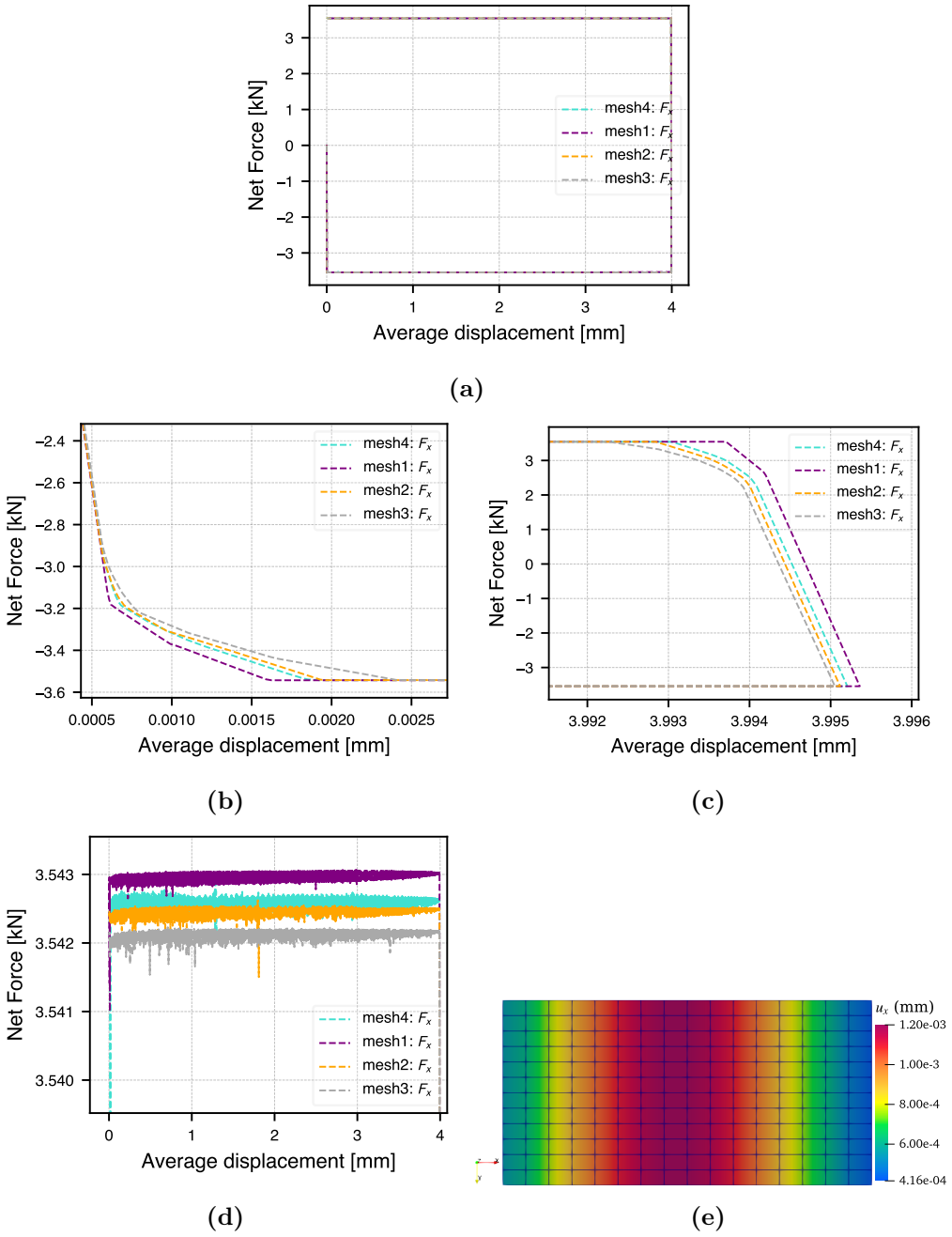

Figure 4.13: Block on slab transitioning from stick to slip mode: force v/s average displacement of the contact surface of the block (a,b,c,d); displacement of the contact surface of block at 115 ms for mesh3 (e).

the top surface. The top surface is then subjected to uniform tangential traction q with net tangential force $Q = 0.5\mu P$. Applying uniform displacement instead of uniform normal pressure on the top surface allows maintaining the top surface of the half-cylinder horizontal, which aids in the application of the tangential traction in the original problem. For the normal reaction in the contact interface, the Hertzian contact solution is directly applicable, and for the tangential loading, an analytical solution of generated tangential traction is also available [7][91]. In this work, the tangential traction formulation is used to calculate the nodal forces for the effect of friction, so the variation of tangential nodal forces normalized against the maximum value of analytical normal contact pressure is plotted on the Fig. 4.14b. Strictly speaking, the nodal forces are not the same as contact pressure. However, in the scope of the presented formulation, where nodal forces are directly evaluated without evaluating the contact pressure, the use of nodal forces for uniformly sized elements serves as an indirect measure of the distribution of the tractions over the contact interface. Also, the primary interest here is to show the demarcation of the stick and slip zone and the traction distribution, for which the presented plot serves a direct utility, as can be observed that the contact interface near the central point of contact is in stick mode whereas the region near the contact edge is in slipping mode.

4.4.3 *Twisting Indentation Problem*

The effect of friction in the case of torsion by a half-spherical indenter is studied through this problem. A relatively hard half-spherical indenter having outer and inner radii of 30 mm and 22 mm, respectively, with the Young's modulus $E_1 = 5E_0$ is pressed against a block having the Young's modulus $E_2 = E_0$ ($E_0 = 210$ GPa) with both materials having density of 7.83×10^{-2}. For contact definition, the normal penalty scaling factor is $f_s = 50$, tangential penalty is $\epsilon_T = 500$, and coefficient of friction is $\mu = 0.3$. Unlike [110], the contact definition has a frictional effect throughout the analysis. A dynamic relaxation coefficient of 90% is chosen for the entire problem to alleviate the dynamic effects through damping. First, the upper surface of the half-spherical indenter is uniformly pressed downwards by $u = 10$

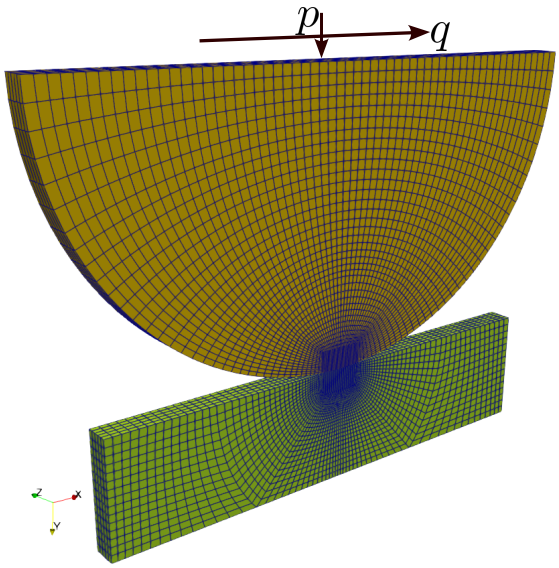

(a) Mesh used for testing frictional hertzian contact

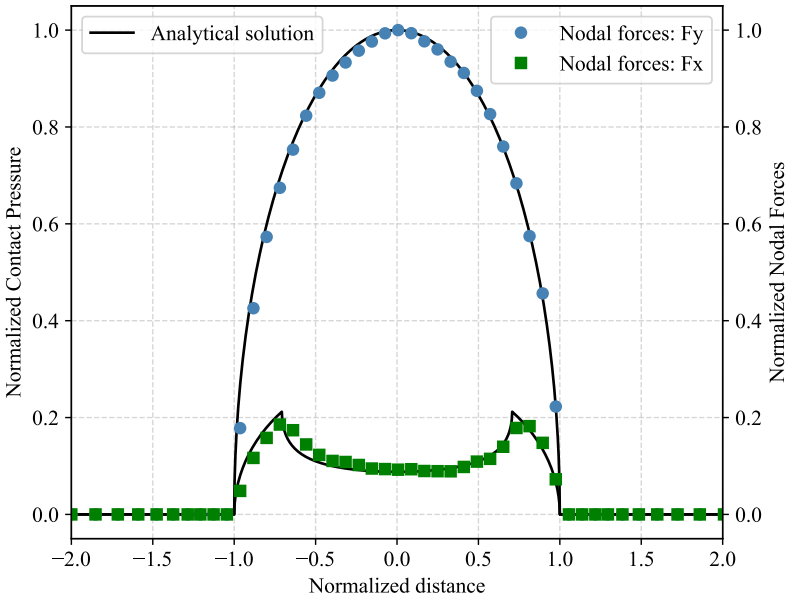

(b) Comparison between the normalised analytical solution of contact traction and normalized nodal forces in the contact region

Figure 4.14: Cattaneo and Mindlin's problem: (a) mesh used for testing micro slip, and (b) comparison between the normalised analytical solution of contact traction and normalized nodal forces in the contact region.

mm, followed by twisting and reversed twisting of 180° while resisting the effect of friction, see Fig. 4.15a. The first stress invariant I_1 at the end of downward pressing for a clipped visualisation of the system is shown in Fig. 4.15b. At the end of twisting and reversed twisting the Figs. 4.15c,4.15d show the stress σ_{xz}, and Figs. 4.15e,4.15f show the stress invariant I_1 in the contact region of the block, respectively. The contact interface undergoes subsequent friction phases of stick-slip-stick-slip with rotation of the indenter. In each stick phase, the contacting region on the block follows the rotation of the indenter, leading to its twisting. Notice how the twisting of the contact interface, in the two stick phases in opposite directions, are mirror images of each other.

The variation of the net vertical force on the block's contact region and the torque exerted over it around the central vertical axis is shown in Fig. 4.16. The vertical force increases during the pressing of the indenter, and the torque only increases in the stick regime of friction (due to the increasingly higher resistance) during twisting, attaining an approximately unchanging value on transitioning to the slip mode. When the sense of rotation of the indenter is reversed, the torque decreases gradually for the elastic unloading of friction, reaching zero value before increasing in the opposite direction and attaining a constant. At the end of the reversed twisting, the constant torque is retained from the elastic regime of friction based on the elastoplastic concept. The variation in torque during twisting and reversed twisting is similar to the variation in the frictional forces during the forward and backward motion of the block over the slab in the Sec. 4.4.1.

4.4.4 *Self-contact test*

The unbiased nature of frictional formulation is tested through a self-contact test by considering block cavities and cracks having dimensions of $200 \times 200 \times 50$ mm^3 as shown in Fig. 4.17a. It is made of isotropic elastoplastic material with linear hardening having Young's modulus, E= 10 GPa, Poisson's ratio $\nu = 0.3$, initial yield stress $\sigma_{y_0} = 1$ GPa, and hardening modulus, H= 0.1 GPa. The top surface of the block is uniformly pressed downwards by a net distance of 40 mm, while

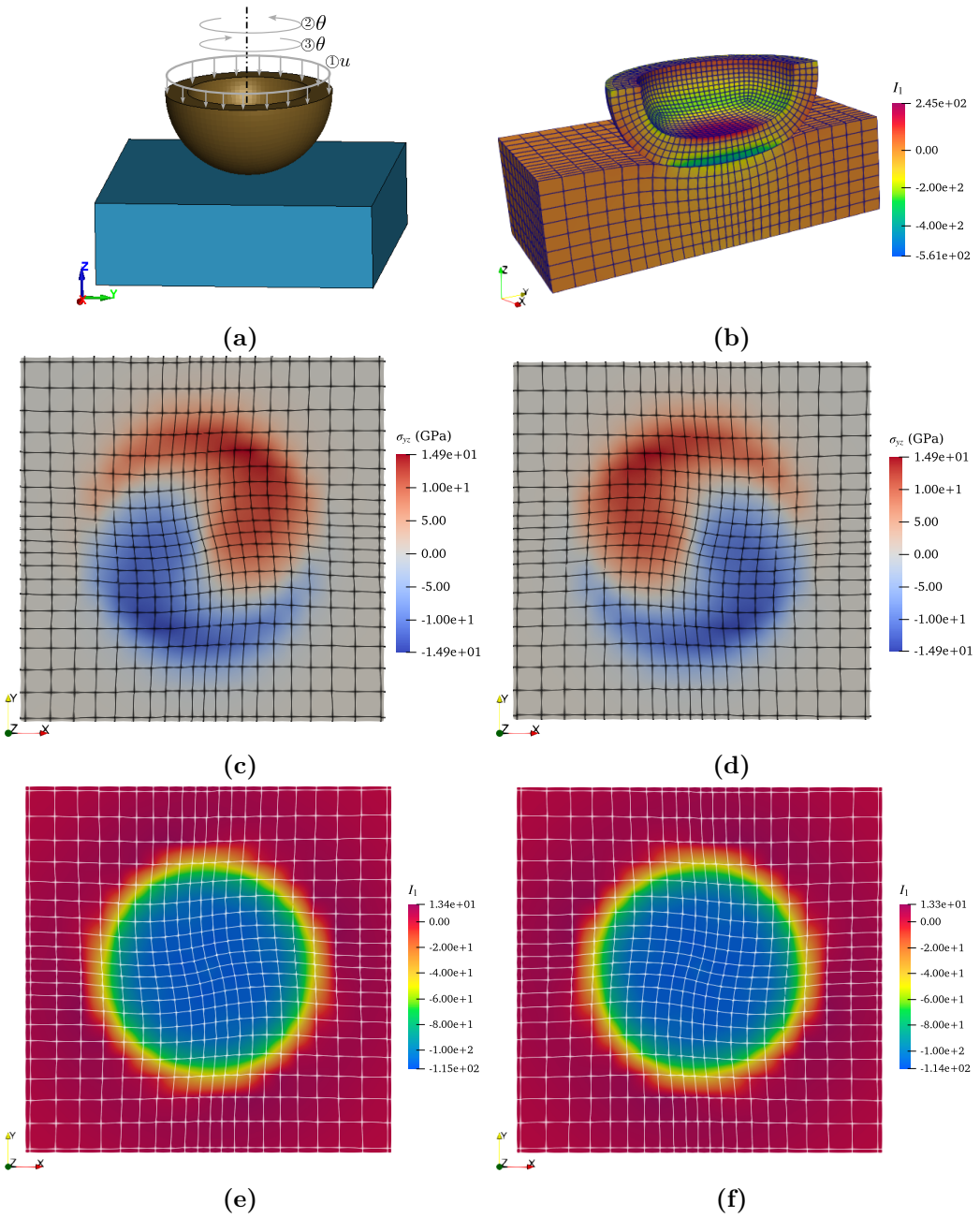

Figure 4.15: Twisting indentation problem: (a) schematic of the problem, (b) stress invariant I_1 after compression, (c) and (d) show the stress component σ_{yz} in and around the contact region of the block at the end of twisting and untwisting, respectively, (e) and (f) show the stress invariant I_1 at the end of twisting and untwisting, respectively.

the bottom surface is fully supported. Both frictionless and frictional cases are considered here for self-contact. For the frictional case, the coefficient of friction and tangential penalty are $\mu = 0.6$ and $\epsilon_T = 10$ GPa/mm, respectively. The resulting deformation for both cases are shown in Figs. 4.17b,4.17c.

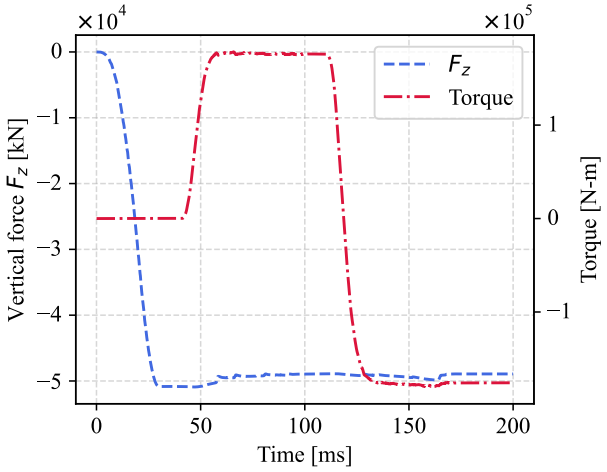

Figure 4.16: Variation of net vertical force and torque on the indenter.

In the frictionless case, the deformation of the block leads to compression of cavities, and there is an unopposed relative sliding between the free surfaces of the cracks. The continuous compression of the block leads to some portions sliding outwards. However, with the presence of a frictional effect, the relative sliding between contacting free surfaces is opposed, leading to a stick-dominant effect that results in the bulging of the block due to the Poisson effect. Additionally, the frictional case also leads to compression and contact in the lower cavity due to the relatively intact configuration of the overall block. This test highlights the seamless working of frictional formulation in a self-contact case, with auto-detection of contact and its resulting influence on the overall configuration. It should be noted that the frictional contact between any opposite facets sharing edge(s) contributes to nodal forces on the shared edge(s) along the direction of the midplane. This is a consequence of the mathematical description of finite elements that convert the traction distribution as nodal forces, and it is preserved in the proposed algorithm to ensure mathematical consistency.

4.4.5 *Impact of a ring at an angle*

This example studies the effect of friction in a dynamic contact by having an oblique impact of a ring over a rigid platform. A ring with an outer and inner diameter

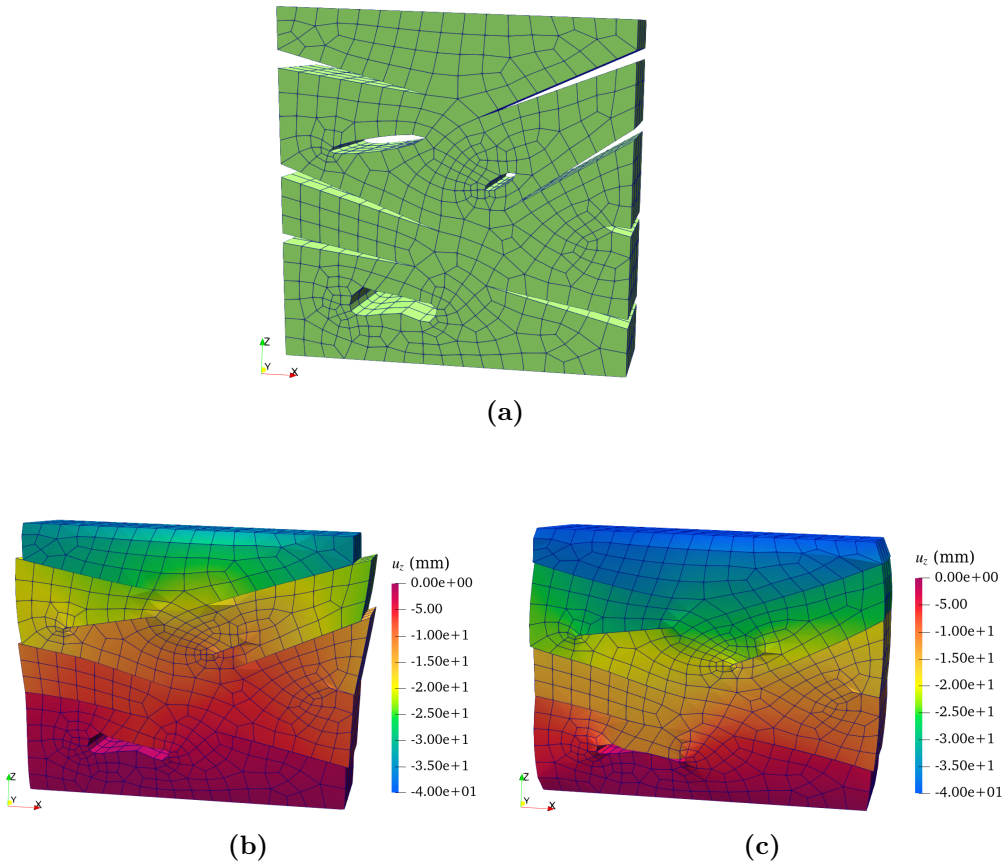

Figure 4.17: Self-contact problem: (a) undeformed block, (b) deformation without frictional effect, and (c) deformation with frictional effect.

of 20 mm and 18 mm, respectively, and having a thickness of 4 mm is impacted with speed $2\sqrt{2}$ m/s at 45° angle as shown in Fig. 4.18a. It has Young's modulus of elasticity as E = 200 GPa, no Poisson's effect $\nu = 0$ and the density of $\rho = 10^{-4}$ kg/mm^3. For contact definition, the penalty scaling factor is $f_s = 1$ for normal contact, and the penalty is $\epsilon_T = 100$ for tangential contact, and the coefficient of friction between the two bodies is $\mu = 0.4$. Both frictionless and frictional impacts are considered with the same set of parameters and boundary conditions. While in frictionless impact, there is no rotation of the ring after rebound (Fig. 4.18b), the ring gains angular motion after rebound in the frictional impact (Fig. 4.18c). Due to the frictional effect, the tangential forces acting on the ring exert a torque on the ring, imparting an angular motion which is retained in the ring past the collision. These frictional forces also reduce the ring's momentum in the tangential direction, Fig. 4.19. For the frictionless impact, the angle of rebound, measured from the

horizontal direction, is 39.25°, whereas, in the presence of friction, it rebounds with the angle of 58.28°, which also follows the trend in [111].

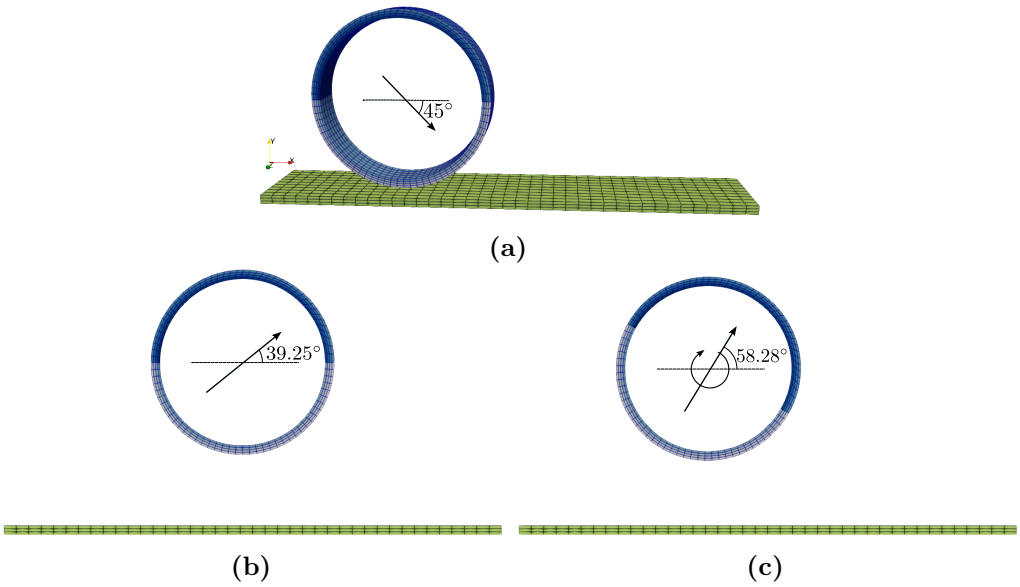

Figure 4.18: Impact of a ring on a rigid platform: (a) Impact at 45° angle, (b) rebound with no rotation for frictionless contact, and (c) rebound with rotation for frictional contact. The colours in the ring are only intended to show the different parts of the mesh.

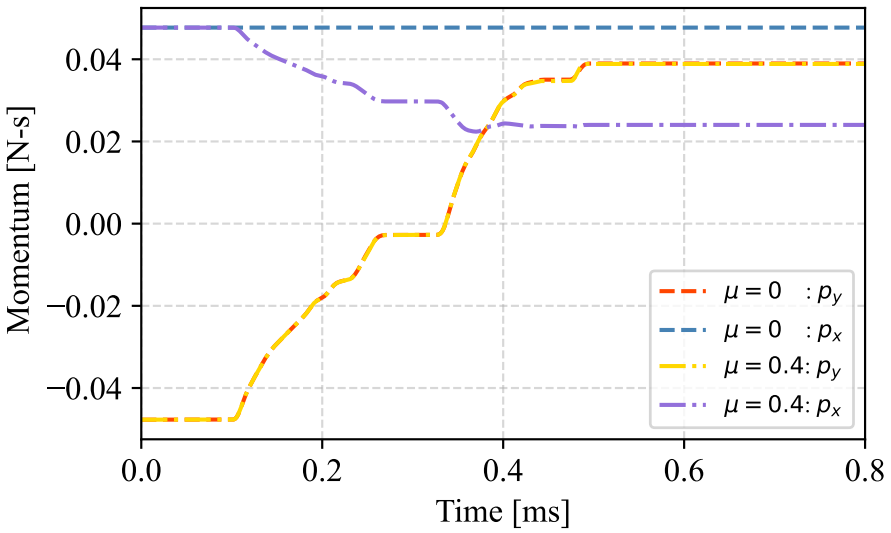

Figure 4.19: Comparison of change in components of momentum for the both frictionless and frictional impact of the ring.

4.4.6 *Rolling of a cylinder*

The working of the frictional formulation and the algorithm are tested for the effect of rolling an elastic disc over a rigid platform. A disc with diameter $d = 100$ mm and thickness 40 mm is chosen with discretisation as shown in Fig. 4.20a. It has Young's modulus of Elasticity as 210 GPa, density 7.83×10^2 kg/mm^3, and zero Poisson's ratio. For contact definition, the normal penalty scaling factor is chosen as $f_s = 1$ and tangential as 400, and the coefficient of friction as $\mu = 0.7$. The nodes in the central axis of the disc are initially uniformly displaced downward by 2 mm, followed by horizontal motion dragging it to a total distance of πd. The entire system is damped by using the dynamic relaxation coefficient of 90%. Both frictionless and frictional cases are considered, and the initial point of contact shown as A in Fig. 4.20b is examined. In the frictionless case, the sharp corner A coming into contact is not stable during the dragging of the axial nodes; thus, the disc gets rotated in the initial phase by the same amount as its discretisation and remains in this configuration for the rest of the time, see Fig. 4.20c. On the other hand, the disc undergoes a full rotation in the presence of friction with the point A returning to be in contact with the platform at its initial position, see Fig. 4.20d, thus producing a complete rolling effect.

4.5 Conclusion

In this paper, a patch-based frictional contact algorithm is presented that evaluates states of friction - stick or slip - on each patch in the contact interface formed by the overlap of segments on opposite surfaces. By considering the relative motion between the contacting segments over their respective midplanes along with the elastoplastic analogy of friction, the frictional traction is evaluated unbiasedly without focusing on the sliding of individual slave nodes over the master surface that is classically employed. The equality of the tangential tractions applied on both surfaces is inherently maintained in the formulation. The tractions applied on both surfaces allow for some sliding in the stick phase, and it can be reduced

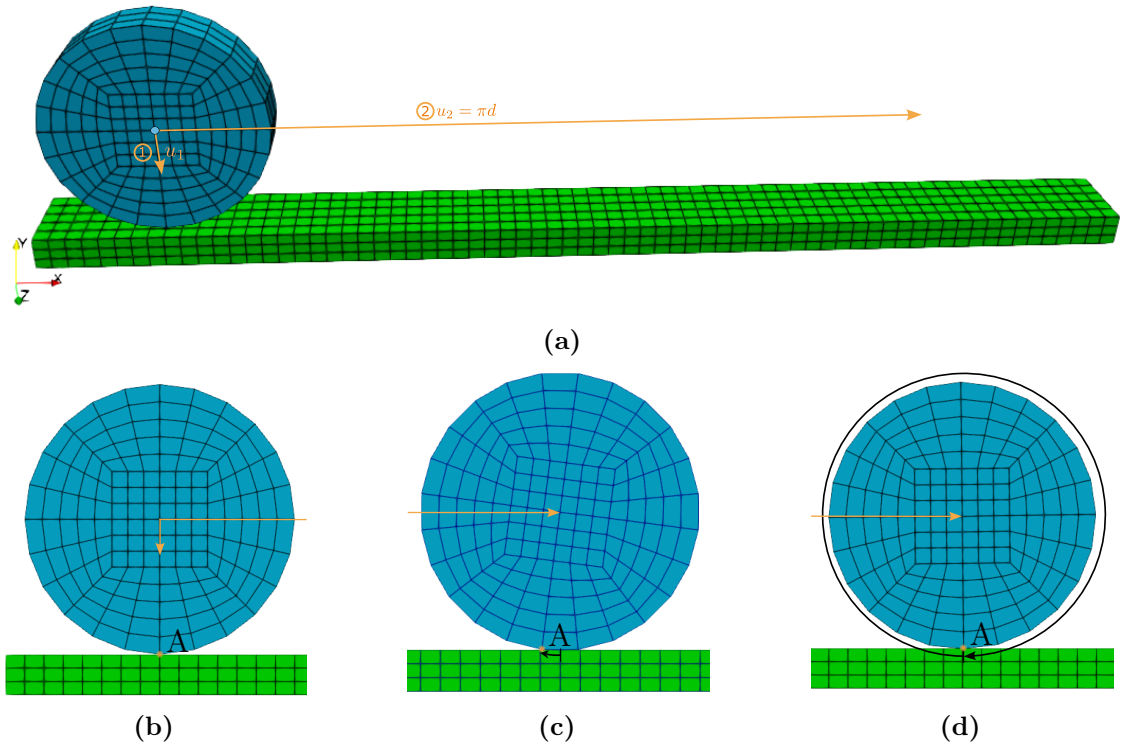

Figure 4.20: Rolling of a cylinder: (a) mesh used for rolling of a deformable cylinder over a rigid platform, (b) view at $t = 0$, (c) view at $t = t_f$ for frictionless contact showing a very small tilt due to the sharp corner at A due to first-order discretisation, (d) view at $t = t_f$ for frictional contact experiencing rolling and having a full rotation while the axial nodes traverse a distance of πd, where d is the diameter.

by employing a high penalty. The formulation provides complete stick, partial slip, and smooth transition between stick and slip phases of friction, depending on varying geometries and loading conditions. The inherent unbiased nature of the formulation is of direct utility in the self-contact problems applied in a single pass. Any error incurred in the algorithm due to the rotational effect can be mitigated by refined discretisation in the contact zone. A multitude of examples presented in the paper demonstrate the high accuracy, versatility and robustness of the presented formulation in a diverse set of conditions. Further research can be carried out to explore the frictional properties with the effect of velocity, temperature and a possible anisotropy of the interacting surfaces.

References

[7] K. L. Johnson. *Contact mechanics*. en. Cambridge University Press, 1985.

[13] Michael A. Puso and Tod A. Laursen. “A mortar segment-to-segment frictional contact method for large deformations”. en. In: *Computer Methods in Applied Mechanics and Engineering* 193.45 (2004), pp. 4891–4913.

[15] Peter Wriggers. *Computational contact mechanics*. en. Hoboken, NJ: J. Wiley & Sons, 2002.

[16] Tod A. Laursen. *Computational Contact and Impact Mechanics*. en. Berlin, Heidelberg: Springer Berlin Heidelberg, 2003.

[17] Roger A. Sauer and Laura De Lorenzis. “An unbiased computational contact formulation for 3D friction”. en. In: *International Journal for Numerical Methods in Engineering* 101.4 (2015), pp. 251–280.

[24] Fionn Dunne and Nik Petrinic. *Introduction to computational plasticity*. en. Oxford ; New York: Oxford University Press, 2005.

[31] A. Curnier. “A Theory of Friction”. en. In: *Unilateral Problems in Structural Analysis*. Ed. by Gianpietro Del Piero and Franco Maceri. International Centre for Mechanical Sciences. Vienna: Springer, 1985, pp. 47–56.

[32] R Michalowski Z Mroz. “Associated and non-associated sliding rules in contact friction problems.” In: *Archiv. Mech.* 30 (1978), pp. 259–276.

[33] Vladislav Yastrebov. “Computational contact mechanics: geometry, detection and numerical techniques”. en. PhD thesis. École Nationale Supérieure des Mines de Paris, 2011.

[55] Ivan E. Sutherland and Gary W. Hodgman. “Reentrant polygon clipping”. In: *Communications of the ACM* 17.1 (1974), pp. 32–42.

[85] G. R. Cowper. “Gaussian quadrature formulas for triangles”. en. In: *International Journal for Numerical Methods in Engineering* 7.3 (1973), pp. 405–408.

[86] D. A. Dunavant. “High degree efficient symmetrical Gaussian quadrature rules for the triangle”. en. In: *International Journal for Numerical Methods in Engineering* 21.6 (1985), pp. 1129–1148.

[87] Indrajeet Sahu. *Bilinear-Inverse-Mapper: Analytical Solution and Algorithm for Inverse Mapping of Bilinear Interpolation of Quadrilaterals*. en. SSRN Scholarly Paper. Rochester, NY, 2024.

[91] Valentin L. Popov, Markus Heß, and Emanuel Willert. *Handbook of Contact Mechanics: Exact Solutions of Axisymmetric Contact Problems*. en. Berlin, Heidelberg: Springer Berlin Heidelberg, 2019.

[96] Frank Philip Bowden and David Tabor. *The Friction and Lubrication of Solids*. en. Clarendon Press, 2001.

[97] J.R Barber and M Ciavarella. “Contact mechanics”. en. In: *International Journal of Solids and Structures* 37.1-2 (2000), pp. 29–43.

[98] Bharat Bhushan. *Principles and Applications of Tribology*. en. John Wiley & Sons, 1999.

[99] L. Krstulović Opara, P. Wriggers, and J. Korelc. “A C1-continuous formulation for 3D finite deformation frictional contact”. en. In: *Computational Mechanics* 29.1 (2002), pp. 27–42.

[100] Reese E. Jones and Panayiotis Papadopoulos. “A yield-limited Lagrange multiplier formulation for frictional contact”. en. In: *International Journal for Numerical Methods in Engineering* 48.8 (2000), pp. 1127–1149.

[101] F. J. Gallego and J. J. Anza. “A mixed finite element model for the elastic contact problem”. en. In: *International Journal for Numerical Methods in Engineering* 28.6 (1989), pp. 1249–1264.

[102] M. Tur, F. J. Fuenmayor, and P. Wriggers. “A mortar-based frictional contact formulation for large deformations using Lagrange multipliers”. en. In: *Computer Methods in Applied Mechanics and Engineering* 198.37 (2009), pp. 2860–2873.

[103] A.E. Giannakopoulos. “The return mapping method for the integration of friction constitutive relations”. en. In: *Computers & Structures* 32.1 (1989), pp. 157–167.

[104] Djordje Perić and D. R. J. Owen. “Computational model for 3-D contact problems with friction based on the penalty method”. en. In: *International Journal for Numerical Methods in Engineering* 35.6 (1992), pp. 1289–1309.

[105] Kathrin A. Fischer and Peter Wriggers. “Mortar based frictional contact formulation for higher order interpolations using the moving friction cone”. In: *Computer Methods in Applied Mechanics and Engineering*. John H. Argyris Memorial Issue. Part I 195.37 (2006), pp. 5020–5036.

[106] P. Wriggers and A. Haraldsson. “A simple formulation for two-dimensional contact problems using a moving friction cone”. en. In: *Communications in Numerical Methods in Engineering* 19.4 (2003), pp. 285–295.

[107] L. De Lorenzis, Peter Wriggers, and C. Weißenfels. “Computational Contact Mechanics with the Finite Element Method”. en. In: *Encyclopedia of Computational Mechanics Second Edition*. John Wiley & Sons, Ltd, 2017, pp. 1–45.

[108] Indrajeet Sahu and Nik Petrinic. “Midplane based 3D single pass unbiased segment-to-segment contact interaction using penalty method”. In: *forthcoming* (2024).

[109] J. Lubliner. “A simple theory of plasticity”. In: *International Journal of Solids and Structures* 10.3 (1974), pp. 313–319.

[110] Thang X. Duong and Roger A. Sauer. “A concise frictional contact formulation based on surface potentials and isogeometric discretization”. en. In: *Computational Mechanics* 64.4 (2019), pp. 951–970.

[111] P. Wriggers, T. Vu Van, and E. Stein. “Finite element formulation of large deformation impact-contact problems with friction”. en. In: *Computers & Structures* 37.3 (1990), pp. 319–331.

4.6 Supplementary discussion

This final section clarifies some additional points not elaborated on in the paper, which will help in a more comprehensive understanding of the work.

This work has solely focused on regularised Coulomb friction with penalty method by utilising elastoplastic analogy. For the sake of completeness, the original unregularised Mohr-Coulomb friction is mentioned below

$$||\mathbf{t}_T|| - \mu||\mathbf{t}_N|| \leq 0,\ \mathbf{t}_T - \mu||\mathbf{t}_N||\frac{\mathbf{g}_T}{||\mathbf{g}_T||} \leq 0,\ ||\mathbf{g}_T||(||\mathbf{t}_T|| - \mu||\mathbf{t}_N||) = 0 \quad (4.27)$$

where all symbols have their usual meanings, as presented in the paper. This is similar to the Karush-Kuhn-Tucker condition of impenetrability in the case of compressive loads. The above condition enforces a strict stick with no sliding, and any sliding corresponds to the slipping case with the application of limiting friction. This classical Coulomb's friction law, with the geometric enforcement of the stick condition, has a nonsmooth nature in the transition from the stick to the slip condition. Also, it has multiple possible values of tangential tractions for a perfect stick (i.e. zero relative tangential sliding) that is dependent upon the boundary conditions.

Cattaneo and Mindlin's problem

The frictional Hertzian contact problem considers two elastic cylinders pressed against each other and subjected to a tangential load. When the applied load is within the limiting friction, it gives rise to two distinct stick and slip zones. In the slip zone, which is around the periphery of the contact zone, a small relative motion occurs, called slip or micro-slip. In the remaining part, surfaces adhere to each other, and there is no relative motion [7][112].

If the x-axis aligns with the contact interface such that the origin corresponds to the first point of contact, the stick zone is in the region $-c \leq x \leq +c$, and the slip zone in the region $\{-a \leq x \leq -c\} \bigcup \{+c \leq x \leq +a\}$. The size of the stick region, c, is defined as

$$\frac{c}{a} = \left(1 - \frac{Q}{\mu P}\right)^{\frac{1}{2}} \quad (4.28)$$

The shear traction or tangential traction distribution $q(x)$ on the contact interface is continuous, but it is composed of tangential traction in the stick and slip zone.

It can be written as

$$q(x) = \frac{\mu p_0}{a}\{(a^2 - x^2)^{1/2} - H(c^2 - x^2)(c^2 - x^2)^{1/2}\}, \quad -a < x < a \tag{4.29}$$

where $H(\cdot)$ is the Heaviside step function demarcating the stick and slip zones.

Some other key aspects related to the frictional formulation and future possibilities are mentioned below -

- Static and kinematic friction: While the present work considers a fixed value of the coefficient of friction, a possibility of including effects of static and dynamic coefficients can proceed by including the effect of relative velocity as

$$\mu = \mu_k + (\mu_s - \mu_k)e^{-c|v_{\text{rel}}|} \tag{4.30}$$

  where v_{rel} is the velocity of sliding and c (ms/mm) is the velocity weakening of the friction coefficient [113].

- An alternative choice of basis thought during the conceptualisation was to choose any parametric line of either facet at the centroid together with its orthogonal direction. However, in the case of non-rectangular projection, the change in the first parametric line, e.g., ξ_1 line ($\xi_2 = constant$) from the previous to the new one, might have a relative rotation which will lead to a rotation in the basis. This will incur high errors.

- Modelling of anisotropic friction is a complex challenge, which, although not undertaken in the current work, the proposed formulation has the potential to account for this effect given that its framework naturally includes the relative orientation of the parametric lines.

In conclusion, this chapter has introduced a novel unbiased frictional formulation that effectively enforces stick-slip constraints over patches on the contact interface in a single pass, moving away from the traditional notion of enforcing constraints between nodes of the slave surface and the segments of the master surface. Numerous examples demonstrated its robustness and versatility in static as well as dynamic frictional contact problems, including self-contact.

5

Higher-order elements in frictional contact

Higher-order elements representing curved surfaces can better represent the continuous deformation in contact. In this chapter, the work on unbiased compressive load and frictional effect presented in the previous two chapters is further extended to higher-order elements by considering pairwise interaction between subdivided segments on opposite surfaces. As is shown here, these elements provide better results for curved surfaces compared to first-order elements.

Some of the major highlights of this work are

- High-accuracy unbiased frictional contact formulation is presented for higher-order finite elements
- Higher-order elements provide smoother contact pressure in static contact and more accurate momentum transfer in dynamic contact
- The unbiased nature of the formulation aids in the smooth handling of frictional self-contact problems
- The provided formulation can represent the nonlinear distribution of frictional forces on contacting nodes

Unbiased Higher-order frictional contact using midplane and patch based segment-to-segment penalty method

Indrajeet Sahu, Nik Petrinic

Abstract

A highly accurate, unbiased frictional contact algorithm for higher-order elements based on the concept of midplane is presented. Compressive and frictional contact constraints are applied to the contact pairs of sub-segments obtained by the subdivision of higher-order segments. Here, normal traction depends upon the penalisation of interpenetration, and frictional traction depends upon relative sliding between sub-segments corresponding to its shared patch. An additional step of midplane correction is presented to improve accuracy in dynamic contact. In both static and dynamic cases, the use of higher-order elements surpasses the accuracy of first-order elements, as shown through Hertzian contact and dynamic collisions. The contact patch test also yielded results that matched the accuracy of the corresponding element patch test. The frictional sliding is able to represent the expected nonlinear distribution of nodal forces for the higher-order elements. Two other examples of frictional self-contact and high-rate deformation are also shown to highlight the versatility of the proposed approach.

5.1 Introduction

The finite element solution of physical problems having frictional contact among solids warrants special attention for surfaces having complex descriptions. Higher-order elements offer an attractive choice in such finite element solutions, as they can better represent the curvature owing to their higher-order basis functions. They are also effective in modelling flexure without reduced quadrature and hourglass control, as well as in the issues of volumetric locking in unstructured meshes [114]. Contact constraint enforcement methodologies, however, need to account for the

complexities associated with the higher-order basis functions on surfaces along both normal and tangential directions. Although finite element solutions using first-order elements together with h-refinement can generate practical solutions, the recently increased development on p-refinement and, in particular, second-order elements provides an active opportunity for techniques that can offer higher accuracy in solutions [82][115][70]. Additionally, the higher-order elements can often achieve the same level of accuracy as linear ones with fewer elements, which has the potential for better computational efficiency. The higher-order elements also have a better convergence rate with the refinement of meshes. In light of this, a contact interaction methodology accounting for the higher-order interpolation of geometry and solution on the surface nodes is presented in this work.

Typically, the general architecture of solving contact problems with finite element methods involves two aspects - contact discretisation and constraint enforcement. When two bodies composed of finite elements interact, pairs of discrete entities are formed on the surface to enforce contact constraints over them. The Node-to-segment (NTS) based discretisation [40][62] is the most widely used technique, wherein pairs between nodes on one surface and the segments on opposite surfaces are formed to define contact interaction and impose the contact constraint disallowing nodes on slave surface from penetrating the master surface. Due to its limited accuracy and inability to transfer even a uniform pressure in contact patch test [65], segment-to-segment (STS) methods are more appropriate for problems where contact traction accuracy is critical. In STS methods, constraints are applied on pairs of segments (or facets) on opposite discretised surfaces in a continuous manner [12], and this is a physically more realistic approach, as is evident in its robustness and accuracy. Constraint enforcement generally employs either penalty or Lagrange multiplier-based methods. While Lagrange multiplier methods enforce the impenetrability condition better than the penalty method, it incurs an additional cost due to increased system size, whereas the penalty method obviates the need for additional equations and is computationally more efficient, thus being the preferred choice in the present work.

In the last decade and a half, a significant interest has developed in formulating methods for contact between higher-order elements for both implicit and explicit finite element methods. In implicit methods, mortar methods initially used for domain decomposition [75] have been extensively studied for STS interaction by having enforcement of non-penetration condition in a weak (weighted) sense instead of the strong imposition on the entire surface, thereby having the continuity of traction through a weak formulation. In this approach, the traction is defined on one side chosen as mortar by using Lagrange multiplier basis functions together with the discrete nodal Lagrange multipliers [13, 82][78]. It has been used in both 2D frictionless contact [105] and frictional cases [116][102], as well as in 3D problems [81][76][117] with the dual-mortar formulation for linear[77][118] and quadratic shape functions [115][119]. The dual-mortar methods employ a biorthogonality relationship between Lagrange multipliers and dual-shape functions, such that these methods are able to condense Lagrange multipliers to avoid large system sizes. The mortar methods, however, have a natural bias in the definition of contact with the choice of mortar and non-mortar sides. Some other works on second-order elements can be referred to in [120] for smoothing procedure with multi-point constraints, [121] for covariant contact description, and [122] for 2D frictional contact using splines and Hermite cubic interpolation.

Second-order elements have also been recently extensively studied for their performance in explicit methods for different numbers of nodes and integration rules [123] [124] and for a contact using double pass NTS scheme [70] where the solution is the weighted average of both passes. However, the use of the NTS scheme with complex higher-order elements significantly affects the accuracy of the solution, and the imposition of contact constraints on higher-order elements is a complex challenge with the definition of contact region and enforcement of constraints. Although, in general, the use of explicit methods in common high-speed impact cases might not require high accuracy of surface traction, its use in slower applications where it can potentially compete with implicit methods would depend upon the accuracy of contact detection and contact traction. This

accuracy is better achievable using surface interaction-based methods where the contact constraint is imposed continuously over the entire surface represented by complex higher-order basis functions. Additionally, applications involving multiple successive contacts transferring momentum will also be majorly affected by the direction of motion imparted to different bodies.

In the recent STS method-based work [108][125], contact traction is resolved in an unbiased manner using the midplane between interacting facets by employing a uniformly imposed penalty. This methodology, initially proposed for facets represented by linear shape functions, is being extended here to contact between facets having higher-order basis functions and stronger curvature. The single-pass unbiased nature of the midplane-based method is preserved here, thereby avoiding the weighted dual pass route of eliminating bias in contact definition generally used in most NTS and STS methods. In this paper, contact between higher-order elements is primarily studied through contact between 27-noded second-order Lagrangian elements; however, a conceptual idea for similar implementation using a 20-noded serendipity element is also provided. Focusing on the second-order Lagrangian finite element, a facet-to-facet (or segment-to-segment) pair refers to the contact between two 9-noded facets, and a subfacet-to-subfacet (or subsegment-to-subsegment) pair refers to the contact between 4-noded subfacets decomposed from the main 9-noded facet as is typical in the literature. This work utilises an explicit finite element method with HRZ lumping of mass matrix and solved using a central difference scheme.

This paper is organised as follows- Section 5.2 describes the strong form of contact problem between two solids and its development into a weak form for formulating the finite element-based problem. Section 5.3 introduces and explains the unbiased frictional contact methodology by focusing on second-order Lagrangian elements and brings attention to a source of error due to the linear approximation of the subfacets which is inherent in the typical facet subdivision strategies. A pseudo-code for algorithmic implementation of the methodology is presented in Section 5.4 before proposing an idea for facet division in serendipity elements.

Numerous examples are presented in Section 5.6 to test the robustness of the proposed method for both frictionless and frictional contact. Finally, a conclusion to the paper is presented in Section 5.7.

5.2 Problem description

For contact between any two solids $\Omega^i (i = 1, 2)$ in $\mathbb{R}^3$, their reference and current configurations can be denoted using any spatial point in the domain as $\boldsymbol{X}^i$ and $\boldsymbol{x}^i$ connected by its displacement $\boldsymbol{u}^i(\boldsymbol{X}, t)$, i.e., $\boldsymbol{x}^i = \boldsymbol{X}^i + u^i$. The force-momentum equation representing the boundary value problem in the strong form at any point can be written as

$$\begin{aligned} \nabla \cdot \boldsymbol{\sigma}^i + \boldsymbol{b}^i &= \rho^i \partial_t^2 \boldsymbol{x} \qquad && \forall\ \boldsymbol{x}^i \in \Omega^i \times (0, T) \\ \boldsymbol{u}^i(\boldsymbol{x}^i) &= \overline{\boldsymbol{u}}^i && \forall\ \boldsymbol{x}^i \in \gamma_u^i \times (0, T) \\ \boldsymbol{\sigma}^i \boldsymbol{n}^i &= \overline{\boldsymbol{t}}_\sigma^i && \forall\ \boldsymbol{x}^i \in \gamma_\sigma^i \times (0, T) \end{aligned} \tag{5.1}$$

where the symbols $\boldsymbol{\sigma}^i, \boldsymbol{b}^i$ and ρ^i represent Cauchy stress, body force per unit volume and density at any point $\boldsymbol{x}^i$ in Ω^i. While the first equation is a result of the conservation of momentum, the second and third equations impose Dirichlet and Neumann boundary conditions on the γ_u^i and γ_σ^i, respectively. The contact zone formed between the two bodies during the motion and deformation is represented by $\gamma_c (= \gamma_1 \cap \gamma_2)$, such that $\gamma_u^i, \gamma_\sigma^i, \gamma_c \subset \gamma^i$. The different subsets of the boundaries do not overlap, i.e., $\gamma_\sigma^i \cap \gamma_u^i = \gamma_\sigma^i \cap \gamma_c^i = \gamma_u^i \cap \gamma_c^i = \emptyset$. While both γ_u^i and γ_σ^i represent the known boundary conditions, γ_c is an unknown boundary with unknown tractions $\boldsymbol{t}_c^i$ ($\boldsymbol{t}_c^1 = -\boldsymbol{t}_c^2$) which come into effect during any mechanical interaction between the two solids. The contact traction $\boldsymbol{t}_c^i$ at any point in γ_c can be decomposed into the normal and tangential parts, $\boldsymbol{t}_N^i$ and $\boldsymbol{t}_T^i$, as

$$\boldsymbol{t}_c^i = (\boldsymbol{t}_c^i \cdot \boldsymbol{n}^i)\boldsymbol{n}^i + (\boldsymbol{I} - \boldsymbol{n}^i \otimes \boldsymbol{n}^i)\boldsymbol{t}_c^i \tag{5.2}$$

where the first term denotes $\boldsymbol{t}_N^i$, the second term denotes $\boldsymbol{t}_T^i$, and $\boldsymbol{n}^i$ denotes the outward normal at this point with respect to the body Ω^i. The methodology presented in this paper focuses on the finite element decomposition of the pristine

domains Ω^1 and Ω^2 using higher-order elements for better capturing the smoothness of the boundary descriptions γ^i and evaluating the contact tractions $\boldsymbol{t}_N^i$ and $\boldsymbol{t}_T^i$ acting over γ_h^i.

5.2.1 Variational formulation

The above-presented strong form of the governing equation is converted into a weak form using variational methods over the domains of solids Ω^1 and Ω^2. For all kinematically admissible deformations $\boldsymbol{u}^i$ contained in the space $\mathscr{U}^i$ and their variations $\delta\boldsymbol{u}^i$ contained in the space $\mathscr{V}^i$, the weak form of the governing equations representing the dynamic equilibrium at any point in time for the solid Ω^i is

$$\begin{aligned}\int_{\Omega^i} \rho^i \partial_t^2 \boldsymbol{u}^i \cdot \delta\boldsymbol{u}^i \, dV + \int_{\Omega^i} \boldsymbol{\sigma}^i(\boldsymbol{u}^i) : \nabla(\delta\boldsymbol{u})^i \, dV \\ = \int_{\Omega^i} \rho^i \boldsymbol{b}^i \cdot \delta\boldsymbol{u}^i \, dV + \int_{\gamma_\sigma^i} \boldsymbol{t}_\sigma^i \cdot \delta\boldsymbol{u}^i \, d\gamma^i + \int_{\gamma_c^i} \boldsymbol{t}_c^i \cdot \delta\boldsymbol{u}^i \, d\gamma^i, \quad \forall \delta\boldsymbol{u}^i \in \mathscr{V}^i \end{aligned} \tag{5.3}$$

Here, the spaces $\mathscr{U}^i$ and $\mathscr{V}^i$ are defined as

$$\mathscr{U}^i = \{\boldsymbol{u}^i : \Omega^i \to \mathbb{R}^3 | \boldsymbol{u}^i \in [H^1(\Omega^i)]^{n_{sd}}, \boldsymbol{u}^i = \overline{\boldsymbol{u}}^i \;\; \forall \boldsymbol{x} \in \gamma_D^i\} \tag{5.4}$$

$$\mathscr{V}^i = \{\delta\boldsymbol{u}^i : \Omega^i \to \mathbb{R}^3 | \delta\boldsymbol{u}^i \in [H^1(\Omega^i)]^{n_{sd}}, \delta\boldsymbol{u}^i = \boldsymbol{0} \;\; \forall \boldsymbol{x} \in \gamma_D^i\} \tag{5.5}$$

where $H^1(\Omega^i)$ denotes the Sobolev space of functions. The last term in the virtual work eq. 5.3, representing the virtual work contribution of contact, exhibits the nonlinear nature of contact problems as neither the contact zone γ_c nor the contact traction distribution $\boldsymbol{t}_c^i$ are known apriori, and depend upon the evolving states of the two domains.

For active contact constraint between the solids Ω^1 and Ω^2, the total virtual work of contact is

$$\delta\Pi_c(\boldsymbol{u}, \delta\boldsymbol{u}) = \int_{\gamma_c^1} \boldsymbol{t}_c^1 \cdot \delta\boldsymbol{u}^1 d\gamma + \int_{\gamma_c^2} \boldsymbol{t}_c^2 \cdot \delta\boldsymbol{u}^2 d\gamma \tag{5.6}$$

$$= \int_{\gamma_c} \boldsymbol{t}_c^1 \cdot (\delta\boldsymbol{u}^1 - \delta\boldsymbol{u}^2) d\gamma \tag{5.7}$$

Note that if a single body is considered, then as a result of its geometry and boundary conditions, its own boundary might experience a mechanical interaction,

thereby leading to a possibility of self-contact. While this virtual work equation is denoted for only two bodies, this can also simultaneously extend to multibody interactions, where contact between any two bodies can be considered similarly.

5.3 Contact problem with higher-order elements

This section presents the unbiased frictional contact interaction between surfaces discretised by higher-order finite elements. Firstly, the geometrical aspects of the contact region construction using a midplane-based methodology are described by taking the second-order Lagrangian elements. This is used to evaluate the normal traction and the normal nodal forces, which are then considered with the unbiased segment-to-segment frictional contact algorithm over midplanes to find the frictional forces between the surfaces. Further, a subsection is devoted to describing the error incurred in the use of decomposed main facets leading to four first-order subfacets and the associated linear shape functions used in lieu of the higher-order shape functions to locate the quadrature points in the parametric space over the midplanes between subfacet-to-subfacet pairs.

5.3.1 Midplane-based contact for higher-order elements

Consider the discretised form of the ith surface γ_h^i, which is represented by spatial interpolation of the discrete nodal points $\tilde{\mathbf{x}}_j^i$ as

$$\tilde{\boldsymbol{x}}^i = \sum_{j=1}^{m} \psi_j^i(\xi_1, \xi_2)\tilde{\mathbf{x}}_j^i, \quad \text{where, } \tilde{\boldsymbol{x}}^i, \tilde{\mathbf{x}}_j^i \in \gamma_h^i \tag{5.8}$$

where ψ_j^i represents the shape function associated with the node $\tilde{\mathbf{x}}_j^i$ and summation is over all total m nodes on the discrete surface. Any contact which is detected by interpenetration between the two surfaces leads to the application of contact interaction between the two surfaces.

The contact interaction is studied through pairwise interaction between discrete facets on the boundaries of the discretised domains. For domains discretised by second-order Lagrangian elements having 27 nodes with the topological connectivity

as shown in Fig. 5.1a, such discrete facets refer to the 9-noded outer facets, which can also be seen as Lagrangian rectangular elements.

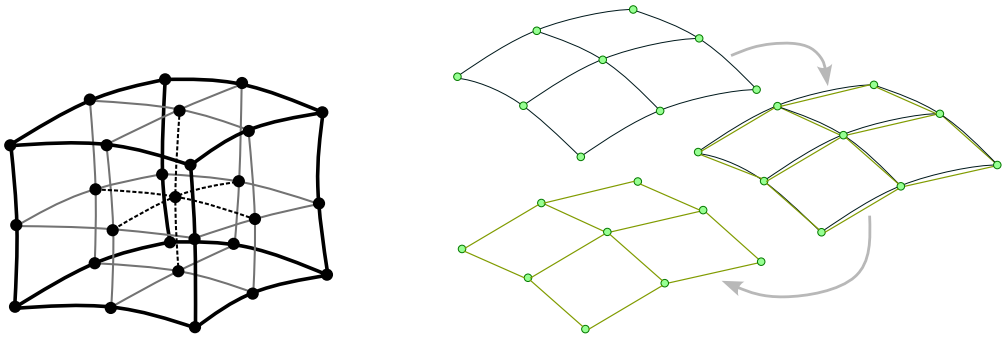

Figure 5.1: (a) Schematic of a 27-noded hexahedral element, (b) conversion of a curved 9-noded facet of into four bilinear subfacets which are solely used to define respective midplanes in the subfacet-to-subfacet pair.

In the case of contact between first-order elements as presented in [108], a midplane is constructed between opposite finite element facets by approximating each facet a plane passing through both parametric lines at the parametric centre of the facet. In this work, considering the case of a 27-noded hexahedron element, any outer facet will be a 9-noded quadratic element with a potentially higher curvature than the first-order element. So, while the potential contact pairs are searched using two main 9-noded facets on the opposite surfaces, each main facet is subdivided into four subfacets (see Fig. 5.1b) and potentially 4×4 subfacet-to-subfacet pairs are considered for contact interaction.

For any interpenetration between two opposite subfacets, the use of linear penalty results in the generation of normal traction, which is also directly proportional to the interpenetration gap g_N between the two interpolated surfaces, i.e., $\boldsymbol{t}_N = f_s \epsilon_N g_N H(-g_N) \boldsymbol{n}_{\text{mp}}$, where $\boldsymbol{n}_{\text{mp}}$ is normal to the midplane, ϵ_N is the normal penalty (chosen as minimum of the two bulk moduli), f_s is the scaling factor and $H(\cdot)$ is the Heaviside function. Normal traction, as an effect of interpenetration with respect to the normal plane, is applied equally and oppositely on the two physical facets.

Based on the mathematical nature of the finite element, any surface traction on the outer boundary leads to a set of effective external forces acting on the boundary

nodes, the calculation of which depends upon the interpolation functions associated with those boundary nodes. So, using the shape functions on the facet γ_{h_A}, the set of effective nodal forces $\mathbf{R}$ on this facet can be written as

$$\mathbf{R} = \int_{\gamma_{h_A}} \mathbf{\Psi} \boldsymbol{t} d\gamma \tag{5.9}$$

When contact interactions between all pairs of subfacets between main facets are considered, the net force acting on the nodes of the discretised surfaces γ_h^1 and γ_h^2 are from overall contribution from all subfacet pairs between them. Note that each subfacet pair has its own midplane, so all the nodal forces due to interpenetration in subfacet pairs are aligned normally to the midplane.

For interpenetration between two 9-noded Lagrangian rectangular facets, the contact region γ_{h_c} between two main facets is essentially a union of contact regions between the pairs of subfacets. The subdivision of main facets aids in reducing the inaccuracy in determining the parametric coordinates of each physical facet at the point of intersection of normal passing from the quadrature point with the physical facet. These parametric coordinates are utilised to evaluate the gaps (or heights) of both physical facets from the midplane at quadrature points. A schematic of the contact between main facets using subfacets can be seen in Fig. 5.2 So, the net nodal forces can be written as the sum of the contribution from each subfacet-to-subfacet pair, i.e.

$$\mathbf{R}^N = \sum_{s=1}^{4\times 4} \int_{\gamma_{h^s_{c_A}}} \mathbf{\Psi} \boldsymbol{t}^s_N d\gamma^s \tag{5.10}$$

Here, the normal traction $\boldsymbol{t}^s_N$ is along the direction of the midplane between the respective subfacet-to-subfacet pair, and its magnitude is the penalisation of the normal gap between them. Effectively, this allows us to write the set of nodal forces on the ith node as

$$\mathbf{R}^N_{i_A} = \sum_{s=1}^{4\times 4} \int_{\gamma_{h^s_{c_A}}} \psi_i \epsilon_N g^s_N H(g_N) \boldsymbol{n}^s_{\text{mp}} d\gamma^s \tag{5.11}$$

As these calculations are developed in an average sense, the net contact region between main facet-to-facet pairs is a union of the contact region between subfacet-to-subfacet pairs (defined as the polygon of intersection between their projections over the midplane), so it lacks the continuity in space. However, the finite element solution developed in this manner is considerably accurate for the full facet-to-facet pair, as demonstrated through multiple numerical experiments.

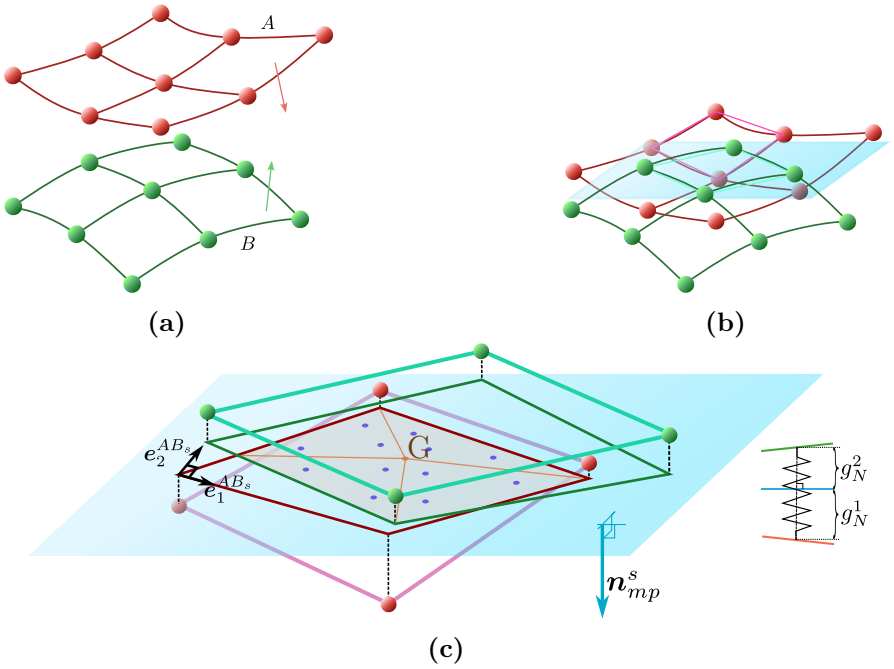

Figure 5.2: (a) Two 9-noded facets approaching each other (arrows show the outward direction from the underlying 27-noded element) to come into contact at potentially 4×4 subfacet-to-subfacet pairs, (b) one highlighted pair of interpenetrating subfacets and the midplane between them, (c) normal projections of the two opposite subfacets over the midplane and the triangulation of the intersection polygon along with the quadrature points in all triangles for traction evaluation. Also shown is the basis for storing frictional traction.

For progressing towards the numerical solution using quadrature points, the integral over the intersection polygon (contact region) between projections of pairs of subfacets over their respective midplanes can be subdivided over all triangles, and integration is performed using the Gaussian quadrature points over each triangle [86][85]. The interpenetration gap between subfacets is evaluated pointwise by finding the physical points on both surfaces having intersections with virtual lines

normal to the midplane for all quadrature points. The gap of each subfacet at quadrature point $\mathbf{x}_q$ can be written as

$$\boldsymbol{g_N}^i(\boldsymbol{x}_m) = \sum_{j=1}^{w^i} \psi_j^i \Big|_{(\xi_1^i, \xi_2^i)} \boldsymbol{x}_j^i - \boldsymbol{x}_m$$
$$\text{where } \left(\xi_1^i, \xi_2^i\right) : \text{Proj}_{\gamma_{\text{mp}}} \left(\sum_{j=1}^{w^i} \psi_j^i \Big|_{(\xi_1^i, \xi_2^i)} \boldsymbol{x}_j^i \right) = \boldsymbol{x}_m, \quad \boldsymbol{x}_m \in \gamma_{\text{mp}} \tag{5.12}$$

where w^i is the number of nodes, and $\mathbf{x}_j^i$ represent nodes on either main facet. The gap vector of interpenetration at each quadrature point $\boldsymbol{x}_q$ can then be written as

$$\boldsymbol{g}_N = \boldsymbol{g}_N^2 - \boldsymbol{g}_N^1 = \sum_{j=1}^{w^2} \psi_j^2(\xi_1^2, \xi_2^2)\mathbf{x}_j^2 - \sum_{j=1}^{w^1} \psi_j^1(\xi_1^1, \xi_2^1)\mathbf{x}_j^1 \tag{5.13}$$

The eq. 5.12 requires a set of parametric coordinates (ξ_1^i, ξ_2^i) on each ith physical facet. While these can be accurately evaluated using an iterative scheme for the nonlinear shape functions of the main facets, an alternative of using the quadrilateral formed by the projection of linearised subfacets is used here. For each quadrature point on the midplane, a pair of parametric coordinates of bilinear interpolation is found with respect to each projected quadrilateral using inverse bilinear mapping [87]. These parametric coordinates are then mapped to the coordinates (ξ_1^i, ξ_2^i) on each physical facet using an affine mapping, as can be seen in [82][78].

This affine mapping from a projection of linearised subfacet to the main facet is an indirect measure and has been depicted in parametric space in Fig. 5.3. As an example, the mapping from parametric coordinates $(u, v) \in ([0, 1] \times [0, 1])$ of subfacet I, to the parametric coordinates $(\xi_1, \xi_2) \in ([-1, 1] \times [-1, 1])$ of the main facet is as following

$$u = \xi_1 + 1, v = \xi_2 + 1 \tag{5.14}$$

The equations of affine mapping for other subfacets with the main facet can be written in a similar manner. Using this affine mapping, the parametric coordinates of physical facets corresponding to the quadrature points can be evaluated. Using the shape functions of the original main facet, the gap (or height) of the physical

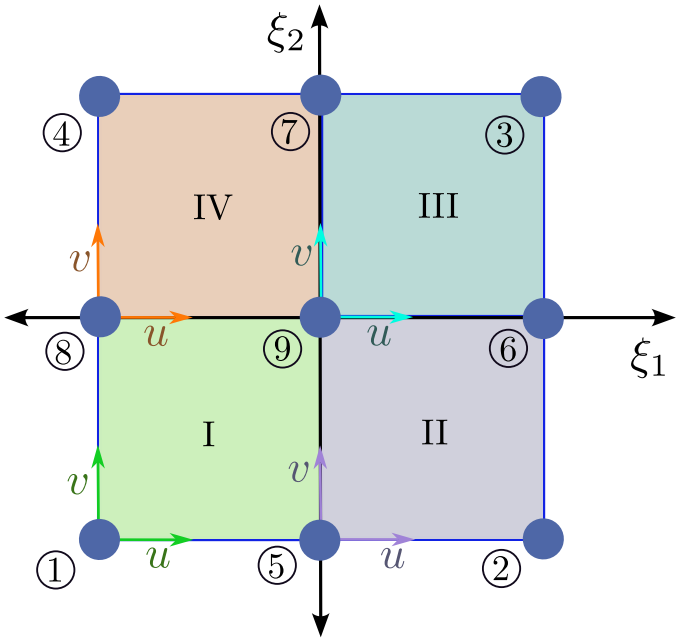

Figure 5.3: Subdivision in the parametric domain for affine mapping between the main facet and its subfacets in case of a 9-noded Lagrangian rectangular facet

facet from the quadrature point can be evaluated. This enables the numerical evaluation of the integral for calculating the nodal forces corresponding to the normal traction using the interpenetration gap.

5.3.2 An additional midplane correction

The construction of the midplane using the subsegments as described previously relies upon the linearised sub-facets that do not carry any information about the curvature of the physical surface. This leads to a poor approximation of the midplane. To improve the accuracy of the solution, the midplane can be corrected by utilising the knowledge of interpenetration between the physical surfaces. The midplane correction fundamentally tries to follow the curvature of the opposite facets corresponding to the centroid of the interpenetration volume. To correct the midplane, an average of all quadrature points weighted by their respective interpenetration gaps is taken to locate the normal projection of the centroid of interpenetration volume over the midplane. As the solution procedure is only affected by the midplane direction and not its position, the midplane can also be assumed to be passing through the centroid itself. Physical points on both surfaces

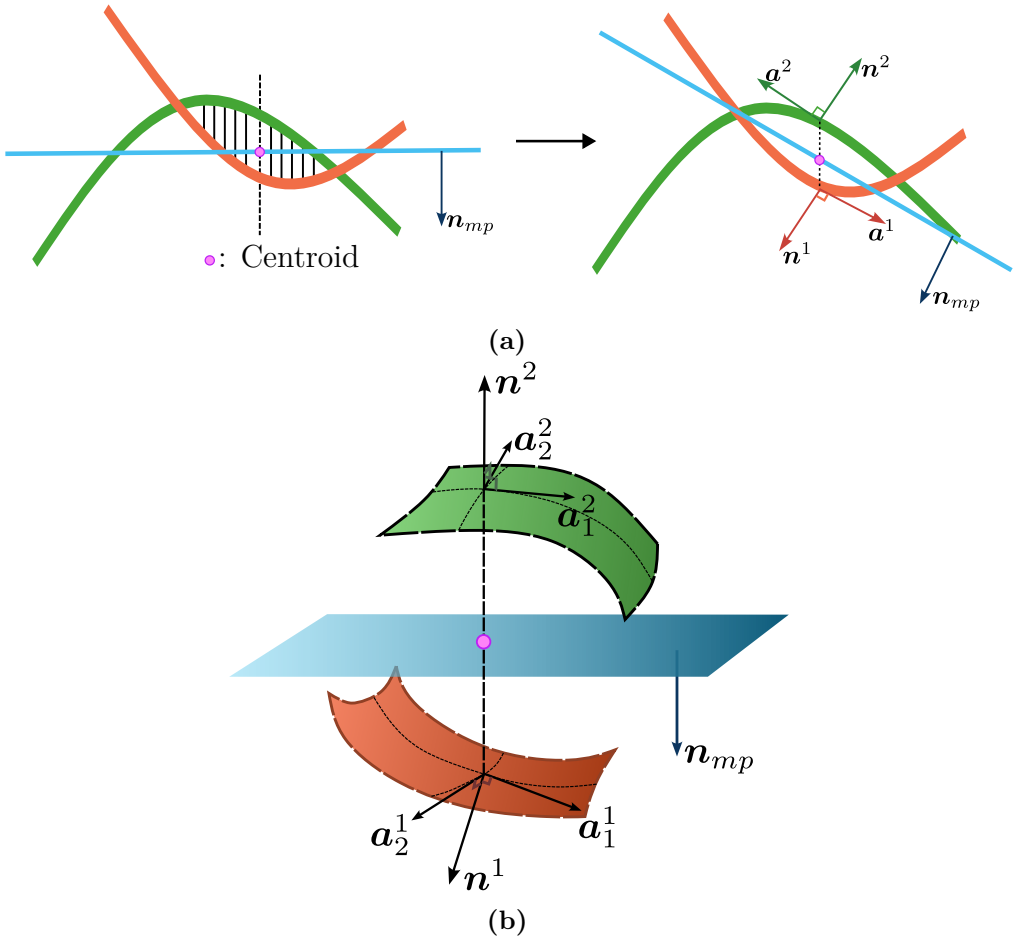

Figure 5.4: Midplane correction procedure: (a) 2D equivalent showing the initial and final midplane direction, (b) illustration in 3D showing the initial midplane direction and the normal to both physical surfaces corresponding to the interpenetration centroid.

corresponding to this centroid are evaluated. The tangents to the parametric lines at both points are utilised to define the normal directions $\boldsymbol{n}^1$, $\boldsymbol{n}^2$ on the two surfaces. A schematic of this procedure is shown in Fig. 5.4 for a 2D equivalent problem and a 3D problem. The updated midplane normal can be written as

$$\boldsymbol{n}_{\text{mp}} = \frac{\boldsymbol{n}^1 - \boldsymbol{n}^2}{\|\boldsymbol{n}^1 - \boldsymbol{n}^2\|} \tag{5.15}$$

This midplane correction can be continued iteratively to further correct the tilt of the midplane, only a single midplane correction has been studied in this work and is influential only for dynamic collision cases.

5.3.3 Unbiased frictional contact

In this work, the frictional contact methodology uses relative sliding between the facets to evaluate the nodal frictional forces in an unbiased manner using the concepts presented in [125]. The frictional effect resisting the tangential motion is also evaluated through the pairwise interaction of subfacets on the interacting boundaries using the predictor-corrector approach. Similar to the use of subfacets for calculating normal nodal forces, the relative motion between the subfacets, about the shared patch of overlap on the midplane, is penalised, and their contribution is added to the nodal forces as frictional forces.

The predicted tangential traction $\mathbf{t}^{\text{trial}}_{T_{n+1}}$ between any pair of subfacets due to relative sliding between solution steps n and $(n+1)$ causing changes in the local parametric coordinates of the centroid of overlap with respect to opposite subfacets is written as

$$\mathbf{t}^{\text{trial}}_{T_{n+1}} = \mathbf{t}^{\text{up}}_{T_n} + \epsilon_T[({}^1\xi^{\alpha}_{C_{n+1}} - {}^1\,\xi^{\alpha}_{C_n})\mathbf{a}^1_{\alpha_{n+1}} - ({}^2\xi^{\alpha}_{C_{n+1}} - {}^2\,\xi^{\alpha}_{C_n})\mathbf{a}^2_{\alpha_{n+1}}] \tag{5.16}$$

where C refers to the centroid of overlap and $({}^1\xi^1, {}^1\,\xi^2)$ are the parametric coordinates of the centroid of overlap with respect to the interpolation of one main facet, and $\{\mathbf{a}^1_{\alpha_{n+1}}, \mathbf{a}^2_{\alpha_{n+1}}\}$ denote the co-variant vectors along the parametric lines of both main facets at the centroid. Alternatively, the tangential traction can also be written using the relative velocity of the two facets at the centroid

$$\mathbf{t}^{\text{trial}}_{T_{n+1}} = \mathbf{t}^{\text{up}}_{T_n} + \epsilon_T[(\mathbf{I} - \boldsymbol{n}_{\text{mp}} \otimes \boldsymbol{n}_{\text{mp}})(\dot{\mathbf{x}}^1 - \dot{\mathbf{x}}^2)\Delta t_{n+1}] \tag{5.17}$$

where $\{\dot{\mathbf{x}}^1, \dot{\mathbf{x}}^2\}$ denote the velocities of the physical point on both main facets corresponding to the centroid of the overlap of both subfacet projections. In the present finite element scheme, this essentially refers to interpolating the nodal velocities of all nodes on the main facets by using their shape functions at the centroid of the overlap of subfacets. This requires evaluating the parametric coordinates (ξ^1, ξ^2) at the centroid for finding the shape functions. While $(\dot{\mathbf{x}}^1 - \dot{\mathbf{x}}^2)$ is the relative velocity in the physical 3D space, its projection over the midplane is considered to

define the relative tangential velocity, and subsequently, the displacement which is penalised for predicting the tangential traction.

The predicted tangential traction $\mathbf{t}_T^{\text{trial}}$ for relative motion between any two subfacets is corrected using the return-mapping algorithm in the friction cone for cases where its magnitude exceeds the limiting friction. The corrected (or updated) traction is

$$\mathbf{t}_{T_{n+1}}^{\text{up}} = \begin{cases} \mathbf{t}_{T_{n+1}}^{\text{trial}} & \text{if } ||\mathbf{t}_{T_{n+1}}^{\text{trial}}|| \leq \mu||\mathbf{t}_{N_{n+1}}|| \\ \mu||\mathbf{t}_{N_{n+1}}||\frac{\mathbf{t}_{T_{n+1}}^{\text{trial}}}{||\mathbf{t}_{T_{n+1}}^{\text{trial}}||} & \text{if } ||\mathbf{t}_{T_{n+1}}^{\text{trial}}|| > \mu||\mathbf{t}_{N_{n+1}}|| \end{cases} \tag{5.18}$$

This tangential traction is applied equally and in opposite directions over the midplane to oppose the relative motion between the two surfaces. To maintain the consistency with the normal nodal forces, the contribution of each subfacet-to-subfacet pair towards the tangential force on the kth ($k = 1, ..., 9$) node in the main facet on one side is written as

$${}^i\mathbf{R}_k^T = \beta\mu||{}^i\mathbf{R}_k^N||\frac{\mathbf{t}_T^i}{||\mathbf{t}_T^i||} \quad , \qquad 0 \leq \beta \leq 1 \tag{5.19}$$

$$\beta = \frac{||\mathbf{t}_T^{\text{up}}||}{\mu\frac{||\Sigma_k \ {}^i\mathbf{R}_k^N||}{A}} \tag{5.20}$$

where μ is the coefficient of friction, $\mathbf{R}_k^N$ is the nodal force on the kth node and $\mathbf{t}_T^i$ is the corrected (or updated) tangential traction in the current solution step. It can be observed in the eq. 5.20 that the predicted-corrected tangential traction provides the direction of frictional forces and indicates the fraction of the limiting friction that acts on the subfacet-to-subfacet pair. It should be noted that the frictional contact between the main facets depends upon the net contribution to the nodal forces by all subfacet-to-subfacet pairs between them, which will all have independent tangential traction calculation.

5.3.4 Error of interpolation

The approximation of subfacets by first-order elements serves two main purposes - (a) defining the midplane for each subfacet-to-subfacet pair and their projections over the midplane to define the contact region (intersection polygon) and (b) finding the

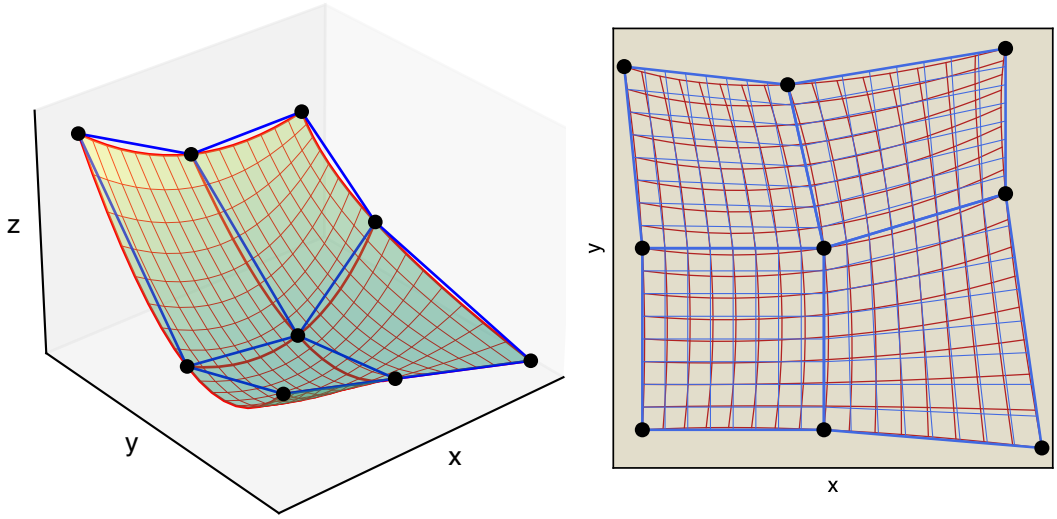

Figure 5.5: Illustration of the cause of error on using bilinear shape functions for finding parametric coordinates of quadrature points on the midplane. (a) A highly distorted 9-noded Lagrangian shell element with parametric lines (red) and linear edges of subfacets (blue), (b) projection of parametric lines (red) of quadratic element over the z=0 plane and the lines of bilinear interpolation (blue) of subfacets. Notice the differences between the parametric lines of quadratic interpolation and bilinear interpolation on projection in (b).

gap between the two physical facets at the quadrature points for contact integral. In the above sections, the affine mapping between the parametric coordinates of bilinear interpolation of subfacets to the parametric coordinates of higher-order interpolation is prone to error due to differences in the straight lines of bilinear interpolation and curved lines of higher-order interpolation. This difference is explained in this section as a potential source of error in the overall contact algorithm that will also help understand the limitations of the similar approach generally seen in the literature [82][78] for higher-order elements.

The physical surfaces formed by first-order and second-order Lagrangian elements in 3D have different mathematical descriptions. While the facets of a first-order element have bilinear interpolation, thereby having an equal spacing between straight parametric lines, the facets of second-order elements have nonlinear interpolation, and the parametric lines are, in general, curved and have unequal spacing between them. Similarly, when the projections of both first-order subfacets and the higher-order main facet over the midplane are considered, the discrepancies in their

parametric lines are evident. At each quadrature point in the contact region, the normal gap requires finding the points on opposite main physical facets that normally project over the quadrature point. However, using first-order subfacet and the subsequent affine mapping results in an error when evaluating the parametric coordinates of the required point on the physical facets. This eventually leads to inaccuracies in the contact integral and the evaluated normal nodal forces. The discrepancies in the parametric lines of the projections of higher-order interpolation and the first-order interpolation are illustrated in Fig. 5.5. Intuitively speaking, if the bilinear interpolation was used on the quadrilateral formed by the four corner nodes of the main facet, there would be an even stronger disparity between its parametric lines and the quadratic parametric lines. It also shows that the four subfacets, with their linear nature, cannot capture the curvature of the main facet at their edges, which also adds to the error in the contact region evaluation.

5.4 Solution algorithm

For computational implementation and numerical solution of any multibody contact problems, the solution schemes generally progress in two stages - spatial search and contact detection. The spatial search is the first stage where intersections between the bounding boxes confining solids are utilised to form a first list of spatial pairs between solids. Using a two-tier approach, the list of potential contacting body pairs is initially formed for the solids with intersecting bounding boxes. Subsequently, a list of potential contacting main facet pairs is formed by running a search algorithm to find main facet pairs with intersecting bounding boxes. This list also includes potential contact pairs on the same body, thereby accounting for any possibility of self-contact. For the sake of simplicity, a case of 2-dimensional (2D) contact between facets with Lagrangian interpolation is shown in Fig. 5.6. Similar bounding boxes are considered in a 3-dimensional case (3D), and all possible 4×4 subfacet-to-subfacet pairs are tested for interpenetration between them. Using this two-tier contact interaction enables better accounting of the curvature of the interpolated facet and its impact on the evaluated traction.

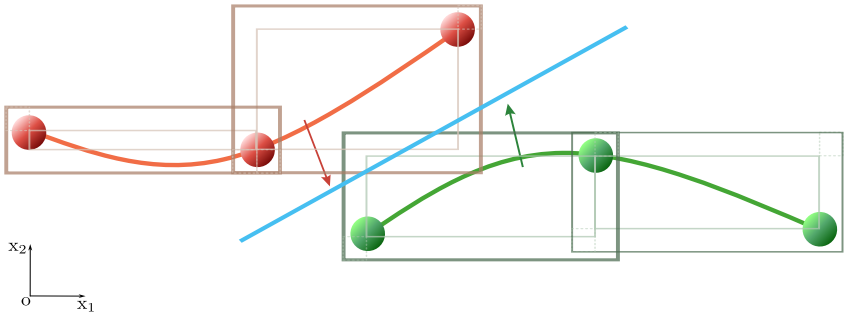

Figure 5.6: Contact search between two Lagrangian interpolated quadratic facets using bounding boxes around all subfacets.

For contact detection between main facets that confirm interpenetration, the decomposed versions of the main facets in the form of their respective four subfacet are considered to detect contact between subfacet-to-subfacet pairs. Firstly, the intersection between the bounding boxes over the subfacets is considered to reduce the potential subfacet-to-subfacet pairs. The bounding boxes used in this work are axis-aligned and are expanded along each dimension by a small amount to confine the possible curvature effect of the main facets. The subfacet-to-subfacet pairs with intersecting bounding boxes are then run through a series of contact checks to confirm any geometrical interpenetration between them. These geometrical checks over first-order approximation of subfacets progress in the same manner as the interpenetration checks for the contact between solids discretised by first-order elements, as presented in [108] using the clipping algorithm[55] over midplane for defining the contact region for each subfacet-to-subfacet pair.

The subfacet pairs with well-defined contact regions (intersection polygon) are considered for contact traction evaluation using the penalty method based on contact constraint enforcement. Firstly, the normal traction is evaluated for interpenetrating subfacet pairs, and subsequently, the history-dependent frictional traction is calculated for relative motion between the subfacets. The steps involved in these calculations are shown in the Algorithm3. While the pairs of subfacets are taken into account, the effect of traction over any subfacet results in forces over all nodes due to the mathematical nature of the nonlinear interpolation of higher-order element facets.

One important thing to note is that the distribution of nodal forces, following the nonlinear mathematical description of the finite elements, might result in the direction of nodal forces being outside the facets (i.e. appearing to be opposite to the compressive nature)[70]. These nodal forces, in both their magnitude and direction, are dependent upon the behaviour of all the shape functions of the element that are used in the integral process. These are, however, consistent with the mathematical behaviour of elements to bring out the compressive effect on the displacement of the finite elements. In this regime of nonlinear elements, these nodal forces do not give an intuitive understanding of the traction direction. But, the stress states generated inside the elements are consistent with the traction direction, and their extraction onto the surface is a better representation of the traction.

5.5 Case of serendipity elements

While this paper focuses on second-order Lagrangian elements for concept description and validation through experiments, the presented methodology can also be extended to serendipity elements by using a virtual node on the 8-noded serendipity quadratic facet to subdivide it into four subfacets. By considering the point in the parametric centre $(\xi_1, \xi_2) = (0, 0)$ of the 8-noded quadratic facet, a physical point on the 8-noded facet can be located ($\mathbf{x} = \sum_{i=1}^{8} \mathbf{x}_i \psi_i(\xi_1 = 0, \xi_2 = 0)$) using the serendipity shape functions. This virtual node will serve as the central node, similar to the case of the 9-noded facet in the Lagrangian element. With such a division, the contact methodology developed for the Lagrangian element can be directly applied here. Here, the similar use of the first-order subfacets will determine the midplane and contact region through the intersection polygon for maximum 4×4 subfacet-to-subfacet pairs. The main difference will be the change of shape function matrix in the eq. 5.10, replaced by eight shape functions of the serendipity rectangular element. The use of a virtual node for the purpose of surface subdivision to form the subfacet pairs will not impact the integral as only forces on the physical nodes will be applied, thereby being consistent with the mathematical nature of the facet. This use subdivision is in contrast to the subdivision procedure of [82][78] as it can

Algorithm 3 Contact constraint enforcement in normal and tangential direction for each subfacet-to-subfacet pair

get the polygon of the intersection of projections of opposite subfacets approximated by first-order interpolation
triangulate the intersection polygon using edges and its centroid
find the area of all triangles
set $[\Psi_q V_{encl}]_i = 0$
for each triangle **do**
    for each quadrature point **do**
        locate this quadrature point on this triangle using its physical coordinates [85, 86]
        find the parametric coordinates $({}^i u, {}^i v)$ for this quadrature point w.r.t both projected quadrilaterals using inverse bilinear mapping[87]
        Use the affine mapping (e.g. eq. 5.14 to find the corresponding pair of parametric coordinates $({}^i\xi_1, {}^i\xi_2)$ of higher-interpolation of main facet
        find the physical points on both facets at this quadrature point using the parametric coordinates
        find the signed gaps g_N^1 and g_N^2 of both physical facets with respect to this quadrature point on the midplane
        find the interpenetration gap $g_N (= g_N^1 + g_N^2)$
        if $g_N < 0$ **then**
            continue to the next quadrature point as there is no interpenetration
        else
            update the quantity $[\Psi V_{encl}]_i$ for both facets by taking contribution from this quadrature point.
        end if
    end for
end for
calculate the normal forces $\epsilon_N [\Psi_q V_{encl}]_i$ on each node of both main facets, with the direction being decided by the midplane
find the parametric coordinates and shape functions of higher-order interpolation at the centroid of overlap using the affine mapping
find the relative velocity between the centroid using the shape functions of nodes on both main facets
using the current time-step increment and the midplane, find the predicted (eq. 5.17) and corrected tangential traction (eq. 5.18)
calculate the frictional nodal forces using eq. 5.20

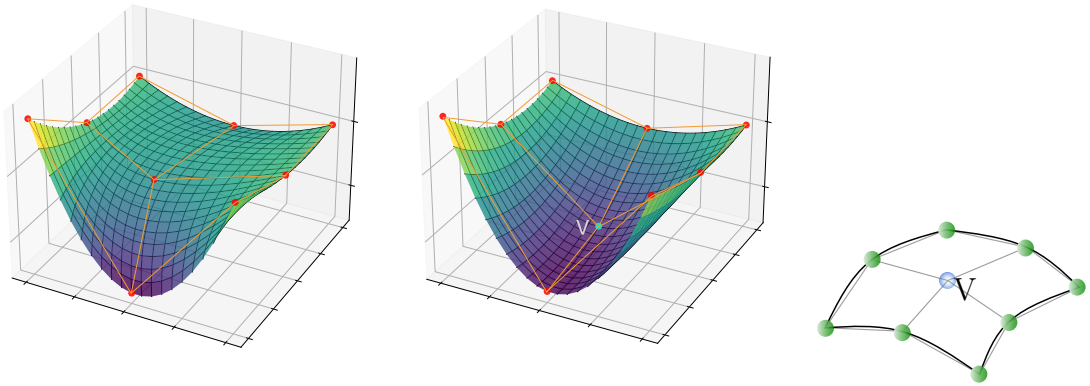

Figure 5.7: (a) Comparison of subdivision of 9-noded Lagrangian and 8-noded serendipity facet, and (b) schematic for facet subdivision of 8-noded serendipity facet using a virtual node at the parametric centre of the physical facet.

better capture the local curvature, see Fig. 5.7a for visualisation of facets with exaggerated distortion having same first eight nodes. The 9-noded facet has just one extra node that changes the surface curvature drastically.

Similar to the case of second-order Lagrangian element, the use of approximating subfacets with first-order interpolation and the mapping between subfacets and physical facets will also induce error in the solution due to the discrepancies in the alignment of the parametric lines of both main facets and subfacets.

5.6 Numerical experiments

The unbiased contact methodology for higher-order elements proposed in this work is studied for its robustness and superiority over first-order elements through multiple examples presented below. Here, the primary objective is to demonstrate the advantage of having higher-order discretisation of the original domain in terms of the accuracy of the solution. Standard benchmarks of contact between flat and curved surfaces through contact patch test and Hertzian contact, respectively, are presented for comparison. The contact pressure variation in Hertzian contact is compared for its smoothness against first-order discretisation. Both of these tests and frictional sliding are conducted in a quasi-static manner using the dynamic relaxation technique. Further, cases of dynamic contact are studied through collision

between spherical balls, and a comparison is made with first-order elements. For the contact integral, 13 Gauss points are used over each triangle to evaluate contact forces. The midplane correction is only applied in dynamic collision problems, as it has relatively no effect on quasi-static problems.

5.6.1 *Contact patch test*

This test checks the robustness of the contact algorithm to transfer uniform contact pressure between two flat surfaces with frictionless contact. Consider two rectangular blocks with the same geometrical size of $20 \times 20 \times 10$ mm^3 but different discretisation using 27-noded Lagrangian hex elements with varying sizes to have strong contrast in their discretisation throughout the contact interface; see Fig. 5.8. The Young's modulus of elasticity and Poisson's ratio for the upper and lower blocks are ($E_1 = 10$ GPa, $\nu_1 = 0.3$) and ($E_2 = 100$ GPa, $\nu_2 = 0.35$), respectively, and a scaling factor of $f_s = 10$ is used in the contact definition. The top surface of the upper block is pressed downwards by 0.01 mm, while the lateral surfaces of both upper and lower blocks are restricted against motion in their respective normal directions. The distribution of the vertical stress σ_{zz} extrapolated to the corner nodes, and the result of the element patch test using just the upper block mesh are also shown in Fig. 5.8. While theoretically, the same values of stress will be expected throughout the domains in both the contact patch test and the element patch test, the numerical implementation of the finite element scheme introduces machine errors in the solution. However, as can be observed with the digits in the range of stress values, the precision of the contact patch test is nearly the same as the accuracy of the element patch test. So, a direct conclusion can be made that the presented contact algorithm for contact between flat surfaces performs as accurately as the elements underneath the surfaces of contacting bodies.

5.6.2 *Hertzian contact*

In this classical test based on the Hertzian contact theory[6], two cylindrical bodies are loaded against each other frictionlessly under plane strain assumption. The

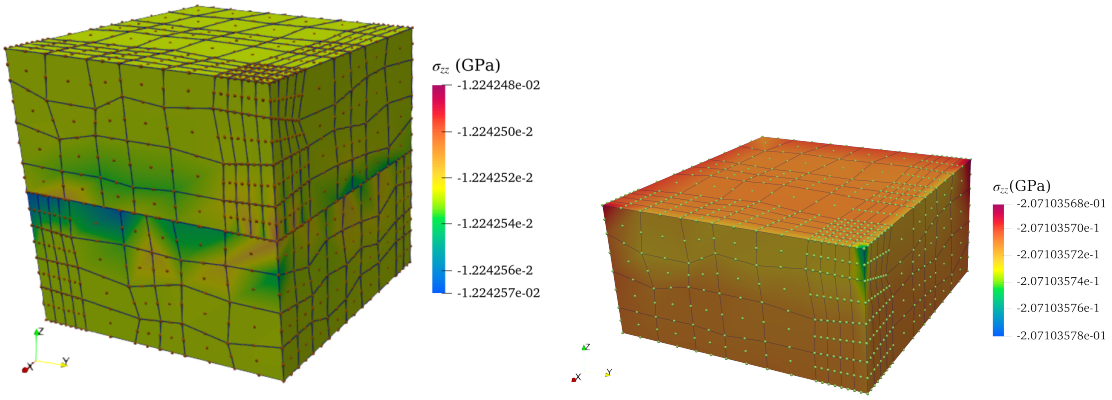

(a) **(b)**

Figure 5.8: (a) Contact patch test with two blocks arbitrarily discretised using second-order Lagrangian elements, and (b) element patch test by just using the upper block in the contact patch test.

contact pressure theoretically follows an elliptical (or ellipsoidal in 3D) profile, maximum at the central point and vanishing at the periphery of the contact region. Consider two isotropic elastic bodies as quarter parts of two cylinders with radii R_1 = 200 mm and R_2 = 250 mm, respectively, and having Young's modulus and Poisson's ratio as E_1 = 10 GPa, ν_1 = 0.3, and, E_2 = 1000 GPa, ν_2 = 0.35, respectively, see Fig. 5.9a.

The boundary conditions over the geometries for adhering to the plane strain assumption are as follows: the bottom surface of the lower cylinder is restricted against motion in the vertical direction but allowed to expand horizontally. The surfaces at planes of vertical symmetry and front and back flat surfaces are restricted against motion in their normal directions. The top surface of the upper cylinder is pressed downwards by applying a uniform pressure that corresponds to the case of actual full cylinders having a line loading of P= 9 kN/mm.

Four kinds of discretisations are considered in this experiment, two types each for 8-noded first-order and 27-noded second-order hex elements, such that there are two pairs of first-order–second-order discretisations having the same nodes and just different connectivities for defining the elements, see Fig. 5.9. In other words, if all elements in each mesh of second-order discretisation are subdivided into eight first-order elements, the corresponding mesh of first-order elements can be

obtained. While both first and second-order element meshes have the same number of nodes, the mathematical description of second-order elements will preserve the curvature of the original geometry. In contrast, first-order elements will have linear boundary facets with non-smooth variation of surface normal. This difference in mathematical description is being studied in this experiment to examine the variation in the contact pressure using different types of elements but the same number of nodes, thereby, the same number of degrees of freedom. For strong contrast in non-conformal meshes at the contact zone between the two cylinders, subdomains of both bodies near the interface are discretised with different sizes of elements, as shown in Figs. 5.9b, 5.9c, 5.9d, and 5.9e.

The variation of the contact pressure for both types of elements and discretisation ratios with $f_s = 10$ by directly using the subsurface quadrature points inside elements and their locations are shown in Fig. 5.10. For first-order elements, the smaller mesh ratio of 12:22 with less non-conformity provides relatively smoother contact pressure variation compared to the higher ratio of 8:22, where the oscillations are significant. This increase in the oscillations is a consequence of the stronger influence of the non-smooth nature of the first-order elements with a higher mesh ratio. On the other hand, the use of second-order elements not only provides a smoother variation of contact pressure for the mesh ratio of 6:11 compared to first-order meshes having the ratio of 12:22, but its use for the higher contrast in mesh ratio of 4:11 is also relatively better compared to its first-order counterpart of mesh ratio 8:22. The increased anomaly in the contact pressure in the outward contact region, on moving from mesh ratio 6:11 to 4:11, is a result of the discrete nature of the finite elements and consideration of a flat midplane for each subfacet-to-subfacet pair. Nevertheless, if the contacting meshes have a higher contrast in the sizes of elements coming into contact, the use of second-order elements provides a better solution compared to the first-order elements. This benefit results from the second-order elements being able to describe the curved physical surface, which gets accounted for in the interpenetration and its subsequent penalisation in the normal traction evaluation. The second-order contact problem shown in Fig. 5.10d

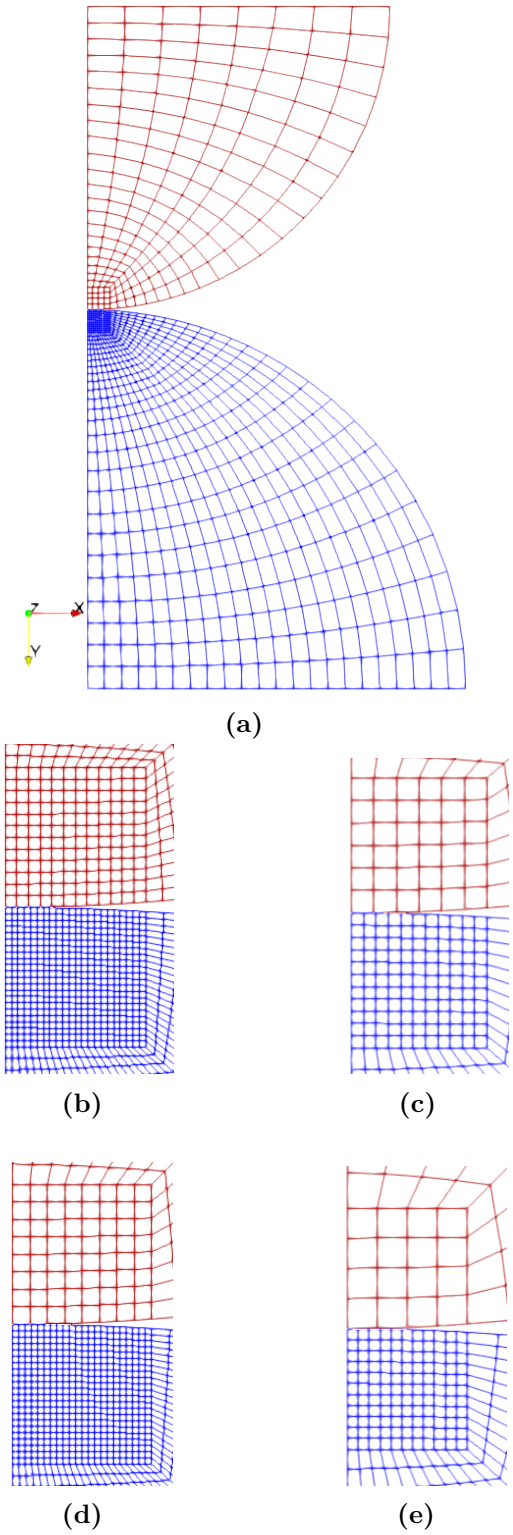

Figure 5.9: Hertz contact: (a) Discretised cylinders with mesh ratio 4:11 near contact region, and the meshing scheme near the contact region for discretisation in (b) First-order elements with mesh ratio 12:22, (c) Second-order elements with mesh ratio 6:11, (d) First-order elements with mesh ratio 8:22, and (e)Second-order elements with mesh ratio 4:11.

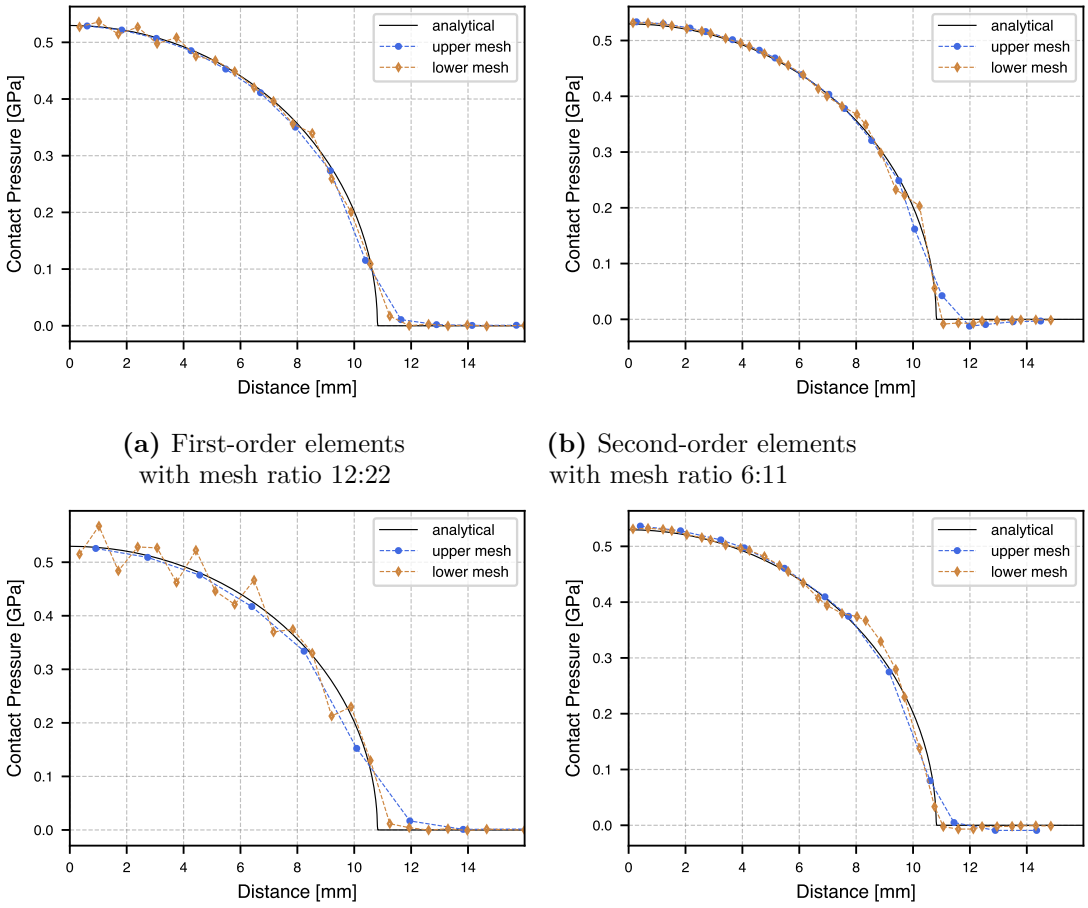

(a) First-order elements with mesh ratio 12:22

(b) Second-order elements with mesh ratio 6:11

(c) First-order elements with mesh ratio 8:22

(d) Second-order elements with mesh ratio 4:11

Figure 5.10: Hertzian Contact: Contact pressure variation between meshes discretised using first-order elements (a, c) and second-order elements (b, d) with both cases having the same number of degrees of freedom in the system and $f_s = 10$ in all cases. Observe that even though when the coarser upper mesh is used, the second-order mesh does not have oscillations like the first-order mesh.

was also tested with additional midplane correction; however, the resulting contact pressure variation showed no improvement in this quasi-static test.

For testing effects of softer penalties, the same meshes with second-order discretisation are also studied for $f_s = 1, 5$, and their plots are shown in Fig. 5.11. As can be seen, using a softer penalty with $f_s = 1$ provides a relatively smoother solution; however, it is at the cost of increased interpenetration, thereby inaccurately predicting a larger contact zone. The smoothness is a result of the increased interpenetration that attenuates the influence of the discrete nature of finite element

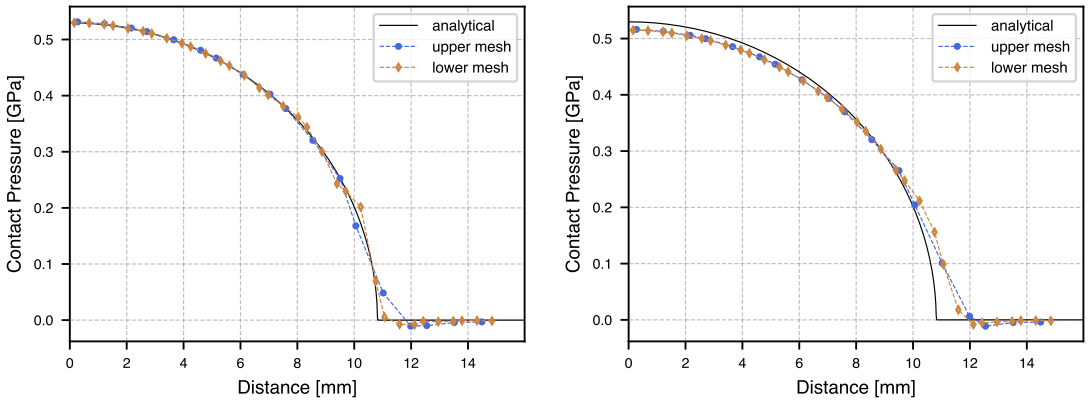

(a) Mesh ratio 6:11, fs = 5

(b) Mesh ratio 6:11, fs = 1

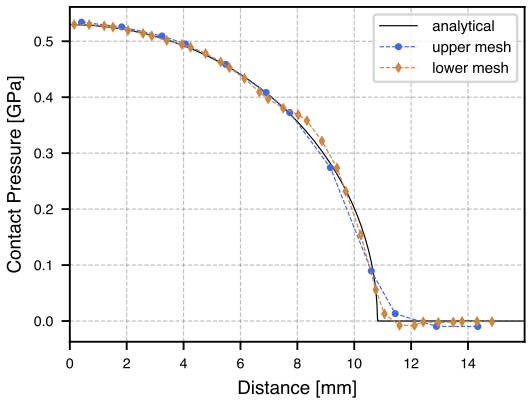

(c) Mesh ratio 4:11, fs = 5

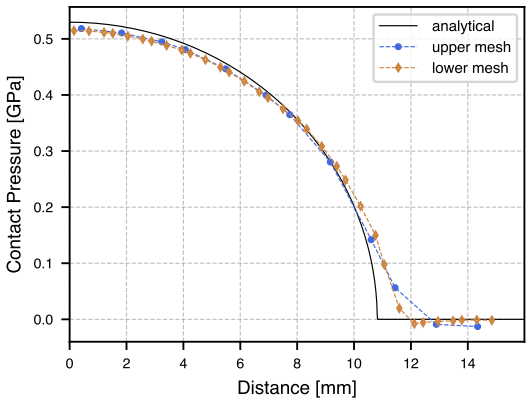

(d) Mesh ratio 4:11, fs = 1

Figure 5.11: Hertzian Contact: Contact pressure variation for only second-order discretisation for different mesh ratios and penalty scaling factors.

contact pairs; see the Fig. 5.12 where mid edge nodes are ignored for simplicity and line segments directly connecting the corner nodes are shown. With softer penalties, the rate of change in the gap along the contact interface between meshes is smaller, so the effect of changes in discrete element features is less pronounced.

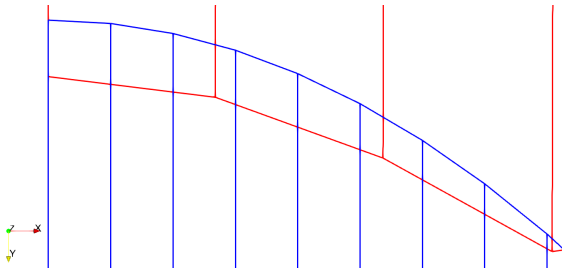

Figure 5.12: Interpenetration between second-order element mesh with ratio 4:11 and $f_s = 1$, shown by vertically scaling the meshes by a factor of 20 to highlight the gap.

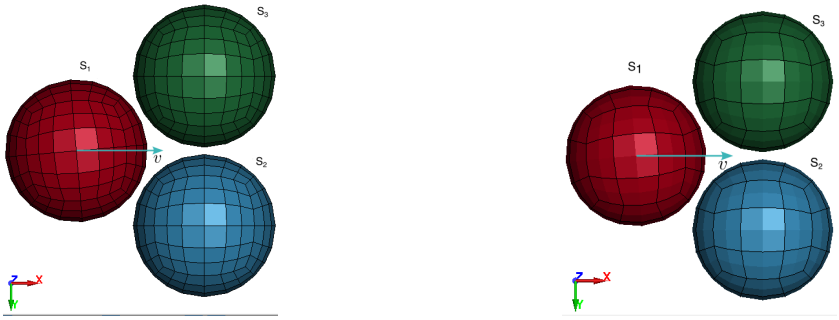

(a) (b)

Figure 5.13: Two meshes having same nodes used in collision for (a) first-order elements, and (b) second-order Lagrangian elements

5.6.3 *Elastic collision of spheres*

In this test of frictionless elastic collision between spherical solids, two cases are considered for comparing first-order and second-order Lagrangian elements. In each case, the two types of discretisation schemes have the same nodes, with the only difference being their connectivity for defining the elements. Their different shape functions lead to differences in the physical surface descriptions. So, they both have the same degrees of freedom. All the spherical bodies used in this section have a radius of R = 10 mm, Young's modulus of elasticity, E = 100 GPa, Poisson's ratio $\nu = 0.3$, density $\rho = 0.1$ kg/mm^3, and for contact definition, scaling factor is $f_s = 1$. Both cases demonstrate that preserving the original curvature of the surface using second-order elements aids in correctly timed contact detection and subsequent constraint enforcement.

Ball striking against symmetrically placed balls

In the first case, three balls are placed in a triangular arrangement, as shown in Fig. 5.13. While the orientations of the discretised balls S_2 and S_3 are the same, the ball S_1 is rotated by 5° about z-direction to induce a lack of symmetry in the discretised setting of the system. While the physical surfaces in the case of second-order elements will be able to capture the curvature, the case of first-order elements will have a discrepancy with the actual surface and a loss of material in the physical space.

The ball S_1 is given a velocity of 0.1 m/s to collide with the two symmetrically placed balls S_2 and S_3. The time-based changes in momentum in the x and y directions for three different types of discretisations are shown in Fig. 5.14. Numerous observations can be made here on how the surface description discrepancy between first-order and second-order elements influences changes in momentum. Firstly, the initial momentum of the ball S_1 is slightly lower in the case of first-order elements compared to second-order elements as they suffer from material loss due to their straight edges being unable to capture the curvature. The collision in the case of first-order elements is also slightly delayed due to the loss of surface material, hence delayed detection, as can be seen in all plots in p_x and p_y. For original spherical geometry, the same momentum p_x will be expected for balls S_2

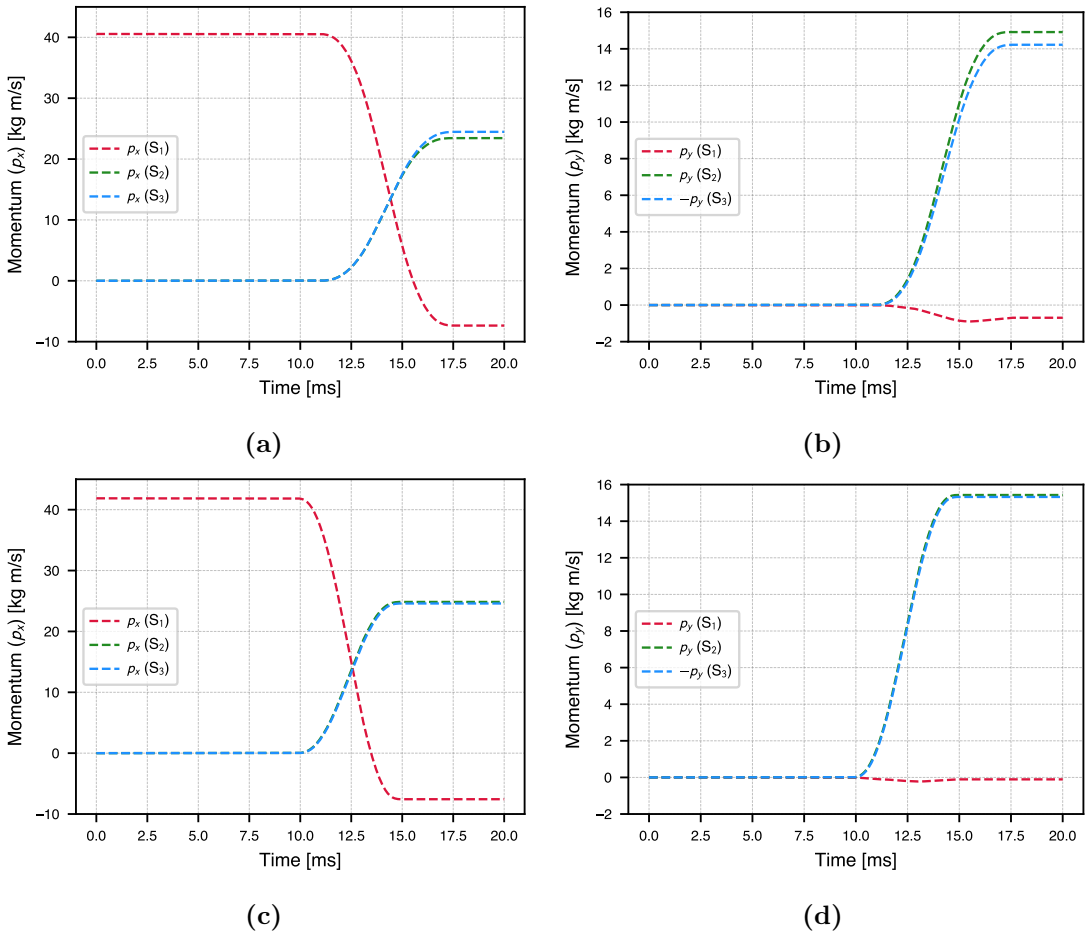

Figure 5.14: Symmetric collision of balls: Variation of net momentum of three balls along the x-direction (a,c) and the y-direction (b,d) for first-order elements (a,b) and second-order Lagrangian elements (c,d).

and S_3; however, due to higher discrepancy from the original geometry, first-order discretisation has a higher discrepancy in p_x. Although second-order elements capture the original curvature, the consideration of finite-sized contact pairs with their respective flat midplanes causes a slight difference in p_x. Nonetheless, it is very small compared to the first-order elements. The same reasoning can also be extended to explain the differences in momentum p_y in both cases where the balls S_2 and S_3 gain similar momentum upon collision in the case of second-order elements with a stark contrast to the error in the use of first-order elements.

Successive collision in an array of balls

In the second case, inspired by Newton's cradle, ten spherical bodies are arranged with a uniform gap of 0.5 mm between them as shown in Fig. 5.15a. Each ball is rotated by 5° about the z-axis with respect to the ball on its left. The ball S_1 is given a velocity of 0.1 m/s and collides head-on with S_2, and the motion is transferred to subsequent balls on respective collisions. The changes in the momentum p_x and p_y are shown in Fig. 5.15 where it can be observed that the momentum p_x is transferred from ball S_1 to the last ball S_10 with successive collisions. The twin benefits of using second-order elements can also be noted here. Firstly, all collisions are quicker in second-order elements with a better representation of curvature, and the error in timing increases until the last collision. Secondly, the error in momentum due to the motion gained in the lateral direction (p_y) is much smaller with the use of second-order elements, so it provides superior accuracy.

5.6.4 *Frictional sliding: Block sliding against a slab*

The frictional interaction capability of the proposed contact algorithm is studied here by sliding a deformable block against a rigid slab. The rectangular block of size $5 \times 5 \times 10$ mm^3 consists of an isotropic elastic material with Young's modulus, E= 207 GPa, Poisson's ratio of, $\nu = 0$, and the contact definition between both bodies has a coefficient of friction, $\mu = 0.3$, and the tangential penalty, $\epsilon_T = 10$ GPa/mm. Its top surface is uniformly displaced downwards by 6×10^{-3} mm against

a rigid slab of size $9 \times 25 \times 50$ mm^3 while keeping the scaling factor, $f_s = 1$. It is pushed forward while maintaining the downward push before being returned and held at its original position, thereby completing a full loop, see Fig. 5.16a. The components of the net force on the contacting surface of the block are shown in Fig. 5.16c where it can be observed that the normal force (F_z) increases during the pressing of the block and stays constant during the sliding. On the other hand, the frictional force (F_x) starts increasing in the backward direction during the forward

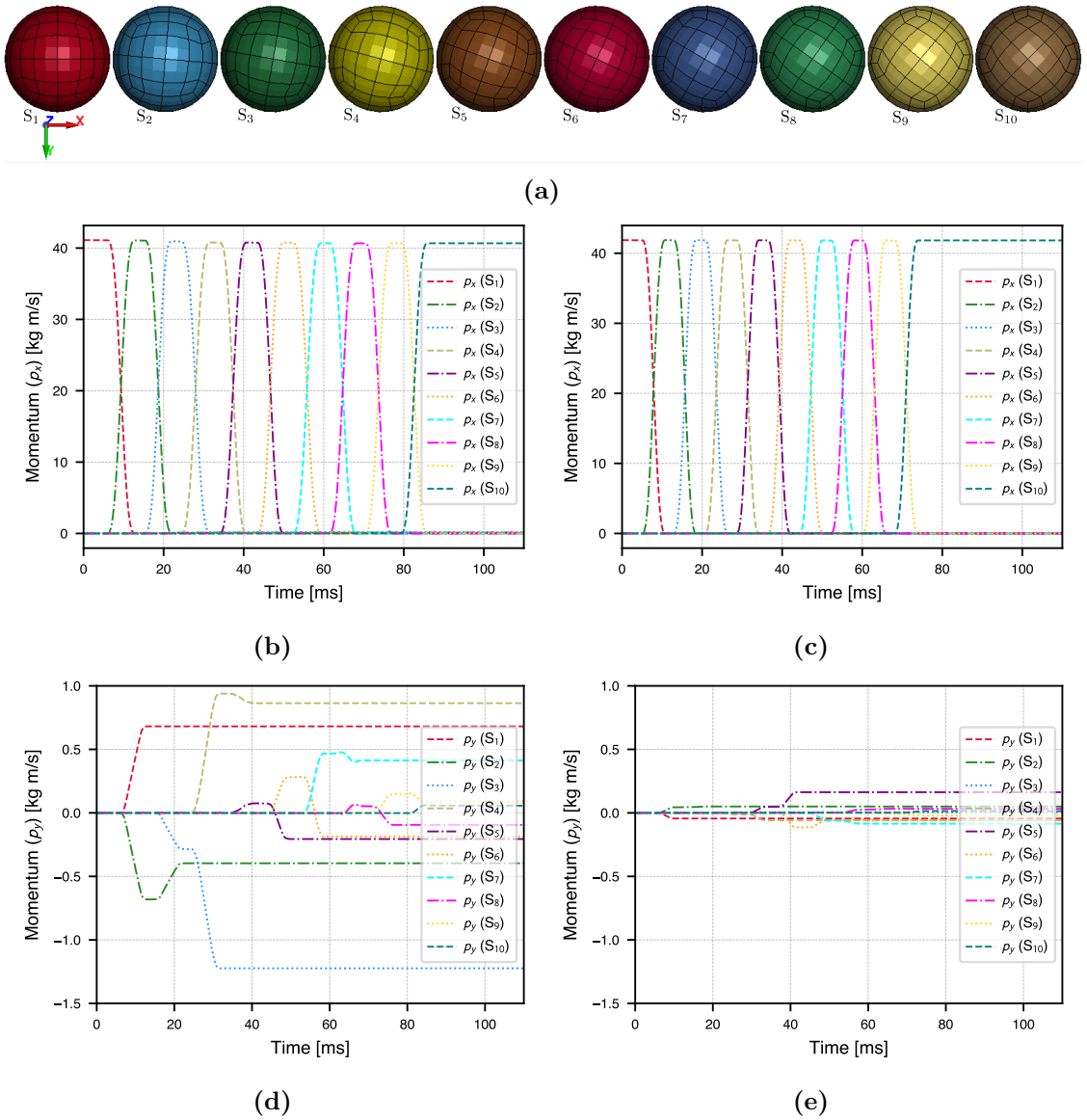

Figure 5.15: Successive head-on collision of 10 balls: (a) configuration of spheres, (b,c) momentum variation p_x in first-order elements, and (d,e) momentum variation p_y in second-order elements.

push on the block and stays constant once it reaches the limiting value. As soon as the backward push is initiated on the block, the frictional force, acting backwards, starts diminishing and losing the traction retained from the plastic effect before increasing in the forward direction and staying at the limiting value. Due to the history of dependency on friction and retention of the tangential traction during sliding, the block retains the frictional forces in the contact region at the end of sliding when the top surface of the block is brought to its original position. The nodal forces acting on the top surface of the block to maintain its position and the contact forces that include the frictional effect are shown in Fig. 5.16b. Notice the distribution of the nodal forces follows the mathematical behaviour of traction distribution over second-order Lagrangian elements.

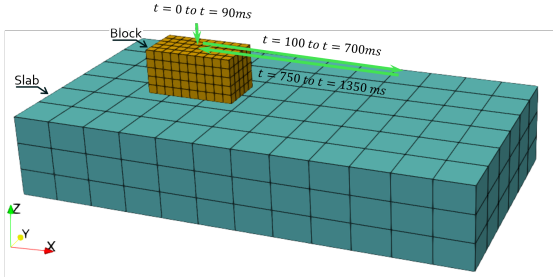

(a) Mesh with boundary conditions

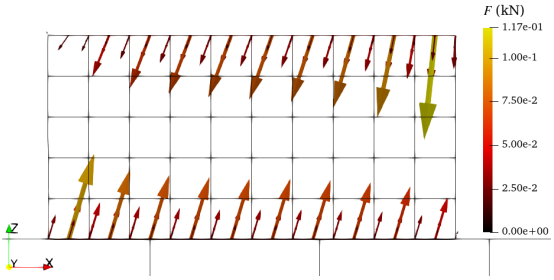

(b) Nodal forces at the end of sliding

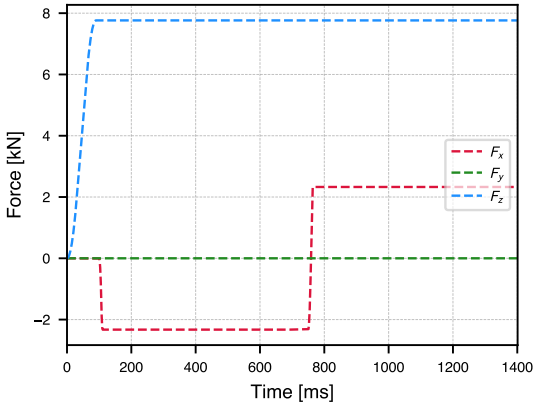

(c) Variation of net forces along x,y, and z directions with time

Figure 5.16: Frictional sliding, with a block being first pressed against a slab and then taken in a to-and-fro motion along it. The retention of frictional force (F_x) in (c) at the end of sliding shows the hysteresis effect due to the elasto-plastic analogy of friction.

5.6.5 *Frictional self-contact*

A self-contact test with frictional effect is performed to emphasise the auto-detection of contact between surfaces of a single body along with contact constraint enforcement. This test is studied with both Hex27 and Hex8 elements with the same nodes in the discretised body in the originally undeformed configuration having size $200 \times 200 \times 50$ mm^3, see Fig. 5.17a. The original body discretised with Hex27 elements is shown in Fig. 5.17b. Its counterpart for first-order elements is obtained by discretising each element in this mesh into eight Hex8 elements, thereby having the same nodes in the two meshes. While the second-order elements have smooth surfaces at all circular surfaces, first-order elements have nonsmooth surfaces at element corners. In both cases, isotropic elastoplastic material with linear hardening is used. It has Young's modulus, E= 10 GPa, Poisson's ratio $\nu = 0.3$, initial yield stress $\sigma_{y_0} = 1.0$, and hardening modulus H= 0.1 GPa. The bottom surface of the block is held fixed while the top surface is prescribed downward displacement by 62.5 mm. For contact definition, the coefficient of friction is $\mu = 0.4$, the normal penalty scaling factor is $f_s = 10$, and the tangential penalty factor is $\epsilon_T = 10$ GPa/mm, and three gauss points per triangle are used in the contact integral. The continuous deformation leads to gradual self-contact between different parts of the surfaces. The deformed configuration for discretisation with Hex27 elements is shown in Fig. 5.17c overlayed with nodes of both first-order and second-order discretisation. As can be seen, the nodes in the two types of discretisation have position differences around the circular surfaces. This is a result of the differences in first-order and second-order surface representation.

5.6.6 *Inelastic collision of two bars*

In this example of high-rate deformation, two bars with the same original geometry collide axially at the same very high speed, which should ideally result in a flat interface of contact upon deformation as seen in symmetric Taylor's impact test. Here, both first-order and second-order elements are used to discretise the two bars such that they both have the same nodes in the undeformed meshes and the

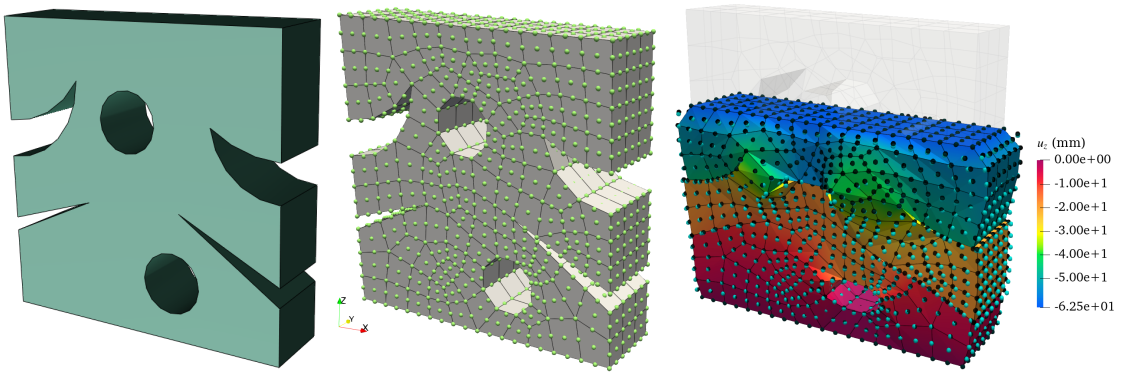

Figure 5.17: Self-contact test: (a) original undeformed geometry, (b) mesh used for Hex27 elements, and (c) deformed mesh along with nodes of both Hex27 (black) and Hex8 (cyan) discretisations. Note that straight edges connecting the corner nodes shown here are a limitation of visualisation, however, the nodal positions are accurately visualised.

two meshes are non-matching, as shown in Fig. 5.18. Both bars are made of the same elastoplastic material with linear hardening having Young's modulus E = 69 GPa, Poisson's ratio $\nu = 0.33$, initial yield stress $\sigma_{y_0} = 0.276$ GPa, and hardening modulus H = 0.2 GPa. Their maximum dimensions are $10.5 \times 1 \times 1$ mm^3, and axial speed is 320 m/s towards each other. Both bars undergo continuous deformation upon collision, with the region near the interface undergoing plastic deformation. The deformed configuration of the two bars is shown in Fig. 5.19 for both first-order and higher-order discretisations. As can be observed, the deformation in the case of first-order discretisation results in a mismatch in the two bars at the interface, with the right mesh bulging outwards. On the other hand, second-order elements have a relatively flat interface in the contact region upon deformation. Only one side view is shown here to highlight the differences in contact region deformation due to curved surfaces in the original geometry. Also, the overall dimensions of the two deformed meshes are different in both cases. While the two undeformed bars have mismatching element sizes, the second-order elements retain the original curvature, whereas the first-order elements have differences. This difference also results in differences in the overall masses of the two bars, thus adding to the asymmetry in the net momentum exchange.

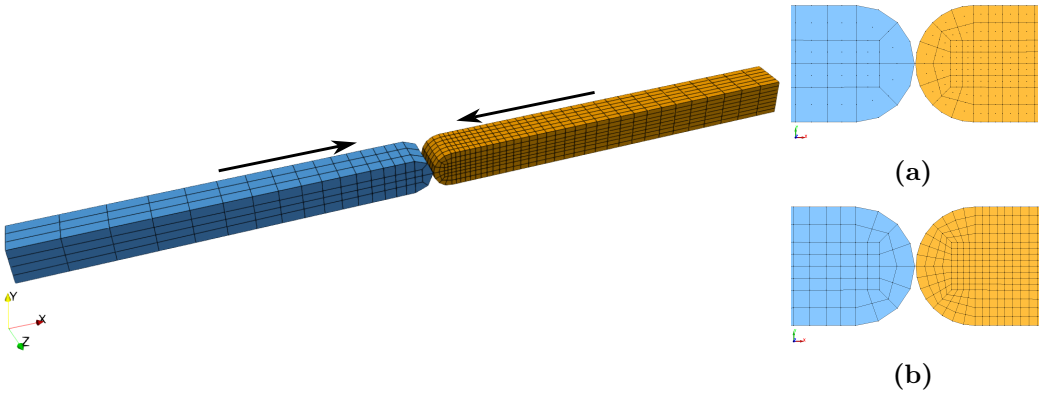

Figure 5.18: Inelastic collision: (a) two bars with Hex27 discretisation moving towards each other, (b) contacting part of the mesh with Hex27 discretisation, and (c) contacting part of the mesh with Hex8 discretisation. Segmented straight edges in Hex27 mesh are only for visualisation.

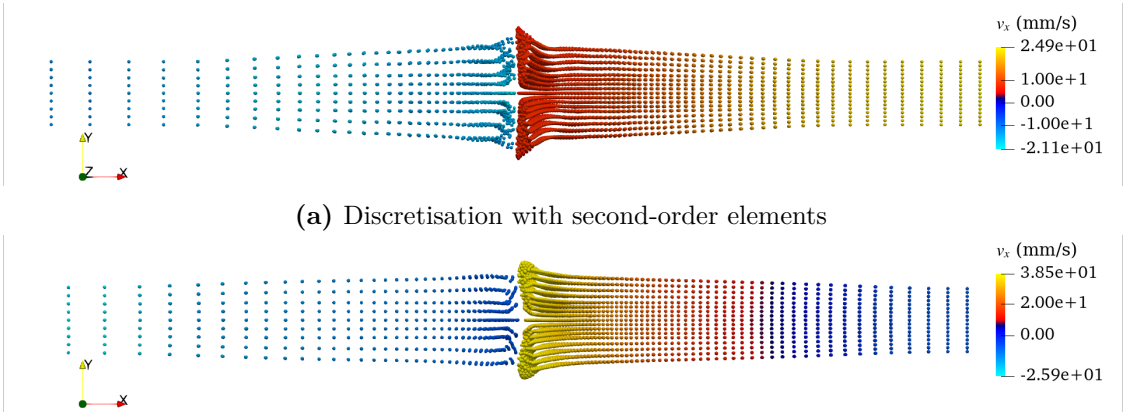

(a) Discretisation with second-order elements

(b) Discretisation with first-order elements

Figure 5.19: Inelastic collision: Comparison of deformed configurations with only nodes shown for two types of discretisation at time $t = 0.02$ ms.

5.7 Conclusion

In conclusion, this paper has proposed a frictional contact formulation for higher-order elements that can comprehensively outmatch the accuracy of first-order elements in both static and dynamic contact. Penalty method-based contact constraints are enforced on a midplane between pairs of subfacets obtained by subdividing the contacting facet pair. This subdivision allows the application of normal and tangential constraints on a refined region of the otherwise complex topology of facets. Unlike first-order elements, the midplane in second-order elements can be corrected to follow the curvature of interpenetrating regions of the subfacets

by accounting for the surface normals corresponding to the interpenetration centroid. While this midplane correction is critically important in gaining high accuracy in dynamic events like collisions, it did not have a similar benefit for static cases of Hertzian contact. The affine mapping between a main facet and its subfacets incurs errors due to the mismatch in the parametric lines of the original higher-order facet and the linearised subfacets. The proposed formulation passes the benchmark of the contact patch test for uniform transmission of contact pressure with accuracy nearly the same as the element patch test. For increasingly higher dissimilarity in element sizes in the case of Hertzian contact, first-order elements suffer from increased oscillations, whereas the second-order elements, having nonlinear shape functions that can better represent the continuous deformation of boundaries, provide a more accurate solution. The smoothness of the solution can be improved by better controlling the interpenetration through a suitable choice of penalty parameter. Finally, the formulation can also produce the atypical distribution of nodal forces for higher-order elements, thus maintaining consistency with the nonlinear nature of these elements. Hence, it can be argued that using higher-order elements in complex geometries can better capture the surface curvature and help in modelling the contact problems with better predictions.

References

[6] Heinrich Hertz. “Ueber die Berührung fester elastischer Körper.” en. In: *crll* 1882.92 (1882), pp. 156–171.

[12] Michael A. Puso and Tod A. Laursen. “A mortar segment-to-segment contact method for large deformation solid mechanics”. en. In: *Computer Methods in Applied Mechanics and Engineering* 193.6 (2004), pp. 601–629.

[13] Michael A. Puso and Tod A. Laursen. “A mortar segment-to-segment frictional contact method for large deformations”. en. In: *Computer Methods in Applied Mechanics and Engineering* 193.45 (2004), pp. 4891–4913.

[40] Thomas JR Hughes, Robert L Taylor, and Worsak Kanoknukulchai. “A finite element method for large displacement contact and impact problems”. In: *Formulations and computational algorithms in FE analysis* (1977), pp. 468–495.

[55] Ivan E. Sutherland and Gary W. Hodgman. “Reentrant polygon clipping”. In: *Communications of the ACM* 17.1 (1974), pp. 32–42.

[62] J. O. Hallquist. *NIKE2D: An implicit, finite-deformation, finite-element code for analyzing the static and dynamic response of two-dimensional solids*. Tech. rep. California Univ., Livermore (USA). Lawrence Livermore Lab., 1979.

[65] R. L. Taylor and Panayiotis Papadopoulos. "On a patch test for contact problems in two dimensions". In: *Computational methods in nonlinear mechanics* 690 (1991), p. 702.

[70] Kent T. Danielson. "Curved node-to-face contact schemes for higher-order finite elements in lumped-mass explicit methods". en. In: *Computer Methods in Applied Mechanics and Engineering* 395 (2022), p. 115056.

[75] Christine Bernardi, Naïma Debit, and Yvon Maday. "Coupling finite element and spectral methods: first results". en. In: *Mathematics of Computation* 54.189 (1990), pp. 21–39.

[76] Michael A. Puso. "A 3D mortar method for solid mechanics". en. In: *International Journal for Numerical Methods in Engineering* 59.3 (2004), pp. 315–336.

[77] Alexander Popp et al. "A dual mortar approach for 3D finite deformation contact with consistent linearization". en. In: *International Journal for Numerical Methods in Engineering* 83.11 (2010), pp. 1428–1465.

[78] R. Pinto Carvalho et al. "An efficient algorithm for rigid/deformable contact interaction based on the dual mortar method". en. In: *Computational Mechanics* (2022).

[81] T. W. McDevitt and T. A. Laursen. "A mortar-finite element formulation for frictional contact problems". en. In: *International Journal for Numerical Methods in Engineering* 48.10 (2000), pp. 1525–1547.

[82] Michael A. Puso, T. A. Laursen, and Jerome Solberg. "A segment-to-segment mortar contact method for quadratic elements and large deformations". en. In: *Computer Methods in Applied Mechanics and Engineering* 197.6 (2008), pp. 555–566.

[85] G. R. Cowper. "Gaussian quadrature formulas for triangles". en. In: *International Journal for Numerical Methods in Engineering* 7.3 (1973), pp. 405–408.

[86] D. A. Dunavant. "High degree efficient symmetrical Gaussian quadrature rules for the triangle". en. In: *International Journal for Numerical Methods in Engineering* 21.6 (1985), pp. 1129–1148.

[87] Indrajeet Sahu. *Bilinear-Inverse-Mapper: Analytical Solution and Algorithm for Inverse Mapping of Bilinear Interpolation of Quadrilaterals*. en. SSRN Scholarly Paper. Rochester, NY, 2024.

[102] M. Tur, F. J. Fuenmayor, and P. Wriggers. "A mortar-based frictional contact formulation for large deformations using Lagrange multipliers". en. In: *Computer Methods in Applied Mechanics and Engineering* 198.37 (2009), pp. 2860–2873.

[105] Kathrin A. Fischer and Peter Wriggers. "Mortar based frictional contact formulation for higher order interpolations using the moving friction cone". In: *Computer Methods in Applied Mechanics and Engineering*. John H. Argyris Memorial Issue. Part I 195.37 (2006), pp. 5020–5036.

[108] Indrajeet Sahu and Nik Petrinic. "Midplane based 3D single pass unbiased segment-to-segment contact interaction using penalty method". In: *forthcoming* (2024).

[114] Robert S. Browning, Kent T. Danielson, and David L. Littlefield. "Second-order pyramid element formulations suitable for lumped-mass explicit methods in nonlinear solid mechanics". In: *Computer Methods in Applied Mechanics and Engineering* 405 (2023), p. 115854.

[115] A. Popp et al. "Dual Quadratic Mortar Finite Element Methods for 3D Finite Deformation Contact". In: *SIAM Journal on Scientific Computing* 34.4 (2012), B421–B446.

[116] Bin Yang, Tod A. Laursen, and Xiaonong Meng. "Two dimensional mortar contact methods for large deformation frictional sliding". en. In: *International Journal for Numerical Methods in Engineering* 62.9 (2005), pp. 1183–1225.

[117] Christopher Steimer, Matthias Mayr, and Alexander Popp. "Targeting a faster time-to-solution of mortar-based contact problems". en. In: *PAMM* (2023), e202300157.

[118] Markus Gitterle et al. "Finite deformation frictional mortar contact using a semi-smooth Newton method with consistent linearization". en. In: *International Journal for Numerical Methods in Engineering* 84.5 (2010), pp. 543–571.

[119] A. Popp and W. A. Wall. "Dual mortar methods for computational contact mechanics – overview and recent developments". en. In: *GAMM-Mitteilungen* 37.1 (2014), pp. 66–84.

[120] Dongyu Liu et al. "An interface-enriched generalized finite element formulation for locking-free coupling of non-conforming discretizations and contact". en. In: *Computational Mechanics* 70.3 (2022), pp. 477–499.

[121] Alexander Konyukhov and Karl Schweizerhof. "Incorporation of contact for high-order finite elements in covariant form". In: *Computer Methods in Applied Mechanics and Engineering*. HOFEM07 198.13 (2009), pp. 1213–1223.

[122] V. Padmanabhan and T. A. Laursen. "A framework for development of surface smoothing procedures in large deformation frictional contact analysis". en. In: *Finite Elements in Analysis and Design* 37.3 (2001), pp. 173–198.

[123] Kent T. Danielson and James L. O'Daniel. "Reliable second-order hexahedral elements for explicit methods in nonlinear solid dynamics". en. In: *International Journal for Numerical Methods in Engineering* 85.9 (2011), pp. 1073–1102.

[124] Kent T. Danielson, Mark D. Adley, and T. Neil Williams. "Second-order finite elements for Hex-Dominant explicit methods in nonlinear solid dynamics". en. In: *Finite Elements in Analysis and Design* 119 (2016), pp. 63–77.

[125] Indrajeet Sahu and Nik Petrinic. "Patch based unbiased 3D frictional contact formulation for finite element algorithms". In: *forthcoming* (2024).

5.8 Supplementary discussion

As contact is essentially a constraint of boundary conditions, a better retention of original curvature aids in the accurate modelling. This final chapter has taken the arc of frictional contact modelling to its concluding point by presenting the contact model for the most complex challenge of higher-order elements that can represent curved surfaces with higher accuracy compared to the first-order elements. The methodology presented here extended the work on first-order elements by a careful subdivision of higher-order element facets into subfacets that helped in high-accuracy constraint enforcement on the sharp curvatures.

First-order elements are still widely used in practice, more often than the second-order elements. As this work has shown the benefits of higher-order elements in contact problems and knowing that the contact is a boundary-driven effect, a hybrid approach of using second-order elements on the outer surface and first-order elements in the rest of the internal bulk can provide their dual benefit. However, to maintain the continuity of the displacement field in the discretised domain, a layer of transition elements will be needed to ensure the compatibility of shape functions. Finite element solutions without these transition elements will be invalid. Yet, the collision problem of three spheres was studied using a hybrid approach but without any transition elements. The momentum variation in the plot was visibly indistinguishable from the case of using higher-order elements in the entire domain shown in the paper. So, while this solution is mathematically invalid, it provided a promising result for the hybrid approach. However, this problem has not been included in the paper to maintain the sanctity of the FEM.

This chapter solely focused on the development of algorithms for second-order elements. However, the core idea of subdividing facets to form contact pairs of subfacets for enforcing both compressive load and frictional constraints can be readily extended to all other higher-order elements, thus providing a single-pass unbiased contact model for all complex surfaces.

6
Conclusion and outlook

In this final chapter, the body of the research presented in this work is briefly redescribed with a bird's eye view by highlighting major achievements in the summary, some potential limitations and their remedies, and a future perspective on possibilities that lie ahead.

6.1 Summary and achievements

In this thesis, novel computational contact formulations have been proposed in the context of nonlinear solid mechanics with a special focus on the development of unbiased frictionless and frictional contact techniques for both first and higher-order finite element discretisation. Initially, a brief account of continuum mechanics and finite elements was provided prior to outlining some fundamental concepts in computational contact mechanics and the challenges therein. A description of currently used methodologies and their disadvantages was presented to elucidate the gaps in the literature. These shortcomings motivated the inception of unbiased contact formulations that can model physical systems with high accuracy in a single pass. Enforcing contact constraints in systems adds to the numerical complexity and computational cost, so developing a single-pass strategy with the choice of penalty method allows us to keep the system size unchanged.

The development of unbiased contact formulations with explicit finite element method allows to expand the scope of applicability of explicit FEM with high accuracy being a direct and major contribution in this work. Besides high accuracy, proposed methodologies render benefits on multiple fronts. The unbiased normal traction and equivalent nodal force determination are directly based on the contact region between interacting segments, which implies a direct benefit to corner cases like self-contact problems. Similar consideration of contact region in the unbiased frictional contact formulation also accounts for the self-contact problems. Initiating the developments for first-order elements and further advancing them for higher-order elements to provide improved accuracy offers a wide range of element choices for analysis. The work has been presented in three pieces which can be summarised as -

Firstly, the concept of using midplane to determine the normal contact tractions in an unbiased manner was proposed with first-order elements. Without master-slave discrimination of contacting surfaces, the proposed approach directly penalises the true interpenetration between the surfaces along normal to the midplane. The approach of using STS contact by focusing on the overlap between contacting segments and evaluating tractions over the common region provides robustness and versatility, which was demonstrated through a multitude of numerical experiments. A contact patch test with nonconformal meshes and a range of materials with stiffness varying in magnitudes of order yielded results that matched the accuracy of the element patch test. In other words, the contact algorithm performs as accurately as the underlying elements for contact between flat surfaces. This result was far superior to the error observed when using NTS-AR ([89]) even though it was modified into a double-pass version. Hertzian contact, for testing contact with curved surfaces, provided very accurate results for a wide range of material stiffness. However, the contact pressure distribution showed oscillations in the fine mesh when the disparity in contacting element sizes was high, and a high penalty was used. These oscillations are a result of irregular interpenetration gaps and the linear shape functions used in the first-order discretisation of surfaces, thus highlighting the importance of allowing and controlling the interpenetration gap to reduce the

oscillations in contact pressure. A two-beam test with flat and curved surfaces showed the physical and locking-free behaviour of the proposed algorithm. The indentation test with a rigid flat punch converged towards the analytical solution with mesh refinement and increasing penalty. The unbiased nature is significantly advantageous in self-contact tests, showing a realistic behaviour for compression of a block with cracks and cavities. It also showed excellent accuracy with carefully chosen two other problems, having flat and curved surfaces in contact. Further tests of collision between two bars and between the sphere and a platform showed the algorithm's capability to handle dynamic problems. In particular, the high-speed collision between two inelastic bars with curved interface showed its effectiveness in high-rate large deformation problems.

Secondly, a completely new patch-based frictional contact formulation was developed that retains the advantages of an unbiased and single-pass strategy. Directly continuing the focus on contact between segments and enforcement of contact constraints on their shared region, the predictor-corrector approach with penalty regularisation was utilised in devising the frictional formulation. By leveraging the changes in the convective coordinates of representative contact points between the contacting segments, relative sliding between them can be defined for use in tangential traction prediction. This is in complete contrast to the notion of considering the sliding of slave nodes over the master surface. The return mapping algorithm applied over the cone of friction helps in correcting the tangential traction to enforce the notion of stick or slip on each patch of the shared region between STS pairs. This information is further relayed to apply tangential nodal forces based on normal nodal forces calculated with respect to each patch, consequently maintaining consistency in normal and tangential nodal forces per shared patch. The robust, wide-ranging applicability of this formulation was shown through stick-slip study in static as well as dynamic cases. As this formulation is based on the elastoplastic analogy of friction, it allows a very small sliding in the stick phase; however, a stick case of friction using a block on a slab with varying penalties showed a decrease in sliding length with the increasing tangential

penalty. Subsequent tests on the transition between the stick-slip phase and a study on microslip were studied through the sliding of a block over a slab and the frictional Hertzian problem, respectively. Further, frictional torque, frictional impact and rolling were studied through twisting indentation problems, oblique impact of a ring, and rolling of the cylinder, respectively. Thus verifying its excellent performance in a diverse range of problems.

Thirdly, unbiased single-pass contact between higher-order elements was developed by extending and refining the frictionless and frictional contact methodologies proposed with first-order elements. Higher-order elements can better capture the complexity of surface description with their higher-order basis functions. The complexity of multiple nodes defining the nonlinear facets was reduced by subdivision into subfacets for considering subfacet-to-subfacet interaction. Both normal and tangential tractions were evaluated per pair of subfacets and concurrently applied on main facets in the form of nodal forces. A parametric affine mapping from linearised subfacets to main facets is utilised in providing an approximation of the convective coordinates of the main facet at each quadrature point in the overlap projections of linearised subfacets. Errors incurred in the solution due to this linear approximation depend upon variation of parametric lines, which has been explained graphically. The construction of midplanes using linearised subfacets is more approximate in nature, so an additional midplane correction can be carried out depending on the curvature of physical surfaces about the interpenetration centroid. This is particularly required in obtaining high-accuracy results in dynamic contact and has been shown through the elastic collision between spherical balls. The use of higher-order elements exceeds the accuracy of first-order elements in minimising errors appearing in terms of the misaligned direction of momentum transfer. Similar to first-order elements, the algorithm was studied for contact patch test and Hertzian contact. Similar to first-order elements, the contact patch test, in this case, showed an accuracy level matching the accuracy of underlying finite elements. Its performance in Hertzian contact offered superior results compared to first-order elements due to its ability to better model surface curvature with continuous deformation in contact region

owing to the nonlinear shape functions. Lastly, a sliding frictional contact problem showed an expected atypical nonlinear distribution of nodal forces due to nonlinear shape functions in both stick and slip phases of friction.

In conclusion, this thesis has provided a holistic framework of frictional contact modelling with an overarching theme of integrating various finite element topologies. The development started with the conception of techniques for frictionless contact between the simple yet non-trivial, first-order elements. Subsequent advancements made to devise the friction formulation retained the unbiased capability introduced for consideration of normal contact. Knowing that the most general contact problems involve curved surfaces, the increased complexity of higher-order elements was introduced and studied for normal and frictional traction evaluation with the same key characteristics - unbiased and single-pass. Here, a key advantage of single-pass technique over a similar dual-pass technique is that the computational cost is halved.

6.2 Limitations and remedies

The range of developments presented in this thesis provides a holistic set of methodologies to model frictional contact problems with high accuracy. While this modelling achieves a high accuracy, there are some limitations to the approach.

The proposed methodology is based on the penalty method, so it naturally inherits the limitation of solution dependency upon the penalty parameter. The original contact problem mandates physical impenetrability, but it is violated by the penalty method. While a soft penalty will lead to higher interpenetration, the use of a very high value leads to oscillations in the solution, and an extremely high value will induce instability. The effect of interpenetration did not affect the uniformity of stress distributions in contact patch tests. However, their absolute values were different, but the variation was minor for increasingly higher penalties, implying a convergence. Also, the interpenetration between surfaces is not completely problematic, as has been shown in the case of first-order elements in Chapter 3, Fig. 3.23 for Hertzian contact between curved surfaces with higher discrepancy in element sizes. For first-order elements having linear shape functions, higher discrepancy from

the original curved surface, and sharper changes in boundary normals at corner nodes, the oscillations in contact traction can be minimised by allowing interpenetration in a controlled manner with suitable penalties for obtaining a smooth solution.

In events of large deformation, the discrepancy between any original domain Ω and its discretised version Ω_h gets accentuated on the boundaries. Enforcing contact constraints on such boundaries with dissimilar element sizes would lead to an increased deviation from the physical behaviour as has been shown for inelastic collision with dissimilar meshes in Chapter 3 Fig. 3.31. Thus, having prior knowledge of contact at boundaries of bodies undergoing large deformation can aid in careful, conformal or sufficiently fine discretisation of boundaries.

In frictional contact between segments on opposite surfaces, configurational changes only account for the relative sliding and not any relative rotation about the representative contact point. This causes an apparent loss in the frictional behaviour prediction. However, this is not entirely irremediable, as relative motion between neighbouring segment pairs can account for rotation between the surfaces. Moreover, an increase in mesh refinement will also better factor in local relative configurational changes.

The frictional formulation presented here is based on the elastoplastic analogy, so it allows relative sliding in the stick state with a gradual increase in the tangential traction before transitioning to the slip state with the limiting value of friction. The sliding in the stick state implies a restriction on the minimum size of the shared patch between contacting segments for a given penalty and normal load to allow the transition to the slip zone well before the contact breaks due to relative sliding. Such a restriction will also exist in the traditional formulations [16][15][17] considering sliding of slave nodes over the master surface. However, in the practical scenarios, the chosen penalties are sufficiently high, and the sliding corresponding to the stick zone is much smaller than the facet sizes. It is only in the case of extremely high penalties that even a tiny amount of sliding due to numerical disturbances will lead to a sudden shift to the slip state.

In the higher-order elements, the use of linearised subsegments with affine mapping to estimate the physical gap of interpenetration incurs an error due to the mismatch in the parametric lines of projection of the physical segment and linearised subsegment. Although inverse mapping of bilinear segments is used for computational speed in this work so far, an iterative approach to evaluate the exact convective coordinates of the physical surface normally over the quadrature points will be able to avoid the error incurred with the use of affine mapping.

6.3 Future perspectives

Research presented in this thesis has provided numerous advances in frictional contact algorithms for complex surface descriptions, yet the landscape of possible research opportunities in computational contact mechanics is huge, some of which are discussed below.

In the context of the presented research, numerous capabilities can be developed and studied. The presented discretisation approaches focused only on first and higher-order hexahedral elements. However, the proposed methodology can also be extended to tetrahedral elements, often used in some applications, along with their first and higher-order discretisation [82][78]. Constraint enforcement only utilised linear penalty in this work; however, studying non-linear penalties together with varying interpenetration gaps can provide some new insights. The algorithm of finding interpenetration and subsequent application of nodal forces can be directly used together with the consideration of barycentric coordinates for triangular facets in lieu of the parametric coordinates of bilinear interpolation used for quad facets here. Generally, there is a high-stress gradient around contact regions in most geometries, so the use of adaptive meshing will provide a better representation of stress distribution.

Modelling the complete tribological phenomenon would require integrating the effects of friction, wear and lubrication [49]. Although the effect of friction studied in this work has been considered for a constant coefficient, models should consider including the effect of relative velocity, surface roughness, normal load and state

variables like temperature. Based on the frictional formulation proposed in this work, it can be easily seen that the specific alignments of material lines of both surfaces can be directly incorporated in any future work so that the effect of frictional anisotropy can be conveniently analysed. Further, studying adhesion in combination with compressive and frictional effects will provide a more comprehensive contact model. Further practical tribological models that include the effect of elastohydrodynamics (EHL) will be of immense practical utility.

Strictly speaking, contact is a multiscale phenomenon that encompasses atomistic interactions to the micromechanical contact between asperities [111] spanning different timescales, see [1]. So, a more realistic model should incorporate changes across multiple length scales and timescales. Additionally, many engineering systems also have a multiphysics nature, so physical models should have a coupled integrated effect of different phenomena - thermal, electrical, magnetic, and even surface chemistry. Contact between two solids having different temperature profiles induces thermoelastic deformation, which alters the contact pressure distribution, resulting in changes in the contact area, which in turn affects the boundary conditions for the heat conduction problem, thereby representing a coupled thermo-mechanical problem[97]. Some systems can experience mutual influence between electromagnetic fields and mechanical deformation and require a coupled computational approach. Contact between fluids and structure is a common engineering problem, so studying fluid-structure interaction with contact is an ongoing research endeavour.

With increasing computational power, ambitious predictive capabilities are now being targeted towards large-scale simulation using high-performance computing. Here, parallelisation of contact together with load balancing is a complex challenge, especially when problems of self-contact are considered. Large-scale systems like gas turbine engines require multiphysics capabilities with a refined approach to handle critical operations like contact.

For establishing trust in computational models, their verification and validation are critical. While verification by analysing code and comparing numerical solutions against analytical solutions is a computational procedure, validation requires

comparison against experimental results. However, contact interfaces are generally internal to the system, so *in situ* analysis is a complex challenge, so indirect measures like X-ray tomography are used to characterise the surfaces.

Finally, ideas of developing digital twins [126][11], which are virtual systems replicating the physical behaviour using real-time sensor data for continuous accurate prediction of systems, are an emerging trend in industrial space and offer a powerful framework for data-driven insights and performance optimisation.

References

[1] A.I. Vakis et al. “Modeling and simulation in tribology across scales: An overview”. en. In: *Tribology International* 125 (2018), pp. 169–199.

[2] D. M. Neto, M. C. Oliveira, and L. F. Menezes. “Surface Smoothing Procedures in Computational Contact Mechanics”. en. In: *Archives of Computational Methods in Engineering* 24.1 (2017), pp. 37–87.

[3] Yanhong Bei and Benjamin J. Fregly. “Multibody dynamic simulation of knee contact mechanics”. In: *Medical Engineering & Physics*. This issue contains a special section on Neuromodelling 26.9 (2004), pp. 777–789.

[4] James M. Johnston et al. “Simulation, fabrication and impact testing of a novel football helmet padding system that decreases rotational acceleration”. en. In: *Sports Engineering* 18.1 (2015), pp. 11–20.

[5] Udo Nackenhorst. “Finite element analysis of tires in rolling contact”. en. In: *GAMM-Mitteilungen* 37.1 (2014), pp. 27–65.

[6] Heinrich Hertz. “Ueber die Berührung fester elastischer Körper.” en. In: *crll* 1882.92 (1882), pp. 156–171.

[7] K. L. Johnson. *Contact mechanics*. en. Cambridge University Press, 1985.

[8] J.R. Barber. *Contact Mechanics*. en. Vol. 250. Solid Mechanics and Its Applications. Cham: Springer International Publishing, 2018.

[9] Wing Kam Liu, Shaofan Li, and Harold S. Park. “Eighty Years of the Finite Element Method: Birth, Evolution, and Future”. en. In: *Archives of Computational Methods in Engineering* (2022).

[10] Alberto Ferrari and Karen Willcox. “Digital twins in mechanical and aerospace engineering”. en. In: *Nature Computational Science* 4.3 (2024), pp. 178–183.

[11] Mengnan Liu et al. “Review of digital twin about concepts, technologies, and industrial applications”. en. In: *Journal of Manufacturing Systems*. Digital Twin towards Smart Manufacturing and Industry 4.0 58 (2021), pp. 346–361.

[12] Michael A. Puso and Tod A. Laursen. “A mortar segment-to-segment contact method for large deformation solid mechanics”. en. In: *Computer Methods in Applied Mechanics and Engineering* 193.6 (2004), pp. 601–629.

[13] Michael A. Puso and Tod A. Laursen. “A mortar segment-to-segment frictional contact method for large deformations”. en. In: *Computer Methods in Applied Mechanics and Engineering* 193.45 (2004), pp. 4891–4913.

[14] M.A. Puso and J.M. Solberg. “A dual pass mortar approach for unbiased constraints and self-contact”. en. In: *Computer Methods in Applied Mechanics and Engineering* 367 (2020), p. 113092.

[15] Peter Wriggers. *Computational contact mechanics*. en. Hoboken, NJ: J. Wiley & Sons, 2002.

[16] Tod A. Laursen. *Computational Contact and Impact Mechanics*. en. Berlin, Heidelberg: Springer Berlin Heidelberg, 2003.

[17] Roger A. Sauer and Laura De Lorenzis. "An unbiased computational contact formulation for 3D friction". en. In: *International Journal for Numerical Methods in Engineering* 101.4 (2015), pp. 251–280.

[18] K. Schweizerhof and A. Konyukhov. "Covariant description for frictional contact problems". en. In: *Computational Mechanics* 35.3 (2005), pp. 190–213.

[19] C. S. Jog. *Continuum mechanics*. en. Third edition. Foundations and applications of mechanics volume 1. Delhi, India: Cambridge University Press, 2015.

[20] Javier Bonet and Richard D. Wood. *Nonlinear Continuum Mechanics for Finite Element Analysis*. en. Cambridge University Press, 1997.

[21] Gerhard A. Holzapfel. *Nonlinear solid mechanics: a continuum approach for engineering*. en. Chichester ; New York: Wiley, 2000.

[22] Lallit Anand and Sanjay Govindjee. *Continuum Mechanics of Solids*. en. 1st ed. Oxford University PressOxford, 2020.

[23] A. J. M. Spencer. *Continuum mechanics*. en. Dover ed. Mineola, N.Y: Dover Publications, 2004.

[24] Fionn Dunne and Nik Petrinic. *Introduction to computational plasticity*. en. Oxford ; New York: Oxford University Press, 2005.

[25] Nam-Ho Kim. *Introduction to Nonlinear Finite Element Analysis*. en. New York, NY: Springer US, 2015.

[26] Peter Howell and J. R. Ockendon. *Applied solid mechanics*. eng. Cambridge, UK: Cambridge University Press, 2009.

[27] E. A. De Souza Neto, D. Perić, and D. R. J. Owen. *Computational Methods for Plasticity: Theory and Applications*. en. 1st ed. Wiley, 2008.

[28] R. W. Ogden. *Non-linear elastic deformations*. en. Mineola, N.Y: Dover Publications, 1997.

[29] Martin H. Sadd. *Elasticity: theory, applications, and numerics*. en. Amsterdam ; Boston: Elsevier Butterworth Heinemann, 2005.

[30] Stephen Timoshenko and James Norman Goodier. *Theory of Elasticity*. en. McGraw-Hill, 1969.

[31] A. Curnier. "A Theory of Friction". en. In: *Unilateral Problems in Structural Analysis*. Ed. by Gianpietro Del Piero and Franco Maceri. International Centre for Mechanical Sciences. Vienna: Springer, 1985, pp. 47–56.

[32] R Michalowski Z Mroz. "Associated and non-associated sliding rules in contact friction problems." In: *Archiv. Mech.* 30 (1978), pp. 259–276.

[33] Vladislav Yastrebov. "Computational contact mechanics: geometry, detection and numerical techniques". en. PhD thesis. École Nationale Supérieure des Mines de Paris, 2011.

[34] Klaus-Jürgen Bathe. *KJ Bathe – Finite element procedures*. en. 2nd ed. Englewood Cliffs, N.J: Prentice-Hall, 2014.

[35] Ted Belytschko et al. *Nonlinear finite elements for continua and structures*. Second edition. Chichester, West Sussex, United Kingdon: Wiley, 2014.

[36] Ted Belytschko, Thomas JR Hughes, and P Burgers. "Computational methods for transient analysis". In: (1985).

[37] O. C. Zienkiewicz, Robert L. Taylor, and J. Z. Zhu. *The finite element method: its basis and fundamentals*. Seventh edition. Amsterdam: Elsevier, Butterworth-Heinemann, 2013.

[38] O. C. Zienkiewicz, Robert L. Taylor, and David Fox. *The finite element method for solid and structural mechanics*. en. 7th ed. Amsterdam ; Boston: Elsevier/Butterworth-Heinemann, 2014.

[39] Junuthula Narasimha Reddy. *An introduction to the finite element method*. eng. reprinted. McGraw-Hill series in mechanical engineering. Oxford: Oxford Univ. Press, 2006.

[40] Thomas JR Hughes, Robert L Taylor, and Worsak Kanoknukulchai. "A finite element method for large displacement contact and impact problems". In: *Formulations and computational algorithms in FE analysis* (1977), pp. 468–495.

[41] Jacob Fish and Ted Belytschko. *A First Course in Finite Elements*. en.

[42] Ray W. Clough and Joseph Penzien. *Dynamics of structures*. 2nd ed. New York: McGraw-Hill, 1993.

[43] David V. Hutton. *Fundamentals of finite element analysis*. eng. Internat. ed. McGraw-Hill series in mechanical engineering. Boston: McGraw-Hill, 2004.

[44] S. Duczek and H. Gravenkamp. "Mass lumping techniques in the spectral element method: On the equivalence of the row-sum, nodal quadrature, and diagonal scaling methods". en. In: *Computer Methods in Applied Mechanics and Engineering* 353 (2019), pp. 516–569.

[45] Robert Browning, Kent Danielson, and Mark Adley. "Higher-order finite elements for lumped-mass explicit modeling of high-speed impacts". In: *International Journal of Impact Engineering* 137 (2020), p. 103458.

[46] Vladislav A. Yastrebov. *Numerical methods in contact mechanics*. en. Numerical methods in engineering series. London : Hoboken, NJ: ISTE ; Wiley, 2013.

[47] Alexander Konyukhov and Karl Schweizerhof. *Computational Contact Mechanics*. en. Vol. 67. Lecture Notes in Applied and Computational Mechanics. Berlin, Heidelberg: Springer Berlin Heidelberg, 2013.

[48] Alexander Konyukhov. *Introduction to computational contact mechanics: a geometrical approach*. en. John Wiley & Sons, 2015.

[49] Alexander Popp and Peter Wriggers, eds. *Contact Modeling for Solids and Particles*. en. Vol. 585. CISM International Centre for Mechanical Sciences. Cham: Springer International Publishing, 2018.

[50] Giorgio Zavarise and Peter Wriggers, eds. *Trends in Computational Contact Mechanics*. en. Lecture Notes in Applied and Computational Mechanics. Berlin Heidelberg: Springer-Verlag, 2011.

[51] Alexander Popp. “Mortar Methods for Computational Contact Mechanics and General Interface Problems”. PhD thesis. Technical University of Munich, 2012.

[52] Diogo Mariano Simões Neto. “Numerical Simulation of Frictional Contact Problems Using Nagata Patches in Surface Smoothing”. English. Ph.D. Portugal: Universidade de Coimbra (Portugal), 2014.

[53] Peter Wriggers. *Chapter Summaries for Computational Contact Mechanics - Summary*. en. Berlin, Heidelberg: Springer Berlin Heidelberg, 2006.

[54] Javier Bonet and Jaime Peraire. “An alternating digital tree (ADT) algorithm for 3D geometric searching and intersection problems”. en. In: *International Journal for Numerical Methods in Engineering* 31.1 (1991), pp. 1–17.

[55] Ivan E. Sutherland and Gary W. Hodgman. “Reentrant polygon clipping”. In: *Communications of the ACM* 17.1 (1974), pp. 32–42.

[56] A. Munjiza, D.R.J. Owen, and N. Bicanic. “A combined finite-discrete element method in transient dynamics of fracturing solids”. en. In: *Engineering Computations* 12.2 (1995), pp. 145–174.

[57] Thomas J. R. Hughes et al. “A finite element method for a class of contact-impact problems”. en. In: *Computer Methods in Applied Mechanics and Engineering* 8.3 (1976), pp. 249–276.

[58] Seungmin Jin et al. “A node-to-node scheme with the aid of variable-node elements for elasto-plastic contact analysis”. en. In: *International Journal for Numerical Methods in Engineering* 102.12 (2015), pp. 1761–1783.

[59] Seungmin Jin, Dongwoo Sohn, and Seyoung Im. “Node-to-node scheme for three-dimensional contact mechanics using polyhedral type variable-node elements”. en. In: *Computer Methods in Applied Mechanics and Engineering* 304 (2016), pp. 217–242.

[60] Weiwei Xing, Chongmin Song, and Francis Tin-Loi. “A scaled boundary finite element based node-to-node scheme for 2D frictional contact problems”. In: *Computer Methods in Applied Mechanics and Engineering* 333 (2018), pp. 114–146.

[61] Weiwei Xing et al. “A node-to-node scheme for three-dimensional contact problems using the scaled boundary finite element method”. en. In: *Computer Methods in Applied Mechanics and Engineering* 347 (2019), pp. 928–956.

[62] J. O. Hallquist. *NIKE2D: An implicit, finite-deformation, finite-element code for analyzing the static and dynamic response of two-dimensional solids*. Tech. rep. California Univ., Livermore (USA). Lawrence Livermore Lab., 1979.

[63] J. O. Hallquist, G. L. Goudreau, and D. J. Benson. “Sliding interfaces with contact-impact in large-scale Lagrangian computations”. In: *Computer Methods in Applied Mechanics and Engineering* 51.1 (1985), pp. 107–137.

[64] D. P. Flanagan and T. Belytschko. “A uniform strain hexahedron and quadrilateral with orthogonal hourglass control”. en. In: *International Journal for Numerical Methods in Engineering* 17.5 (1981), pp. 679–706.

[65] R. L. Taylor and Panayiotis Papadopoulos. “On a patch test for contact problems in two dimensions”. In: *Computational methods in nonlinear mechanics* 690 (1991), p. 702.

[66] Giorgio Zavarise and Laura De Lorenzis. “A modified node-to-segment algorithm passing the contact patch test”. en. In: *International Journal for Numerical Methods in Engineering* 79.4 (2009), pp. 379–416.

[67] Giorgio Zavarise and Laura De Lorenzis. “The node-to-segment algorithm for 2D frictionless contact: Classical formulation and special cases”. en. In: *Computer Methods in Applied Mechanics and Engineering* 198.41 (2009), pp. 3428–3451.

[68] Chao Sun et al. “A novel node-to-segment algorithm in smoothed finite element method for contact problems”. en. In: *Computational Mechanics* (2023).

[69] Seung-Hoon Kang, Seok-Min Lee, and SangJoon Shin. “Improved area regularization technique for penalty-method-based node-to-segment contact analysis”. en. In: *Computational Mechanics* 71.4 (2023), pp. 801–825.

[70] Kent T. Danielson. “Curved node-to-face contact schemes for higher-order finite elements in lumped-mass explicit methods”. en. In: *Computer Methods in Applied Mechanics and Engineering* 395 (2022), p. 115056.

[71] Juan C. Simo, Peter Wriggers, and Robert L. Taylor. “A perturbed Lagrangian formulation for the finite element solution of contact problems”. In: *Computer Methods in Applied Mechanics and Engineering* 50.2 (1985), pp. 163–180.

[72] G. Zavarise and P. Wriggers. “A segment-to-segment contact strategy”. en. In: *Mathematical and Computer Modelling* 28.4-8 (1998), pp. 497–515.

[73] Nagi El-Abbasi and Klaus-Jürgen Bathe. “Stability and patch test performance of contact discretizations and a new solution algorithm”. en. In: *Computers & Structures* 79.16 (2001), pp. 1473–1486.

[74] Laura De Lorenzis, Peter Wriggers, and Thomas J. R. Hughes. “Isogeometric contact: a review”. en. In: *GAMM-Mitteilungen* 37.1 (2014), pp. 85–123.

[75] Christine Bernardi, Naïma Debit, and Yvon Maday. “Coupling finite element and spectral methods: first results”. en. In: *Mathematics of Computation* 54.189 (1990), pp. 21–39.

[76] Michael A. Puso. “A 3D mortar method for solid mechanics”. en. In: *International Journal for Numerical Methods in Engineering* 59.3 (2004), pp. 315–336.

[77] Alexander Popp et al. “A dual mortar approach for 3D finite deformation contact with consistent linearization”. en. In: *International Journal for Numerical Methods in Engineering* 83.11 (2010), pp. 1428–1465.

[78] R. Pinto Carvalho et al. “An efficient algorithm for rigid/deformable contact interaction based on the dual mortar method”. en. In: *Computational Mechanics* (2022).

[79] Philipp Farah, Alexander Popp, and Wolfgang A. Wall. “Segment-based vs. element-based integration for mortar methods in computational contact mechanics”. en. In: *Computational Mechanics* 55.1 (2015), pp. 209–228.

[80] T. A. Laursen and J. C. Simo. “A continuum-based finite element formulation for the implicit solution of multibody, large deformation-frictional contact problems”. en. In: *International Journal for Numerical Methods in Engineering* 36.20 (1993), pp. 3451–3485.

[81] T. W. McDevitt and T. A. Laursen. “A mortar-finite element formulation for frictional contact problems”. en. In: *International Journal for Numerical Methods in Engineering* 48.10 (2000), pp. 1525–1547.

[82] Michael A. Puso, T. A. Laursen, and Jerome Solberg. “A segment-to-segment mortar contact method for quadratic elements and large deformations”. en. In: *Computer Methods in Applied Mechanics and Engineering* 197.6 (2008), pp. 555–566.

[83] G. Zavarise et al. “Real contact mechanisms and finite element formulation—a coupled thermomechanical approach”. en. In: *International Journal for Numerical Methods in Engineering* 35.4 (1992), pp. 767–785.

[84] P. Papadopoulos and R.L. Taylor. “A simple algorithm for three-dimensional finite element analysis of contact problems”. en. In: *Computers & Structures* 46.6 (1993), pp. 1107–1118.

[85] G. R. Cowper. “Gaussian quadrature formulas for triangles”. en. In: *International Journal for Numerical Methods in Engineering* 7.3 (1973), pp. 405–408.

[86] D. A. Dunavant. “High degree efficient symmetrical Gaussian quadrature rules for the triangle”. en. In: *International Journal for Numerical Methods in Engineering* 21.6 (1985), pp. 1129–1148.

[87] Indrajeet Sahu. *Bilinear-Inverse-Mapper: Analytical Solution and Algorithm for Inverse Mapping of Bilinear Interpolation of Quadrilaterals*. en. SSRN Scholarly Paper. Rochester, NY, 2024.

[88] Kevin Bronik et al. *DEST documentation*. University of Oxford, 2022.

[89] Seung Lee Kwon et al. “A fully nonlinear three-dimensional dynamic frictional contact analysis method under large deformation with the area regularization”. en. In: *Engineering with Computers* (2023).

[90] K L Johnson. “One Hundred Years of Hertz Contact”. en. In: *Proceedings of the Institution of Mechanical Engineers* 196.1 (1982), pp. 363–378.

[91] Valentin L. Popov, Markus Heß, and Emanuel Willert. *Handbook of Contact Mechanics: Exact Solutions of Axisymmetric Contact Problems*. en. Berlin, Heidelberg: Springer Berlin Heidelberg, 2019.

[92] Nicholas J. Carpenter, Robert L. Taylor, and Michael G. Katona. “Lagrange constraints for transient finite element surface contact”. en. In: *International Journal for Numerical Methods in Engineering* 32.1 (1991), pp. 103–128.

[93] Mengyan Zang, Wei Gao, and Zhou Lei. “A contact algorithm for 3D discrete and finite element contact problems based on penalty function method”. en. In: *Computational Mechanics* 48.5 (2011), pp. 541–550.

[94] James Paul Ahrens, Berk Geveci, and Charles Law. “ParaView: An end-user tool for large-data visualization”. English. In: *Visualization Handbook*. Elsevier, 2005, pp. 717–731.

[95] Utkarsh Ayachit. *The ParaView Guide: A Parallel Visualization Application*. Clifton Park, NY, USA: Kitware, Inc., 2015.

[96] Frank Philip Bowden and David Tabor. *The Friction and Lubrication of Solids*. en. Clarendon Press, 2001.

[97] J.R Barber and M Ciavarella. “Contact mechanics”. en. In: *International Journal of Solids and Structures* 37.1-2 (2000), pp. 29–43.

[98] Bharat Bhushan. *Principles and Applications of Tribology*. en. John Wiley & Sons, 1999.

[99] L. Krstulović Opara, P. Wriggers, and J. Korelc. “A C1-continuous formulation for 3D finite deformation frictional contact”. en. In: *Computational Mechanics* 29.1 (2002), pp. 27–42.

[100] Reese E. Jones and Panayiotis Papadopoulos. “A yield-limited Lagrange multiplier formulation for frictional contact”. en. In: *International Journal for Numerical Methods in Engineering* 48.8 (2000), pp. 1127–1149.

[101] F. J. Gallego and J. J. Anza. “A mixed finite element model for the elastic contact problem”. en. In: *International Journal for Numerical Methods in Engineering* 28.6 (1989), pp. 1249–1264.

[102] M. Tur, F. J. Fuenmayor, and P. Wriggers. “A mortar-based frictional contact formulation for large deformations using Lagrange multipliers”. en. In: *Computer Methods in Applied Mechanics and Engineering* 198.37 (2009), pp. 2860–2873.

[103] A.E. Giannakopoulos. “The return mapping method for the integration of friction constitutive relations”. en. In: *Computers & Structures* 32.1 (1989), pp. 157–167.

[104] Djordje Perić and D. R. J. Owen. “Computational model for 3-D contact problems with friction based on the penalty method”. en. In: *International Journal for Numerical Methods in Engineering* 35.6 (1992), pp. 1289–1309.

[105] Kathrin A. Fischer and Peter Wriggers. “Mortar based frictional contact formulation for higher order interpolations using the moving friction cone”. In: *Computer Methods in Applied Mechanics and Engineering*. John H. Argyris Memorial Issue. Part I 195.37 (2006), pp. 5020–5036.

[106] P. Wriggers and A. Haraldsson. “A simple formulation for two-dimensional contact problems using a moving friction cone”. en. In: *Communications in Numerical Methods in Engineering* 19.4 (2003), pp. 285–295.

[107] L. De Lorenzis, Peter Wriggers, and C. Weißenfels. “Computational Contact Mechanics with the Finite Element Method”. en. In: *Encyclopedia of Computational Mechanics Second Edition*. John Wiley & Sons, Ltd, 2017, pp. 1–45.

[108] Indrajeet Sahu and Nik Petrinic. “Midplane based 3D single pass unbiased segment-to-segment contact interaction using penalty method”. In: *forthcoming* (2024).

[109] J. Lubliner. “A simple theory of plasticity”. In: *International Journal of Solids and Structures* 10.3 (1974), pp. 313–319.

[110] Thang X. Duong and Roger A. Sauer. “A concise frictional contact formulation based on surface potentials and isogeometric discretization”. en. In: *Computational Mechanics* 64.4 (2019), pp. 951–970.

[111] P. Wriggers, T. Vu Van, and E. Stein. “Finite element formulation of large deformation impact-contact problems with friction”. en. In: *Computers & Structures* 37.3 (1990), pp. 319–331.

[112] J. R. Barber. *Elasticity*. en. Vol. 172. Solid Mechanics and Its Applications. Dordrecht: Springer Netherlands, 2010.

[113] Shingo Ozaki, Chihiro Inanobe, and Ken Nakano. "Finite Element Analysis of Precursors to Macroscopic Stick–Slip Motion in Elastic Materials: Analysis of Friction Test as a Boundary Value Problem". en. In: *Tribology Letters* 55.1 (2014), pp. 151–163.

[114] Robert S. Browning, Kent T. Danielson, and David L. Littlefield. "Second-order pyramid element formulations suitable for lumped-mass explicit methods in nonlinear solid mechanics". In: *Computer Methods in Applied Mechanics and Engineering* 405 (2023), p. 115854.

[115] A. Popp et al. "Dual Quadratic Mortar Finite Element Methods for 3D Finite Deformation Contact". In: *SIAM Journal on Scientific Computing* 34.4 (2012), B421–B446.

[116] Bin Yang, Tod A. Laursen, and Xiaonong Meng. "Two dimensional mortar contact methods for large deformation frictional sliding". en. In: *International Journal for Numerical Methods in Engineering* 62.9 (2005), pp. 1183–1225.

[117] Christopher Steimer, Matthias Mayr, and Alexander Popp. "Targeting a faster time-to-solution of mortar-based contact problems". en. In: *PAMM* (2023), e202300157.

[118] Markus Gitterle et al. "Finite deformation frictional mortar contact using a semi-smooth Newton method with consistent linearization". en. In: *International Journal for Numerical Methods in Engineering* 84.5 (2010), pp. 543–571.

[119] A. Popp and W. A. Wall. "Dual mortar methods for computational contact mechanics – overview and recent developments". en. In: *GAMM-Mitteilungen* 37.1 (2014), pp. 66–84.

[120] Dongyu Liu et al. "An interface-enriched generalized finite element formulation for locking-free coupling of non-conforming discretizations and contact". en. In: *Computational Mechanics* 70.3 (2022), pp. 477–499.

[121] Alexander Konyukhov and Karl Schweizerhof. "Incorporation of contact for high-order finite elements in covariant form". In: *Computer Methods in Applied Mechanics and Engineering*. HOFEM07 198.13 (2009), pp. 1213–1223.

[122] V. Padmanabhan and T. A. Laursen. "A framework for development of surface smoothing procedures in large deformation frictional contact analysis". en. In: *Finite Elements in Analysis and Design* 37.3 (2001), pp. 173–198.

[123] Kent T. Danielson and James L. O'Daniel. "Reliable second-order hexahedral elements for explicit methods in nonlinear solid dynamics". en. In: *International Journal for Numerical Methods in Engineering* 85.9 (2011), pp. 1073–1102.

[124] Kent T. Danielson, Mark D. Adley, and T. Neil Williams. "Second-order finite elements for Hex-Dominant explicit methods in nonlinear solid dynamics". en. In: *Finite Elements in Analysis and Design* 119 (2016), pp. 63–77.

[125] Indrajeet Sahu and Nik Petrinic. "Patch based unbiased 3D frictional contact formulation for finite element algorithms". In: *forthcoming* (2024).

[126] David Jones et al. “Characterising the Digital Twin: A systematic literature review”. en. In: *CIRP Journal of Manufacturing Science and Technology* 29 (2020), pp. 36–52.